OBSERVATION OF THE PARITY-VIOLATING POSITRON-SPIN CORRELATION FROM A MAGNETICALLY TRAPPED ^{82}Rb SOURCE

by

Scott G. Crane

A dissertation submitted in partial fulfillment
of the requirements for the degree

of

DOCTOR OF PHILOSOPHY

in

Physics

Approved:

V. Gordon Lind Major Professor	Charles G. Torre Committee Member
W. Farrell Edwards Committee Member	James T. Wheeler Committee Member
Jerry Ridenhour Committee Member	David J. Vieira Committee Member

Thomas L. Kent
Dean of Graduate Studies

UTAH STATE UNIVERSITY
Logan, Utah

2001

ABSTRACT

Observation of the Parity-Violating Positron-Spin

Correlation from a Magnetically

Trapped ^{82}Rb Source

by

Scott G. Crane, Ph.D of Science

Utah State University, 2001

Major Professor: Dr. Gordon V. Lind
Department: Physics

Low-energy nuclear physics experiments have been a key tool used to understand the weak interaction ever since the first demonstration of parity violation by Wu et al. in 1957. Since this time, there has been a need to develop a polarized source of nuclei that can be utilized to test the form of the weak interaction to high-precision. The recently developed atomic physics techniques of laser cooling and magnetic trapping can be employed to confine and polarize radioactive atoms for this purpose. This dissertation demonstrates the feasibility of using trapped radioactive atoms as a source of polarized nuclei through the observation of the parity-violation distribution of positrons originating from a magnetically trapped and polarized ^{82}Rb sample.

(210 pages)

ACKNOWLEDGMENTS

Looking back, I realize that I have many people to thank for making the completion of this degree a reality. First and foremost I thank my parents, Sharon A. and Gary W.Crane, who, to my amazement, were able to raise ¯ve kids with enough attention and love for all of us to succeed. My siblings, Wendy Stroschein, Tammy Cronin, Laurel Abeyta, and Travis Crane, are the great \Crane family" support network and I am so thankful that we have each other. I thank Dr. Gordon V. Lind for helping me ¯nd a direction of research at Los Alamos when I was at a loss for what to do. Many thanks go to Dr. David J. Vieira for giving me the opportunity to work on a world-class experiment. I have learned a great deal from observing the way that you conduct your research. Dr. Ralf Guckert and Dr. Xinxin Zhao were two of the very best teachers that I could have hoped for when I ¯rst arrived at Los Alamos. Ralf taught me the German method of oiling a creaking government machine and Xixin's passion for life and for physics is simply contagious. Thanks to Dr. Andrew Hime for many fruitful discussions and for helping me to understand the nuclear physics aspects of this experiment. All of the experimenters owe a great deal to Loyal D. Benham, who possesses the knowledge and skill to make beautiful electronic devises. Also thanks to all of those who have read and commented on this dissertation.

My stay in Los Alamos has been a great experience because of the many interesting people that I've met here. Thanks to Glenn Michel for being a great friend and for re-introducing me to the world of the great outdoors. Despite the best e®orts of Jon Haradon, Matt Holmes, and Gary Parker, I have ¯nished this dissertation. It's just a good thing that I started bringing the laptop on all the road trips. Finally, thanks to the many other people who have been so important to me over the last few years.

Scott G. Crane

CONTENTS

Page

ABSTRACT iii

ACKNOWLEDGMENTS iv

LIST OF TABLES viii

LIST OF FIGURES ix

CHAPTER

1 PARITY VIOLATION AND THE WEAK INTERACTION 1

I. THE ELUCIDATION OF THE WEAK INTERACTION 2
II. BEYOND THE STANDARD MODEL 10
III. DISSERATAION OUTLINE 14

2 MAGNETO-OPTICAL TRAPPING OF RADIOACTIVE ^{82}Rb ATOMS 16

I. ATOMIC COOLING AND TRAPPING 26
II. TRAPPING RADIOACTIVE ATOMS 37
III. A SYSTEM FOR TRAPPING RADIOACTIVE ATOMS 41

A. Zr foil implantation and release studies 41
B. Multiple isotope laser trapping set-up 42
C. Calculating the number of trapped atoms 50
D. SC-77 dry-film cell coatings 53

3 PARITY VIOLATION OBSERVED IN THE BETA DECAY OF MAGNETICALLY TRAPPED ^{82}Rb ATOMS 57

I. THE TOP TRAP AS A TOOL FOR PRODUCING A POLARIZED SOURCE 68

A. Magnetic trapping and the TOP trap 68
B. The B-field of a single loop of wire 71
C. An accurate Approximation 74

Page

D. The TOP trap potential 78
E. The density distribution of the atom cloud 79
F. The bias frequency 80
G. Polarization 81
H. Results of the TOP trap model 86

II. HARDWARE FPR THE MAGNETIC TRAP AND BETA-DETECTION 88

A. Double MOT system 88
B. The beta-chamber 92
C. The TOP quadrupole and bias coils 96
D. Experiment control system 102
E. Beta-detector and data acquisition 103

III. TRANSFER AND TRAPPING IN THE BETA-CHAMBER 109

A. MOT-to-MOT Transfer 109
B. Molasses cooling, optical pumping and TOP loading 112
C. TOP, MOT and Quad Trapping Characteristics 117

IV. ^{82}Rb POSITRON-SPIN CORRELATION IN THE STANDARD MODEL 122
V. ANGULAR DISTRIBUTION 130

A. Experimental measurement of the angular distribution 130
B. Wiggle and phase corrections to the angular distribution 134

VI. BACKGROUND ANALYSIS AND INFERRED POLARIZATION 136

A. Source of background 136
B. Tests performed to determine background 141
C. Background analysis in the beta-asymmetry experiment 142
D. Inferred polarization 149

Page

VII. POSITRON ENERGY DISTRIBUTION 152

4 HYPERFINE STRUCTURE AND ISOTOPE SHIFT OF ^{82}Rb D_1 AND D_2 TRANSITIONS 161

I. INTRODUCTION 162
II. EXPERIMENT 163
III. RESULTS AND DISCUSSION 166

A. Frequency references 166
B. D_1 transition 166
C. D_2 transition 168
D. Line broadening 170

5 TRAPPING AND ISOTOPIC MIXTURE OF FERMIONIC ^{82}Rb AND BOSONIC ^{87}Rb ATOMS 174

6 SUMMARY AND DISCUSSION 187

REFERENCES 190

APPENDIX 196

CURRICULUM VITAE 208

LIST OF TABLES

Table		Page
I	Reference transition and frequency shifts for trapping several di®erent isotopes of Rb and Cs	51

LIST OF FIGURES

Figure		Page
1	An illustration of the observed distribution of electrons from ^{60}Co nuclei	5
2	Search for physics beyond the standard model in terms of probing for a right-handed charged-current boson of mass m_2	13
3	A schematic of the ^{82}Rb trapping cell	20
4	Pulsed release and trapping of ^{82}Rb	22
5	^{82}Rb trapping signal measured with a photodiode as a function of trapping laser detuning under continuous heating of the foil	23
6	Doppler slowing of atoms using cw laser light	28
7	The one-dimensional magneto-optical trap (MOT)	33
8	Schematic for constructing a MOT in the laboratory	35
9	Hyper¯ne energy level structure for ^{85}Rb	36
10	Comparison of yttrium and zirconium for use as an implantation foil	43
11	Energy level diagrams (not to scale) for the D_2 line of four Rb isotopes	45
12	Energy level diagrams (not to scale) for the D_2 line of three Cs isotopes	46
13	Laser system used for trapping various isotopes of Rb and Cs.	48
14	Frequency-modulated saturated absorption signal for the $6S_{1=2}$! $6P_{3=2}$ transition from both the F = 3 and F = 4 ground state hyper¯ne levels in ^{133}Cs	49

Figure		Page
15	Data collected in the °uorescence method of determining the coating quality using stable ^{133}Cs	56
16	Experimental system for producing a trapped and polarized source of ^{82}Rb (not drawn to scale)	61
17	(a) Fluorescence and (b) beta decay data collected using 60 s detection interval	63
18	^{82}Rb beta decay data accumulated over a period of six hours	66
19	Diagram showing the coils used to produce the time-averaged orbiting potential magnetic trap	70
20	Schematic showing how polarization arises in the TOP trap	72
21	The approximate expression for the polarization as a function of B_q^0 for various values of B_b	84
22	The expected polarization as a function of temperature for the magnetic ¯eld con¯gurations used in the beta-asymmetry experiment	89
23	Top view of the double MOT system used in the parity violation experiment	91
24	Inside view of the beta-chamber showing the quadrupole coil wells and the beta-collimator	93
25	Circuit used to quickly switch the current in the quadrupole coils of the TOP trap	98
26	Circuit for the parallel LRC resonator used in driving the large and small bias coils	100
27	The detector used in the parity violation experiment that houses both the plastic scintillator and the CsI crystal	105
28	Scatter plot of beta-decay data as a function of the energy deposited in the plastic scintillator vs. energy deposited in the CsI	108

Figure		Page
29	(a) Demonstration of MOT to MOT transfer of ^{82}Rb into the beta-chamber	113
30	Optical pumping scheme for preparing ^{82}Rb atoms for TOP loading	116
31	Typical TOP loading sequence	118
32	(a) MOT I, MOT II, and quadrupole magnetic trap lifetime measurements made with trapped ^{85}Rb	120
33	Beta-decay scheme for ^{82}Rb	123
34	The theoretical shape for the $1^+ \rightarrow 0^+$, the $1^+ \rightarrow 2^+$; and the branching-ratio-scaled shape for these two dominant transition in ^{82}Rb	127
35	Plot showing the calculation of the factors $\bar{}$(E) and A(E) separately and $\bar{}$(E) £ A(E) that contributes to the energy-dependent parity-violating cosine amplitude in ^{82}Rb	128
36	Plot showing the energy-dependent part of the positron-nuclear spin correlation amplitude $< \bar{}A >$ averaged from the threshold energy (represented by the x-axis) to the endpoint of the ^{82}Rb energy spectrum	129
37	Schematic showing the relevant angles for detection of a position with momentum vector p– parameterized by angles ® and '	132
38	(a) The ^{82}Rb raw angular data taken with a lower energy threshold of 800 keV and plotted as a function of the measured bias current phase angle © with a ¢ = 5± bin width	135
39	(a) Angular distribution now plotted with wiggle removed as a function of the angle £ (i.e. phase removed) between the average nuclear spin and the detection axis	137
40	Diagram showing the detection geometry for the TOP trap	139

Figure		Page
41	Accumulated data taken during the 250 s lifetime background test	145
42	The accumulation of data taken for the pulse-&-drop background test	146
43	Determination of the total background-to-signal ratio and also the three background components plotted as a function of the threshold energy in the plastic scintillator	150
44	Polarization inferred from the TOP data using the standard model values for $< \bar{A} >$ and the background analysis	153
45	The positron energy distribution for the high-statistics, pulse-&-drop, and ambient background data sets integrated over all polarization directions	156
46	The positron energy distribution for the high-statistics data set with the normalized pulse-&-drop and ambient background subtracted	157
47	A Monte Carlo showing the details of the beta detector energy deposition	159
48	The lowest three energy levels of ^{82}Rb (not to scale)	165
49	Laser frequency scan through the FM saturation absorption signal of the ^{85}Rb D_2 line $F = 3 \rightarrow F' = 2;3;4$ transitions and their associated cross-over peaks using a rubidium vapor cell	167
50	The D_1 ($5S_{1=2} \rightarrow 5P_{1=2}$) transition light shifts for (a) the ^{85}Rb $F = 3 \rightarrow F' = 3$ and $F = 3 \rightarrow F' = 2$ transitions and (b) the ^{82}Rb $F = 3=2 \rightarrow F' = 3=2$ and $F = 3=2 \rightarrow F' = 1=2$ transitions as a function of trapping laser power	169
51	The $5S_{1=2} \rightarrow 5P_{3=2}$ D_2 transition light shifts for (a) the ^{85}Rb $F = 3 \rightarrow F' = 4$ and $F = 3 \rightarrow F' = 3$ transitions and (b) the ^{82}Rb $F = 3=2 \rightarrow F' = 5=2$ and $F = 3=2 \rightarrow F' = 3=2; 1=2$ transitions as a function of trapping laser power	171

Figure		Page
52	Line broadening for the D_1 transition	172
53	The ^{84}Rb atomic energy levels (not to scale) relevant for atomic trapping	178
54	A typical trapping signal showing the time sequence for the pulsed release and trapping of ^{84}Rb that has accumulated in the yttrium catcher foil for several minutes	181
55	Plot showing the decay of half a million ^{84}Rb atoms from a MOT	183
56	A normalized lifetime plot for ^{84}Rb without (dotted line) with (solid gray line) an overlapped cloud of ^{87}Rb	185

CHAPTER 1

PARITY VIOLATION AND THE WEAK INTERACTION

The weak interaction is perhaps the most mysterious of the four fundamental forces of nature. Unlike the commonly acknowledged forces of gravity and electromagnetism, the weak force does not have a macroscopic range and its purpose is not as (immediately) distinguishing when compared to that of the strong interaction which binds protons and neutrons within the nucleus, allowing for a great diversity of elements to form and tangible matter, as we know it, to exist.

The weak interaction is a short-range force that acts between elementary particles (leptons and quarks). It can be identi…ed as being responsible for the short lifetime of exotic leptons such as the muon and the tau. Hadrons and leptons can also interact with each other through the weak force, which is the process that causes some nuclei to undergo beta-decay. In beta-decay, the nucleus is transformed to a di¤erent state where the number of nucleons remains the same but the number of protons either increases or decreases by one with the emission of an electron or a positron, respectively. The simplest case is where the free neutron decays into a proton and emits a high-energy electron and an electron anti-neutrino.

Physicists, through experience, have developed a preference for the theories of nature that possess a high degree of symmetry. The study of beta-decay (on the other hand) revealed a very surprising feature of the weak interaction in that this process does not obey the principle of spatial re‡ection symmetry. Otherwise known as parity conservation, this symmetry principle maintains that fundamental processes should be the same under a spatial inversion of all vector parameters. In such a transformation, position vectors (for example) are re‡ected through the origin ($\mathbf{r} \rightarrow -\mathbf{r}$) and motion vectors such as momentum are reversed ($\mathbf{p} \rightarrow -\mathbf{p}$).

Consider a simple example of a ping-pong ball that scatters elastically from a bowling ball positioned at the origin. If initially the ping pong ball is incident from the left, under parity inversion of the experiment it would approach the bowling ball from the right. One would not expect the results of the experiment to change under such an inversion of circumstances, but in fact particles that interact through the weak force exhibit just this sort of odd behavior when they interact or decay. This discovery shocked the physics community in the late 1950's. Despite the astounding progress that has been made in the understanding of the fundamental forces over the past …fty years, the origin of parity violation in the weak interaction is still not understood and remains one of the mysteries of modern science.

I. THE ELUCIDATION OF THE WEAK INTERACTION

One of the early considerations of the weak interaction came about from attempts to explain the energy distribution of electrons emitted in the beta-decay of atomic nuclei. In a 1914 experiment, Chadwick showed that the beta-decay electron is emitted with a continuous range of energy. This caused a great deal of confusion because the nucleus undergoes a transition between two distinct states and the emitted electron should, in principle, have an energy equal to that of the nuclear transition. The continuous spectrum made it appear as though the principles of energy and momentum conservation were violated in the beta-decay process. In 1930 Pauli …rst suggested that this missing energy could be explained by the existence of a new neutral particle (later termed the "neutrino" or "little neutral one" by Fermi) that carries o¤ the extra energy.

The …rst theoretical description of beta decay came from Fermi who developed a theory in analogy with quantum electrodynamics (QED), having an interaction where the transforming nucleus takes the role of the charged particles and the

emitted electron and neutrino are analogous to the QED photon. This theory was successful in accurately describing the observed continuous spectrum of the emitted electrons with a maximum energy equal to the mass difference between the initial and final nuclei. Due to its close analogy to QED, the Fermi Lagrangian was constructed from the scalar product of two Lorentz vectors and so was invariant with respect to Lorentz transformations and also conserved parity.

In 1956 Lee and Yang [1] were first to point out that the principle of parity conservation in the weak interaction had not been sufficiently tested. The suggestion of parity nonconservation came as a possible solution to the θ, μ meson puzzle where two particles were measured to have an identical mass and lifetime and yet their decay products had different parity. If parity were not conserved in the weak interaction, these particles could simply be two different decay modes of the same particle.

Lee and Yang extended Fermi's theory of the weak interaction to a more general form that did not include any presupposition for the discrete symmetries of parity, charge conjugation (replacing all particles with their corresponding anti-particles) or time-reversal. The most general nonderivative form of the weak interaction Hamiltonian [1], which includes scalar S, vector V, axial-vector A and tensor T terms, can be written as

$$
\begin{aligned}
H = \frac{G_F}{\sqrt{2}} \int \; & \bar{\psi}_e \gamma_\lambda \left(C_V + C_V' \gamma_5 \right) \psi_p \gamma^\lambda \psi_n \\
& + \bar{\psi}_e \gamma_\lambda \gamma_5 \left(C_A + C_A' \gamma_5 \right) \psi_p \gamma^\lambda \psi_n \\
& + \bar{\psi}_e \left(C_S + C_S' \gamma_5 \right) \psi_p \psi_n \\
& + \bar{\psi}_e \sigma_{\lambda\mu} \left(C_T + C_T' \gamma_5 \right) \psi_p \sigma^{\lambda\mu} \psi_n \, d^3x
\end{aligned}
\qquad + \text{h.c.} \qquad (1)
$$

where G_F is the Fermi coupling constant and ζ contains the nuclear matrix elements related to the strength of the transition. Here the players in neutron decay

(i.e., the neutron n, proton p, electron e, neutrino º, and their anti-particles) are represented by corresponding spatial …elds $\tilde{A}_i$. A more general nuclear transition can be described by replacing p and n with the daughter and parent nuclei, respectively. This general interaction is constructed from quantities that are invariant with respect to Lorentz transformations via the Dirac formalism (° matrices) which have the following Lorentz transformation properties:

$$\begin{array}{ll} 1 & \text{Scalar} \\ °_{¸} & \text{Vector} \\ °_{¸}°_5 & \text{Axial-Vector} \\ ¾_{¸\cdot} & \text{Tensor.} \end{array} \qquad (2)$$

The eight complex constants (C_i's, referred to as coupling constants) determine the strength for the various types of transitions in the general Hamiltonian. These constants are to be determined by experimental measurements.

Performing an experiment suggested by Lee and Yang, Wu et al. [2] observed a parity-violating asymmetry in the distribution of emitted electrons from a nuclear-polarized sample of ^{60}Co atoms in 1957. The observed asymmetry showed that the emitted electrons tend to come out predominantly anti-aligned with the nuclear spin. To see how this violates parity conservation, consider a parity inversion of this experiment (see Fig. 1). After parity inversion the electrons would be (predominantly) emitted in the opposite direction, but the nuclear spin direction remains the same. The nuclear spin does not change sign because it transforms as an axial-vector similar to angular momentum $L = r \times p$; which is formed from the product of two vectors that do change sign under parity. This mode of decay (where the electrons are predominantly emitted parallel to the nuclear spin) is not observed in experiments; therefore the weak interaction violates parity conservation.

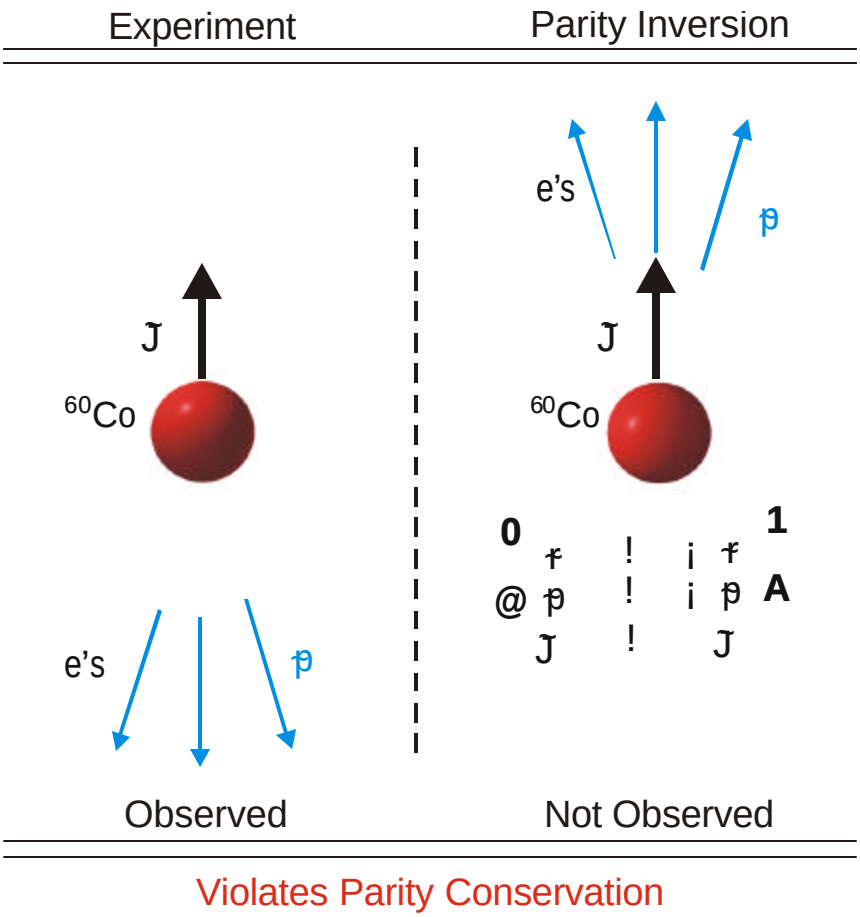

FIG. 1: An illustration of the observed distribution of electrons from ^{60}Co nuclei. The observed electrons are predominantly anti-aligned with respect to the direction of the nuclear spin. On the right-hand side of the vertical line a parity inversion of the experiment is shown. The position and momentum vectors for the emitted electrons are reversed, but the nuclear spin, being an axial-vector, is not. This leads to a situation that is not observed in the experiment. The conclusion must be that the weak interaction does not conserve parity.

The discovery of parity violation made it clear that the structure of the weak interaction could not be determined by symmetry principles alone. Experimental work began to determine the correct form for the weak interaction Hamiltonian, which required the determination of the eight coupling constants from the general form (Eq. 1). This was in part guided by Jackson, Trieman, and Wyld [3] who (in 1957) from the general form of the weak interaction Hamiltonian derived a beta-decay transition amplitude W that has experimentally measurable correlation terms constructed from the beta, neutrino, and nuclear (initial and final state) degrees of freedom. A subset of the more common correlations can be written in terms of an overall phase space factor dW_0 (due to Fermi), the beta momentum $\vec{p}$ and energy E, neutrino momentum $\vec{p}_\circ$ and energy $E_\circ$, the initial state average nuclear polarization $\langle \hat{J} \rangle$ and the beta spin σ as

$$dW = dW_0 \left(1 + \frac{\vec{p} \cdot \vec{p}_\circ}{E E_\circ} a + \frac{m_e}{E} b + \langle \hat{J} \rangle \cdot \left(\frac{\vec{p}}{E} A + \frac{\vec{p}_\circ}{E_\circ} B + \frac{\vec{p} \times \vec{p}_\circ}{E E_\circ} D \right) + \sigma \cdot \left(\frac{\vec{p}}{E} G + \frac{\vec{p} \, \vec{p}_\circ \cdot \langle \hat{J} \rangle}{E^2 - m_e^2} Q' + \langle \hat{J} \rangle \times \frac{\vec{p}}{E} R \right) \right) . \quad (3)$$

Each of the correlation terms in Eq. 3 has definite properties under the discrete symmetry transformations (e.g., $\vec{p} \cdot \vec{p}_\circ$ is P-even, that is, it does not change sign under parity inversion, whereas $\langle \hat{J} \rangle \cdot \vec{p}$ is P-odd). The correlations coefficients $(a; b; A; B; D; G; Q'; R)$ can be written in terms of the coupling constants (C_i's). Therefore, measurement of the correlations reveals information about the symmetries properties of the weak interaction and how they arise through the form of the Hamiltonian.

Individual terms can be measured by ignoring (hence integrating over) the undesired parameters in the decay. For example, by observing only the correlation between the emitted beta and the nuclear spin, the original Madame Wu experiment made the first determination of the beta-spin correlation coefficient A (called

"big A") by measuring the ^{60}Co transition amplitude

$$dW = dW_0 \cdot (1 + A \langle \hat{J} \rangle \vec{v}/c \cos\mu): \tag{4}$$

at two discrete angles, $\mu = 0^{\pm}$ and $\mu = 180^{\pm}$:

One bene…t of measuring beta-decay in nuclei is that pure Gamow-Teller (GT) and pure Fermi (F) transitions can be studied [4]. Pure transitions can be used to remove the dependence of the correlation coe¢cients on the nuclear matrix elements which cannot be calculated except for the most simple nuclei, such as the neutron which requires matirx element determination since it is a mixed F + GT transition. Pure transitions also narrow the types of interaction to be studied in a particular measurement. For example, the beta-neutrino correlation coe¢cient can be expressed as [3]

$$a = \frac{M_F^2(|C_V|^2 + |C_V'|^2 - |C_S|^2 - |C_S'|^2) + \frac{1}{3}M_{GT}^2(-|C_A|^2 - |C_A'|^2 + |C_T|^2 + |C_T'|^2)}{M_F^2(|C_V|^2 + |C_V'|^2 + |C_S|^2 + |C_S'|^2) + M_{GT}^2(|C_A|^2 + |C_A'|^2 + |C_T|^2 + |C_T'|^2)}: \tag{5}$$

Where M_{GT} and M_F are the Gamow-Teller and Fermi nuclear matrix elements. Pure transitions can be written simply in terms of the coupling constants after applying the Gamow-Teller or Fermi selection rules (i.e., $M_F = 0$ for pure GT or $M_{GT} = 0$ for pure F).

$$a_F = \frac{|C_V|^2 + \mathrm{Re}(C_V C_V'^*) - |C_S|^2 - \mathrm{Re}(C_S C_S'^*)}{|C_V|^2 + |C_V'|^2 + |C_S|^2 + |C_S'|^2} \tag{6}$$

$$a_{GT} = -\frac{1}{3}\frac{|C_A|^2 + \mathrm{Re}(C_A C_A'^*) - |C_T|^2 - \mathrm{Re}(C_T C_T'^*)}{|C_A|^2 + |C_A'|^2 + |C_T|^2 + |C_T'|^2} \tag{7}$$

Measurements of the recoiled nuclei after beta-decay in pure Fermi transitions were found to have (relatively) large recoil energies, which is consistent with the

preferred colinear emission of the electron and the anti-neutrino. These measurements indicated that $a_F \simeq +1$ (for a recent measurement see Ref. [5]). According to Eq. 6, this effectively selects the vector V transition to be strongly favored compared to the scalar S. Measurements of pure Gamow-Teller beta-neutrino correlations [6] give $a_{GT} \simeq -1/3$; and therefore selects the axial-vector A form to be strongly favored over tensor T.

Instrumental knowledge came from measurements of the direction of the beta or neutrino spin relative to its momentum. This quantity

$$H = \frac{\vec{p} \cdot \vec{\sigma}}{|\vec{p}|\,|\vec{\sigma}|} \tag{8}$$

is called the particle helicity. It was found [7] that the beta-decay electrons always have (as far as measurements could discern) a left-handed helicity of $-v/c$, and emitted positrons always have a right-handed helicity $+v/c$. Another enlightening experiment [8] found the helicity of the neutrino to be -1. This evidence suggested the weak interaction only couples to left-handed particles and right-handed anti-particles.

The helicity measurements can be shown to be equivalent to a constraint for the coupling constants of $C_V = -C_V'$, and $C_A = -C_A'$: The relative strengths of the vector and axial-vector coupling can be obtained using a ratio of lifetime measurements for a pure and a mixed transition (or from a correlation parameter) [9] and gives $|C_A/C_V| \simeq 1.3$ (for recent results see Refs. [10, 11]). Correlation measurements using polarized neutrons and ^{19}Ne give evidence that C_V and C_A are both real, indicating time-reversal invariance at the 10^{-3} level, and that C_V and C_A are both positive (for the convention used here) [12].

The standard electroweak model that describes the interaction of leptons and quarks was developed in the mid 1960's by Weinberg, Salam, and Glashow [13–15]. It makes an exact assumption for the form of the weak interaction that was

originally due to Sakurai [16] and also Feynman and Gell-Mann [17] in 1958. In terms of the coupling constants, the standard model can be summarized as

$$\begin{aligned} C_T ; C_T^{'} ; C_S ; C_{S^{'}} &= 0 \\ C_V / g_V &= -C_V^{'} / g_V = 1 \\ C_A / g_A &= -C_A^{'} / g_A = 1 \end{aligned} \tag{9}$$

where $g_V = 1$ and $g_A \simeq 1.3$ are the nuclear form factors that arise from vector and axial-vector quark transitions bound within the nucleons (e.g., the up quark, down quark $u \leftrightarrow d$ transitions that occur in beta-decay). For the standard model, the weak interaction Hamiltonian can be written

$$H^{SM} = \frac{G_F}{\sqrt{2}} V_{ud} \int \tilde{\psi}_e \gamma_\mu (1 - \gamma_5) \tilde{\psi}_{\nu_e} \tilde{\psi}_u \gamma^\mu (1 - \gamma_5) \tilde{\psi}_d d^3x + \text{h.c.} \tag{10}$$

where V_{ud} is the ud element of the CKM (Cabibbo, Kobayashi, Maskawa) quark mixing matrix. Note that the form of the interaction is expressed as $\gamma_\mu - \gamma_\mu \gamma_5$, in other words a pure vector minus axial-vector ($V - A$) interaction.

The standard model's $V - A$ law violates parity conservation. In fact, it is maximally parity-violating as it takes place through the coupling of left-handed charged currents only (that is the $W_L^{\pm}$ gauge bosons). The standard model makes an ad hoc exclusion of right-handed currents. It also maximally violates charge conjugation symmetry, but on the other hand, preserves time-reversal invariance.

In some sense, we have gone full circle. Prior to 1956, the discrete symmetries were assumed to be conserved for all interactions. We have discovered that this is not universally true for the weak force; however, once again we have a discription of nature that makes exact symmetry assumptions (that is anti-symmtry for P & C; and symmetry for T in standard model) without explanation for how or why the weak interaction should have these properties. Unanswered questions such

as these employ the search for a better description of the fundamental forces of nature.

II. BEYOND THE STANDARD MODEL

The standard model has been wildly successful in describing all of the experimental phenomenology of nuclear and particle physics collected during the latter half of the past century. Despite this success, there is general suspicion among the physics community that the standard model may be only a low-energy approximation to a more illuminating theory ¡ one that would include a description of gravity, predict elementary particle masses and reveal the origin of discrete symmetry breaking. While work along this front continues in many di¤erent directions, nuclear beta-decay measurements remain a very sensitive way to probe our understanding of the forces of nature.

The standard model V ¡ A law is so far consistent with the most precise measurements of the coupling constants C_i's. However, even after more than 40 years of investigation, only a small subset of the correlation coe¢cients have been measured and the coupling constants are known [9] only to a precision of between 1 and 10% owing to the di¢culty of performing these type of measurements. It is certainly possible for there to exist some small contribution from the other types of currents (e.g., scalar or tensor with measured constraints of $\left|\frac{C_S}{C_V}\right| \lesssim 0.07$ and $\left|\frac{C_T}{C_A}\right| \lesssim 0.10$, respectively) that are not now included in the standard model.

Since the correlation coe¢cients depend, in a less than straightforward way, on the coupling constants, multiple measurements will be required to understand any measured deviation from the standard model. For example, if deviations were to be found in neutron decay (a mixed F + GT transition), measurements from both pure Fermi and pure Gamow-Teller transitions would be required to sort out which

of the eight coupling constants contribute to the observed e¤ect.

In our experiment, we look at the positron-spin correlation for ^{82}Rb, which is a pure Gamow-Teller positron emitter. The beta-spin correlation coe¢cient can be written as

$$A_{GT} = \frac{2\mathrm{Re}\left[\S\, \lambda_{JJ'}(C_A C_A'^{\,\alpha} - C_T C_T'^{\,\alpha})\right]}{|C_A|^2 + |C_A'|^2 + |C_T|^2 + |C_T'|^2}. \tag{11}$$

The § refers to electron and positron emission, respectively; $\lambda_{JJ'}$ depends only on the initial J and …nal J' state nuclear spin and can be determined without calculation uncertainty

$$\lambda_{J',J} = \begin{array}{ll} 1 & J' = J - 1 \\ 1/(J+1) & J' = J \\ -J/(J+1) & J' = J+1. \end{array} \tag{12}$$

Note that for the standard model (that is, using the coupling constants values from Eq. 9), A_{GT} reduces to a very simple form,

$$A_{GT}^{SM} = \mp \lambda_{JJ'}. \tag{13}$$

The general expression for A_{GT} (Eq. 11) shows that a precision measurement of the beta-spin correlation for a pure Gamow-Teller transition would be sensitive in the search for tensor currents (i.e. nonzero C_T; C_T') and deviations from left-right asymmetry (i.e., $C_A \neq -C_A'$).

One of the disconcerting features of the standard model is the exclusion of right-handed currents that should be allowed by the full SU(2) group symmetry of the weak interaction. There are extensions beyond the standard model that re-invoke the left-right symmetry by introducing right-handed currents of the form (V + A)

into the weak interaction (for a recent review see Ref. [18]). In these theories, a right-handed particle is introduced through the parameter $\pm = (m_1/m_2)^2$ that has a mass m_2 much greater than the observed » 81 GeV/c^2 left-handed $W_L^{\S}$ gauge bosons. The standard model can be considered a low-energy approximation of this left-right symmetric model through the introduction of a mixing angle ^{3}, where the eigenstates for the weak interaction can be written

$$W_L = W_1 \cos {}^3 + W_2 \sin {}^3$$
$$W_R = \text{¡} W_1 \sin {}^3 + W_2 \cos {}^3 : \qquad (14)$$

The minimal left-right symmetric model parameters ($\pm$; ^{3}) can be related to the coupling constant for the general weak interaction Hamiltonian

$$C_V \text{»} g_V (1 \text{¡} 2^3 + \pm)$$
$$C_V^{0} \text{»} g_V (1 \text{¡} \pm)$$
$$C_A \text{»} g_A (1 + 2^3 + \pm)$$
$$C_A^{0} \text{»} g_A (1 \text{¡} \pm); \qquad (15)$$

and

$$C_S ; C_S^{0} ; C_T ; C_T^{0} = 0: \qquad (16)$$

A precision measurement of beta-nuclear spin-correlation parameter for a pure GT transition can be employed to search for the heavy right-handed charged currents. Fig. 2 shows the current status in the search for right-handed gauge bosons, predicted from the minimal left-right symmetric models, for several di¤erent experiments. These include the direct search at accelerator facilities, muon decay, and the ratio of pure Gamow-Teller and Fermi ¯-polarization measurements. Also

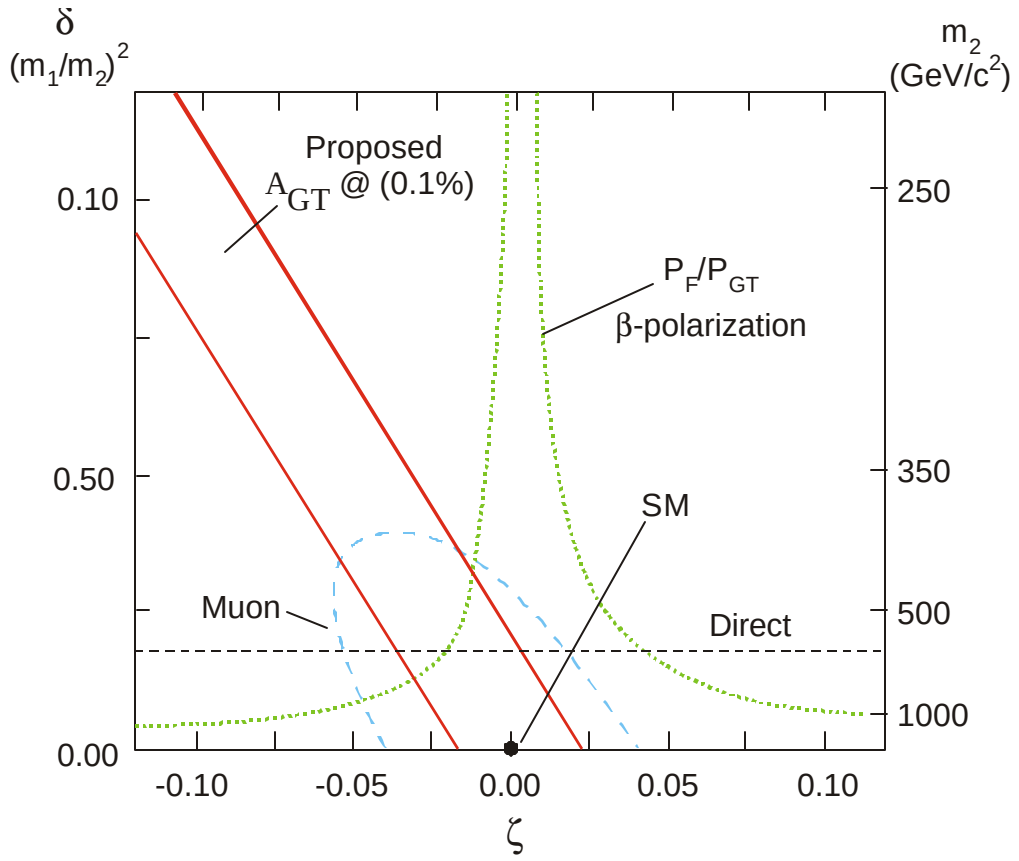

FIG. 2: Search for physics beyond the standard model in terms of probing for a right-handed charged-current boson of mass m_2. The phase space for the existence of right-handed bosons is constrained by measurements of the muon, direct accelerator production and the ratio of pure Fermi and Gamow-Teller β-polarization. Also shown is a proposed pure Gamow-Teller measurement of the beta-nuclear spin correlation parameter at the 0.1% level.

included in the plot is a proposed A_{GT} measurement at the level of 0.1%. With this precision, a table-top beta-asymmetry experiment could be useful in the search for right-handed currents that have mass of greater than 500 GeV/c^2. Such a measurement is also desirable since one, in principle, would like to test all sectors of the weak interaction. Muon decay probes pure lepton-lepton interactions, direct accelerator production probes pure hadronic-hadronic interactions, and a nuclear beta-decay experiment would probe hadron-lepton interactions.

The best current measurement of a pure Gamow-Teller beta-spin correlation comes from a more modern Wu-type experiment where ^{60}Co atoms are implanted in a solid ferromagnetic host and polarized through low-temperature nuclear orientation. This experiment is limited by systematic e¤ects associated with the scattering of the electrons in the solid host material and the determination of the average nuclear polarization in the implanted source. A measured value of $A_{GT} = ¡1:01 \S 0:02$ was reported for ^{60}Co ($\overline{\ }^{i}$ decay) from this work [19]. Given the di¢culty in reducing the systematic uncertainties in this experiment, improved precision appears unlikely using such technology. A new approach is called for in order to increase the precision of beta-asymmetry experiments.

III. DISSERTATION OUTLINE

This dissertation describes a proof-of-principle beta-asymmetry experiment in which a nuclear polarized sample of ^{82}Rb atoms was produced using atomic cooling and trapping techniques. This new method of polarization has clear advantages over past techniques due to its ability to con…ne and manipulate atoms in an atomic trap. Unlike the earlier measurement with ^{60}Co, the trapping allows for isolation of the sample away from solid material that can scatter the emitted electrons (or positrons) and alter their energies and trajectories. With the use of magnetic traps,

a very high-degree of polarization can be achieved and, in principle, measured independently, allowing for a precise measurement of the positron-nuclear spin correlation without intrinsic systematic e¤ects. The work presented here shows that the di¢culties in producing such a polarized source have been overcome and that the advantages of trapping beta-decaying atoms are realizable.

The multiple-paper format has been used for this dissertation. At the beginning of Chapters 2-5, a Physical Review style publication is presented. The main theme of the work performed in this experiment can be gained by reading this introduction, the four publications, and the summary. Further details about the experiment and the techniques involved are presented as separate sections that follow the publications. Each chapter is self-contained when taken together with the publication. Chapter 2 describes the original work done in trapping radioactive ^{82}Rb in a magneto-optical trap. The demonstration of parity-violation from a magnetic trap is presented in Chapter 3. Chapters 4 and 5 describe additional work that was done with trapped radioactive samples as relevant to the parity-violation experiment both in terms of understanding the ^{82}Rb atomic transitions and understanding the characteristics of the atomic traps.

CHAPTER 2

MAGNETO-OPTICAL TRAPPING OF RADIOACTIVE ATOMS[1]

ABSTRACT

We report the successful trapping of 6 million ^{82}Rb ($t_{1=2}$ = 75 s) atoms with a trap lifetime of »30 seconds in a magneto-optical trap that is coupled to an o¤-line mass separator. E¢cient sample introduction is achieved by implanting ^{82}Rb ions into a small yttrium catcher foil located inside the trapping cell. Upon heating, the radioactive atoms are released from the foil and trapped without signi…cant gas loading. This advancement makes a variety of high-precision electroweak interaction experiments possible including the measurement of beta-decay correlations associated with spin-polarized ^{82}Rb nuclei.

[1]Coauthored by R. Guckert, X. Zhao, S.G. Crane, A. Hime, W.A. Taylor, D. Tupa, D.J. Vieira, and H. Wollnik, Phys. Rev. A. 58, R1637 (1998).

Since the demonstration of laser cooling [20] and magneto-optical trapping [21] of neutral atoms, there has been a growing interest in exploiting this technology in atomic, nuclear and particle physics. Trapped radioactive atoms will enable a new generation of fundamental symmetry experiments including nuclear beta decay, atomic parity nonconservation, and the search for parity and time-reversal violating electric dipole moments. In particular, trapped beta-decaying species will enable a new set of high-precision measurements that will elucidate our understanding of the helicity structure of the electroweak interaction and aid in the search of physics beyond the standard model. In many ways, trapped radioactive atoms make an ideal source for beta-decay correlation measurements since relatively intense sources can be harnessed which are e¤ectively massless, point-like, and nearly 100% spin polarized. Consequently, systematic e¤ects associated with electron scattering e¤ects and polarization uncertainties can be greatly reduced if not eliminated altogether.

It is well known that pure Gamow-Teller transitions, such as those available in ^{82}Rb, are useful candidates to study parity violation since these transitions are driven solely by the axial vector coupling between leptons and quarks. Given that trap lifetimes can be achieved that are comparable to the 75 second half-life of ^{82}Rb, this species is an excellent choice for a magneto-optical trap (MOT)-based experiment. Moreover, since ^{82}Rb is fed by the long-lived ^{82}Sr ($t_{1=2}$ = 25 d) parent, this experiment can be performed o¤-line (i.e., not associated with an accelerator).

Although several radioactive species have been trapped [22–26], the current challenge is to trap su¢cient numbers of radioactive atoms to undertake a meaningful measurement. For example, one would need to detect approximately 150,000 beta-decay events in order to determine the beta-nuclear spin correlation function of polarized ^{82}Rb to a precision of 1%. Given a realistic detection geometry, these

counting statistics could be achieved in one hour with one million trapped atoms. In a multi-day experiment, a 0.1% measurement could be obtained. Until this work, as many as 40,000 radioactive atoms have been trapped [27]. Herein we report on the development of a new sample introduction method involving the ion implantation and heated release of mass-separated atoms using a catcher foil located inside the trapping cell of a MOT. This has resulted in the …rst reported trapping of over a million radioactive atoms.

The ^{82}Sr source is produced at the isotope production facility of the Los Alamos Neutron Scattering Center (LANSCE) by 750-MeV proton irradiation of a molybdenum target. Handled within a hot cell, the target is dissolved in hydrogen peroxide and the strontium fraction extracted using an ion exchange column. The strontium sample containing both ^{82}Sr (»9 mCi) and ^{85}Sr (»50 mCi) is precipitated as $SrCO_3$ and loaded into a tantalum crucible. The crucible is then installed into a thermal ion source of the hot-cavity type [28] and heated to a temperature where the ionization e¢ciency is low for strontium, but high for rubidium. A collimated NaI counter looking at the ion source region monitors the gamma-rays emitted by ^{85}Sr ($E_\circ$=514 keV, branching ratio=96%) and ^{82}Rb (776 keV, 13%). Under appropriate operating conditions, we observe a 42% drop in the ^{82}Rb gamma-decay rate while the ^{85}Sr gamma-decay rate remains essentially constant. Once ionized, the ions are electrostatically extracted from the ion source, accelerated to 20 keV, and separated using a high-transmission mass separator [29]. $^{82}Rb^+$ ions are mass selected and refocused by a quadrupole triplet through a stainless steel collimator located just before the entrance of the trapping cell (see Fig. 3). The ions then enter the quartz trapping cell through a 5 mm Á opening and are implanted into a small yttrium catcher foil. Final focusing and steering of the beam onto the foil is achieved by maximizing the current measured on the foil while minimizing the

current measured on the collimator. Typical ion beam intensities of $1 £ 10^8$ ions/s are measured with a picoammeter. A second, collimated NaI °-counter viewing the foil region monitors the ^{82}Rb activity collected on the foil. By comparing the 776 keV count rates at the source and foil positions, we …nd that »35% of the ^{82}Rb produced in the source is ionized, separated, and implanted into the foil. A small rf-coil located outside the cell is used to inductively heat the foil to temperatures of 750-850 $^{\pm}$C to release the implanted ^{82}Rb as a vapor within the cell. The cell is coated with a nonstick coating of octadecyltrichlorosilane (OTS) dry…lm to enhance the trapping probability [30].

The magneto-optical trap is formed by six circularly-polarized laser beams (45 mm Á, 100 mm $1=e^2$ width) which enter the cubic cell through each surface. Each beam has a power of 200 mW. A set of anti-Helmholtz coils generates the quadrupole …eld gradient of 7 G/cm in the axial direction. A Ti:Sapphire laser tuned to the D_2 line of Rb at 780 nm forms the trapping beams. The laser frequency is locked to the $5S_{1=2}$, $F = 3 \; ! \; 5P_{3=2}$, $F^{0} = 3;4$ cross-over transition of ^{85}Rb using a FM sideband technique [31]. A double-pass acoustic optical modulator (AOM) driven at 268 MHz provides the 536 MHz frequency shift needed to excite the $5S_{1=2}$, $F = 3=2 \; ! \; 5P_{3=2}$, $F^{0} = 5=2$ trapping transition in ^{82}Rb [32]. In order to repump atoms which fall into the $5S_{1=2}$, $F = 1/2$ ground state, sidebands are added to the trapping beam by using an electro-optical modulator (EOM) tuned to 1.470 GHz which excites the $5S_{1=2}$, $F = 1=2 \; ! \; 5P_{3=2}$, $F^{0} = 3=2$ transition. For trapping ^{85}Rb, however, the EOM is tuned to 1.463 GHz and the second harmonic generates the repump light. Trapped atoms are detected by chopping the EOM at 4 kHz that modulates the trap ‡uorescence signal. A 58 mm f/1.4 lens images the trap ‡uorescence onto a photomultiplier tube or a photodiode through a 10 nm interference …lter and a 2 mm pinhole; a lock-in ampli…er is then used

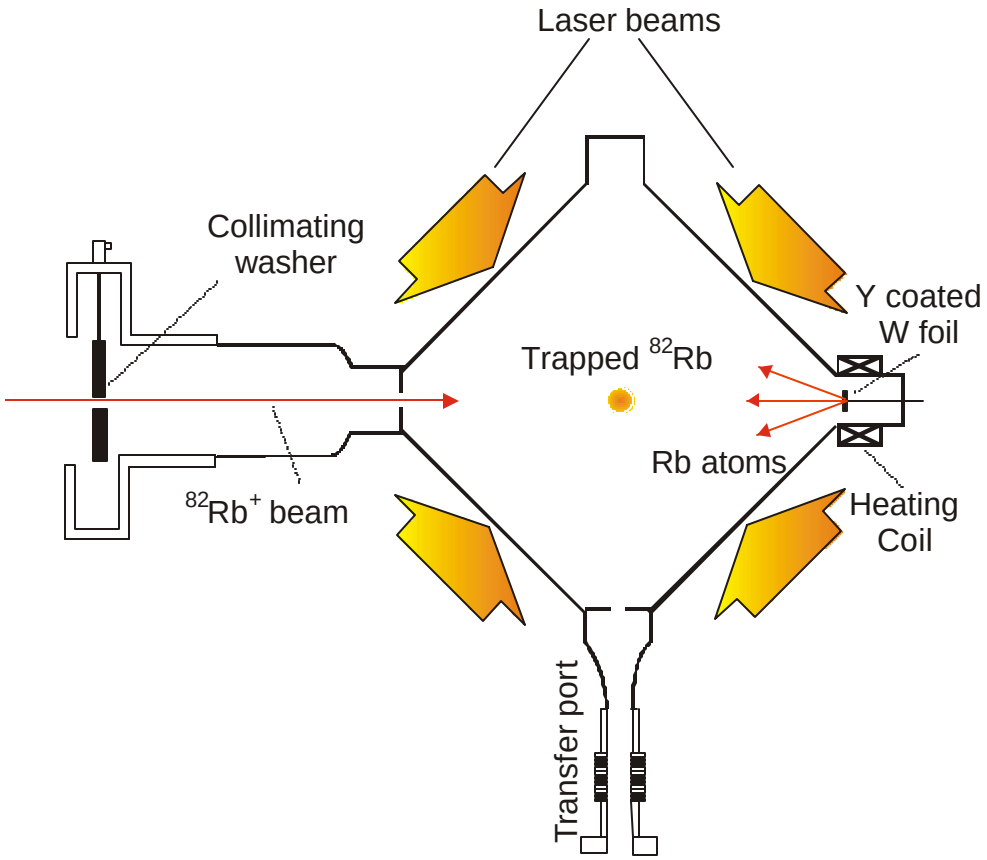

FIG. 3: A schematic of the ^{82}Rb trapping cell. The mass-separated ^{82}Rb ion beam passes through a collimator (5 mm Á) and the opening (5 mm Á) of the OTS dry…lm-coated quartz cell (a 75 mm cube) and is implanted into a yttrium catcher foil (6 mm Á). The coil inductively heats the foil to temperatures of 750-850 ±C to release the implanted ^{82}Rb atoms into the cell where they are trapped by a MOT. Not shown are the anti-Helmholtz coils (170 mm Á) located above and below the plane of view.

to demodulate the trapping signal. In addition, a CCD camera with a f/1.2 lens provides an image of the trapped cloud.

Due to the low pressure in the cell (» 10^{-10} torr) and a corresponding long trapping lifetime (30 s with the foil on and 90 s with the foil o¤), ^{82}Rb can be accumulated either in the foil (pulsed mode) or in the trap by continuous heating of the foil (continuous mode). Shown in Fig. 4 is the pulsed release and trapping signal for ^{82}Rb after implanting 3 mCi of ^{82}Rb into the catcher foil. In the top half of Fig. 4, we show the temperature of the foil (a) as measured with an optical pyrometer upon excitation of the heating coil; (b) shows the count rate for the 776 keV °-rays coming from the decay of ^{82}Rb as a function of time. The drop in count rate indicates that » 35% of the ^{82}Rb atoms are released from the foil and leave the region viewed by the collimated °-counter upon heating. Measurements with and without -300 V applied to the foil indicate that essentially all of the activity is released as neutral atoms. The 1/e release time from the foil is measured to be 5 s.

In the bottom half of Fig. 4, the lock-in trapping signal is plotted as a function of time. A strong trapping signal is evident with a risetime consistent with the release pro…le of ^{82}Rb. Additional measurements with shorter foil heating times indicate that the trapping signal decays with a 1/e lifetime of 50 s, corresponding to a 90 s trap lifetime and the 75 s half-life of ^{82}Rb. In Fig. 5, we show the trap ‡uorescence signal as a function of laser detuning for continuous foil heating. No trapping signal is observed if: (1) the foil is not heated; (2) the foil is heated, but no ^{82}Rb is implanted into the foil; or (3) the magnetic …eld of the MOT is reversed. All of these cross-checks attribute the signal to trapped ^{82}Rb.

The center frequencies of the trapping transitions in trapped ^{82}Rb and ^{85}Rb were determined by using a separate probe beam of 80 ^{1}W and 5 mm which is split o¤

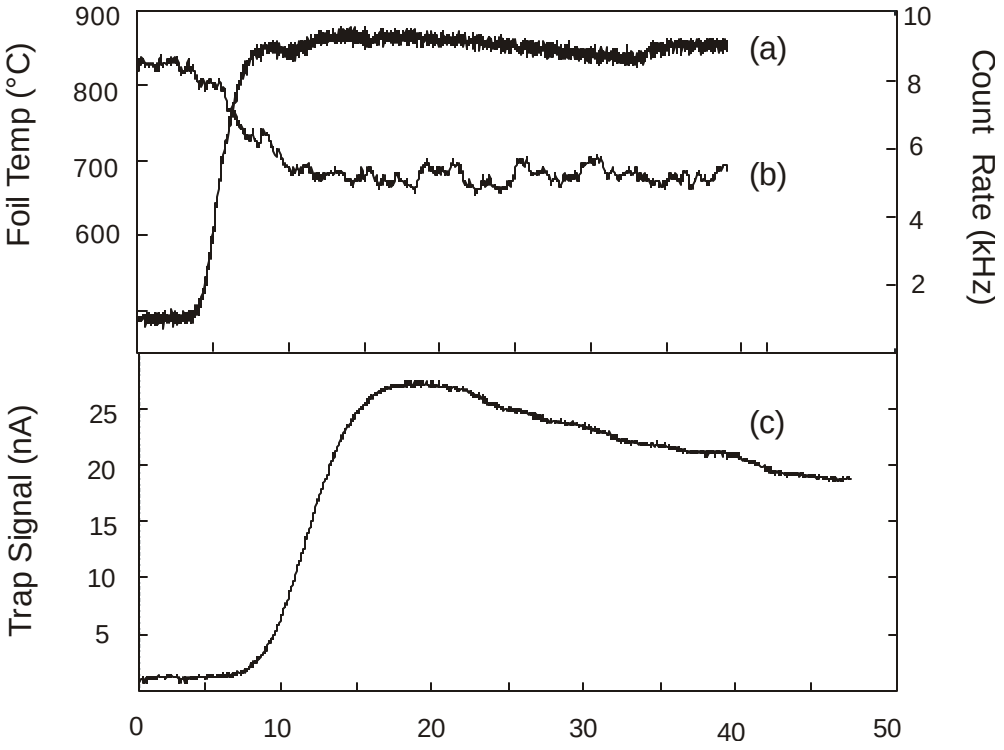

FIG. 4: Pulsed release and trapping of ^{82}Rb. The top …gure shows the foil temperature (a, left axis), and 776 keV °-count rate (b, right axis) of ^{82}Rb accumulated and then released from the foil upon heating. The modulated ‡uorescence trapping signal as measured with a photomultiplier and a lock-in ampli…er is shown in the bottom …gure (c). The lock-in ampli…er has an integration time constant of 3 s.

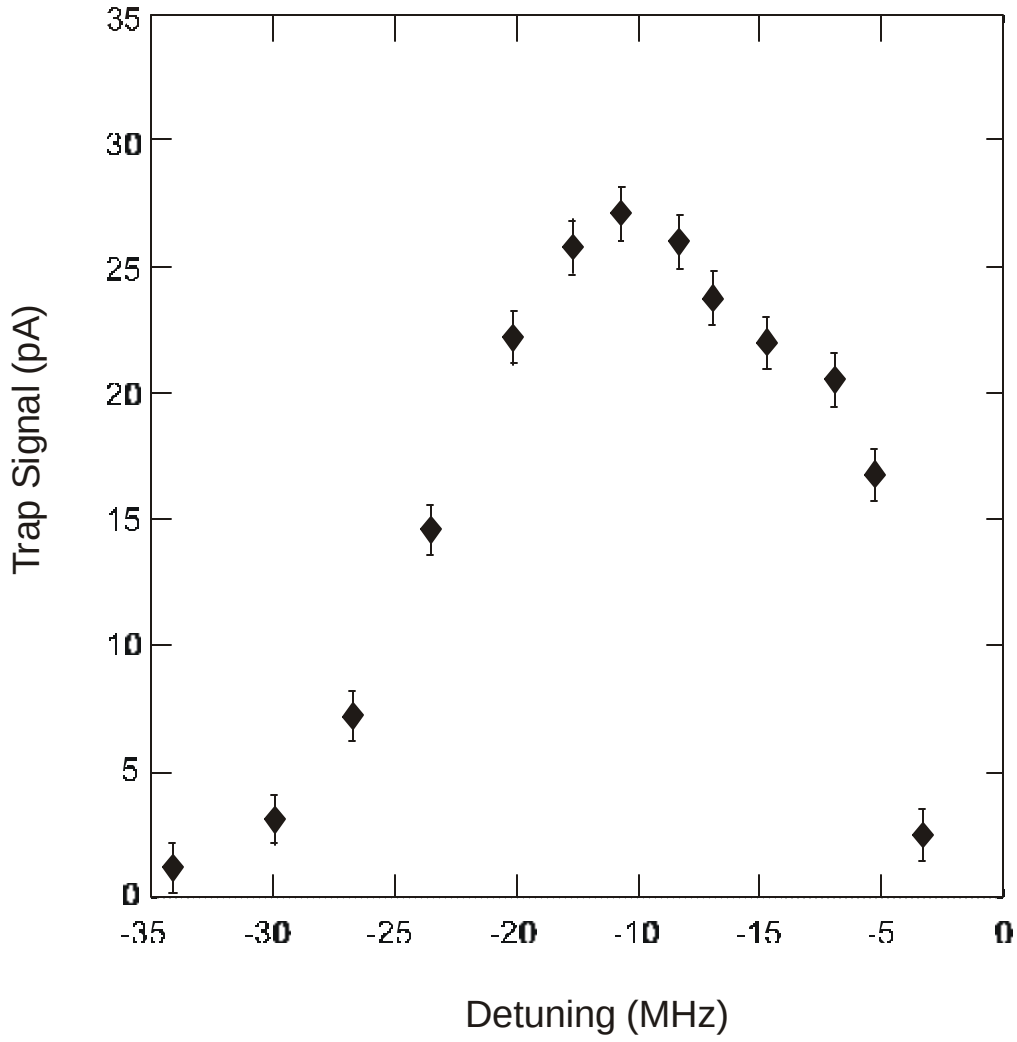

FIG. 5: ^{82}Rb trapping signal measured with a photodiode as a function of trapping laser detuning under continuous heating of the foil. The zero on the detuning scale corresponds to the center of the $5S_{1=2}; F = 3=2 \; ! \; 5P_{3=2}; F^{0} = 5=2$ transition in trapped ^{82}Rb. Relative frequency uncertainties, as limited by the laser locking system, are estimated to be 1 MHz.

from the main trapping beam and frequency shifted using two AOMs arranged in series, giving a net shift of -25 to 25 MHz. The second AOM is chopped on and o¤ to modulate the probe beam at a rate of 7 kHz. When the circularly polarized, counter-propagating probe beam is overlapped with the trapped cloud, the result is to partially modulate the trapping ‡uorescence signal. Maximum modulation in the trapping signal occurs when the probe beam is on resonance. In this way, we determine the trap detuning to be -17 §1 MHz for both ^{82}Rb and ^{85}Rb. The resulting frequency di¤erence between the $5S_{1=2}$, $F = 3=2 \rightarrow 5P_{3=2}$, $F' = 5=2$ transition in ^{82}Rb and the $5S_{1=2}$, $F = 3 \rightarrow 5P_{3=2}$, $F' = 4$ transition in ^{85}Rb is thus measured to be 536 §5 MHz, in agreement with the previous measurement of 540 §7 MHz [32].

The number of trapped atoms is deduced from the trapping signal using a calibrated photodiode, yielding $(6 \pm 2) \times 10^6$ and $(3 \pm 1) \times 10^6$ trapped ^{82}Rb atoms for the pulsed and continuous operation, respectively. From CCD image measurements of the cloud size (FWHM), we obtain a density of $\approx 10^{10}$ atoms/cm^3, consistent with re-radiation limited densities reported in the literature [33]. Calculating the overall trapping e¢ciency as $\eta_{total} = N_{trap}/(\tau_{trap} A_{Rb})$, where $N_{trap} = 3 \times 10^6$ is the number of trapped atoms, $\tau_{trap} = 30$ s is the lifetime of the trap, and $A_{Rb} = 3 \times 10^8$ disintegration per second is the ^{82}Rb activity in the ion source, we obtain an overall e¢ciency of $\approx 3 \times 10^{-4}$. Breaking this down stepwise, we obtain an ionization and separation e¢ciency of 35%, a catcher foil release e¢ciency of 30% at 750 $^{\pm}$C, and a trapping e¢ciency of $\approx 3 \times 10^{-3}$.

Using a third collimated NaI counter, we attempted to measure the number of trapped ^{82}Rb atoms through the detection of 776 keV gamma-rays. We failed in this respect, …nding a constant count rate with or without a ^{82}Rb cloud present which indicates that a large portion of the ^{82}Rb sticks to the cell walls. This is sup-

ported by a calculation that predicts that »30 bounces (i.e., collision and release from the wall) are required to account for our measured trapping e¢ciency. When compared to the »600 bounce pump-out estimate from the ratio of entrance/exit area to total surface area of the cell, we conclude that the coating performance is less than optimal when compared to previous work [30, 34]. We suspect that improvements in the cell coating could lead to a sizable gain in the trapping e¢ciency. To this end, we are using the gamma-ray monitoring technique to select the best type of dry…lm coating.

Given the success in trapping large numbers of ^{82}Rb, we plan to transfer the atoms to a second, low-background MOT using a laser push / magnetic guide approach [35]. After retrapping, the atoms will be optically pumped into a spin-aligned magnetic substate and loaded into a time-orbiting-potential (TOP) trap [36]. Presently under construction, this pure magnetic trap will be used as a rotating beacon of spin-polarized ^{82}Rb nuclei. Exploiting the point-like geometry and rotating spin features of the TOP trap, we will measure the ¯-nuclear spin asymmetry function as a continuous function of beta energy and angle between the ¯-particle and nuclear spin alignment vector using a single (or small set of) positron detector(s). Not only is the symmetry of this system attractive from the standpoint of reduced systematic errors, but the complete mapping of the parity-violating correlation may also enable the simultaneous extraction of recoil order corrections, such as the weak magnetism term, which are expected to lead to small deviations in the asymmetry ($\cos\mu$) and anisotropy ($\cos^2\mu$) terms. With a proof-of-principal measurement in hand, we will then include the detection of ¯-recoiling nuclei to reconstruct the neutrino degrees of freedom relevant for the simultaneous measurement of the neutrino-spin asymmetry and the electron-neutrino correlation functions.

In summary, this work reports the trapping of over a million radioactive ^{82}Rb atoms in a MOT coupled to an o¤-line mass separator. This represents two orders of magnitude improvement in the number of trapped atoms over previous work. Essential to this success is the development of a more e¢cient method of introducing the sample into the MOT with minimal gas loading using an ion implantation / internal catcher foil release method. Combined with other recent atom trapping developments, a new generation of high-precision β-decay correlation experiments are foreseen.

We wish to acknowledge Z.-T. Lu, M. Stephens, and C. Wieman for many valuable discussions and the early involvement of D. W. Preston, V. D. Sandberg, and M. J. Smith in getting this work started. We also thank L. D. Benham, E. P. Chamberlin, F. O. Valdez, the LANL glass shop, and the CST-Division machine shop for their excellent technical support. This work was supported in large part by the Laboratory Directed Research and Development program at the Los Alamos National Laboratory, operated by the University of California for the US Department of Energy. Part of this work was funded directly by the US Department of Energy.

I. ATOMIC COOLING AND TRAPPING

The history of laser cooling goes back to the …rst proposals made simultaneously by Dave Wineland and Hans G. Dehmelt of the University of Washington [37] and Theodore Hänsch and Arthur L. Schawlow of Standford University [38]. Since then, there has been a "virtual rebirth" in the …eld of atomic physics that has greatly enhanced our ability to manipulate neutral atoms. The 1997 Nobel prize in physics was given to Steve Chu, William Phillips and Claude Cohen-Tannoudji

for their work in demonstrating and explaining laser cooling of atoms.

The …rst suggestions for cooling hinged on the Doppler e¤ect observed by an atom that moves relative to a …xed laser. For a laser (of frequency f_{laser}) directed along the x-axis, an atom with velocity $v_x << c$ will experience a Doppler-shifted frequency of $f_{laser}(1 \S v_x=c)$; where the "+" sign is used for an atom moving toward the laser. Consider shining a laser, which is tuned slightly below an atomic transition f_o by a small amount ±, on an atomic vapor (see Fig. 6). Since the vapor has a Maxwell-Boltzman distribution of velocities, there will be a group of atoms that have the appropriate velocity (v_x ' $c±=f_{laser}$) in order to "see" the laser as shifted into resonance with the atomic transition. This group of atoms interacts strongly with the laser, absorbing and re-emitting photons at a high rate, while the remaining atoms in the vapor are essentially una¤ected.

Each time that an atom absorbs a photon, it receives a momentum kick ~k in the direction of the laser light. If the laser intensity is low enough so that stimulated emission is negligible, then photons will be re-emitted isotropically due to spontaneous emission. Therefore, to a …rst-order approximation, the momenta imparted by the emission of photons over many cycles averages to zero, and the atoms are slowed by net force in the direction of the laser beam. Collisions between the slowed atoms and the rest of the atomic vapor can lead to a reduced equilibrium temperature when using several of counterpropagating lasers beams.

The strength of the laser force depends strongly on the scattering rate $¡_{scatt}$ for the atomic transition. The quantum treatment of the atom-light …eld interaction leads to an expression for the scattering rate in terms of the laser intensity I; the laser light detuning $(!_{laser} ¡ !_o) = 2¼(f_{laser} ¡ f_o) = 2¼±$, and the excited state lifetime ¿

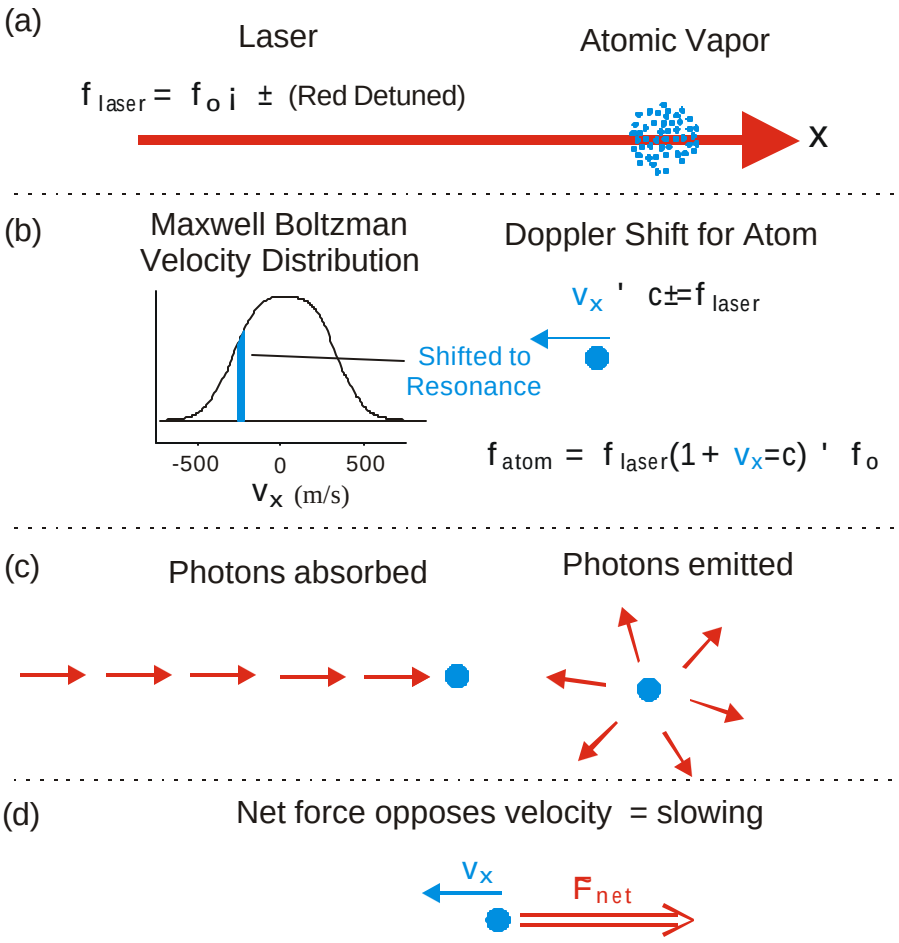

FIG. 6: Doppler slowing of atoms using cw laser light. Atoms moving in the opposite direction of a laser detuned slightly below an atomic resonance will observe the laser light as shifted into resonance via the Doppler e¤ect. This results in a net force that opposes the atomic velocity and causes the atoms to slow down.

$$\Gamma_{scatt} = \frac{1}{2\tau}\frac{I/I_{sat}}{1 + I/I_{sat} + 4\tau^2(\omega_{laser} - \omega_o - \vec{k}\cdot\vec{v})^2}. \quad (17)$$

$I_{sat} = \pi hc/3\lambda_{laser}^3\tau$ is the saturation intensity, which for alkali species is normally a few mW/cm^2. From the arguments given above, an expression for the force experienced by the atom can be written as

$$\vec{F} = -\hbar\vec{k}\Gamma_{scatt}. \quad (18)$$

For strong atomic transitions the scattering rate can be on the order of $\approx 10^7$ Hz, resulting in a force on the atoms that is roughly 10,000 times that of gravity.

In typical cooling experiments, several counterpropagating laser beams are overlapped with an atomic sample. For the one dimensional case (two lasers shining from opposite directions) the force from each beam can be summed and expanded for v close to zero to show that it depends linearly on the velocity.

$$\vec{F} = -\alpha v_x\hat{\imath}, \quad (19)$$

where

$$\alpha = -4\hbar k^2 I/I_{sat}\frac{2\tau(\omega_{laser} - \omega_o)}{(4\tau^2(\omega_{laser} - \omega_o)^2 + 1 + I/I_{sat})^2}.$$

Here α is greater than zero for red detuning so that the force opposes the atom velocity. This expression is exactly the form for the frictional (drag) force experienced by a particle moving in a viscous fluid. This analogy led to the coining of the well know term “optical molasses” for this type of laser cooling.

To express a lower limit for optical molasses cooling, we must remember that laser scattering will also induce a heating effect on the atoms because of the absorption and re-emission of the photons. Consider that when an atom absorbs a photon, it receives the momentum kick $\hbar k$. Therefore, it also gains a small amount

of kinetic energy $\sim^2 k^2/2M$: All the energy transferred to the atoms comes from the laser …eld so that the energy of the absorbed photon must be equal to the energy di¤erence between the excited and ground-state level plus the additional kinetic energy given to the atoms or $\sim!_{absorbed} = E_2 - E_1 + \sim^2 k^2/2M$: Upon decay of the excited atomic level, the atom releases the stored energy of amount $E_2 - E_1$. Since the atoms also receives a momentum kick in the re-emission, this additional energy must be extracted from the emitted photon $\sim!_{emitted} = E_2 - E_1 - \sim^2 k^2/2M$: The result is a net gain in kinetic energy of the atoms of $\sim!_{absorbed} - \sim!_{emitted} = \sim^2 k^2/M$ for a complete cycle. The competition between the energy lost due to molasses cooling αv^2 and the energy gain from heating $\sim k^2/M$ $_{scatt}$ results in an equilibrium temperature whose limit depends on the laser detuning. With optimal detuning, the low-temperature limit for optical molasses can be shown [39, 40] to be

$$T_D = \frac{\sim}{2k_B}: \tag{20}$$

This is known as the Doppler cooling limit (or Doppler limit), and for most alkali atoms this is on the order of a few hundred micro kelvin.

The …rst demonstration of optical molasses was performed on an atomic vapor of sodium atoms by Steve Chu et al. [41] at AT&T Bell Laboratories in 1985. They found that the temperature of a cooled atomic beam was near the Doppler limit in a three-dimensional optical molasses (six intersecting beams). Further investigations by P.D. Lett et al. [42] at the former National Bureau of Standards (now NIST), however, led to the discovery that this method of cooling achieved temperatures well below the Doppler limit. This could only be due to the presence of a previously unforeseen cooling mechanism that was later described by Jean Dalibard and Claude Cohen-Tannoudji [43]. Subdoppler cooling mechanisms (known as polarization-gradient cooling) are understood for two types of laser polarization,

linear ? linear and circular-circular ($¾^+$ k $¾^i$) and work because of the redistribution m_F states in a multi-level atom that results in larger friction coe¢cients. For a more detailed description of the polarization-gradient cooling, see the review articles by Adams and Riis [44] and also by Metcalf and van der Straten [45].

The time that an atoms spends in an optical molasses can be on the order of a second because of the extremely low atomic vapor temperature. However, optical molasses is not a trap for neutral atoms. To trap the atoms, it is necessary to provide a restoring force that brings the atoms back to some central position. Since there is no position-dependent force associated with the optical molasses, the atoms will eventually wander (albeit quite slowly at only a few cm/s) out of the laser intersection region. A clever technique to provide a restoring force was demonstrated by E.L. Raab et al. in 1987 [46]. The method exploits the Zeeman e¤ect where the degeneracy of the magnetic sublevels m_F is removed due to the presence of a magnetic …eld. Recall that the Zeeman splitting ($¢E = {}^1{}_b g_F m_F B$) depends linearly upon the magnitude of the magnetic …eld is di¤erent for each m_F sublevel: Because this trap uses both an optical and a magnetic …eld, it has been given the name magneto-optical trap, or a MOT for short.

To understand how the MOT works, consider a simpli…ed one-dimensional case (see Fig. 7). As with optical molasses, the lasers are tuned by a small amount ± below an optical transition f_0 and now made to be circularly polarized so that they have a preferred photon spin direction $¾$. The lasers shine onto a hypothetical vapor of two-level atoms having angular momentum $J^0 = 1$ in the excited state and $J = 0$ in the ground state. Lastly, a magnetic …eld gradient is introduced that has zero magnitude at the origin ($x = 0$); it increases in magnitude and has opposite direction for $x > 0$ and $x < 0$. The local magnetic …eld de…nes the quantization axis for each atom (i.e., the angular momentum of the $J^0 = 1$; $m_{J^0} = 1$ atomic

state will be aligned with the magnetic …eld vector).

First consider just the (shaded) laser that is incident from the right in Fig. 7. For atoms positioned at $x < 0$, the photon spin $\hat{z}$ of the shaded laser is aligned with the magnetic …eld. In this case only the $J = 0; m_J = 0 \rightarrow J' = 1; m_{J'} = 1$ transition is allowed by selection rules. This transition is not in resonance with the laser because the $m_{J'} = 1$ state is Zeeman shifted to higher energy. The resultant force (directed away from the origin) is consequently very weak. However, for an atom at $x > 0$ the photon spin is anti-parallel to the magnetic …eld and the shaded laser drives the $J = 0; m_J = 0 \rightarrow J' = 1; m_{J'} = -1$ transition. In this case the allowed transition of the atom is Zeeman shifted closer to the detuned laser frequency. The forced experienced by the atom, in this case, is strong and directed back towards the origin. The second laser will have an analogous e¤ect; therefore, atoms that are displaced from zero will experience a net force towards the origin where the force from both lasers is balanced.

The generalization of the magneto-optical trap to three dimensions turns out to be a relatively simple experimental task. The magnetic …eld gradient (typically of order $\partial B/\partial z \approx 10$ G/cm) is generally provided by a pair of coils arranged in anti-Helmholtz con…guration to produce a quadrupole …eld gradient. Six laser beams are made to intersect in a vacuum chamber that is maintained at a pressure of $\approx 10^{-8}$ torr or below to reduce the likelihood of collisions with background gas that will expel atoms from the trap. The selection of the appropriate laser polarization always seems to be a point of confusion due to the choice of conventions in signifying left and right ($\hat{\sigma}^-; \hat{\sigma}^+$) circularly polarized laser light. It is more clear to specify the direction of the photon spin $\hat{z}$ which makes the description of the MOT laser polarization have the same symmetry as the quadrupole …eld gradient. The correct choice of the polarization should make the photon spin (as in the 1d case above)

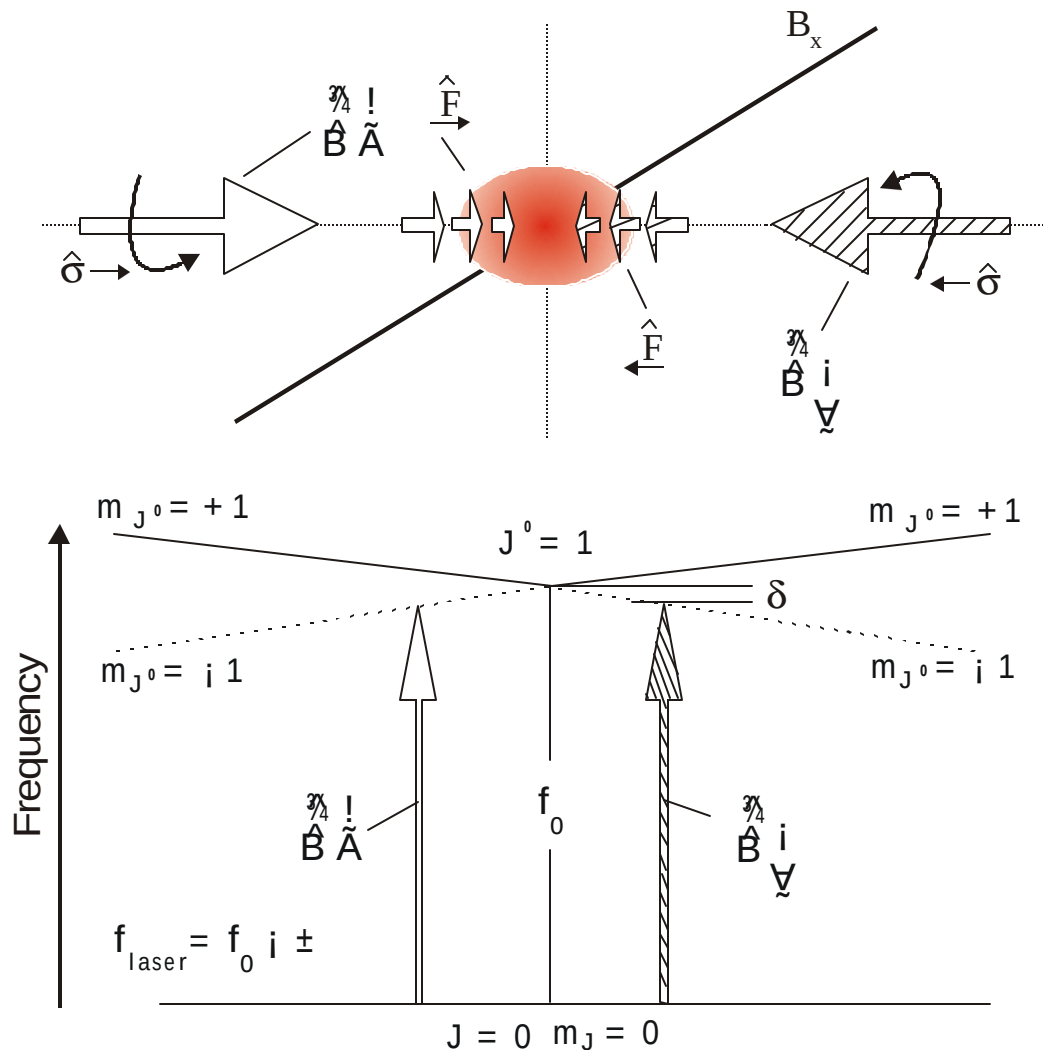

FIG. 7: The one-dimensional magneto-optical trap (MOT). The Zeeman effect is used to bring the atoms into resonance with the laser that is directed toward the origin (as viewed from the atom's position). The circularly polarized light requires that $m_{J'} - m_J = \pm 1$, where the "+" arises when the photon spin $\hbar$ is parallel to the magnetic field $\hat{B}$, and the "−" when they are anti-parallel. Recall that the quantization axis for an atom is defined by the magnetic field direction. The result is that the atoms are pushed back towards the origin where the forces from the two lasers balance.

opposite to the magnetic …eld direction that is along the laser propagation axis and nearest to the direction from which the laser beam is incident (see Fig. 8).

Alkali atoms with their lone valence electron provide the closest approximation to a two-state atom and are therefore the easiest prey to trap in a MOT. To provide a continuous trapping force, it is necessary to drive a cycling transition where the atoms have no choice but to return to the original ground state. Consider the case of ^{85}Rb (the energy level diagram is shown in Fig. 9). The $5P_{3=2}; F^{0} = 4$ state can only decay to the $5S_{1=2}; F = 3$ ground state because of the hyper…ne transition selection rules ¢F = §1; 0: The $5S_{1=2}; F = 3 \; ! \; 5P_{3=2}; F^{0} = 4$ is therefore called the cycling (or trapping) transition, and the lasers that form the MOT will be detuned by ± (usually a few linewidths) from this transition. The scattering rate formula (Eq. 17) shows that for this laser there is some probability of exciting the o¤-resonant $5S_{1=2}; F = 3 \; ! \; 5P_{3=2}; F^{0} = 3$ transition. Electrons that decay from this level can end up in the lower hyper…ne ground state where they cannot be addressed by the trapping lasers. This state must be continually cleaned out because otherwise all of the atoms will end up in the lower hyper…ne ground state and no longer be trapped. To do this a second repump laser frequency must be added. The repump requires much less laser intensity and any polarization will work.

The magneto-optical trap has evolved into the work-horse of atomic physics because it can be used to trap large numbers of atoms (between 10^7 and 10^{10} depending on the laser con…guration) directly from a hot (room temperature) atomic vapor. These traps are relatively deep being able to con…ne atoms with kinetic energy of up to a few mK. In addition, both Doppler cooling and polarization gradient cooling can be realized, to some extent, in a MOT. It can therefore be used to cool atoms to as low as tens of ^{1}K [47] with an appropriate choice of laser

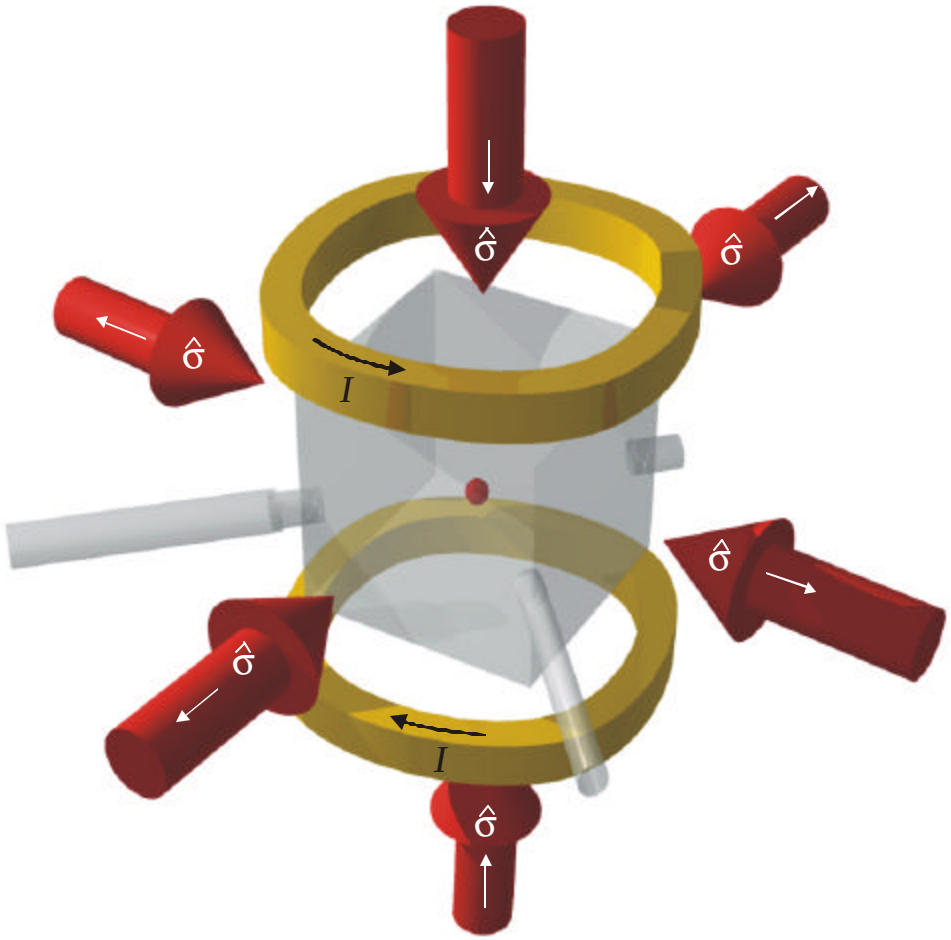

FIG. 8: Schematic for constructing a MOT in the laboratory. A vacuum chamber is maintained at $< 10^{-8}$ torr and contains the atomic vapor that is to be trapped. Anti-Helmholtz coils (current direction shown) are use to provide a magnetic …eld gradient. The correct choice of circular polarization for the six intersecting lasers is indicated by the photon spin direction.

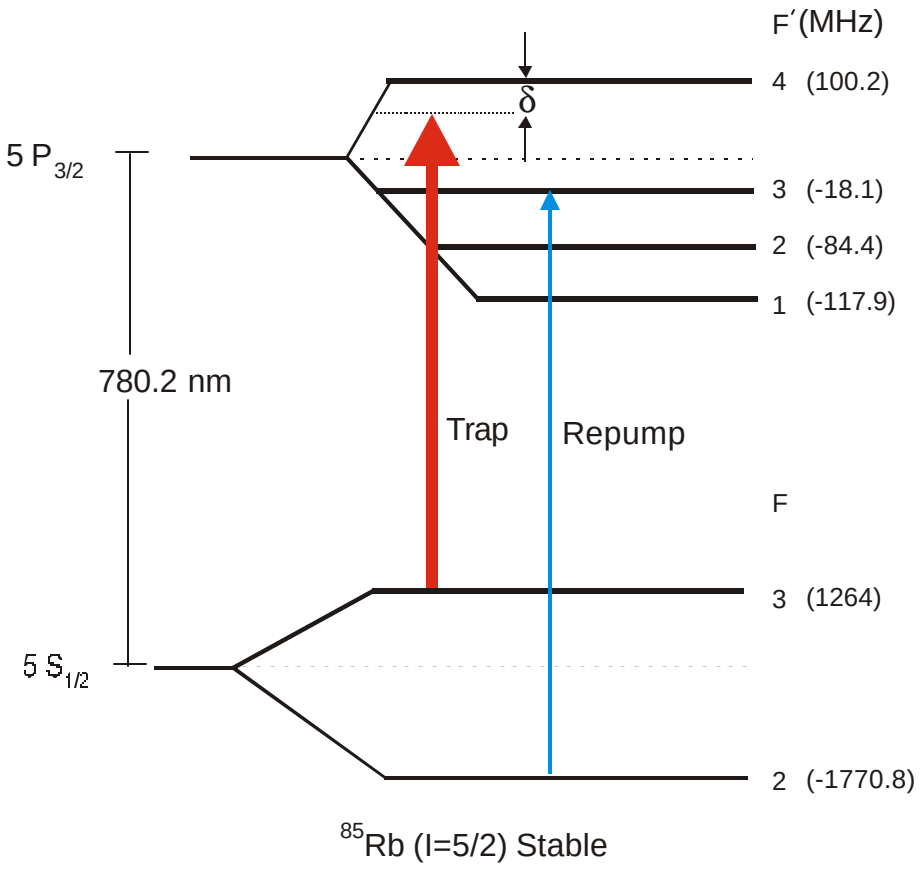

FIG. 9: Hyper…ne energy level structure for ^{85}Rb. To form a magneto-optical trap, the trapping lasers are detuned from the $5S_{1=2}; F = 3 \; ! \; 5P_{3=2}; F^{0} = 4$ cycling transition by a value ±. An additional repump transition needs to be excited in order to keep the atoms from piling up in the lower hyper…ne ground state.

intensity, detuning, and …eld gradient.

II. TRAPPING RADIOACTIVE ATOMS

Cooling and trapping of atoms has advanced to a point where a variety of fundamental experiments and applications that use this technology are being realized. There are several research groups around the world – Lawrence Berkeley National Laboratory (LBNL), State University of New York (Stony Brook), University of Colorado, Tri-University Meson Facility (TRIUMF) in Canada, and the Los Alamos National Laboratory (LANL)) – that have concentrated on trapping radioactive atoms in hopes of exploiting this technology to make fundamental measurements of the weak interaction. However, to gain the advantages of using trapped atomic sources, these groups have had to solve several di¢cult problems.

Atomic traps have a …nite lifetime that is the result of atomic collisions that can cause trap loss (e.g., collisions between trapped atoms and the hot background gas). In a chamber with good vacuum characteristics ($\gg 10^{-11}$ torr), traps can be constructed that have lifetimes of several hundred seconds. To be able to observe atoms undergo beta-decay while being trapped, it is bene…cial to trap short-lived isotopes that have a radioactive lifetime shorter than the atomic trap lifetime. The …rst problem in trapping radioactive atoms is that of how to move these short-lived isotopes from where they are produced into an environment that is suitable for trapping.

Two approaches to this problem have been explored. In the …rst, the trapping apparatus is connected directly to a production source where short-lived radioactive atoms are produced at the target facility of an accelerator. The solid target material can be heated to allow the more volatile alkali species to e¤use out, cre-

ating an atomic vapor. This method was used by Lu et al. at LBNL [48] to demonstrate the magneto-optical trapping of radioactive atoms (^{21}Na, $t_{1=2}$ = 22:5 s) in 1994. To transport the vapor of ^{21}Na atoms from the target region, the Berkeley group used transverse cooling lasers to form an atomic beam that was directed toward their trapping chamber. A Zeeman slower [49] was required to slow the atoms of the beam so that some portion could be captured directly by a MOT.

Stony Brook and TRIUMF also use on-line (in reference to an accelerator) e¤usive sources, but have improved upon the delivery of atoms to the trapping chamber. They ionize the radioactive vapor and transport the isotopes by electrostatic ion optics (including mass separation for TRIUMF) to a collection region. In order to trap the isotopes they must …rst be neutralized, which is done with a suitable choice of metal having work function less than the ionization potential of the species of interest.

A second approach to trapping radioactive atoms involves using a longer-lived parent source that decays into the short-lived species of interest. Major attention was paid to improving the trapping e¢ciency in this approach because in an o¤-line experiment the amount of radioactivity available is quite limited. However, being o¤-line can also be considered as an advantage because it does not require the use of an accelerator and therefore is not subject to the cost and scheduling issues that can go along with these facilities. The Los Alamos group is currently the only group that uses the o¤-line method. This group utilizes a long-lived parent source of ^{82}Sr ($t_{1=2}$ = 26 d) that decays to a short-lived daughter ^{82}Rb ($t_{1=2}$ = 75 s) that is of interest for beta-decay correlation measurements. The ^{82}Rb atoms are introduced into the trapping cell using an ion source and a mass separator coupled to a MOT.

A MOT can trap atoms directly from a room temperature atomic vapor, but even with large and intense laser beams it is only possible to capture the very low velocity tail (< 20 m/s) of the atoms in the Maxwell Boltzmann distribution. The key to attaining good e¢ciency was through the development of cell coatings that prevent the atoms from sticking to the inside walls of the trapping cell. This allows the atoms to pass through the trap region of the MOT many times and increases the probability that an atom will be captured.

Atoms will stick to the walls of a vacuum chamber due to van der Walls interaction between an atom and a polarizable surface. This interaction can be reduced if the cell walls are coated with a polymer …lm having a low polarizability to limit the attractive force. To be used successfully in optical trapping systems, these coatings must also have a low outgassing rate so that good vacuum can be attained.

Stevens et al. at the University of Colorado measured the sticking times and the vacuum properties of several dry…lm coatings [30]. This work led to the successful con…nement of »90 atomic francium atoms in an o¤-line system with a reported capture e¢ciency of » 50% [50]. This very good e¢ciency has not been reproduced by other group for trapping radioactive atoms. We, however, …nd the use of dry…lm to be critical since our trapping e¢ciency increases by more than a factor of 100 with a good coating. The maximum trapping e¢ciency achieved by our group, which is comparable to that achieved by Stony Brook and TRIUMF, is » 1%. The increase in e¢ciency has led to an increase in trapped atom numbers and spurred further measurements that were not before possible.

The group that is closest to reporting a fundamental result from beta-decay measurements of trapped radioactive atoms is TRIUMF. They detect the recoil atoms in coincidence with the emitted beta-particle in order to reconstruct the emitted

neutrino momentum. With this apparatus they are focusing on a measurement of the beta-neutrino correlation (known as little "a_F") in $^{38}K^m$ ($t_{1=2}$ = :924 ms), which is a pure Fermi transition. They have collected enough data to report a statistical accuracy that is at the » 1% level [51], and are now working to understand the systematic errors in their measurement.

The Stony Brook group has focused on measuring the atomic structure and comparing their measurements with theory for di¤erent Francium isotopes [52, 53]. Their long-term goal is to measure atomic parity nonconservation e¤ects, which are predicted to be 18 times larger in francium than in cesium atoms. Comparison of the atomic lifetimes and energies gives con…dence in the atomic structure calculations, which now limit the precision of parity nonconservation tests in atomic cesium [54].

The University of Colorado is not currently working on measurements with trapped radioactive atoms. The Berkeley group has performed a measurement of the hyper…ne splitting of ^{21}Na atoms [55] and, like the TRIUMF group, have the goal of performing a measurement of the beta-neutrino correlation, which for ^{21}Na involves a mixed Fermi and Gamow-Teller transition.

The work of the Los Alamos group (reported in this dissertation) has focused on producing a polarized atomic source to measure the correlation between the emitted positron with the nuclear spin direction in atomic ^{82}Rb (a pure Gamow-Teller transition).

III. A SYSTEM FOR TRAPPING RADIOACTIVE ATOMS

A Zr foil implantation and release studies

The development of our hot-cavity ion source and single-stage mass separator used to produce the $^{82}Rb^{+}$ ion beam is described in Chapter 3 of Ralf Guckert's thesis [56]. There is also an account of the foil implantation and release tests and an explanation for the choice of yttrium. Yttrium was shown to release » 40% of the implanted ^{82}Rb atoms at 850 $^{\pm}$C, representing the best results of the foils tested.

Further implantation and release tests using a zirconium foil [57] have shown it to be an even better choice, releasing slightly more atoms than yttrium at a lower temperature and having a lower outgassing rate. Foil release is tested by implanting ^{82}Rb and monitoring the 776 keV ° ¡ ray (a 12.6 % branch) associated with its decay. A lead collimator is used to limit the viewing angle of the CsI ° ¡ detector to a small region about the foil. As the foil is heated and atoms are released, there is an associated drop in the 776 °-counts as the ^{82}Rb atoms leave the …eld of view for the detector.

Suitable foils must have a work function that is less than the ionization potential for rubidium (IP = 4:18 eV); otherwise the ^{82}Rb atoms will be ionized upon release from the foil and cannot be trapped by the MOT. When a potential of ¡ 300 V is applied to the foil it creates an electric …eld at the surface that is strong enough to prevent ions from escaping. This is used to test whether the ^{82}Rb atoms are ionized upon release. The application of the bias potential was found not to a¤ect the release from either Y or Zr, which have work function of 3.1 eV and 3.8 eV, respectively. As a control, we used this method to test the release from molybdenum (WF = 4:2 eV) and observed the release to drop from 80% to 10%

with the application of the bias potential. This indicates that rubidium is released from Zr and Y as neutral atoms.

Another important characteristic of the implantation and release foils is the vapor pressure of the foil at the temperature where release occurs. Too much outgassing can create a problem for e¢ciently loading the MOT because the background gas can greatly reduce the MOT trap lifetime through trap loss collisions. To test the outgassing of the foils, we make a measurement of the release of ^{82}Rb while trapping stable ^{85}Rb in the trapping cell. The stable atoms are continually loaded from an atomic getter source which is balanced with the collision loss rate of the MOT. If the foil signi…cantly increases the background gas pressure in the cell, then this will negatively a¤ect the MOT signal. A minimal e¤ect on the stable ^{85}Rb MOT is ideal. Fig. 10 shows a release comparison between Y and Zr using this test. The data clearly show that Zr has a vapor pressure that is much lower than Y at temperatures where the ^{82}Rb release from both foils is good (» 40%).

B Multiple isotope laser trapping setup

We have designed a very versatile laser system for trapping several isotopes of rubidium and cesium atoms. We are the …rst group to demonstrate the magneto-optical trapping of radioactive $^{82;83;84}$Rb and $^{135;137}$Cs atoms. The system is also capable of trapping stable ^{85}Rb, ^{87}Rb, and ^{133}Cs atoms as well. Several experiments are being pursued using these di¤erent isotopes including the study of sympathetic cooling between simultaneously trapped isotopes of rubidium, ultra-sensitive detection of the …ssion decay products $^{135;137}$Cs in an optical trap, and the measurement of beta-decay asymmetry in ^{82}Rb.

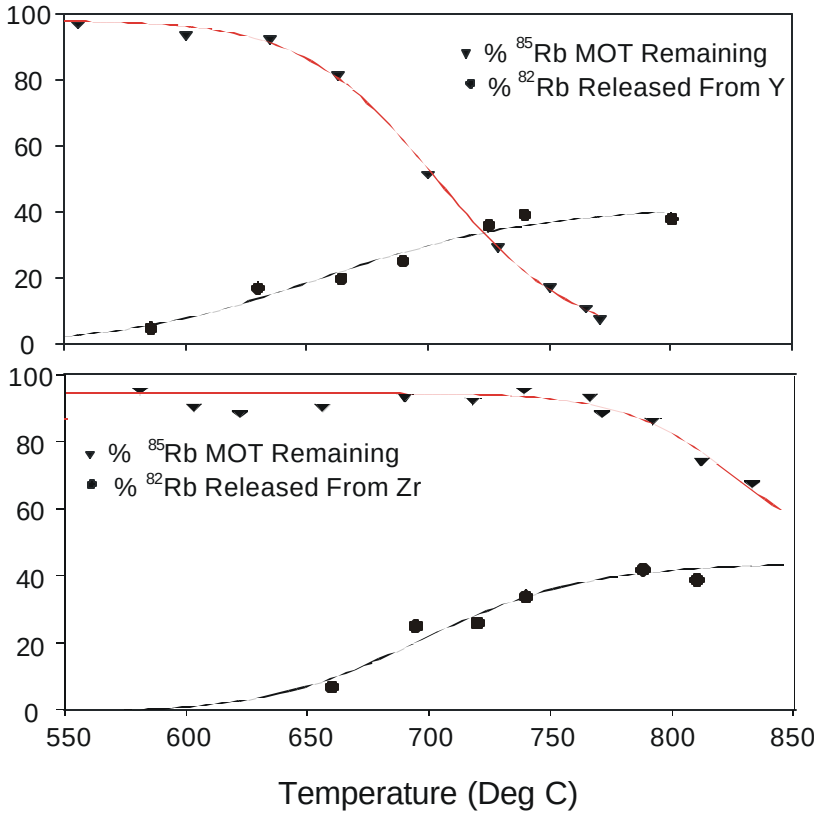

FIG. 10: Comparison of yttrium and zirconium for use as an implantation foil. Zirconium is found to release (measured via ° ¡ counting) slightly more ^{82}Rb atoms at a lower temperature and has less of an outgassing problem. The foil outgassing was tested by studying its e¤ects on a stable ^{85}Rb MOT.

Besides the development of a radioactive source, an added difficulty in trapping radioactive atoms is finding a frequency reference for the trapping and repump lasers of a radioactive MOT. Nuclear effects such as the magnetic dipole and electric quadrupole interaction as well as changes in the nuclear mass (i.e., the isotope shift) cause differences in the hyperfine atomic energy levels for isotopes of the same species. When trapping stable isotopes, laser spectroscopy on atomic vapor cells is used as a reference. For radioactive isotopes such vapor cells are not available, but in most cases the shifts in frequency are small enough that the transitions can be reached from the stable isotopes by shifting the laser with acousto-optic or electro-optic modulators.

Measurements at ISOLDE [58, 59] in the early 1980's have mapped out the D_2 line for many different isotopes of rubidium, cesium, and francium. The hyperfine structure for the rubidium isotopes of interest are shown in Fig. 11 and cesium isotopes in Fig. 12. The isotope shifts from ^{85}Rb and ^{133}Cs measured by ISOLDE are also indicated. Trapping laser frequencies are chosen to be cycling transitions so that the laser is continuously interacting with the atoms. For each isotope an additional repump transition is needed to prevent atoms from piling up in the second hyperfine ground state where it would become invisible to the trapping laser.

The laser system for trapping the different isotopes is shown in Fig. 13. A Coherent Sabre argon ion laser is used to pump two tunable Coherent 899 Ti:Sa ring lasers. For trapping Rb isotopes only one laser is used and an electro-optic modulator (EOM) is added to provide the repump transition. It is crucial to have enough laser power tuned to the trapping transition in order to attain good efficiency for radioactives with the 2^{00} laser beams used in the trapping cell. The Ti:Sa(1) laser is driven with up to 20 W of pump light to give an output of 1:5 ¡ 2

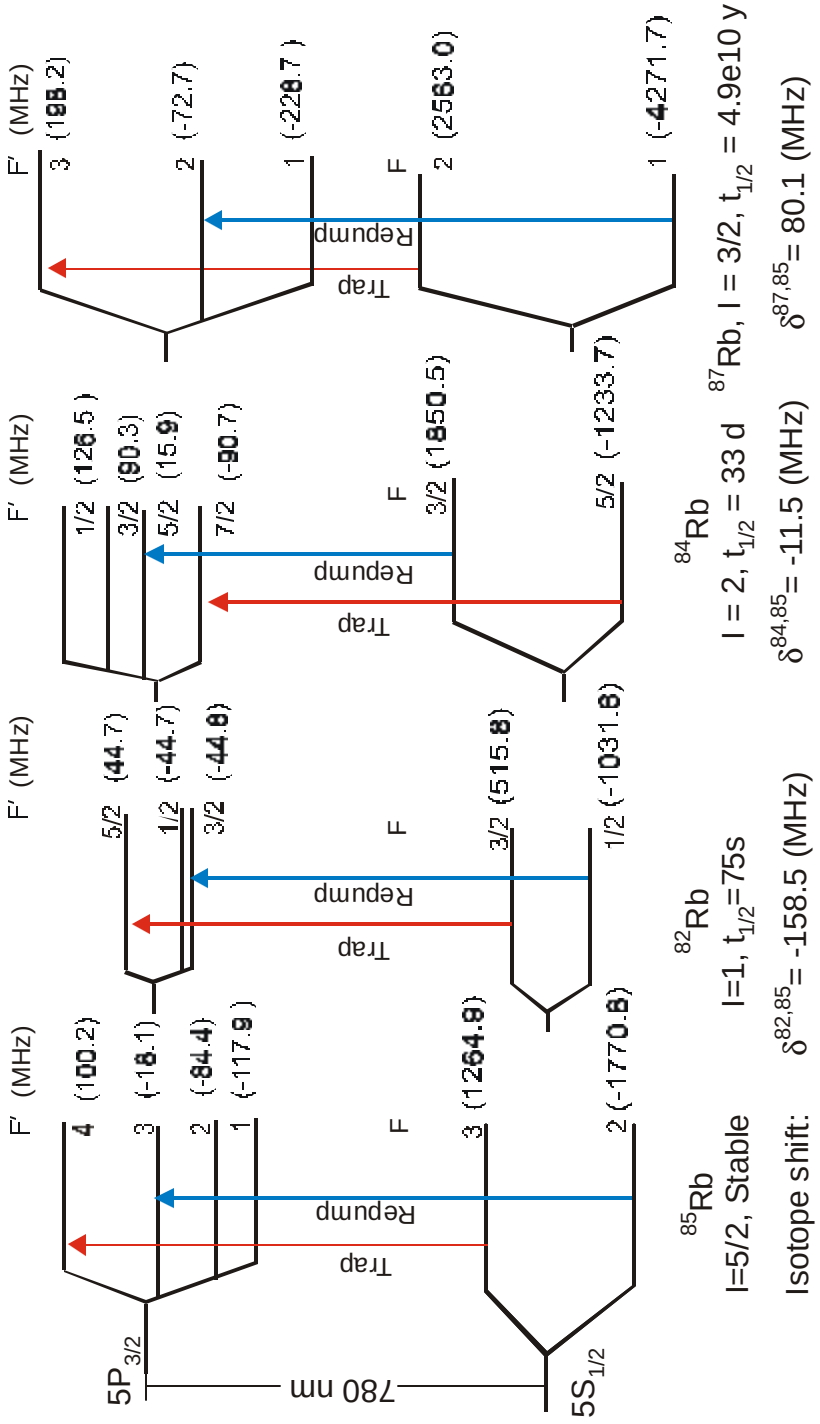

FIG. 11: Energy level diagrams (not to scale) for the D_2 line of four Rb isotopes.

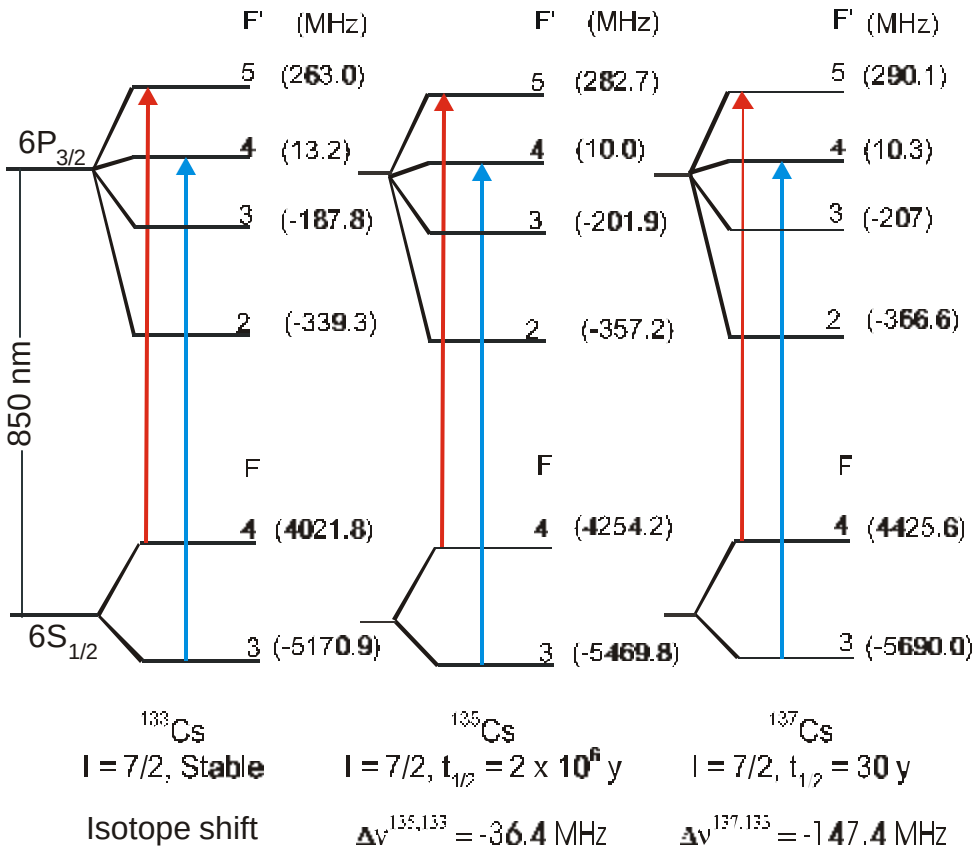

FIG. 12: Energy level diagrams (not to scale) for the D_2 line of three Cs isotopes.

W. The output power is divided into three parts. Approximately 2/3 goes to the trapping cell to form MOT I, 1/6 goes to the beta-chamber (MOT II) and another 1/6 goes to provide additional light for push, pump and probe beams. The second laser Ti:Sa(2) is in low-pump con…guration and has much less power output »300 mW. It provides enough laser intensity to trap stable ^{87}Rb from a getter source in the trapping cell. With this setup, ^{87}Rb can be trapped simultaneously with ^{82}Rb, ^{84}Rb, or ^{85}Rb. For trapping Cs isotopes the short wavelength optics of the Ti:Sa lasers used for Rb isotopes at 780 nm must be replaced with long wavelength optics to reach the 850 nm Cs transitions. Also, since we do not have the EOMs for Cs transitions, two lasers are required for trapping. The Ti:Sa(1) laser is tuned to the trapping transition and Ti:Sa(2) is used to provide the repumping light.

A Burleigh WA-1000 wavemeter is used to tune the lasers within several nm of the alkali transitions and a Coherent Model 240 Fabry-Perot spectrum analyzer is used to monitor the single-mode output of each laser. Fine-tuning of the frequency is done using FM saturated absorption spectroscopy [60] on either Rb or Cs vapor cells This method requires the use of an additional EOM and an acousto-optic modulator (AOM) for each laser, but provides a very nice di¤erential signal (see Fig. 14) that can be used to lock the laser (via negative feedback) to a particular transition. Note that in addition to the real transitions, this method also gives what are called “cross-over” transitions (at exactly half the frequency between two upper-hyper…ne levels) because of the lasers traveling in opposite directions in the vapor cell.

The stable references used for the various isotopic trapping and repump transitions are given in Table I. To shift the laser from the stable transition, an AOM in double pass con…guration is used before the saturated absorption portion of each laser setup. Using this method double pass (twice the AOM driving frequency),

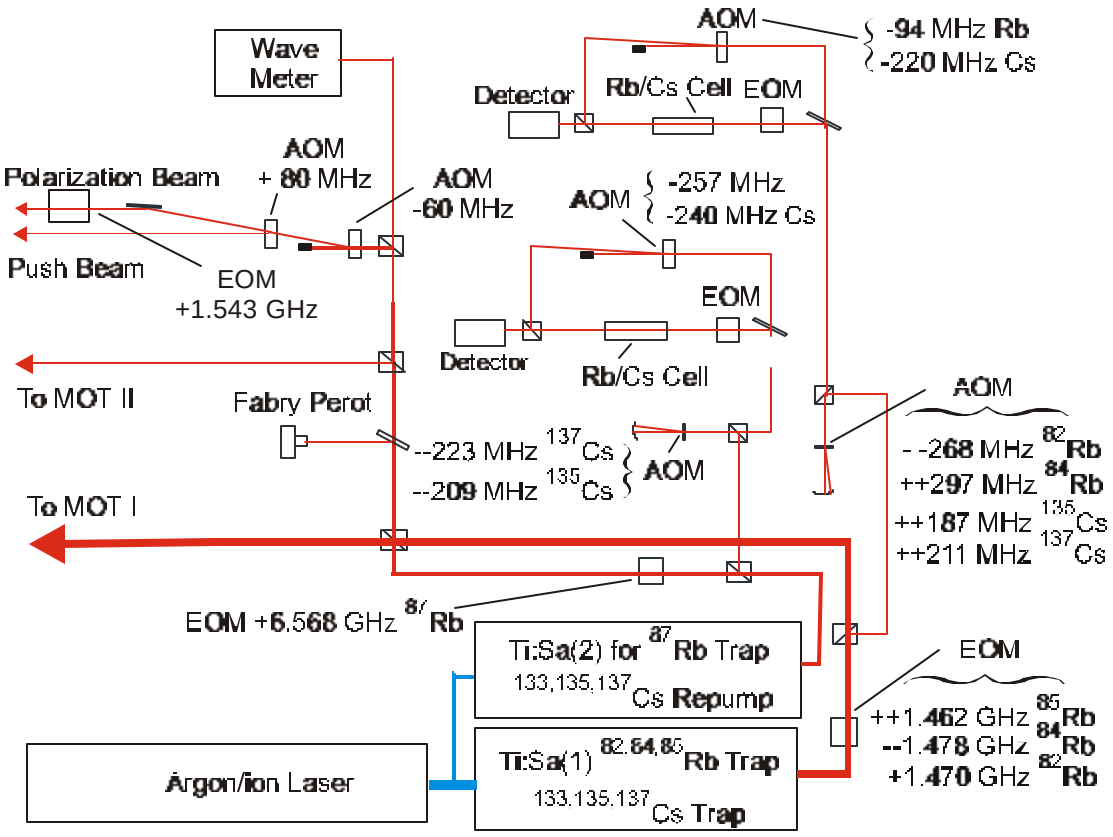

FIG. 13: Laser system for trapping various isotopes of Rb and Cs, "++" stands for the second upper harmonic or the double-pass upper-sideband of an EOM or AOM, respectively. Likewise, the "¡" indicates a lower harmonic or lower side-band.

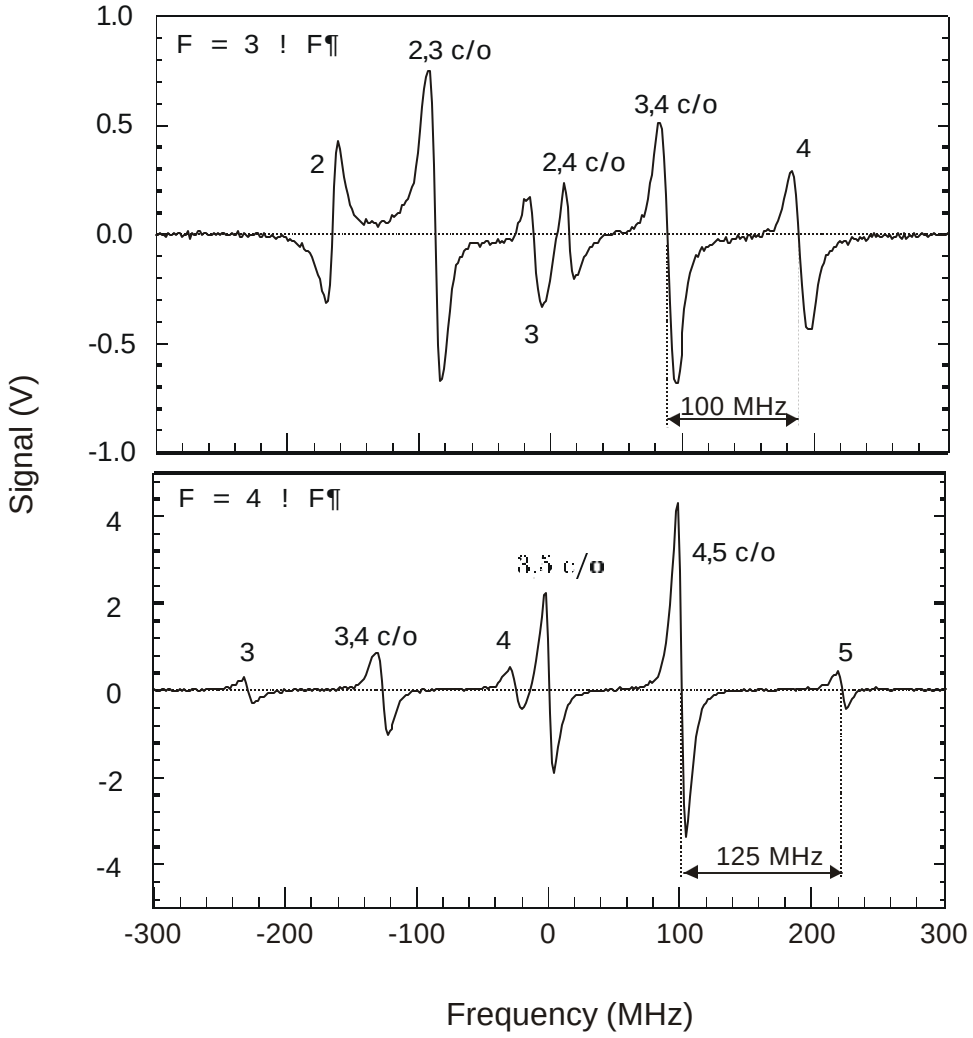

FIG. 14: Frequency-modulated saturated absorption signal for the $6S_{1=2}$! $6P_{3=2}$ transition from both the F = 3 and F = 4 ground state hyper…ne levels in ^{133}Cs. In this di¤erential signal the transition are centered at the zero-crossing point, to which the laser can be locked.

single pass or carrier laser light can be used to do the vapor cell spectroscopy with little or no laser realignment. The EOM and AOM drive frequencies given in Fig. 13 for the various isotopes will provide the frequency shift from the reference transition. Note that when calculating the frequency shift from the laser setup, an upper-sideband in the reference arm corresponds to a lower laser frequency sent to the trap. Also note that the saturation AOM provides a frequency shift that is only 1/2 of its drive frequency because of a counterpropogating e¤ect in the saturation spectroscopy.

C Calculating the number of trapped atoms

The calibration of the number of trapped atoms is accomplished by using a photodiode (P.D.) to determine the number of photons being emitted by the atoms in the MOT. Once this is known, we can simply deduce the scattering rate per atom in order to determine the total number of atoms trapped (N).

$$N = \left[\frac{\text{Photon Emission Rate (R)}}{\text{Scattering rate per atom}} \right] : \tag{21}$$

The light intensity from the ‡uorescing MOT cloud is measured using a calibrated photodiode and detected using a lock-in ampli…er. We can determine the intensity of the ‡ourescing atoms (P) from the lock-in signal current $I_{lock\text{-}in}$ by considering:

1. Photodiode sensitivity. This is measured to be $S_{P.D.}$ = (1 mW=450 ^{1}A) using a calibrated light source.

TABLE I: Reference transition and frequency shifts for trapping several di¤erent isotopes of Rb and Cs. Transitions are on the D_2 line and the trap laser detuning is assumed to be $\pm = ¡17$ MHz for all isotopes except ^{87}Rb where it is -8 MHz.

Isotope	Transition	Reference	¢ (MHz)
^{85}Rb Trap	$(F = 3 ! F^0 = 4) ¡ \pm$	^{85}Rb $(F = 3 ! F^0 = 3;4$ c/o)	42
^{85}Rb Repump	$(F = 2 ! F^0 = 3)$	^{85}Rb Trap	2926
^{82}Rb Trap	$(F = 3=2 ! F^0 = 5=2) ¡ \pm$	^{85}Rb$(F = 3 ! F^0 = 3;4$ c/o)	583
^{82}Rb Repump	$(F = 1=2 ! F^0 = 3=2)$	^{82}Rb Trap	1470
^{84}Rb Trap	$(F = 5=2 ! F^0 = 7=2) ¡ \pm$	^{85}Rb $(F = 2 ! F^0 = 3) ¡ 89$(MHz)	-549
^{84}Rb Repump	$(F = 3=2 ! F^0 = 5=2)$	^{84}Rb Trap	-2960
^{87}Rb Trap	$(F = 2 ! F^0 = 3) ¡ \pm$	^{87}Rb $(F = 2 ! F^0 = 2;3$ c/o)	127
^{87}Rb Repump	$(F = 1 ! F^0 = 2)$	^{87}Rb Trap	6571
^{133}Cs Trap	$(F = 4 ! F^0 = 5) ¡ \pm$	^{133}Cs $(F = 4 ! F^0 = 4;5$ c/o)	125
^{133}Cs Repump	$(F = 3 ! F^0 = 4)$	^{133}Cs $(F = 3 ! F^0 = 3;4$ c/o)	120
^{135}Cs Trap	$(F = 4 ! F^0 = 5) ¡ \pm$	^{133}Cs $(F = 4 ! F^0 = 5)$	-265
^{135}Cs Repump	$(F = 3 ! F^0 = 4)$	^{133}Cs $(F = 3 ! F^0 = 2;3$ c/o)	536
^{137}Cs Trap	$(F = 4 ! F^0 = 5) ¡ \pm$	^{133}Cs $(F = 4 ! F^0 = 3;5$ c/o)	-315
^{137}Cs Repump	$(F = 3 ! F^0 = 4)$	^{133}Cs $(F = 3 ! F^0 = 3)$	570

2. The signal suppression due to detecting the modulation of the cloud ‡uorescence with an lock-in ampli…er. The ac signal measured using the Stanford Research Systems lock-in ampli…er was measured to be a factor of $\eta_{\text{lock-in}} = 5{:}07$ lower than the direct unmodulated signal.

3. Light transmitted to the photodiode. Estimated drop for Interference …lter (50%), glass cell walls (90%), and focusing lens (85%). Combined they give a factor of $\tau^2_{\text{trans}} = {:}383$:

4. The ‡uorescence collection solid angle (relative to 4π) is estimated to be $\Omega = 2{:}75 \times 10^{-3}$ for the trapping cell MOT. This estimate uses the lens f# and the aperture distance from the trapped cloud.

The intensity of the measured ‡uorescing light can be written

$$P = \frac{I_{\text{lock-in}}\, S_{\text{P.D.}}\, \eta_{\text{lock-in}}}{\tau^2_{\text{trans}}\, \Omega}: \tag{22}$$

We therfore have

$$P[\mu W] = 10{:}9 \times 10^3 \times I_{\text{lock-in}}\,[\text{pA}]. \tag{23}$$

The emission rate is given by

$$R = P/h\nu \tag{24}$$

so

$$R[\text{Hz}] = I_{\text{lock-in}}\,[\text{pA}] \times 4{:}3 \times 10^{10}: \tag{25}$$

The atomic scattering rate for a magneto-optically trapped atom depends on many factors. It presents the largest uncertainty in calculating the total number of trapped atoms. The scattering rate is given by

$$i_{scatt} = \frac{1}{2¿}\frac{I=I_{sat}}{1 + I=I_{sat} + 4¿^2(!_{laser} ¡ !_o)^2} \tag{26}$$

where ¿ = 27 ns [61] for the Rb $5S_{1=2}$! $5P_{3=2}$ transition, $I = I_1 + I_2 + ¢¢¢ + I_6$ is the combined laser intensity for six MOT laser beams, $I_{sat} = \frac{h¼c}{3¿} = 4{:}9$ mW/cm^2 for Rb, and $!_{laser} ¡ !_o = 2¼(f_{laser} ¡ f_o)$ is the laser detuning. The Doppler term ($\hbar k ¢ v$) is not included here because it can be neglected for the very cold MOT trapped atoms. This calculation for the number of atoms works best for small clouds. When trapping a large number of atoms in a MOT (> 10^6) the optical density of the cloud itself cannot be neglected when calculating the scattering rate.

Systematic uncertainties arise in the determination of the intensity at the center of the MOT. The intensity in the beams is not quite uniform and being located inside the glass cell it cannot be measured directly. The saturation intensity I_{sat} is a factor of three higher than that typically used for an unpolarized beam because the circular polarization and the magnetic …eld of the MOT e¤ectively remove the degeneracy that is present in the transition for an unpolarized beam. We measure the laser detuning by probing the trap with a modulated laser beam and …nd that it is » 17 MHz. In order to optimize the trapping e¢ciency of a MOT for a given beam size, magnetic …eld and beam alignment, the intensity and detuning of the laser light must be adjusted. These parameters have a tendency to change over time so care must be taken to carefully measure these parameters when calculating the scattering rate.

D SC-77 dry…lm cell coatings

The original OTS cell was used in radioactive trapping experiments for about approximately one year. During this time the trapping e¢ciency of the system

steadily degraded (ultimately by a factor of 500). All other parameters being unchanged, we determined the decline was due to degradation of the OTS dry-…lm coating in the trapping cell. We attempted to reproduce the OTS coating, but were unable to achieve the original e¢ciency. We therefore investigated the vapor-deposited SC-77 type dry…lm [30], which is more widely used by the other radioactive trapping groups.

The recoating procedure involves removing the trapping cell, decontaminating it, performing the coating procedure (see Ref. [30]), reinstalling, baking, and measuring the new trapping e¢ciency. The entire process takes about two weeks and there is some variation in the performance between coatings. In order to avoid repeated recoatings, an e¤ort was made to understand what could causes the degradation. It was found that prolonged heating of the implantation foil (i.e., Zr foil at > 800 ±C) and/or prolonged exposure to large amounts of stable Rb vapor (»10^{-7} torr) could damage the cell coating. Exposure to these degrading elements is now kept to a minimum.

The determination of the coating quality is best made by trapping e¢ciency measurements with radioactive atoms. An accurate estimate of the number of atoms implanted and released from the Zr foil can be determine by monitoring the 776 keV gamma-ray associated with the decay of ^{82}Rb atoms that have originated from the foil region. The trapping e¢ciency in this case is determined by the ratio of atoms trapped in the MOT after heating the foil to the number of ^{82}Rb atoms that are released from the foil. The best e¢ciency attained with SC-77 type dry…lm is approximately 1%.

In the event that a radioactive source is not available, it is convenient to have another method by which to monitor the trapping e¢ciency using stable isotopes. A separate measurement of coating quality was developed using a ‡uorescence

technique [62], where the Doppler pro…le of a released atomic vapor is studied. In this measurement, either ^{85}Rb or ^{133}Cs is …rst implanted into the catcher foil. When the foil is heated, a plume of atoms is released with a thermal distribution of velocities determined by the foil temperature.

A narrow (1 mm Á) probe beam that is passed vertically through the center of the trapping cell is used to excite the released atoms. We image and detect the ‡uorescence from a small portion of this beam located at the center of the trapping cell. This ‡uorescence signal is observed to have two components (see Fig. 15). The …rst arises from atoms being emitted directly from the foil and intersect the probe beam in the detection region at an angle of » 90±. Since these atoms have negligible velocity in the direction of the probe beam, they produce a narrow Doppler pro…le (» 50 MHz, FWHM). The second component is due to atoms that bounce from the cell walls prior to entering the detection region and hence exhibit the full Doppler linewidth (» 1 GHz, FWHM). By measuring the width ($4\grave{A}_{broad}$, $4\grave{A}_{narrow}$) and amplitude (A_{broad}; A_{narrow}) for each component, the average number of bounces taken by atoms that are released from the foil can be estimated as

$$\text{Bouces} \frac{1}{4} (A_{broad}=A_{narrow})(4\grave{A}_{broad}=4\grave{A}_{narrow}): \tag{27}$$

The number of bounces has a strong correlation to the trapping e¢ciency because it provides more opportunity for an atom to pass through and be cooled at the intersection of the trapping lasers. We have not yet correlated the Doppler pro…le method with the radioactive trapping e¢ciency measurements. However, we have used this method as a relative measure of coating quality using stable atoms. Note that care must be taken when performing the Doppler pro…le measurement since the coating may, to some degree, be damaged due to the exposure of the alkali atoms used during the test.

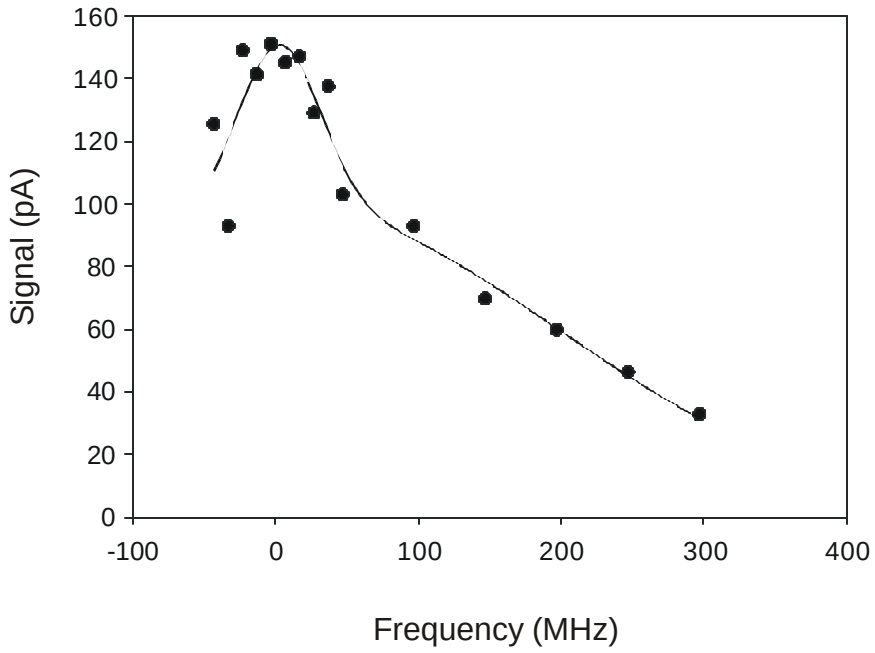

FIG. 15: Data collected in the ‡uorescence method of determining the coating quality using stable ^{133}Cs. Both the narrow (¾ = 29 MHz) and broad (¾ = 194 MHz) contribution to the signal are evident and determined by …tting a double Gaussian to the data (solid line). The relative amplitude for the narrow and broad components (51 and 96 pA, respectively) indicate that the atoms bounce on average 14 times with this coating.

CHAPTER 3

PARITY VIOLATION OBSERVED IN THE BETA DECAY OF MAGNETICALLY TRAPPED ^{82}Rb ATOMS[2]

ABSTRACT

Laser cooling and atomic trapping techniques have been employed to con…ne polarized ^{82}Rb atoms ($T_{1=2}$ = 75 s) in a magnetic Time-Orbiting-Potential (TOP) trap. We have observed the parity-violating correlation between the emitted positron momentum and the parent nuclear spin as a continuous function of angle and positron energy for this pure Gamow-Teller (GT) transition. These proof-of-principle measurements demonstrate the utility of exploring fundamental symmetries in a TOP trap and the steps required to improve sensitivity in the search for physics beyond the standard model.

[2]Coauthored by S.G. Crane, S.J. Brice, A. Goldschmidt, R. Guckert, A. Hime, J.J. Kitten, D.J. Vieira, and X. Zhao, Phys. Rev. Lett. 86, 2967 (2001).

Of the four fundamental forces in nature, the weak interaction is unique in that it violates parity, or space-reflection symmetry. More than four decades have passed since the first suggestion by Lee and Yang that parity could be violated in weak interactions [1] and the subsequent discovery in the beta decay of polarized ^{60}Co nuclei [2]. Today, maximal violation of parity (and of charge-conjugation) symmetry is accommodated in the standard model describing a pure vector-axial vector ($V - A$) helicity structure for weak interactions. This model was developed largely upon the empirical observations of nuclear beta decay during the latter half of the past century [63]. Despite the phenomenological success of the standard model, the fundamental origin of parity violation is unknown. Nuclear beta decay experiments continue to serve as a probe of the origin of parity violation and, more generally, the helicity structure of the weak interaction [64, 9].

One manifestation of parity violation in nuclear beta decay is the asymmetry in the angular distribution of the beta particles emitted relative to the spin orientation of the parent nucleus. Pure Gamow-Teller (GT) transitions offer a direct route to study parity violation because they proceed solely through the axial vector coupling in the standard model. To date, the most precise measure of the beta-spin correlation coefficient (known as A) from a pure GT decay comes from a modern experiment using polarized ^{60}Co nuclei [19]. In that experiment the angular dependence of the asymmetry was verified by measuring the relative electron intensity at a set of discrete angles. A value of $A = -1.01 \pm 0.02$ was deduced for the correlation coefficient in agreement with expectations for a pure GT, electron emitter with $\Delta J = -1$. Given the difficulty in reducing the systematic uncertainties associated with absolute polarization and electron scattering effects in a solid sample, improved precision appears unlikely using such technology. The advent of laser cooling [49], magnetic [65], and magneto-optical [46] trapping of neutral

atoms o¤ers a new approach for isolating and con…ning a cold and e¤ectively massless, radioactive source. A number of new generation experiments are now being pursued that exploit atom trapping technologies to study fundamental symmetries [48, 66, 67].

At Los Alamos, we have mounted an experiment to study the positron-spin correlation in ^{82}Rb beta decay by exploiting the unique features of a Time-Orbiting-Potential (TOP) trap [68]. Our goal is to explore possible deviations from maximal parity violation using this new technology. The TOP trap o¤ers the ability to con…ne a highly polarized sample of atoms in a cloud of order 1 mm diameter. A key feature for this experiment is the magnetic bias …eld that de…nes a polarization vector for the trapped sample and which rotates uniformly in an equatorial plane. This produces a rotating beacon of spin-polarized nuclei that can be used to measure the positron-spin correlation as a continuous function of positron momentum and emission angle using a single positron detector. Mapping the correlation function in this continuous fashion is of signi…cance since one can utilize both dipole (asymmetry) and quadrupole (anisotropy) terms in the angular distribution to measure recoil order corrections that are di¢cult to estimate beyond the allowed approximation when breaching the 1% level of precision [69, 70].

We use »10 mCi of ^{82}Sr ($T_{1=2}$ = 26 d), which decays by electron capture into ^{82}Rb ($T_{1=2}$ = 75 s) to provide a long-lived, o¤-line parent source for our short-lived species of interest. The ^{82}Sr sample is placed in the ion source of a mass separator which selectively ionizes, mass separates, and implants the ^{82}Rb daughter into a Zr foil that is located inside the primary trapping cell (see Fig. 16). Subsequent heating of the implantation foil releases ^{82}Rb atoms as a dilute vapor into the trapping cell where they are cooled and trapped by a magneto-optical-trap (MOT) (see Ref. [71], for more details). The trapped ^{82}Rb atoms are then transferred

through an 11-mm diameter, 40 cm long tube using a short pulse of laser light with magnetic con…nement along the tube axis [72] to guide the atoms into a second, high-vacuum chamber housing the positron detector. The transferred atoms are retrapped in a second MOT and then prepared for loading into the TOP trap.

Once retrapped in the second MOT, the atoms are further cooled using an optical molasses [73] and then optically pumped into the $5S_{1=2}(F = 3=2; m_F = 3=2)$ ground state. This electron-nuclear spin stretched state ensures that the nuclear spin is aligned with the local magnetic …eld. The TOP trap con…nes the atom in a quadrupole …eld gradient ($@B=@½ = 40$ G/cm) to which an 830 Hz rotating bias …eld of 15 G is added. The rotation frequency is small compared to the Larmor precession frequency of the atom, consequently the nuclear spin adiabatically follows the bias magnetic …eld. Monte Carlo calculations indicate that this choice of …eld-settings is appropriate to achieve polarization as high as 96% while ensuring that a false asymmetry associated with magentic de‡ection of positrons is smaller than 0.2%. We are able to trap as many as $500; 000$ ^{82}Rb atoms in a single loading of the TOP trap.

Positrons are detected in a plastic scintillator (76 mm diameter and 20 mm thick) after they pass through a thin (50 ^{1}m) stainless steel window that separates the detector from the second chamber vacuum, which is maintained at less than $3 £ 10^{i 11}$ torr. Passive collimators are employed to de…ne the full opening angle for positron detection of $18:2^{±}$. An event in the plastic scintillator triggers the data acquisition electronics to record the energy deposited in the plastic, the MOT ‡uorescence signal, and the coil currents that produce the quadrupole and rotating bias …eld. From the recorded bias coil currents we construct the direction of the average nuclear spin for each positron event up to a phase shift arising from the resistive skin e¤ect. This phase shift has been measured using a Hall probe

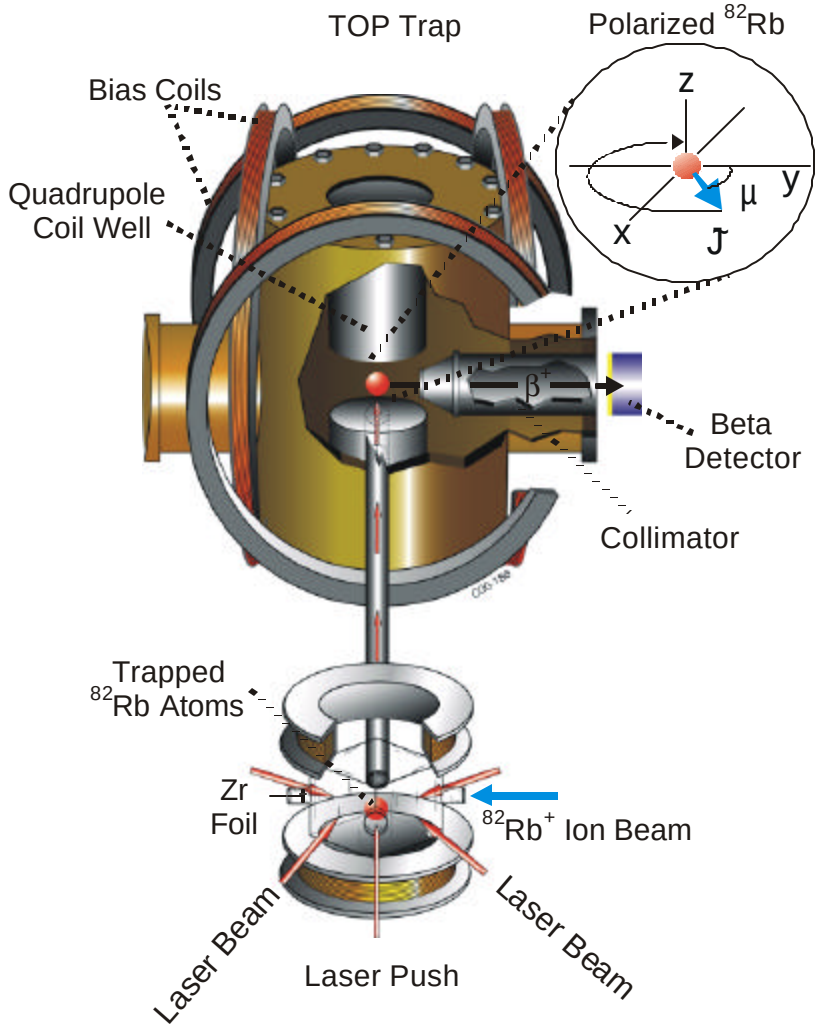

FIG. 16: Experimental system for producing a trapped and polarized source of ^{82}Rb (not drawn to scale). The atoms are trapped by a MOT in the glass cell, then transfered and loaded into a TOP trap in the second chamber. The TOP quadrupole …eld gradient is generated by anti-Helmholtz coils (not shown) located inside the quadrupole coil wells. Two pairs of Helmholtz coils are driven with a relative phase of 90± to produce the rotating bias magnetic …eld that is tracked by the sample polarization vector in the x-y plane. Positrons from the decay of ^{82}Rb emitted along the y-axis are detected by the plastic scintillator.

to be 131 § 2 degrees (zero phase occurs in the absence of the metal chamber). Data are collected in a cyclic fashion where we run through the entire sequence of implantation, release, trapping, transfer, optical pumping, TOP loading, and detection as described above. For each cycle we detect the decay of atoms in the TOP trap for 60 s. Typical positron detector and MOT ‡uorescence signals are shown in Fig. 17.

In order to study the angular distribution the data were binned according to the angle (μ) between the nuclear spin and the emitted positron momentum after integrating over the positron energy (see Fig. 18(a)). The data are well described by a $1 + \mathcal{R}\cos(\mu)$ distribution with a preponderance of positrons emitted in the same direction as the nuclear spin, which is expected for ^{82}Rb positron decay. These data distinctly demonstrate the successful con…nement of a rotating, nuclear-polarized sample of ^{82}Rb in a TOP trap.

For ^{82}Rb there are two dominant transitions that have positron-spin correlation coe¢cients of $A^{1^+ \to 0^+} = 1$ (branching ratio = 86:4%) and $A^{1^+ \to 2^+} = -1/2$ (12:6%) [74] in the standard model (i.e., a $V - A$ interaction): The measured angular distribution can be written as

$$N(\mu) = S(1 + PG\langle \bar{A} \rangle \cos(\mu + X)) + B;$$

where S is the signal arising from the TOP trap with an average nuclear polarization P, and G is a geometric factor that arises after averaging the cosine function over the …nite solid angle of the detector (G = 0:994). $\langle \bar{A} \rangle$ is the product of positron velocity relative to light and the asymmetry amplitude for the multi-branch decay of ^{82}Rb averaged over positron energy. The phase shift (X) extracted from the data of 133:4 § 0:5 degrees is in good agreement with independent measurements using the Hall probe. An uncorrelated background (B)

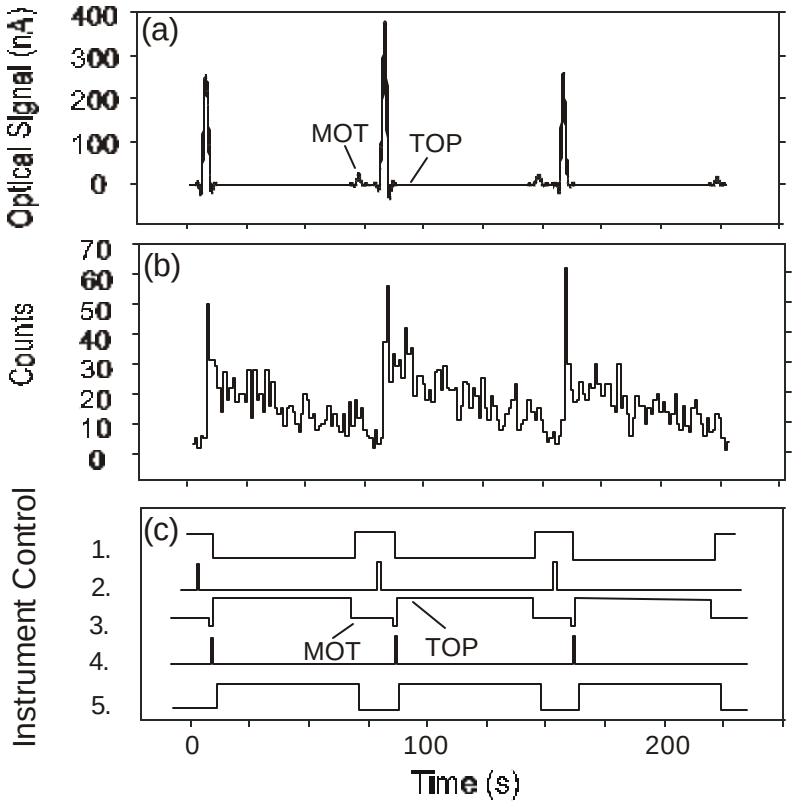

FIG. 17: (a) Fluorescence and (b) beta decay data collected using a 60 s detection interval. The large spikes in the MOT ‡uorescence signal, measured by a photo multiplier tube, indicate a successful MOT-to-MOT transfer of ^{82}Rb into the second chamber. The ‡uorescence abruptly drops when the MOT trapping light is turned o¤ as the TOP magnetic trap is loaded. At this point the beta decay signal drops by half, indicating »50% loading e¢ciency into the TOP trap. Beta-asymmetry data is accumulated from this point until the residual atoms are momentarily retrapped in a MOT just before the next cycle begins. (c) Typical time sequencing showing the on/o¤ pulsing of: 1. MOT lasers; 2. MOT-to-MOT transfer pulse; 3. quadrupole current (notice MOT and TOP levels); 4. molasses cooling and optical pumping; 5. bias coils and counting period.

arises from events that are detected but do not originate from the trapped sample. It is convenient to rewrite the distribution as $N(\mu) = N_0(1 + \mathcal{R}\cos(\mu))$, where $\mathcal{R} = (1 + B/S)^{-1} < A > P_e G$, and $N_0 = S + B$. A cosine fit to the observed angular distribution (Fig. 18(a)) yields $\mathcal{R} = 0.268 \pm .004$. In the standard model we compute $< A >= 0.80$ (using a positron energy threshold of 800 keV), indicating a nonzero background and/or polarization less than 100%.

The uncorrelated background is dominated by ^{82}Rb atoms that are lost in the trapping process and make their way to the walls of the chamber where they subsequently beta decay from an unpolarized state. Positrons can be detected from the walls when ^{82}Rb atoms find their way to the surface of the quadrupole coil wells or the thin window in front of the positron detector. Positrons originating at the quadrupole well do not have a direct line-of-sight to the detector but can still be detected if they scatter from the inside surface of the collimator. Two processes in which atoms are lost to the walls of the chamber give rise to separate background components. In the first place, losses occur due to inefficiencies in the MOT-to-MOT and MOT-to-TOP transfer processes (B_1). A second component (B_2) arises when atoms are lost due to the finite trap lifetime (measured to be 70 s). To determine the background associated with loading inefficiency (B_1), we recorded an independent data sample by loading the TOP trap and then immediately dropping the trap by switching off the quadrupole field. In order to study the effects of the finite trap lifetime, another data sample was recorded while extending the decay detection interval from 60 s to 250 s. The observed temporal decay departs from a single exponential and yields the combined contribution from B_1 and B_2. Analysis of these background experiments yields $B_1/S = 0.41 \pm .02$ and $B_2/S = 0.37 \pm .03$. A third, time-independent component (B_3) arises due to ambient background in the laboratory and is determined from measurements without ^{82}Rb transferred to

the second chamber to be $B_3/S = 0.110 \pm .004$.

Because we do not yet have the means to independently determine the sample polarization P, the extraction of the positron-spin correlation coefficient from the data was not possible. However, by using the total signal-to-background ratio ($B/S = 0.89 \pm 0.04$) along with the standard model value for $\langle \bar{A} \rangle$ of 0.80; we deduce a global nuclear polarization of $64 \pm 2\%$ for our ^{82}Rb sample.

By integrating the data over the observed emission angle, we produce an unpolarized sample and thus the differential energy spectrum for positrons. The spectrum is shown in Fig. 18(b) after subtracting the background components described above. Also shown is the Monte Carlo-derived spectrum expected for ^{82}Rb decay after folding in the energy-dependent response function for positrons in the apparatus. The simulation includes energy loss effects associated with scattering in the passive collimator and the thin window, back-scattering and Bremsstrahlung in the plastic scintillator, summing of 511 keV annihilation radiation in the plastic scintillator, and the intrinsic energy resolution of the detector. The data agree well with the assumption of an allowed shape and indicate that experimental distortions are under control. From this we deduce that the known instrumental effects, if not taken into account, would cause a systematic shift when extracting the positron-spin correlation coefficient that is smaller than 1%.

Analysis of these proof-of-principle experiments clearly points to several requirements and improvements to make a high-precision measurement of the positron-spin correlation coefficient in ^{82}Rb. Reduction of uncorrelated background can be accomplished with improvements in the trap loading efficiency and lifetime. We are also working to implement new detector hardware that will identify positrons that annihilate in the plastic scintillator and which originiate from the trap region. Ultimately, background can be largely eliminated by extracting the recoil ion in

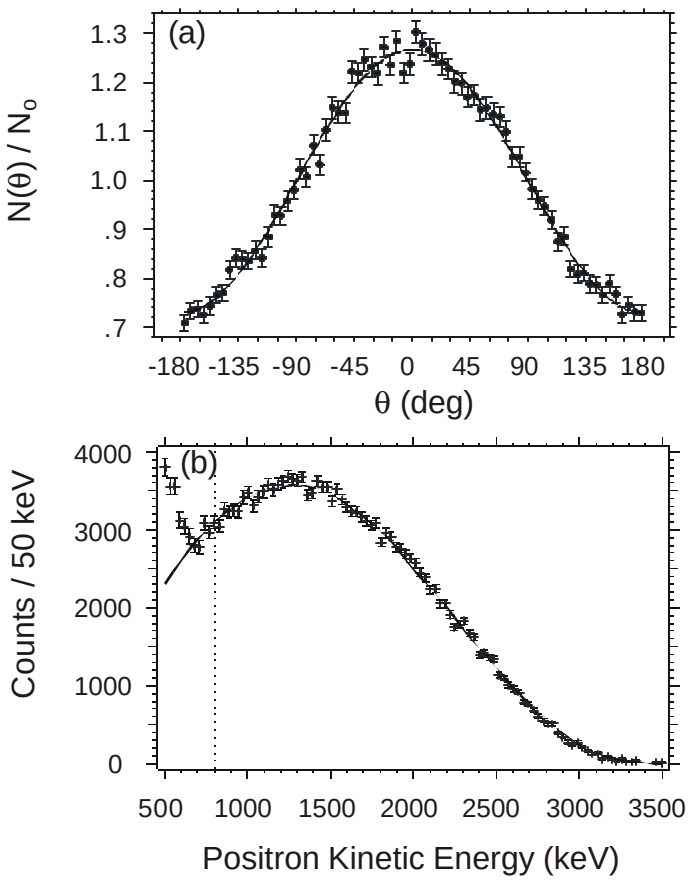

FIG. 18: ^{82}Rb beta decay data accumulated over a period of six hours. (a) The angular distribution obtained after binning the events as a function of positron-spin angle (phase shift removed) and integrating over the positron energy above a threshold of 800 keV. The solid line results from a cosine …t to the distribution from the trapped sample data. (b) The di¤erential positron energy spectrum obtained after integrating over the observed emission angle μ instead. The solid curve is computed assuming an allowed ^{82}Rb spectrum including the two-component decay scheme and folding in the experimental response function. The spectrum departs from a pure positron signal at low energy due to Compton scattering of 776 keV gamma rays from the 2^+ state of the ^{82}Kr daughter.

coincidence with the detected positron [51]. This would also allow for the simultaneous measurement of other correlation coe¢cients depending on the neutrino degrees of freedom. Clearly, an independent measurement of the polarization is required in order to extract the positron-spin correlation coe¢cient from the data. We are currently working to image the trapped sample, which provides information on the position distribution and temperature of atoms in the cloud. Together with a measurement of the magnetic …eld over the trap region, we will be able to determine the polarization of the trapped sample. Models of the atom cloud indicate that at 20 ^{1}K (a temperature that has been achieved using molasses cooling on stable Rb atoms [68]) we can expect polarization greater than 96% with our current experimental set-up. The present polarization of 64% suggests that improvements are required to optimize the optical molasses and optical pumping procedures. In addition, atomic ‡uorescence techniques will be applied to directly measure the atomic m-state population.

In summary, we have demonstrated the feasibility of a new method to study parity violation in nuclear beta decay using a TOP trap. We have recorded the parity violating, positron-spin correlation as a continuous function of positron energy and emission angle. The angular distribution and di¤erential energy spectrum is consistent with allowed ^{82}Rb decay and our knowledge of the positron response function. We have also developed techniques to measure the uncorrelated background and the information gained will be invaluable in reducing background in future experiments. Analysis of these proof-of-principle experiments indicates that, with su¢cient reduction of background and an independent measure of polarization, the positron-spin correlation coe¢cient could be extracted at the 1% level of precision and beyond. Future experiments can then improve the search for physics beyond the standard model that might arise in the presence of right-handed and/or tensor

coupling.

We are grateful to T.J. Bowles, E.A. Cornell, M. Di Rosa, S. Lamoreaux, D. Tupa, and C.E. Weiman for many useful discussions and suggestions. Particular thanks go to M. Anaya, W. Artcher, R. Mier, A.D. Montoya, F.J. Hauser, W. Teasdale, J. Smith and especially L.D. Benham for providing excellent technical support. This work is supported in large part by the Laboratory Directed Research and Development program at Los Alamos National Laboratory, operated by the University of California for the U.S. Department of Energy.

I. THE TOP TRAP AS TOOL FOR PRODUCING A POLARIZED SOURCE

A Magnetic trapping and the TOP trap

The first demonstration of magnetic trapping of atoms was done by A. L. Migdall et al. at the National Institute of Standards and Technology in 1985 [65]. In this experiment, the atoms were confined in a field gradient produced by a set of anti-Helmholtz coils. An atom placed in a field gradient experiences a force according to $\vec{F} = -\nabla(-\vec{\mu}\cdot\vec{B}) = \mu\nabla B$. The last equality follows from the adiabatic alignment (or following) of the atomic magnetic moment μ with the local magnetic field. Atoms with sufficiently low velocity (i.e., if cooled in a magneto-optical trap or from a laser-slowed atomic beam as in the original experiment) will be trapped in the quadrupole gradient provided that the magnetic moment μ of the atomic m_F substate is less than zero. Such states are referred to as weak-field seeking states.

The conditions for adiabaticity require that the change in the magnetic field observed by the atoms as they move about the trap be much less than the Larmor

precession frequency $!_L = {}^1B=\}$: This holds for atoms in the quadrupole …eld gradient except for near the zero …eld point that lies along the centerline and halfway between the coil pair producing the …eld. Atoms passing within some radius of this region will be susceptible to changes of the m_F sub-state (i.e., spin-‡ips) and can end up in a strong-…eld seeking state that is no longer trapped. Spin-‡ip transitions can cause detrimental loss to an atomic sample in a quadrupole trap when cooling the atoms to very low temperature. This occurs because the cold atoms spend more and more time near the zero …eld region of the quadrupole …eld as the temperature is decreased.

The time-average orbiting potential (TOP) magnetic trap, invented at the University of Colorado [68], was used in the …rst observation of atomic Bose-Einstein Condensation (BEC) in 1995. The TOP trap uses two additional sets of coils in Helmholtz con…guration, which are driven with an ac current having a relative phase of 90 degrees. This produces a constant magnitude (bias) magnetic …eld that shifts from center and rotates the zero-point of the …eld gradient (see Fig. 19). The zero-point now forms a circle, which is known as "the circle of death," since atoms coming near this region can be lost from the trap. This trick was used to solve the detrimental lifetime problem of the quadrupole magnetic trap at low temperatures by keeping the …eld region of high-loss away from the trapped sample. As a result, higher densities and colder temperatures could be reached in this trap, which allowed for the observation of a bosonic pile-up of atoms into the motional ground state (BEC).

The TOP trap, as viewed by the trapped atoms, is a time-average harmonic potential with a rotating bias magnetic …eld. Typical rotation frequencies are between 1 ¡ 10 kHz. A range chosen so that the atoms cannot move signi…cantly in response to the change in …eld gradient and below frequencies that could cause

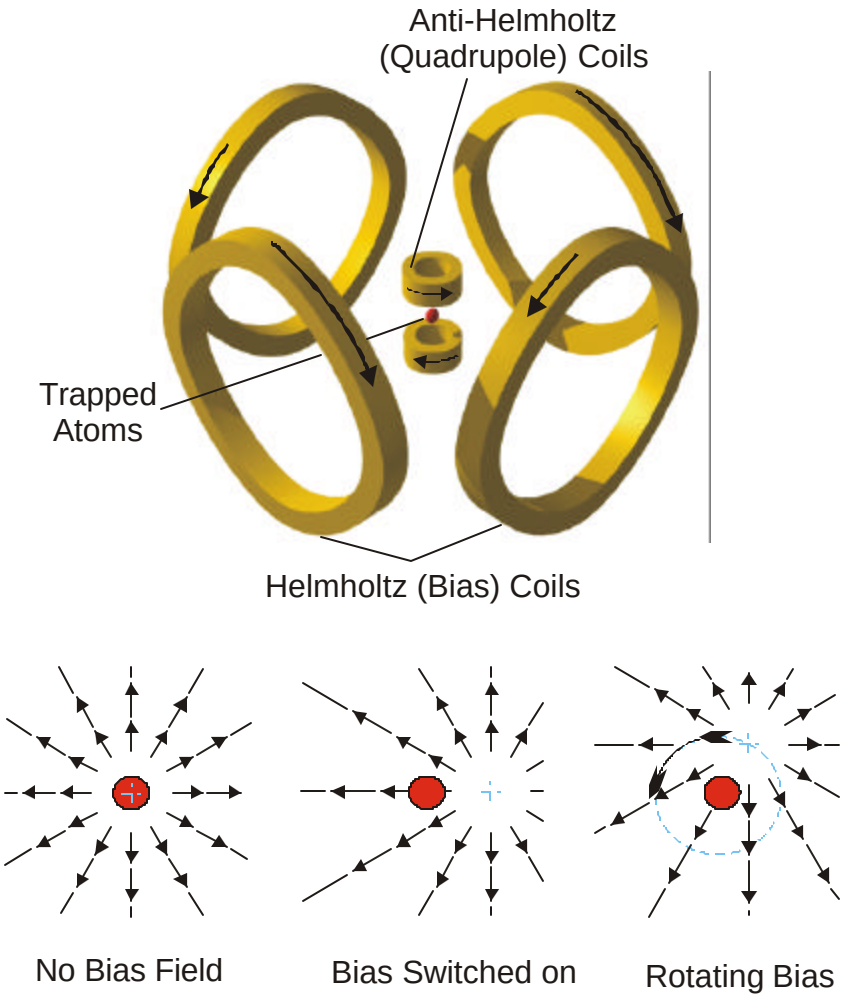

FIG. 19: Diagram showing the coils used to produce the time-averaged orbiting potential (TOP) magnetic trap. The direction of the applied currents is shown by the arrows on the coils. The coils in anti-Helmholtz con…guration provide the quadrupole …eld gradient and a constant rotating bias …eld is produced by two sets of coils in a Helmholtz con…guration. When excited, the bias coils shift the zero of the quadrupole …eld gradient away from the atoms. If the rotation frequency is su¢ciently high, the atoms cannot adjust to this change in …eld and remain trapped in a time-average potential.

adiabatic transitions. This means that the atomic magnetic moment adiabatically rotates along with the bias …eld. The nuclear spin will also precess provided that the atoms have been placed into a "stretched" state having the total atomic angular momentum (sum of the total electron angular momentum and the nuclear spin) aligned, or anti-aligned, with the quantization axis de…ned by the magnetic …eld. This is how nuclear polarization arise in the TOP trap.

Polarization, in this context, can have two di¤erent aspects. The …rst, referred to as state-purity, is the percentage of the trapped sample that is in a speci…c magnetic sublevel m_F. A second cause of depolarization can arise from a nonuniform magnetic …eld direction. Depolarization of this kind is present for a TOP trap due to the quadrupole …eld gradient, which of course is not uniform (see Fig. 20). The extent of the this pointing-type depolarization depends on the size of the TOP trap cloud because larger clouds sample more magnetic …eld non-uniformity. The following is a theoretical model used to describe the …eld con…guration and predict the expected polarization for the TOP trap assuming that all the atoms are in the desired stretched state [75].

B The B …eld of a single loop of wire

The …eld from a closed loop wire of arbitrary shape and carrying current I is given generally by

$$B = \frac{\mu_0 I}{4\pi} \int \frac{dl \times r}{|r|^3} \tag{28}$$

where dl is an element of length along the wire and r is the vector from this length element to the point where the …eld is being calculated.

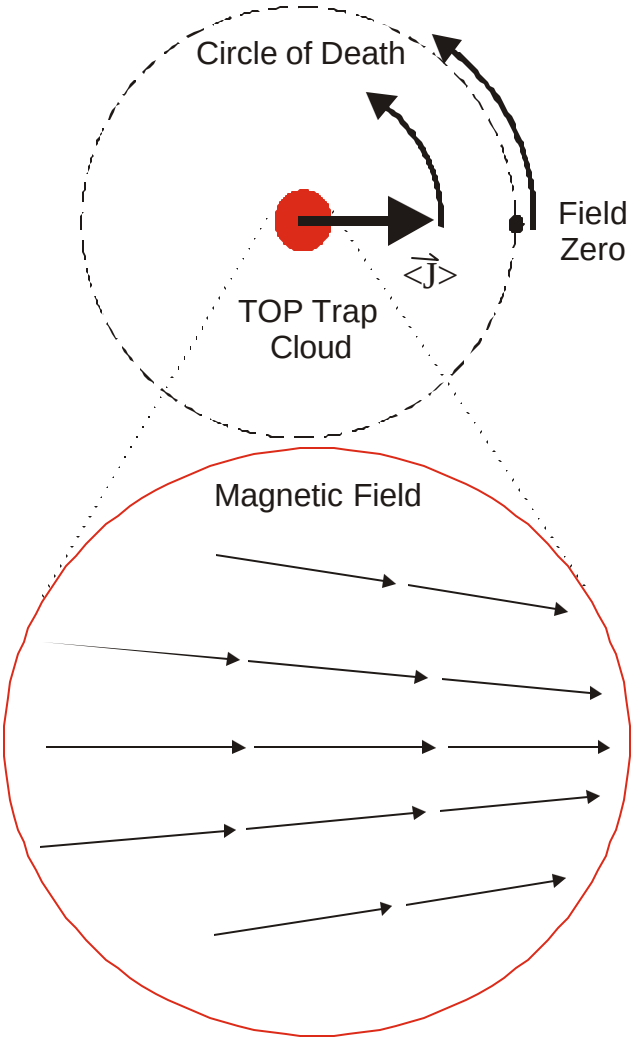

FIG. 20: Schematic showing how polarization arises in the TOP trap. The magnetic moment of the atoms (and hence the nuclear spin Ĵ for a stretched state) will be aligned with the local …eld of the TOP trap. As the bias …eld rotates, the nuclear spin tracks around like a beacon of polarized nuclei. The blowup region shows that the …eld direction over the extent of the cloud is not uniform. This is the cause of less-than-maximum average polarization and depends on the cloud size and temperature.

For a circular loop of wire of radius R in the XY plane, centered at the origin

$$d\mathbf{l} = \begin{pmatrix} -\sin\phi' \\ \cos\phi' \\ 0 \end{pmatrix} R\, d\phi' \qquad \mathbf{r} = \begin{pmatrix} \rho\cos\phi - R\cos\phi' \\ \rho\sin\phi - R\sin\phi' \\ z \end{pmatrix} \tag{29}$$

where (ρ, ϕ, z) is the position of the point (in cylindrical polar coordinates) where the field is being calculated and ϕ' is the azimuthal angle around the loop.

Therefore

$$\mathbf{B} = \frac{\mu_0 I R}{4\pi} \int_0^{2\pi} \frac{d\phi'}{[\rho^2 + R^2 + z^2 - 2\rho R\cos(\phi - \phi')]^{\frac{3}{2}}} \begin{pmatrix} z\cos\phi' \\ z\sin\phi' \\ R - \rho\cos(\phi' - \phi) \end{pmatrix} \tag{30}$$

Using the fact that

$$B_\rho = \mathbf{B}\cdot\hat{\boldsymbol{\rho}} = B_x\cos\phi + B_y\sin\phi \tag{31}$$

then

$$B_\rho = \frac{\mu_0 I R}{4\pi} \int_0^{2\pi} \frac{z\cos(\phi' - \phi)\, d\phi'}{[\rho^2 + R^2 + z^2 - 2\rho R\cos(\phi' - \phi)]^{\frac{3}{2}}}$$

$$B_z = \frac{\mu_0 I R}{4\pi} \int_0^{2\pi} \frac{R - \rho\cos(\phi' - \phi)\, d\phi'}{[\rho^2 + R^2 + z^2 - 2\rho R\cos(\phi' - \phi)]^{\frac{3}{2}}} \tag{32}$$

and $B_\phi = 0$ by an argument of symmetry.

Another symmetry argument leads to the replacement of $\cos(\phi' - \phi)$ by $\cos\phi'$ in the above equations and then using the substitution $2\theta = \pi - \phi'$ and the trig relation $\cos 2\theta = 1 - 2\sin^2\theta$ one can derive

$$B_\rho = \frac{\mu_0 I R}{4\pi} \frac{2Rz}{[(\rho + R)^2 + z^2]^{3/2}} \int_{-\pi/2}^{\pi/2} \frac{1 - 2\sin^2\theta}{[1 - k^2\sin^2\theta]^{3/2}} d\theta$$

$$B_z = \frac{\mu_0 I R}{4\pi} \frac{2Rz}{[(\rho + R)^2 + z^2]^{3/2}} \int_{-\pi/2}^{\pi/2} \frac{1 - 2\frac{\rho}{R+\rho}\sin^2\theta}{[1 - k^2\sin^2\theta]^{3/2}} d\theta \qquad (33)$$

$$k^2 = \frac{4\rho R}{(\rho + R)^2 + z^2}:$$

Using the fact that

$$\int_0^{\pi/2} \frac{d\theta}{[1 - k^2\sin^2\theta]^{3/2}} = \frac{E(k)}{1 - k^2} \qquad \int_0^{\pi/2} \frac{\sin^2\theta d\theta}{[1 - k^2\sin^2\theta]^{3/2}} = \frac{E(k)}{k^2(1 - k^2)} - \frac{K(k)}{k^2} \qquad (34)$$

(where $K(k)$ and $E(k)$ are the complete elliptic integrals of the first and second kind, respectively) and some rearrangement finally leads to

$$B_\rho = \frac{\mu_0 I R}{4\pi} \frac{k}{2(1 - k^2)\sqrt{\rho^3 R}} z(k^2 E(k) - 2[E(k) - (1 - k^2)K(k)])$$

$$B_\phi = 0$$

$$B_z = \frac{\mu_0 I R}{4\pi} \frac{k}{2(1 - k^2)\sqrt{\rho^3 R}} (R + \rho)(k^2 E(k) - 2\frac{\rho}{R+\rho}[E(k) - (1 - k^2)K(k)]):$$

(35)

C An accurate approximation

If the loop sits at $z = S/2$ then Eq. 30 becomes

$$B = \frac{\mu_0 I R}{4\pi}\int_0^{2\pi} \frac{d\phi'}{[\rho^2 + R^2 + (z - S/2)^2 - 2\rho R\cos(\phi - \phi')]^{\frac{3}{2}}} \begin{pmatrix} (z - S/2)\cos\phi' \\ (z - S/2)\sin\phi' \\ R - \rho\cos(\phi' - \phi) \end{pmatrix}. \tag{36}$$

Let

$$\alpha = \rho/R \quad \beta = z/R \quad \gamma = S/(2R) \tag{37}$$

and assume that $\alpha, \beta << 1$ and $\gamma O(1)$.

Therefore,

$$B = \frac{\mu_0 I R}{4\pi}\int_0^{2\pi} \frac{d\phi'}{[\alpha^2 + (\beta - \gamma)^2 + 1 - 2\alpha\cos(\phi - \phi')]^{\frac{3}{2}}} \begin{pmatrix} (\beta - \gamma)\cos\phi' \\ (\beta - \gamma)\sin\phi' \\ 1 - \alpha\cos(\phi' - \phi) \end{pmatrix}. \tag{38}$$

To 2nd order in α and β

$$\left[\alpha^2 + (\beta - \gamma)^2 + 1 - 2\alpha\cos(\phi - \phi')\right]^{-\frac{3}{2}} =$$

$$(1 - \gamma)^{-\frac{3}{2}}\left[1 + \frac{6\beta\gamma - 3(\alpha^2 + \beta^2)}{2(1 - \gamma^2)} + \frac{15\beta^2\gamma^2}{2(1 - \gamma^2)^2}\right] +$$

$$\left(\frac{3\alpha}{(1 - \gamma^2)} + \frac{15\alpha\beta\gamma}{(1 - \gamma^2)^2}\right)\cos(\phi' - \phi) +$$

$$\left(\frac{15\alpha^2}{2(1 - \gamma^2)^2}\right)\cos^2(\phi' - \phi). \tag{39}$$

All integrals in Eq. 38 are now of the form $\int \cos^m(\phi' - \phi)\cos^n\phi' d\phi'$ and can be

easily evaluated to yield (again to 2nd order in ® and ¯)

$$B = \frac{\mu_0 I}{4R}\frac{1}{(1+\epsilon^2)^{\frac{7}{2}}}\begin{pmatrix} [3\beta\bar{\alpha}(1-4\epsilon^2) - 3\beta\epsilon(1+\epsilon^2)]\cos\phi \\ [3\beta\bar{\alpha}(1-4\epsilon^2) - 3\beta\epsilon(1+\epsilon^2)]\sin\phi \\ 2(1+\epsilon^2)^2 + \frac{3}{2}(\beta^2 - 2\bar{\alpha}^2)(1-4\epsilon^2) + 6\bar{\alpha}\epsilon(1+\epsilon^2) \end{pmatrix}. \tag{40}$$

Substituting back in for ® and ¯ and remembering that cosÁ = x=½ and sinÁ = y=½, then

$$B = \frac{\mu_0 I}{4R^3}\frac{1}{(1+\epsilon^2)^{\frac{7}{2}}}\begin{pmatrix} 3(1-4\epsilon^2)xz - 3\epsilon(1+\epsilon^2)Rx \\ 3(1-4\epsilon^2)yz - 3\epsilon(1+\epsilon^2)Ry \\ 2(1+\epsilon^2)^2R^2 + \frac{3}{2}(1-4\epsilon^2)(x^2+y^2+2z^2) + 6\epsilon(1+\epsilon^2)Rz \end{pmatrix}. \tag{41}$$

To form a bias pair one places two coils at z = §S_b=2 with currents in the same direction. For a quadrupole pair one places two coils at z = §S_q=2 with the current in opposite directions. The bias and quadrupole …elds near their centers are then given by

$$B_b = B(-\epsilon_b) + B(\epsilon_b)$$

$$B_q = B(-\epsilon_q) - B(\epsilon_q). \tag{42}$$

De…ning the quantities

$$B_b \acute{} \frac{^1{}_0 I_b}{R_b} \frac{1}{(1 + °_b^2)^{\frac{3}{2}}}$$

$$- \acute{} \frac{3}{4R_b^2} \frac{1 ¡ 4°_b^2}{(1 + °_b^2)^2} \tag{43}$$

$$B_q^{\emptyset} \acute{} \frac{3^1{}_0 I_q}{2R_q^2} \frac{°_q}{(1 + °_q^2)^{\frac{5}{2}}}:$$

Then the bias and quadrupole …elds to 2nd order in $(x; y; z)=R$ are

$$B_b = B_b \begin{pmatrix} 0 \\ 2 - xz \\ 2 - yz \\ 1 + -(x^2 + y^2 ¡ 2z^2) \end{pmatrix} \qquad B_q = B_q^{\emptyset} \begin{pmatrix} 0 \\ x \\ y \\ ¡ 2z \end{pmatrix}: \tag{44}$$

The optimal separation of the bias coils for any particular radius occurs when the …eld is most uniform, i.e., when the gradient of B_b has a minimum as a function of coil separation. This occurs when

$$\frac{d^2}{d°_b^2} \frac{1}{(1 + °_b^2)^{\frac{3}{2}}} = 0: \tag{45}$$

This means that $°_b = 1=2$ or $S_b = R_b$, the separation between the coils equals their radii. Likewise, the coil separation which achieves the maximum quadrupole …eld gradient occurs when

$$\frac{d}{d°_q} \frac{°_q}{(1 + °_q^2)^{\frac{5}{2}}} = 0 \tag{46}$$

which implies that $°_q = 1=2$ or $S_q = R_q$.

D The TOP trap potential

With bias pairs b_1 along the X and b_2 along the Y axes having currents of angular frequency $!$ that are ¼=2 out of phase and with a quadrupole pair on the Z axis, the three …elds making up the instantaneous TOP …eld are

$$B_{b1} = B_b \cos !t \begin{pmatrix} 1 + -(¡2x^2 + y^2 + z^2) \\ 2 - xy \\ 2 - xz \end{pmatrix}$$

$$B_{b2} = B_b \sin !t \begin{pmatrix} 2 - xy \\ 1 + -(x^2 ¡ 2y^2 + z^2) \\ 2 - yz \end{pmatrix} \qquad (47)$$

$$B_q = B_q' \begin{pmatrix} x \\ y \\ ¡2z \end{pmatrix}:$$

The instantaneous TOP …eld is then

$$B_{TOP} = \begin{pmatrix} B_b[(1 + -(¡2x^2 + y^2 + z^2))\cos !t + 2 - xy \sin !t] + B_q' x \\ B_b[2 - xy \cos !t + (1 + -(x^2 ¡ 2y^2 + z^2))\sin !t] + B_q' y \\ 2B_b - (x\cos !t + y \sin !t) ¡ 2B_q' z \end{pmatrix}: \qquad (48)$$

Calculating $jB_{TOP}j$ to 2nd order in $x; y; z$ yields

$$jB_{TOP}j ¼ B_b \left[\left(1 + \frac{1}{2}\left(\frac{B_q'}{B_b}\right) \right)(x^2 + y^2 + 4z^2) + -(x^2 + y^2 + z^2) + \left(\frac{B_q'}{B_b}\right)(x\cos !t + y \sin !t) \right] +$$

$$\left(-\frac{1}{4}\left(\frac{B_q'}{B_b}\right)^2 xy\right)\sin\omega t\cos\omega t + \left(-\frac{3}{2}+\frac{1}{2}\left(\frac{B_q'}{B_b}\right)^2\right)\left(x^2\cos^2\omega t + y^2\sin^2\omega t\right) \qquad (49)$$

The time averaged TOP …eld is then simply given by

$$\overline{|B_{TOP}|} = \frac{1}{2\pi}\int_0^{2\pi} |B_{TOP}|\, d\omega t$$

$$\approx B_b\left[1+\frac{1}{4}\left(\frac{B_q'}{B_b}\right)^2\left(x^2+y^2+8z^2\right) - \frac{1}{2}\left(x^2+y^2-2z^2\right)\right]. \qquad (50)$$

For the optimal bias coil separation ($S_b = R_b$) $\delta = 0$, but even for a non-optimal yet realistic arrangement, it can be shown from Eqs. 43 that $\delta \ll (B_q'/B_b)^2$. Consequently the third term in parentheses above can be dropped.

E The density distribution of the atom cloud

An atom of mass M and magnetic moment μ in the time-averaged …eld of Eq. 50 will have a potential energy given by

$$P.E. = \mu\,\overline{|B_{TOP}|} + Mgz \qquad (51)$$

$$= \mu B_b\left[1+\frac{1}{4}\left(\frac{B_q'}{B_b}\right)^2\left(x^2+y^2+8z^2\right)\right] + Mgz. \qquad (52)$$

Some rearrangement and dropping of terms that do not depend on spatial coordinates leads to

$$P{:}E{:} = \frac{{}^{1}B_q'^2}{4\,B_b}(x^2 + y^2 + 8(z + \pm)^2) \tag{53}$$

$$\pm = \frac{M g}{4\,{}^{1}B_q'}\frac{B_b}{B_q'}{:}$$

If thermal equilibrium can be assumed, statistical mechanics states that the spatial probability distribution of an atom within the cloud is

$$P(x;y;z) \;/\; e^{i\frac{P{:}E{:}}{kT}}{:} \tag{54}$$

Hence the full, normalized density distribution is

$$N(x;y;z) = \frac{N_0}{(¼¾^2)^{\frac{3}{2}}}\, e^{i\left(\frac{x^2 + y^2 + 8(z + \pm)^2}{2¾^2}\right)} \tag{55}$$

where

$$¾^2 = \frac{2kT}{{}^{1}B_b}\left(\frac{B_b}{B_q'}\right)^{2} \tag{56}$$

and N_0 is the total number of atoms in the trap.

F The bias frequency

The frequency at which the bias …eld rotates is constrained at the low end by the need for it to be much greater than the natural oscillation frequency of the atoms in the harmonic trap and at the upper end by the need to avoid spin ‡ip by ensuring that the bias frequency is much lower than the smallest Larmor frequency encountered by the atoms. The natural oscillation frequency of the atoms is

found by equating $\frac{1}{2}M\omega_n^2$, where ω_n is the natural frequency, with the constant multiplying the quadratic term in the potential energy of Eq. 53. Therefore,

$$\omega_n = \sqrt{\frac{\mu B_b}{2M}\frac{B_q'}{B_b}}. \tag{57}$$

The smallest field strength that the atoms encounter is roughly $B_b - 3B_q'/4$ and so the smallest Larmor frequency is

$$\omega_L = \frac{\mu(B_b - 3B_q'/4)}{\hbar} = \frac{\mu B_b}{\hbar}\left[1 - 3\frac{B_b}{B_q'}\sqrt{\frac{2kT}{\mu B_b}}\right]. \tag{58}$$

The constraints on the bias frequency ω_b are therefore

$$\sqrt{\frac{\mu B_b}{2M}\frac{B_b}{B_q'}} < \omega_b < \frac{\mu B_b}{\hbar}\left[1 - 3\frac{B_b}{B_q'}\sqrt{\frac{2kT}{\mu B_b}}\right]. \tag{59}$$

Typical TOP trap natural oscillation frequencies are on the order of 100 Hz. With a reasonably low TOP trap temperature, the Larmor precession frequency will remain larger than a megahertz.

G Polarization

The polarization at any instant in time will be the same as that when the bias field is in the X direction. The polarization is therefore given by

$$P = \int_{-1}^{1}\int_{-1}^{1}\int_{-1}^{1} \frac{B_{TOPx}}{|B_{TOP}|}\frac{N(x,y,z)}{N_0}\,dx\,dy\,dz \tag{60}$$

Substituting in the relevant quantities from Eqs. 48 and 55 this becomes

$$P = \frac{1}{(\pi\sigma^2)^{\frac{3}{2}}}\int_{-1}^{1}\int_{-1}^{1}\int_{-1}^{1} \frac{(B_b + B_q'x)\exp\left[-\frac{x^2+y^2+8(z+\varepsilon)^2}{2\sigma^2}\right]}{\sqrt{[(B_b + B_q'x)^2 + B_q'^2y^2 + 4B_q'^2z^2]}}\,dx\,dy\,dz \tag{61}$$

It does not seem possible to solve this expression for the polarization in a neat closed form, but it is possible to produce a simple and accurate approximation. By transforming to squashed and shifted spherical polar coordinates according to

$$\begin{aligned} x &= r\cos\phi\sin\mu \\ y &= r\sin\phi\sin\mu \\ z &= \tfrac{1}{8}r\cos\mu - \delta \end{aligned} \tag{62}$$

and substituting $\rho = r/R_0; \gamma_4' = \gamma_4/R_0; \delta' = \delta/R_0$, where $R_0 = B_b/B_q'$, the polarization is

$$P = \frac{\int_0^{2\pi}\int_0^{\gamma_4}\int_0^{1} (1+\rho\cos\phi\sin\mu)\sin\mu\,\dfrac{\rho^2 e^{-\frac{\rho^2}{2\gamma_4'^2}}}{(\gamma_4\gamma_4'^2)^{\frac{3}{2}}}\,d\rho\,d\mu\,d\phi}{\sqrt{[1+4\delta'^2+\rho(2\cos\phi\sin\mu-\sqrt{8}\delta'\cos\mu)+\rho^2(\sin^2\mu+\tfrac{1}{2}\cos^2\mu)]}}. \tag{63}$$

Expanding the square root to 2nd order in ρ produces

$$\begin{aligned} &[1+4\delta'^2+\rho(2\cos\phi\sin\mu-\sqrt{8}\delta'\cos\mu)+\rho^2(\sin^2\mu+\tfrac{1}{2}\cos^2\mu)]^{-\frac{1}{2}} \\ &\approx [1+4\delta'^2+\rho F(\mu;\phi)+\rho^2 G(\mu;\phi)]^{-\frac{1}{2}} \\ &\approx \frac{1}{\sqrt{(1+4\delta'^2)}}\left[1-\tfrac{1}{2}F\frac{\rho}{1+4\delta'^2}-\tfrac{1}{2}\left(G-\frac{\frac{3}{4}F^2}{1+4\delta'^2}\right)\frac{\rho^2}{1+4\delta'^2}\right]. \end{aligned} \tag{64}$$

Putting this approximation back into Eq. 63 turns the polarization integral into a series of simple trigonometric integrals multiplied by integrals of the form $\int \rho^{2n}\exp(-\rho^2/2\gamma_4'^2)\,d\rho$ which are also straightforward. Doing these integrals yields the …nal result

$$P = \frac{1}{\sqrt{(1+4\rho^2)}}\left[1-\frac{3}{4}\frac{1+8\rho^2}{(1+4\rho^2)^2}\frac{2kT}{B_b}\right] \tag{65}$$

where $\mathcal{R} = Mg/4\mu B_q'$; gives the ratio of the force due to gravity and the quadrupole confining force. This final expression is interesting showing the maximum polarization for the TOP trap is determined by the droop of the atom cloud under gravity. The spatial size of the cloud which depends on the temperature only appears in the second-order correction term. The approximate expression for the polarization is plotted in Fig. 21 (assuming a cloud temperature of $16\ \mu K$) as a function of B_q' for various values of B_b.

The integral form and analytic approximation for the polarization are only valid if the atoms stay away from the toroidal ring in the XY plane that is swept out by the area around the zero field radius as the bias rotates. In this region non-adiabatic spin flip can distort the density distribution. This zero field radius has been used in the polarization approximation and is given by

$$R_0 = \frac{B_b}{B_q'}. \tag{66}$$

The cross-sectional shape and size of the toroidal ring can be found using the uncertainty principle. At a particular field strength $|B|$ the energy difference between spin states is given in the weak field limit by $\sim \omega_L$ where ω_L is the Larmor frequency at that field strength. In a particular interval of time δt an atom in the cloud will experience a change in the field strength $\delta |B|$. This change in field strength can come either from the motion of the atom through the field or from the motion of the rotating field past the atom. Since the field rotation is required to be much faster than any atomic motion in order for the TOP trap to work, it is the rotation that is the relevant quantity determining $\delta |B|$. At some cylindrical radius r the field moves past the atom at a speed $r\omega_b$, where ω_b is the field rotation frequency in an azimuthal direction. The change in field over an interval of time

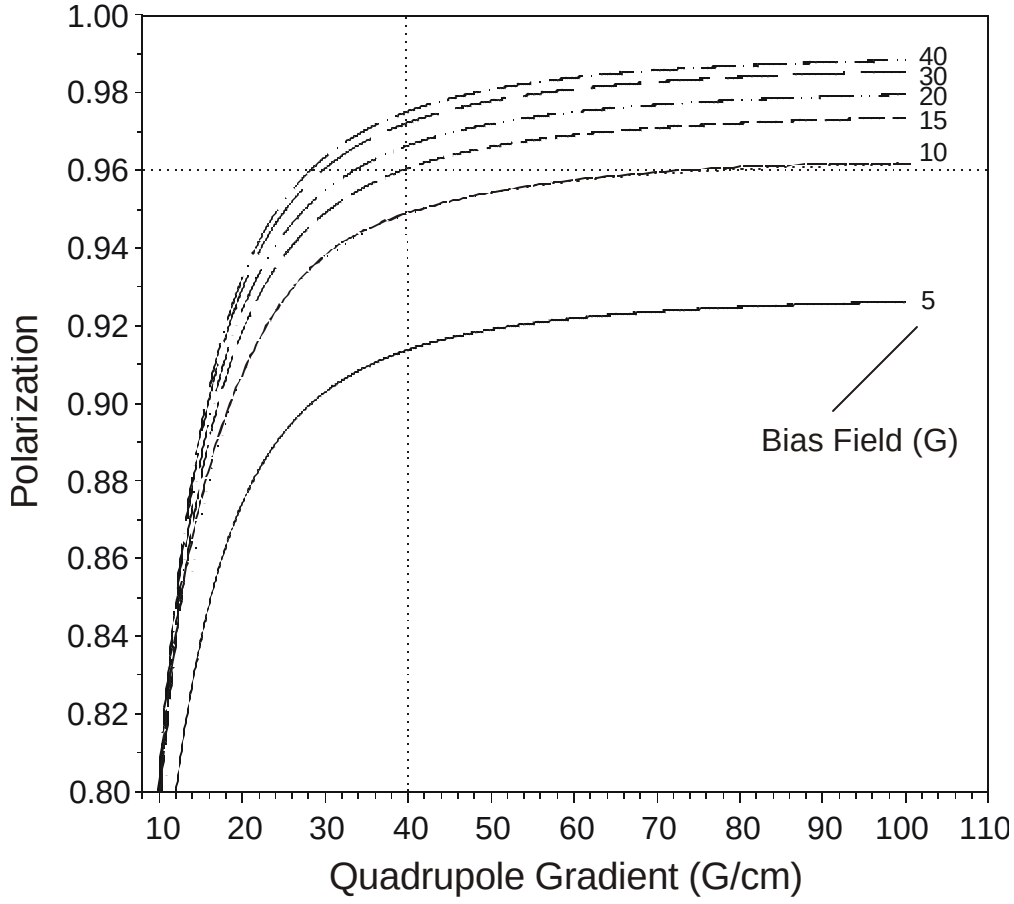

FIG. 21: The approximate expression for the polarization as a function of B_q^0 for various B_b: The temperature is assumed to be 16^1 K in this plot. This calculation was used in choosing a magnetic …eld con…guration (dotted cross-hairs) suitable for the beta-asymmetry measurement.

¢t is then given by

$$¢jBj = ½!_b ¢t \frac{1}{½} \frac{@jBj}{@Á}: \tag{67}$$

This change in …eld strength corresponds to a change in energy of the atom ¹¢jBj. If, during an interval of time ¢t given by one Larmor period 1=!_L, the change in energy exceeds ~!_L, the energy required to ‡ip from one spin state to another, then such a spin ‡ip can occur. Therefore, the boundary of the spatial region where this is possible is determined by

$$~!_L = ¹¢jBj \tag{68}$$

$$= ¹ \frac{½!_b}{!_L} \frac{1}{½} \frac{@jBj}{@Á}: \tag{69}$$

Taking the instant when the bias …eld is along the X axis, Eqs. 47 (neglecting -) shows that jBj is given by

$$jBj = \sqrt{(B_b + B^0_q x)^2 + B^{02}_q y^2 + 4B^{02}_q z^2}: \tag{70}$$

Converting to cylindrical polars, carrying out the di¤erentiation above, and converting back to Cartesians yields

$$\frac{@jBj}{@Á} = ¡\frac{B_b B^0_q y}{jBj}: \tag{71}$$

Using this result and the fact that !_L = ¹jBj=~, Eq. 69 can be written as

$$¡\left(\frac{~!_b}{¹}\right) B_b B^0_q y = jBj^3: \tag{72}$$

Using Eqs. 66 and 70 this can written as

$$(x + R_0)^2 + y^2 + 4z^2 = \left(\frac{~!_b}{¹B^0_q} R_0\right)^{\frac{3}{2}} y^{\frac{3}{2}}: \tag{73}$$

This is the equation of the closed volume within which spin flip can occur (when the bias is exactly along the X axis). This volume looks like the classic dipole shape centered at $(\pm R_0; 0; 0)$ with the two lobes pointing in the direction of the Y axis, and squashed by a factor of 2 in the vertical direction. Projected onto the XZ plane the shape is an ellipse with

$$X_{\text{semiaxis}} = \left(\frac{1}{3}\right)^{\frac{3}{4}} \sqrt{\frac{\sim \omega_b}{{}^1B_b}} R_0 \tag{74}$$

$$Z_{\text{semiaxis}} = \frac{1}{2}\left(\frac{1}{3}\right)^{\frac{3}{4}} \sqrt{\frac{\sim \omega_b}{{}^1B_b}} R_0. \tag{75}$$

Thus, when going from the instant in time to the time-average the spin flip region goes from the dipole-like shape to an elliptical torus in the z = 0 plane with R_0 as the major axis and two semi-axes given by the expressions above.

For realistic values of ω_b and B_b the two semi-axes are considerably smaller than R_0 and so the condition on the polarization expression of Eq. 61 that the atoms stay away from the spin flip region can be modified to a more conservative condition that the Gaussian density distribution has very little strength beyond a distance R_0. In other words the atoms will stay away from the spin flip region if

$$\frac{\sqrt{(R_0^2 + 8\pm^2)}}{\frac{3}{4}} > \gg 3 \tag{76}$$

i.e.,

$$\sqrt{1 + \frac{1}{2}\frac{Mg}{{}^1B_q'}} \Big/ \frac{2kT}{{}^1B_b} > \gg 3. \tag{77}$$

H Results of the TOP trap model

The predicted TOP trap polarization curves for various bias field B_b values are plotted in Fig. 21 as a function of the quadrupole gradient B_q'. The magnetic

moment ($\mu = 9.27 \times 10^{-24}$ J/T) used is that of the ^{82}Rb $5S_{1/2}; F = 3/2; m_F = 3/2$ stretched state and TOP trap temperature assumed to be 16 μK. This is the initial temperature of the cloud after molasses cooling but prior to evaporative cooling as reported by the Univeristy of Colorado BEC team [68]. Notice that the polarization drops dramatically at about 15 G/cm. Near this value the force on the atoms due to the quadrupole gradient nearly balances that of gravity and as a result the cloud polarization plummets. The conditions of the polarization approximation (given in Eq. 77) are no longer valid below a quadrupole field gradient of $\approx$10 G/cm. Since we will be detecting positrons in this experiment, it is desirable to keep the TOP magnetic fields to a minimum in order to avoid false asymmetries that can result from magnetic deflection of the positron. A quadrupole field gradient of $B_q' = 40$ G/cm and rotating bias field of $B_b = 15$ G was used in the beta-asymmetry measurement.

The temperature reached during the molasses cooling stage of the experiment is critical in determining the polarization of the source. In order to predict what effect cloud temperature will have on the polarization, fix the bias field gradient to that used in the experiment and plot the polarization as a function of temperature as in Fig. 22. The dotted line at 60 μK designates the temperature limit below which the polarization model is accurate. Beyond this the model represents an upper limit to the polarization since it does not include the effects of spin flip near R_0 and the harmonic approximation differs by only 5% from the exact TOP field at this radius. The bias field used has a dramatic effect on the declining slope seen in the polarization as the temperature of the cloud is increased. This is the case because the trap depth depends linearly on the bias field so that lower bias fields allow for more disperse clouds and lower polarization. For the bias field used in the beta-asymmetry experiment, we can see that the polarization should drop by

» 20% for a temperature increase of 150 ¹K. The TOP trap depth is 250 ¹K.

II. HARDWARE FOR THE MAGNETIC TRAP AND BETA-DECTECTION

A Double MOT system

It is possible to move cold atoms from one position to another within a vacuum system by coupling two magneto-optical traps. In atomic trapping experiments with stable species (i.e., Bose-Einstein condensation studies), this technique is used to overcome the competing aspects of loading large quantities of atoms into a MOT from an atomic vapor and attaining the long trap lifetimes that are required for performing experiments. This was accomplished by transferring the atoms from a collection cell ‡ooded with atomic vapor to a separate chamber maintained at ultra-high vacuum.

In experiments that study fundamental symmetries of trapped radioactive atoms, the initial collection of atoms into a MOT requires a dry…lm-coated glass cell and large diameter MOT laser beams for high-collection e¢ciency. Even with these features included, only 1% of the atoms released from the foil are collected into the trapping cell MOT (referred to as MOT I). The bulk of the untrapped atoms remain on the walls of the trapping cell. Transferring atoms to a second chamber moves the trapped sample away from this large source of untrapped positron background and allows the beta-detectors to be shielded from the gamma radiation which arises from both the untrapped atoms in the trapping cell and the remaining ^{82}Rb on the foil.

Given that MOT-to-MOT transfer between two connected vacuum chambers has been performed with good e¢ciency [72, 76, 77], it makes sense to design the

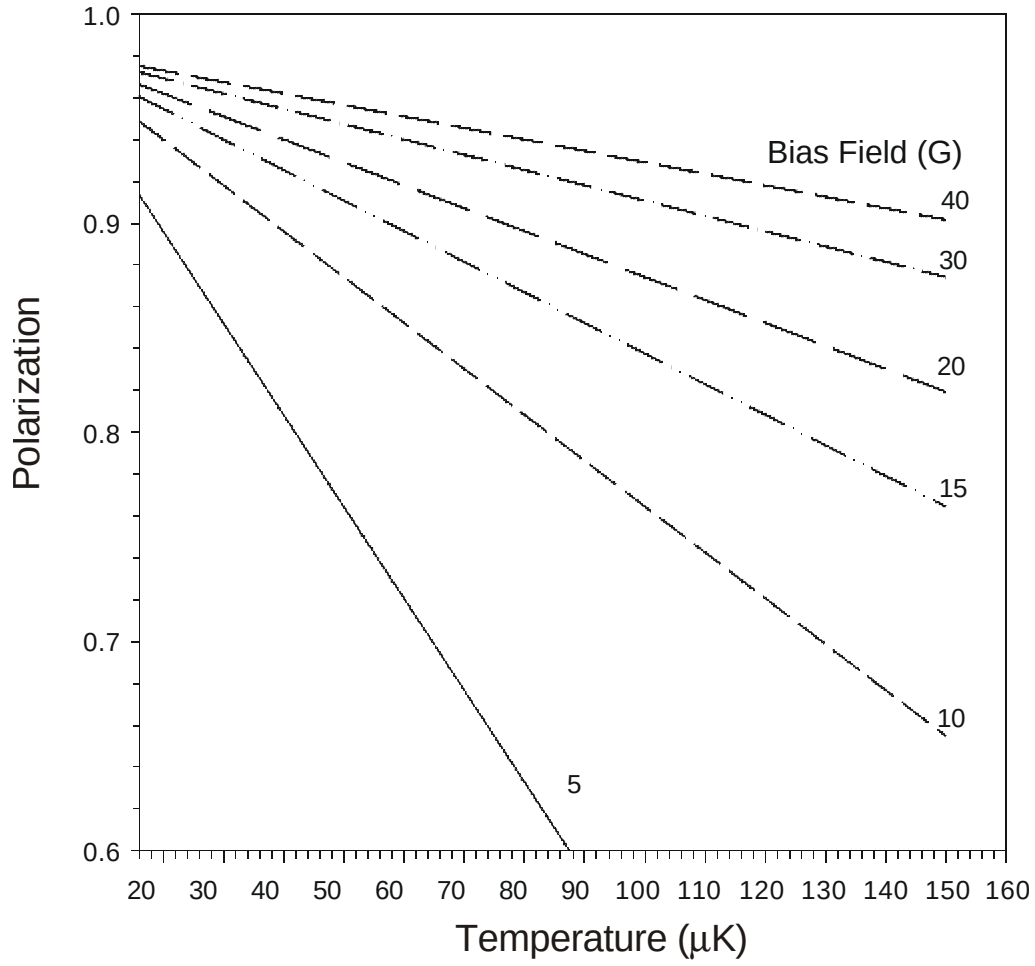

FIG. 22: The expected polarization as a function of temperature for the magnetic …eld con…gurations used in the beta-asymmetry experiment. The dotted line is the temperature limit below which the polarization approximation is accurate. Above this temperature this plot gives an upper limit to the polarization.

experiment in two stages. The …rst stage focuses on the e¢cient collection of radioactive atoms and the second on observing the beta-decay from the trapped sample which requires a special chamber geometry and detection instrumentation.

A schematic of the double MOT system is shown in Fig. 23. The quartz trapping cell is coupled to a stainless steel chamber (referred to as the beta-chamber) through a 30 cm long, 1 cm inside diameter, tube with a ‡exible bellows adjacent to the glass-to-metal seal to prevent breakage of the glass cell during assembly and thermal expansion that occurs in the bake-out process. A valve is very useful for separating the vacuum of the beta-chamber and the trapping cell especially since the trapping cell periodically needs to be removed for re-coating or Zr foil replacement. A bakable (up to 300 $^{\pm}$C) VAT in-line valve is used because it requires much less horizontal space than a typical 45 degree valve and can hold ultra high vacuum against atmosphere.

Ultra-high vacuum is critical for this experiment because the maximal MOT and TOP lifetimes depend linearly on the background gas pressure in the trapping chamber. In the beta-chamber, it is desirable to have a trap lifetime that is signi…cantly longer than the radioactive half-life of ^{82}Rb ($t_{1=2}$ = 75 s). This increases the probability that the atoms will undergo beta-decay before being lost from the trap. The JILA group reported a TOP lifetime of 100 s with a pressure of $< 7 \pounds 10^{i\,11}$ torr [68]. Assuming that this lifetime is limited by background gas collisions and given that our TOP trap is of a similar depth, we would require the beta-chamber pressure to be a factor of 2 to 3 better. The TOP trap depth depends only on the bias …eld $T_{max} \gg \frac{^1 B_b}{2k_B}$; and for JILA B_b = 10 G, which implies $T_{max} \gg 300\ ^1$K (our B_b = 15 G). In the collection cell, the heating and release from the foil takes on the order of 6 s and so the lifetime for MOT I should be long compared to this. Since a MOT has a larger trap depth than a TOP trap, it is

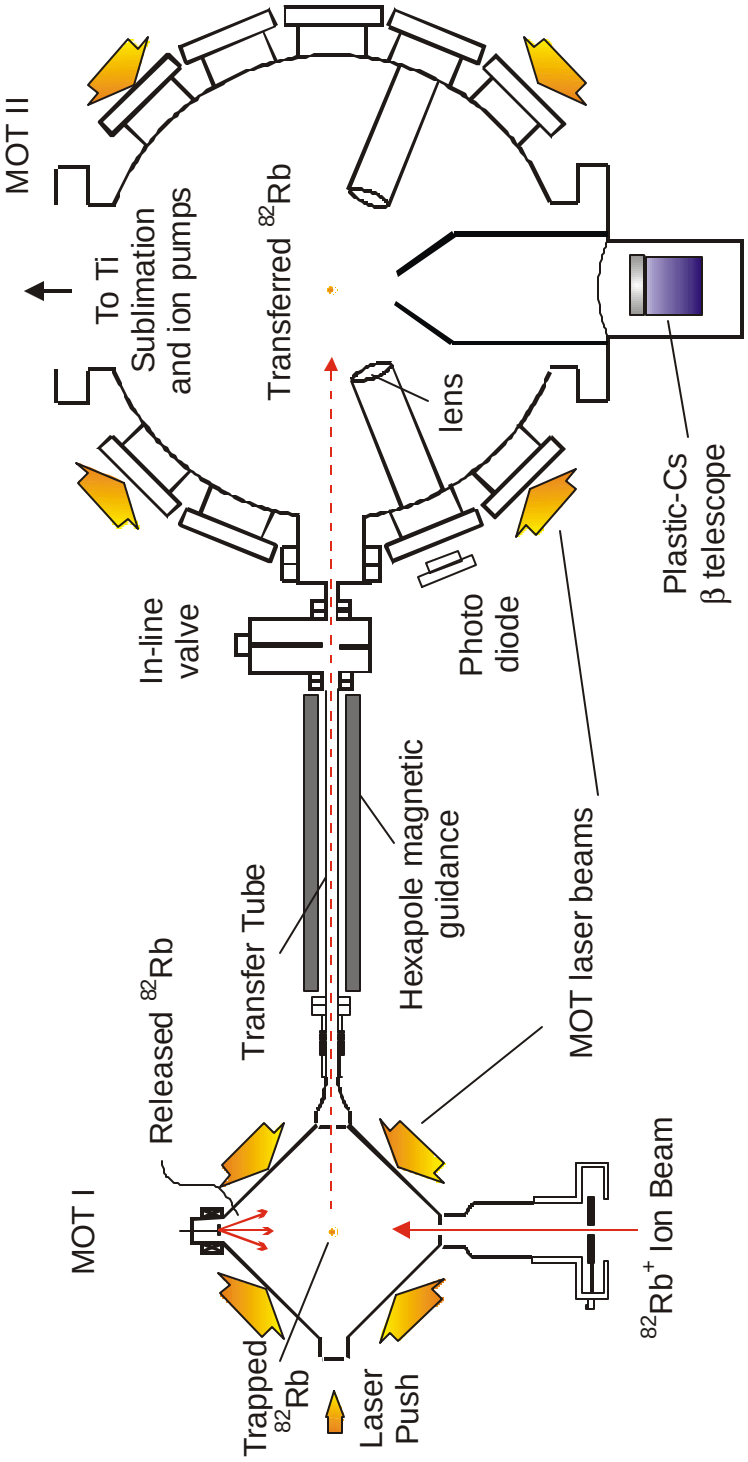

FIG. 23: Top view of the double MOT system used in the parity violation experiment.

not as sensitive to background gas collisions. Previous measurements [78] indicate that background gas pressure in a MOT of $\approx 1 \times 10^{-10}$ torr is sufficient to achieve MOT lifetimes of 100 s.

B The beta-chamber

The beta-chamber has been designed with many features since a good deal of interaction with the atoms is required in this experiment. The beta-chamber must provide access for magneto-optical trapping that requires laser beams from six different directions, imaging of the trapped clouds, beta detection, transfer of atoms from the first MOT, optical polarization beams, and at least three sets of orthogonal magnetic coils for the pure magnetic TOP trap. In addition, it has been designed to minimize the solid material close to the trapped position as to reduce the chance that scattered positrons can be detected. These requirements have been met using a pancake design with various connecting flanges. The positron scattering limitations and the number of ports required determines the size of the chamber. It is enormous compared to the typical size of magnetic trapping chambers (usually glass cubes of a couple inches) and presents several technical problems for magnetic trapping. The main stainless steel tube on which the flanges are welded is $10''$ in diameter and extends in the vertical direction in length by $10''$. The top and bottom of this tube are sealed using $13.25''$ O.D. conflat flanges that accept an $8''$ O.D. flange containing a reentrant port. The re-entrant ports (referred to as quad wells) are used to place the quadrupole coils close to the trap position (see Fig. 24). The quad cell cylinders have a diameter of $5''$ and, when mounted in the beta-chamber, have a separation of $2.75''$. The atoms are trapped at the midpoint of this separation.

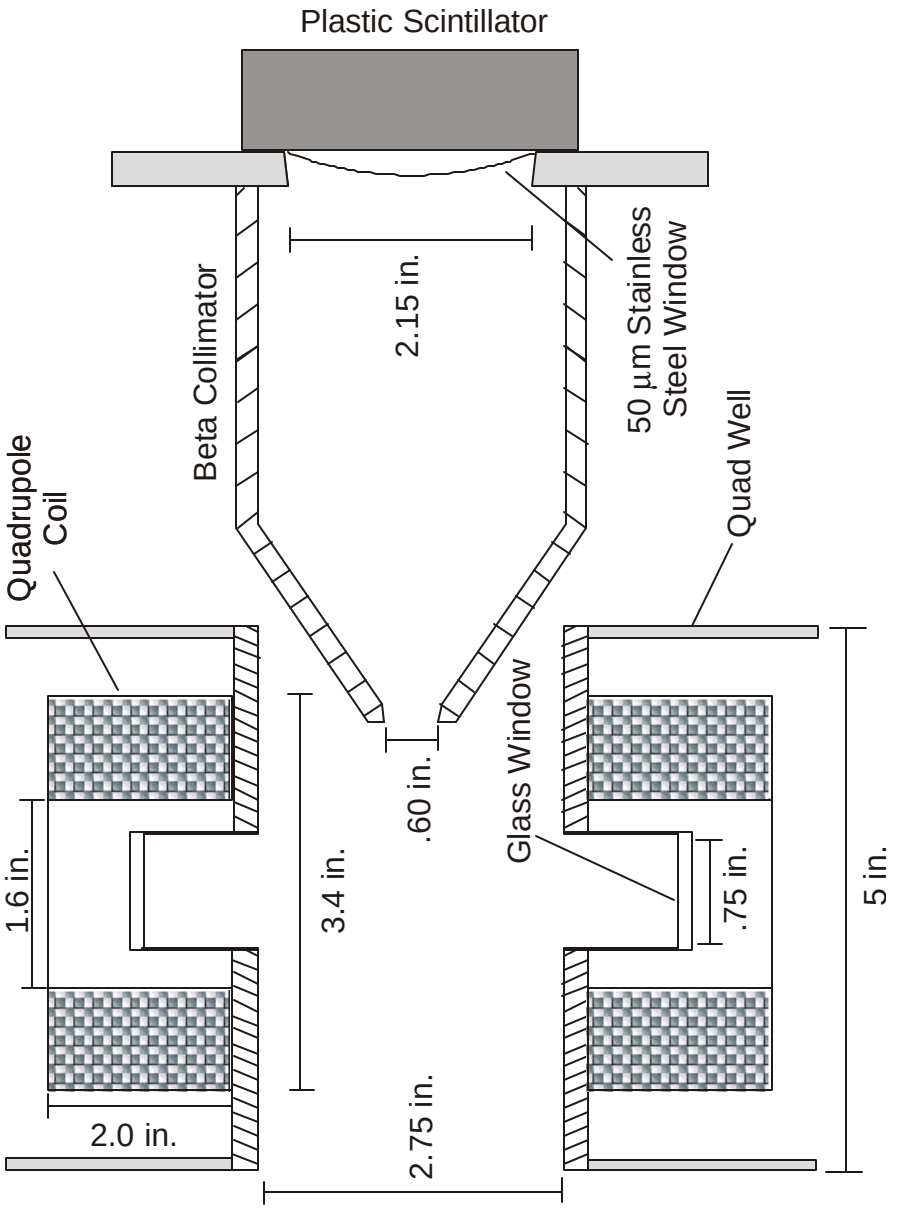

FIG. 24: Inside view of the beta-chamber showing the quadrupole coil wells and the beta-collimator.

Optical access for the MOT II laser beams is gained through four anti-re‡ection coated 2:75^{00} con‡at windows in the plane of the beta-detector through which beams of up to 1.5^{00} in diameter can pass. In the vertical direction there are specially made windows sealed atop 1^{00} standoffs at the bottom of the quad wells allowing for a vertical beam diameter of 0.75^{00}.

We monitor the ‡uorescence of the trapped atoms in MOT II by placing additional re-entrant ports with a window and a lens mounted at the end close to the trap position such that the atoms are near the focal length of the lens (» 3:5^{00}). This increases the solid angle for collecting the ‡uorescence light from the atomic cloud and focuses it so that it can be measured outside the beta-chamber using a photo diode or a photo-multiplier tube (PMT). There is much less scattering of laser light in the beta-chamber when compared with the trapping cell. We have achieved a background-to-signal ratio that should allow us to observe ‡uorescence from as few as 100 atoms in MOT II. Inexpensive security CCD cameras are used to monitor the position and size of the MOT II cloud. Two cameras are placed at orthogonal ports (one looking from the direction of the vacuum pumps and one looking back towards the transfer tube) so that the MOT II cloud can be aligned with the magnetic trap in three dimensions. The remaining viewports are used for optical pumping and probing of the cloud and will eventually house the hardware for absorption and/or phase-contrast imaging of magnetically trapped atoms.

Positrons are detected using a plastic scintillator. Due to the vacuum requirements needed for magnetic trapping, the detector cannot be placed within the beta-chamber. A metal foil window is used to separate the detector from the ultra-high vacuum. The foil must be very thin so as not to signi…cantly distort the energy spectrum of the positrons that will lose energy when passing through. A compromise must be reached so the foil is strong enough to sustain the di¤er-

ential pressure between the beta-chamber and detector housing. One designed was attempted using a 20 ¹m titanium foil sealed to the beta-chamber using a soft indium gasket. This worked to some degree, but failed when attempts were made to bake the chamber. The more robust design currently in place uses a 2.1^{00} diameter, 50 ¹m thick stainless steel foil laser welded directly to a 4^{00} con‡at ‡ange. This design has been shown to survive the bake-out temperature and is strong enough to hold 1 atm of di¤erential pressure so that the detector housing need not be pumped.

Attaining the required vacuum for the beta-chamber with its large number of glass-to-metal seals and special beta window was a daunting task that required approximately one year to accomplish. On the opposite side of the detector is a 6^{00} tube which provides good conductance to the high vacuum pumps. We use a 300 l/s titanium sublimation pump which works very well for pumping hydrogen and a 20 l/s ion pump for noble gasses. The transfer tube limits the conductance from the trapping cell and allows for approximately two orders of magnitude di¤erential pressure between the trapping cell and the beta-chamber. It is necessary to drive o¤ the water vapor in the beta-chamber by baking it to temperatures greater than 200 ±C for about a week. Care was taken to raise and lower the temperature uniformly and slowly so that undue stress to the various seals could be avoided. A crucial step was a bake-out at atmospheric pressure which forms a golden brown metal oxide layer on both the inside and outside of the stainless steel chamber. This works because the water vapor releases more easily from the oxide layer. The beta-chamber pressure is measured using a Bayard Alpart-type nude ion gage made by Varien. This type of pressure gauge has a lower limit of 3 £ 10$^{i 11}$ torr. The bake-out procedure was deemed successful when this gauge bottoms out. Measurements of the MOT, Quad, and TOP trap lifetimes then become the

primary (albeit relative) determination of the pressure.

C The TOP quadrupole and bias coils

The quadrupole coils are used to provide the …eld gradient for both MOT II and the TOP magnetic trap. They are placed at the bottom of the quad wells and centered with respect to the quad well ‡ange. These coils are made from 0.2^{00} rectangular copper tubing wound with an inside (outside) diameter of 1.6^{00} (3.4^{00}), thickness of 2^{00} and have a total of 30 turns (see Fig. 24). Since the separation between the coils is greater than the average coil diameter (2.5^{00}), they are not positioned for producing the maximal …eld gradient for a given current. A true anti-Helmholtz con…guration has the coil separation equal to the coil radius. The purpose of this compact quad coil design was to limit the extent of the magnetic …eld felt by a positron emitted from the trapped sample and to remove background accumulating surfaces from the collimator …eld of view. To compensate, larger current must be used to provide the required …eld gradient. Measurements of the …eld gradient using a Gauss probe show it is constant over the trap region and has a magnitude of $@B=@r = B'_q = 0{:}2$ G/cm per amp of applied current. A current of 40 A is used for MOT II and 160 A for both the Quad and TOP traps, which gives …eld gradients of 8 G/cm and 32 G/cm, respectively. Cooling water is run through the coils to prevent overheating at high current.

In going from MOT II to the TOP, the quad current is initially dropped from the MOT II value to zero current in order to perform the optical molasses cooling and optical pumping steps. The quad current is then ramped up to TOP value for loading of the magnetic trap. Since the cloud is expanding and falling, the rise and fall times for the quad coil should be fast (order of miliseconds) to e¢ciently

load the magnetic trap.

We use a Lambda EMI model ESS-30-333 switching power supply to provide the quad current. This power supply is run in current-control mode that can be remotely controlled with an analog voltage. The power supply is not fast enough when ramping from high current to zero. To enable a fast turn-o¤, we use an IGBT (integrated gate bipolar transistor, Mistsubishi model PM600HSA120) based switch that has the capability of switching up to 600 A in 5 ^{1}s. These devices have their own gate driving circuit which can be controlled with a TTL signal. The drive circuit is optically isolated from the main switching circuit to prevent back-emf voltage ‡uctuations from inadvertently controlling the IGBT. A schematic of the current switching circuit layout is shown in Fig. 25.

The falltime of the quad can be made very short by using a shotky diode and a resister in parallel with the quad coils. When the IGBT is shut o¤, the stored energy in the coils is dissipated through this resister. The resistance is chosen so that the falltime is less than 1 ms. The risetime for the coils is » 3 ms, being determined by the L/R time constant of the quad coils. In an early design, the back-emf of the switch was found to cause the ground potential to pulse by up to 100 V. The ground ‡uctuations were signi…cantly reduced by changing the design to be as compact as possible.

The bias coils of the TOP trap are mounted outside of the beta-chamber. There are two sets of coils having slightly di¤erent diameters (19.5^{00} for the large, 16^{00} for the small) both having 36 turns of 0.17^{00} rectangular copper wire. The large coils are mounted along the beta-detection axis separated by 15^{00} and the smaller along the axis of the transfer tube and are separated by 12^{00}. This is again not the Helmholtz con…guration, but owing to the large size of the bias coils in comparison to the TOP trap dimension (a few mm), a constant magnitude …eld is generated

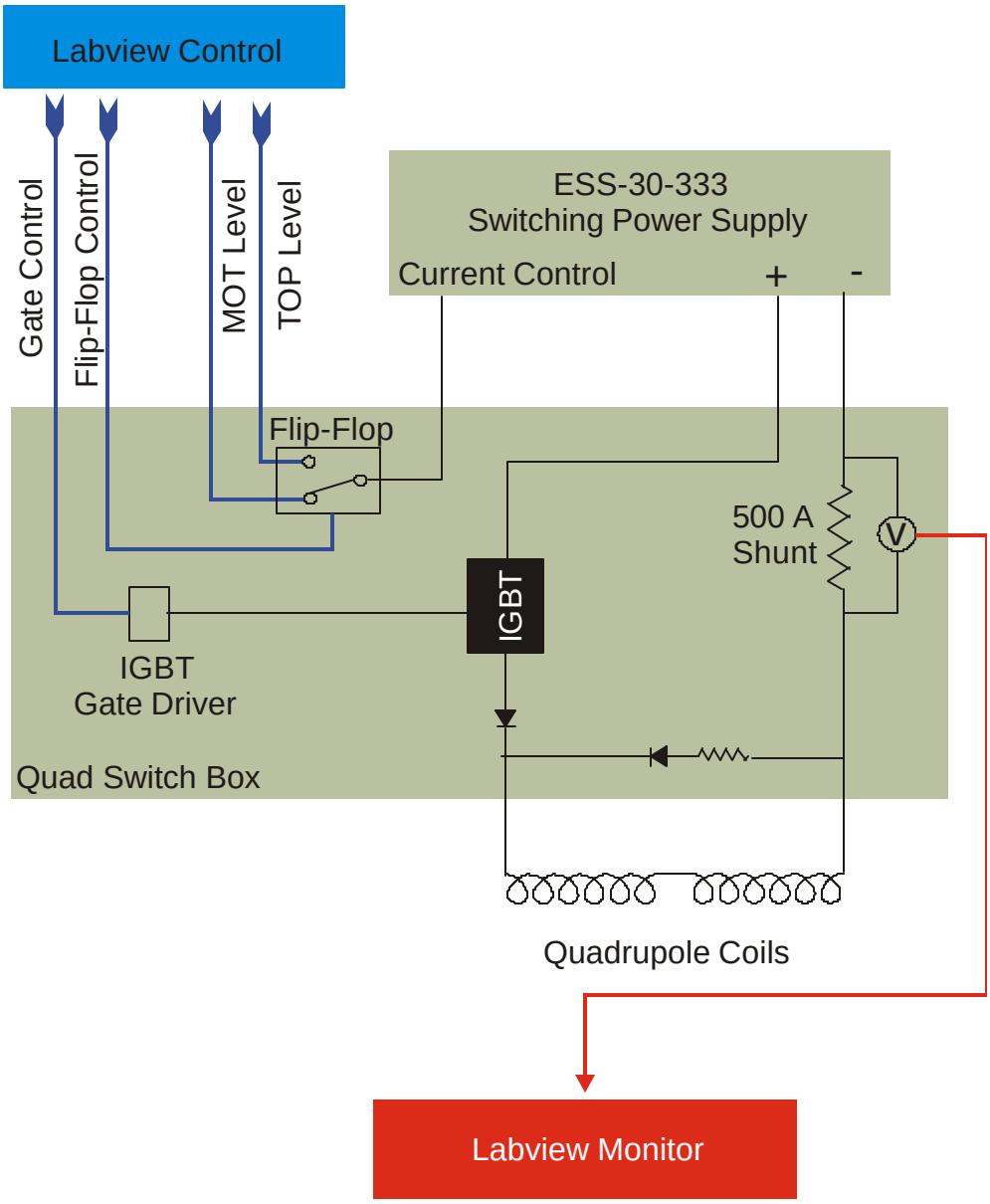

FIG. 25: Circuit used to quickly switch the current in the quadrupole coils of the TOP trap.

over the trap volume. The …eld was measured using an ac Gaussmeter to be 0.428 G/A and 0.549 G/A for the small and large coils, respectively. From a model of the TOP trap, a rotating bias …eld value of 15 G is chosen to provide good polarization (> 96%) at attainable cloud temperatures (20 ¹K).

The bias coil rotation frequency should be signi…cantly greater than the natural oscillation frequency of the TOP trap (with nominal quad and bias values $!_n$ = 60 Hz in the horizontal direction). To excite the coils we use a BGW "grand touring" audio ampli…er rated at 1 kW with a maximum output voltage of 100 V. Since the bias coil pairs have an inductance of »30 mH, the audio amps do not have enough output power to provide the current needed to produce 15 G of bias …eld at frequencies of ! >> 60 Hz (recall that impedance for the coils is Z = ! L). The current in the coils is increased to the desired value using a parallel LRC resonator (see Fig. 26).

The impedance of the resonator is given by

$$Z_{eq} = \frac{R + j(L!(1 - !^2LC) - !CR^2)}{(1 - !^2LC)^2 + !C^2R^2}: \tag{78}$$

At the resonant frequency $! = 1=\sqrt{LC}$; the impedance of the load is maximized and is mostly resistive given that R << ! L for our case. Therefore, on resonance the impedance is given by

$$Z_{eq}^{Res} = \frac{!^2L^2}{R}(1 - jR=!L) ¼ \frac{!^2L^2}{R}: \tag{79}$$

This comes at the cost of chosing a particular resonant frequency set by the capacitance of the resonator. In our case we chose a resonator frequency of ! = 830 Hz, requiring a capacitance of C ' 50 ¹F. The voltage across the coils needed for the 15 G bias …eld amplitude is given by V_p ¼ (15 G=0:5 G/A)$(R^2 + !^2L^2)^{1=2}$ ¼ 750 V. With the resistance of the coil circuit being less than 1 -; the power required

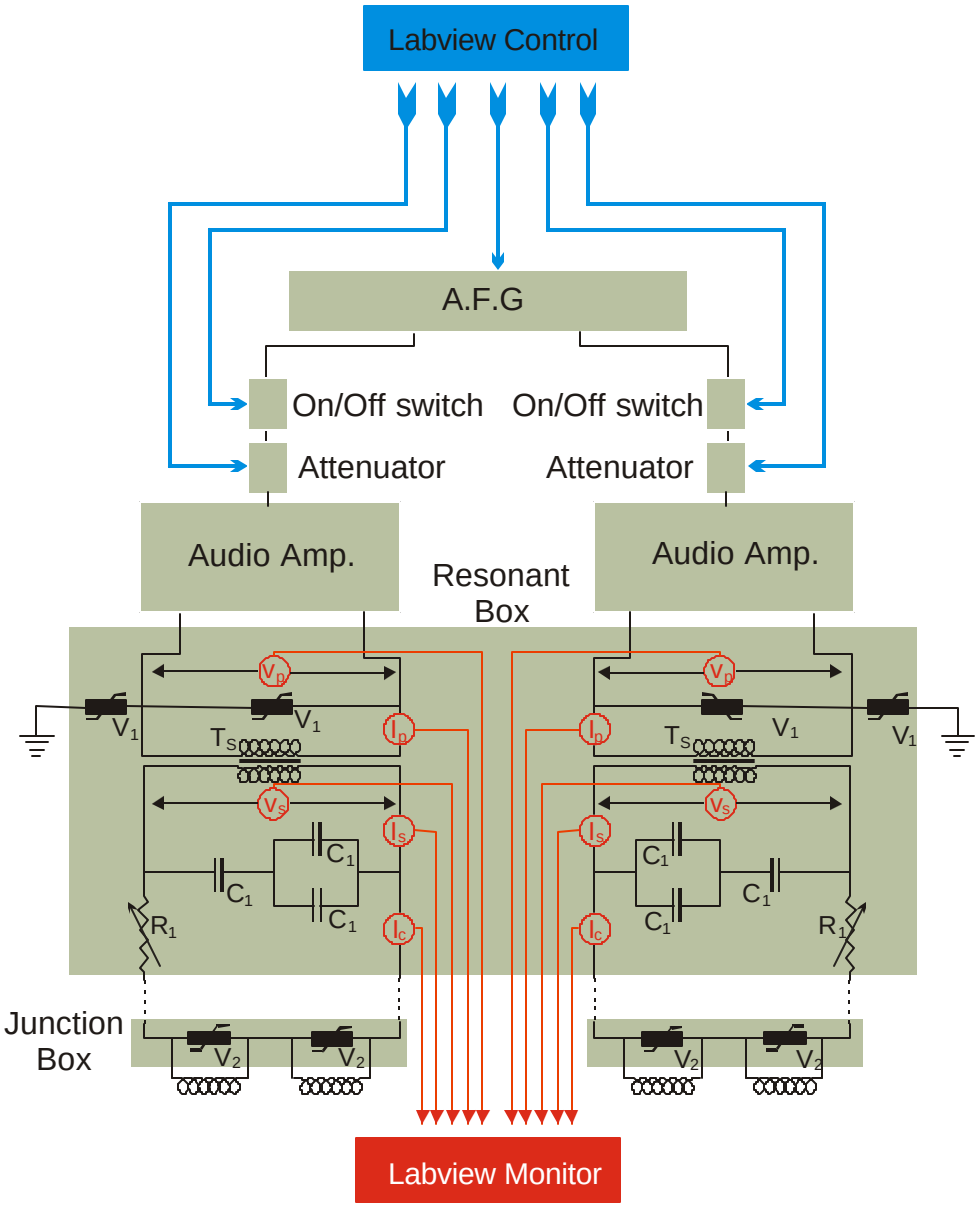

FIG. 26: Circuit with the parallel LRC resonator used in driving the large and small bias coils.

to drive the LRC resonator at this voltage is $P_{rms} = (V_p/\sqrt{2})^2/Z_{eq}^{Res} \approx 500$ W. This power output can be supplied by the audio amps and the voltage required is achieved using a step-up transformer.

The 830 Hz sinusoidal waveform fed to the audio amplifiers comes from a Lecroy 9100 arbitrary waveform generator (AFG). The phase angle of the current in the coils is determined by

$$\tan \phi = \frac{R}{\omega L}. \tag{80}$$

Since the inductance and resistance of the large and small bias coils are not exactly the same, the relative drive phase of the input channels must be adjusted (which turns out to be 98.65°) to provide a relative 90° phase shift between the bias coil currents.

The AFG is remotely controlled using a GPIB interface to a computer. For turning the coils on and off during the loading of the TOP trap, this communication is too slow. To avoid this, the coil currents are directly controlled using an analog switch. We use voltage-controlled attenuators to ramp the bias-coil current down before switching them off. This prevents the energy stored in the coils from propagating back and damaging the amplifiers. For additional protection varisters are placed in several positions to limit the maximum voltage of the circuit, see Fig. 26.

The alternating current in the bias coils induces Eddy currents in the stainless steel beta-chamber. This causes two problems. First, the induced current cause heating of the chamber, after extended operation, to a temperature of up to 50 °C. This causes the vacuum of the beta-chamber, and therefore the TOP trap lifetime, to degrade. The heating can stress the vacuum seals of the beta-chamber because of non-uniform heating. This problem is alleviated by using three cooling fans that blow directly onto the chamber. The second problem is that the Eddy currents

cause a phase shift between the applied bias coil currents and the rotating bias magnetic …eld at the trap position inside the chamber. Since the determination of nuclear spin direction is determined from the measurement of the bias coil currents, this phase shift must be understood. Before the evacuation of the beta-chamber, the phase shift was measured with an ac Gauss probe to be 131 § 2 degrees at the trap position.

D Experiment control system

Various experimental parameters are controlled using National Instruments computer interface cards and National Instruments Labview software. Multi-function cards are available (e.g., AT-MIO series) that support analog output, analog input, digital input/output, and digital counters for precision timing. Several laboratory instruments are also be controlled with a GPIB interface with the computer. The software interfaces easily with the computer cards and the control programs are written in a fairly straightforward object-oriented style.

Labview programs have been written to control the switching of the quad coils, the attenuators and analog switches of the bias coils, and for the rf signal generator used to inductively heat the Zr foil. On the laser table there are several Uniblitz mechanical shutters used to block the laser light during di¤erent trapping and measurement sequences in the experiment. These shutters have an intrinsic delay that must be measured (usually several ms), but shut o¤ relatively fast (< 1 ms). Very short probe or push beams can be produced by sending a digital pulse to a frequency mixer which switches on or o¤ the rf drive to an acousto-optic modulator.

The Labview software cannot be trusted to directly control the DIO channels with precise timing on the order of a milisecond. For precision timing applica-

tions, we use National Instruments counters that can be set using the software and triggered by a global pulse. For example, in the MOT I to MOT II transfer, three counters are used. The …rst for controlling the MOT I shutter (to shut o¤ the MOT I laser light), the second for switching o¤ the MOT I quad coils, and the third for triggering an AOM to generate the transfer pulse. The delay for each counter is set by the program and afterward a separate DIO channel that is wired to the trigger inputs of these three counters starts all of the counter clocks at the same time. The precision of the output pulses using this method is good to 0.5 ^{1}s.

When collecting beta-decay data, the Labview software on the control computer is used to run the experiment in a continuous loop. The automatic operation is very useful for collecting the many hours of data needed to gather enough statistics for the beta-decay measurements. Depending on the type of test being performed, the loop includes heating of the foil, transfer to the beta-chamber, loading of the TOP, detecting beta-decay for a pre-determined interval, and …nally resetting the parameters for MOT I and MOT II before the next cycle begins. The ion beam continually implants atoms on the foil throughout the measurement. The mass-separated ion source of the mass separator and the various ion optics are controlled by a separate computer also using National Instruments cards and Labview software.

E Beta detector and data acquisition

A Bicron scintillation detector is mounted just outside of the 50 ^{1}m foil window on the beta-chamber. It is constructed in a tubular arrangement (see Fig. 27) consisting of a 3^{00} diameter by 0.787^{00} thick plastic (BC-100 organic) scintillator

disk, behind this is a 3^{00} diameter by 4^{00} long CsI crystal. The detectors are contained within an aluminium housing and are in direct contact with a 3^{00} photo-multiplier tube used to detect scintillation light in the plastic and CsI. When mounted on the beta-chamber, the entire detector is encased in cylindrical tube of ¹-metal (not shown in the diagram) to shield the PMT from gain ‡uctuation resulting from the TOP magnetic …eld. The design of this composite plastic-CsI (phoswich) detector is such that the positron is stopped in the plastic while the gamma radiation (from 511 keV ¯ annihilation or the 776 keV ° associated with ^{82}Rb) is detected in the CsI.

By looking at the time dependence of the PMT current, it is possible to delineate between energy deposition in the plastic and the energy deposition in the CsI. The scintillations arising from positrons energy deposition in the plastic decay very quickly ($¿_{plastic}$ » 50 ns) and produces a fast current pulse whose integrated charge is proportional to the incident positron kinetic energy. Because the plastic scintillator is thin and made of light Z material, it has a low detection e¢ciency for °-rays. On the other hand, the CsI crystal has a high detection e¢ciency for gamma rays and the scintillation light produced in the crystal has a much longer time constant than that of the plastic ($¿_{CsI}$ > 150 ns). The PMT current is charged-integrated and sent to two di¤erent shape-to-pulse-height ampli…ers having two di¤erent time constants. One that is short (fast channel) so that the output signal contains mostly the energy deposited in the plastic, and a second that is much longer (slow channel) and contains the energy deposited in both scintillators. The output from these ampli…ers can be written as

$$Q_{fast} = A + ®_1 E_{plastic} + ¯_1 E_{CsI}$$
$$Q_{slow} = B + ®_2 E_{plastic} + ¯_2 E_{CsI}: \qquad (81)$$

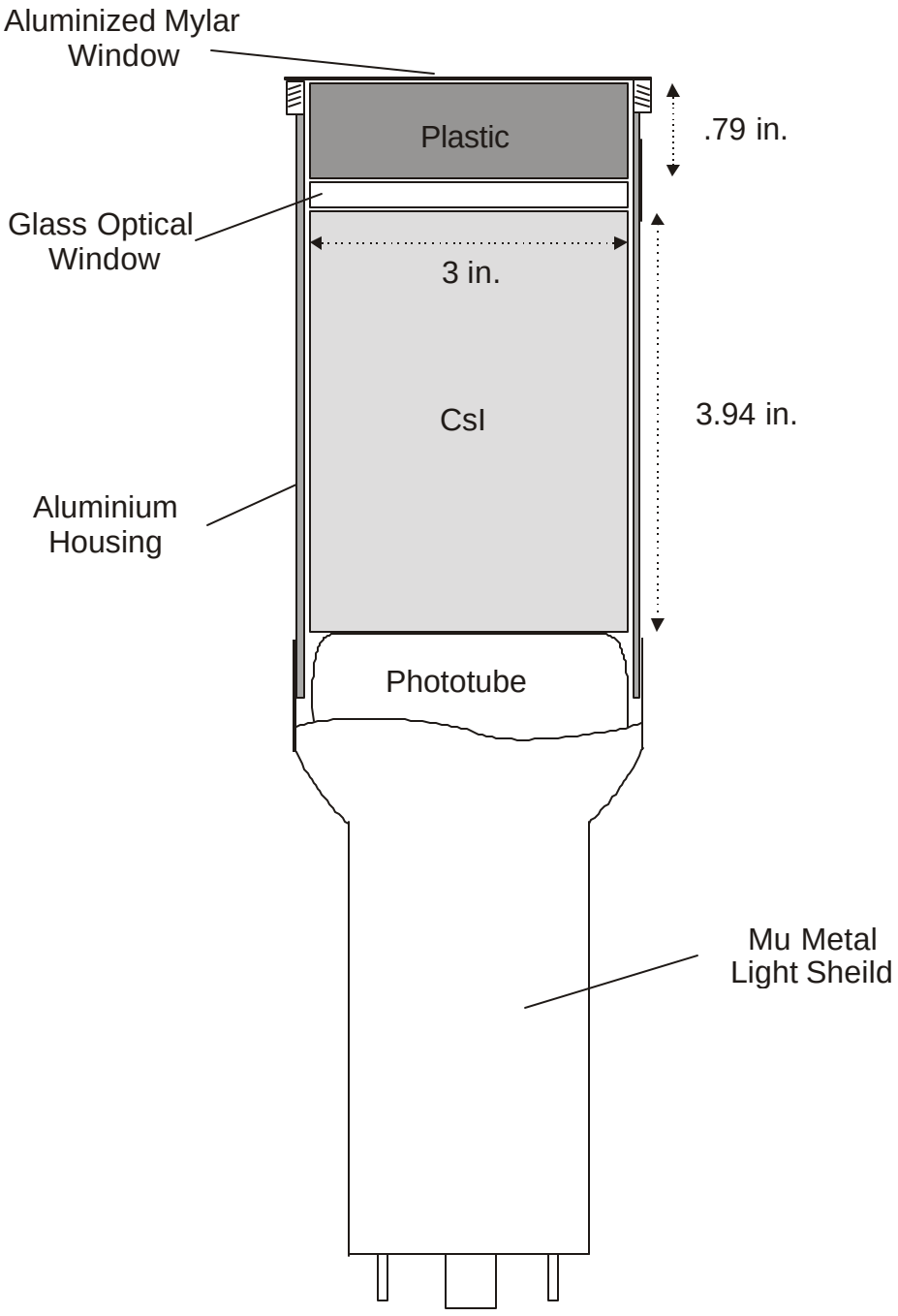

FIG. 27: The detector used in the parity violation experiment that houses both the plastic scintillator and the CsI crystal.

The constants in this relationship are determined by calibration of the detector using known gamma sources (^{22}Na at 1275 keV, 511 keV positron annihilation energy and ^{137}Cs at 662 keV). The amount of signal deposited in the plastic and CsI can be separated by irradiating only one scintillator at a time. This is accomplished by shielding one or the other detector using lead bricks. Use is made of the Compton edge e¤ect in the plastic scintillator, where a gamma ray can Compton scatter from an electron in the plastic, transferring some of its kinetic energy. The maximum energy that can be imparted to the scattered electron (K_{max}, the Compton edge) can be calculated using the gamma energy (h^o) and the mass of the electron (m)

$$K_{max} = h^o \frac{2®}{1 + 2®}; \tag{82}$$

where $® = h^o=mc^2$. The absolute calibration performed in this way is good to about 10%, whereas the relative calibration is closer to 2%.

In the beta-detection electronics, the PMT current is …rst fed to a discriminator that selects the pulses having energy of more than 400 keV. It then triggers a CAMAC gate to record:

1. the time lapse since the last pulse (¿);
2. the detector signals ($Q_{fast}; Q_{slow}$);
3. the large-and small-bias coil currents ($I_{large;} I_{small}$);
4. the quadrupole current (I_{quad}); and
5. the MOT II ‡uorescence signal.

There is a small dead-time e¤ect that arises when the CAMAC dumps the bu¤ered information to the data acquisition computer. This was measured to be about 2% for a counting rate of 100 Hz.

The data acquisition computer writes the recorded information to data …les that

are analyzed on-line using an Igor-based macro. This program has been written to bin the data by:

1. the recorded positron kinetic energy;
2. the nuclear polarization angle (inferred from the bias currents);
3. the absolute event time; and
4. the cycle time (the accumulation of all the completed cycles in the data set).

The program can …lter the data by setting gates in the plastic or CsI energy, and it removes any data that were taken when the TOP trap was not turned on (determined by the recorded bias currents).

The energy data for both the plastic and CsI can be combined on a scatter plot (see Fig. 28). The plot shows a clear peak in the CsI energy range at approximately 500 keV. This peak arises because the CsI detects the 511 keV gamma radiation in coincidence with the annihilation of a positron in the plastic scintillator. This mode (known as phoswich mode) can be used to tag the 511 keV annihilation energy that causes °-summing in the detector. These data also demonstrate that background rejection can be accomplished by selecting only the data within this coincidence peak. However, not enough data were taken in the beta-asymmetry experiment to get the statistics desired for the angular and energy analysis when using phoswich cut. To avoid losing most of the data in this mode, a larger solid angle for detection of the 511 keV gammas will be used in the next generation detector.

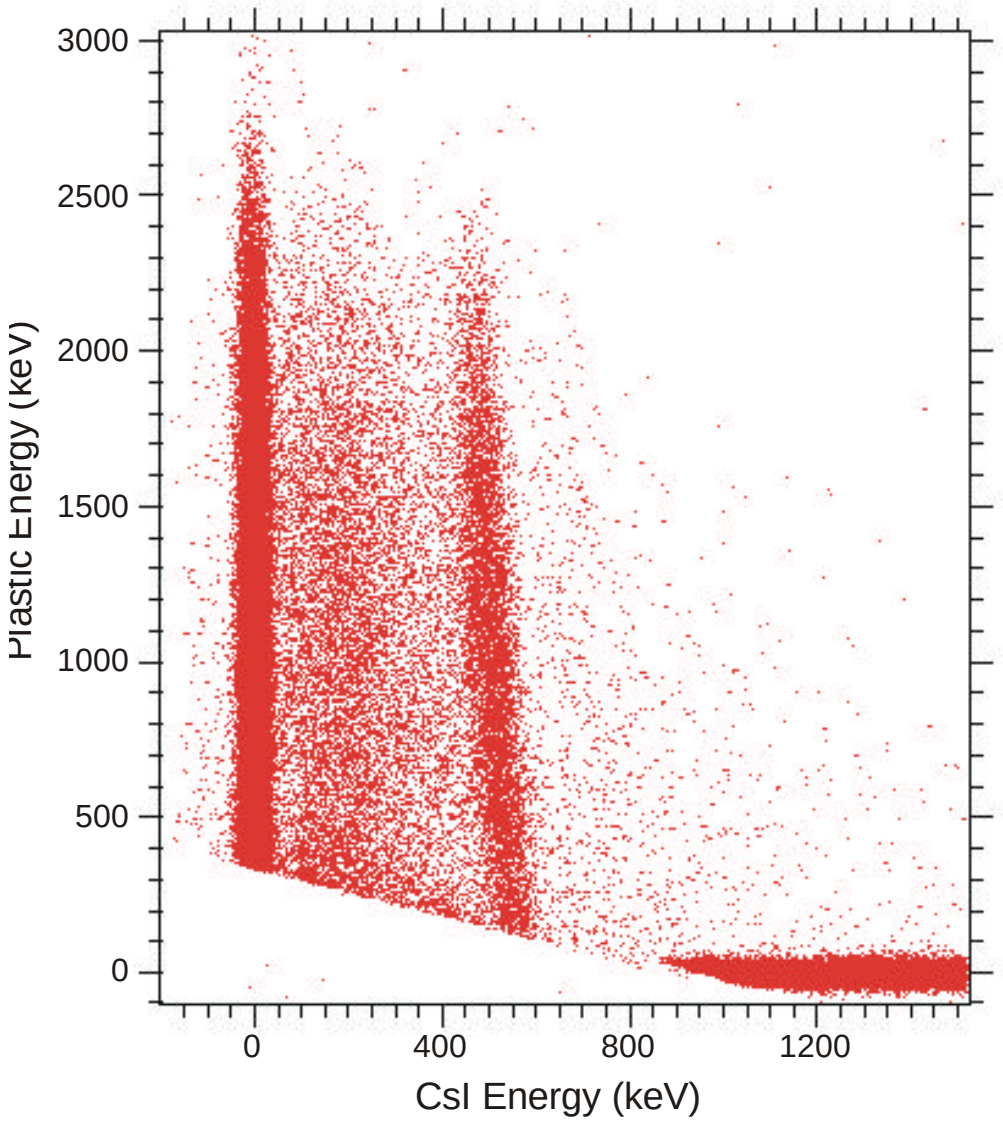

FIG. 28: Scatter plot of beta-decay data as a function of the energy deposited in the plastic scintillator vs. energy deposited in the CsI. The peak at » 500 keV in the CsI corresponds to the coincidence detection of a positron in the plastic and the resultant 511 keV annihilation radiation in the CsI. The vast majority of positron are detected without any deposition in the CsI. The angled cut in the data at low energy arises from the hardware threshold.

III. TRANSFER AND TRAPPING IN THE BETA-CHAMBER

A MOT-to-MOT transfer

Various schemes have been employed to transfer atoms or to produce low-velocity atomic beams. Atoms can be launched from a MOT by creating an imbalance in the trapping force. This has been accomplished by adjusting the detuning of some of the MOT laser beams (a technique known as moving optical molasses [79, 80]) or by purposely blocking the central portion of a single MOT beam [81]. Another technique uses a funnel-type arrangement of laser beams produced from a special trapping cell geometry [77, 82]. Besides the loss of signal, ine¢ciency in the MOT-to-MOT transfer will produce an untrapped background in the beta-chamber and so it is important to attain high transfer e¢ciency. A technique that has demonstrated » 90 % MOT-to-MOT transfer e¢ciency was developed at the University of Colorado [72] which involves shutting o¤ the MOT lasers and using a short pulse of light to push the atoms down a tube, with a magnetic …eld guide along its length, leading to a second chamber. We use this method not only because of its reported high-e¢ciency, but also because it requires minimal additional laser setup and a simple coupling between the two chambers.

With the atoms trapped the in trapping cell, we quickly shut o¤ the laser light and the quadrupole magnetic …eld of MOT I. This is accomplished by using a Uniblitz mechanical shutter before the expansion optics on the laser table and a …eld-e¤ect transistor to switch the .75 A current driving the MOT I anti-Helmholtz coils. After a short delay, we shine a laser push pulse that is directed through the transfer tube toward the center of the beta-chamber. The 3 mm diameter, » 100 mW/cm^2 intensity push beam is derived from the detuned trapping laser beam and shifted back to resonance with the $5S_{1=2}; F = 3=2 \; ! \; 5P_{3=2}; F^{0} = 5=2$

cycling transition in ^{82}Rb using two acousto-optic modulators in series. The laser push can be quickly switched on and o¤ using a fast rf switch located between the AOM drive source and the ampli…cation stage.

This short laser push is enough to accelerate the cold atoms in <1 ms to a velocity measured to be approximately 20 m/s. The atoms travel down the transfer tube and are re-caputured in the beta-chamber MOT. The MOT II laser light is diverted from the same EOM modulated laser beam that feeds MOT I, but requires much less power (» 90 mW as compared to 800 mW of MOT I) due to the smaller trapping beams (1.5^{00} horizontal and $.75^{00}$ in the vertical) and has a capture velocity somewhat larger than 20 m/s.

We use a small bias …eld aligned with the tube axis and a circularly polarized push beam so that the atoms end up in the $5S_{1=2}; F = 3=2; M_F = 3=2$ weak …eld seeking state. A factor of four gain in transfer e¢ciency is achieved by placing six permanently magnetized rubber strips (» 2000 G …eld strength at the surface) with alternating poles at 60 degree intervals around the outside of the transfer tube. These magnets are held in place by a soft iron cover with six machined grooves to ensure that the zero of the …eld axis is concentric with the transfer tube. The magnets produce a hexapole magnetic …eld that essentially forms a two-dimensional magnetic trap to deter atoms placed in a weak-…eld-seeking state from the walls of the transfer tube. Using this technique, we have been able to transfer atoms to the beta-chamber with a typical e¢ciency of 20 § 10%. This e¢ciency is measured by comparing the MOT I and MOT II ‡uorescence signals using calibrated photodiodes.

Attaining good MOT-to-MOT transfer e¢ciency has proven to be a challenging feat to reproduce on a day-to-day basis. The …rst step is to ensure that both the MOT I and MOT II laser beams are aligned and properly balanced. Since there

is a rather long lever arm (2-3 m) on the MOT II beam, this must be done each time the laser is turned on or tweaked for power. To begin with, a stable rubidium getter is used to spray atomic vapor into the trapping cell and another is used in the beta-chamber. The lasers are tuned to the ^{85}Rb trapping transition and the laser beam alignment and intensity are tweaked until each MOT traps a relatively dense and symmetric atomic cloud. Next the push beam is aligned so that it travels through the center of the transfer tube. The beam should pass directly through the MOT I cloud and come close to MOT II, but can be slightly misaligned so that a laser push does not kill the second MOT. With this alignment it is possible to accumulate atoms in MOT II with many transfer pulses. The MOT I cloud can be moved into the transfer beam axis by changing the magnetic zero position with three sets of Helmholtz coils that surround the trapping cell.

At this point the getter in the beta chamber is turned o¤. The atomic vapor is quickly pumped away so that loading of MOT II can only occur by MOT-to-MOT transfer. With a large cloud of ^{85}Rb in MOT I, usually some atoms are transferred into MOT II, which allows for tweaking of the transfer parameters (e.g., pulse duration, pulse delay, and …ne tuning of the transfer pulse alignment) to maximize the ^{85}Rb transfer e¢ciency. Once optimized, the lasers and EOM's are switched to the ^{82}Rb frequencies and another …ne tweaking of the transfer parameters is necessary because of the slight di¤erence in detuning, repump intensity (^{85}Rb uses the second sideband of the EOM while ^{82}Rb uses the …rst) and trap position between ^{82}Rb and ^{85}Rb.

The MOT I and MOT II ‡uorescence signal are shown in Fig. 29(a). As the foil is heated, ^{82}Rb atoms are released from the foil and become trapped in MOT I. The push beam is timed so that atoms are transferred at the peak of the MOT I signal which drops quickly as the shutter is closed. Successful transfer is indicated

by the growth of the MOT II signal. The slow risetime of the MOT II signal is due to the 3 s time constant used on the lock-in ampli…er (the MOT I time constant was 300 ms). The actual transit time for the atoms is approximately 30 ms. The atoms can be accumulated in MOT II by multiple heating, trapping and transferring cycles, see Fig. 29(b). This pulsed loading eventually reaches an equilibrium when the load rate equals the loss rate due to radioactive decay and from ordinary MOT loss of atoms due to background gas and light-assisted collisions.

B Molasses cooling, optical pumping, and TOP loading

To polarize the atomic sample for the beta-asymmetry measurement, the atoms are prepared in a stretched, weak-…eld seeking state and loaded into a magnetic time-average orbiting potential (TOP) trap. Again, attaining good loading e¢-ciency is a key issue that must be addressed to avoid losing signal and creating an untrapped positron background in the beta-chamber. To this end, it is necessary to have a good coupling between MOT II and the TOP trap and to cool the sample to a temperature that is not only below the TOP trap depth, but that will provide good average nuclear polarization in the TOP once loaded.

For a good coupling between MOT II and the TOP, care must be taken to overlap the MOT II cloud with the …nal position in the TOP trap. This ensures that atoms loaded into the TOP do not have a position o¤set that translates into an inital potential energy in the TOP trap …eld. Otherwise, the atoms will slosh back and forth in the TOP trap potential until collisions between trapped atoms damp the oscillatory motion resulting in an increased temperature. The overlapping of the traps is performed by trapping ^{85}Rb atoms in the beta-chamber

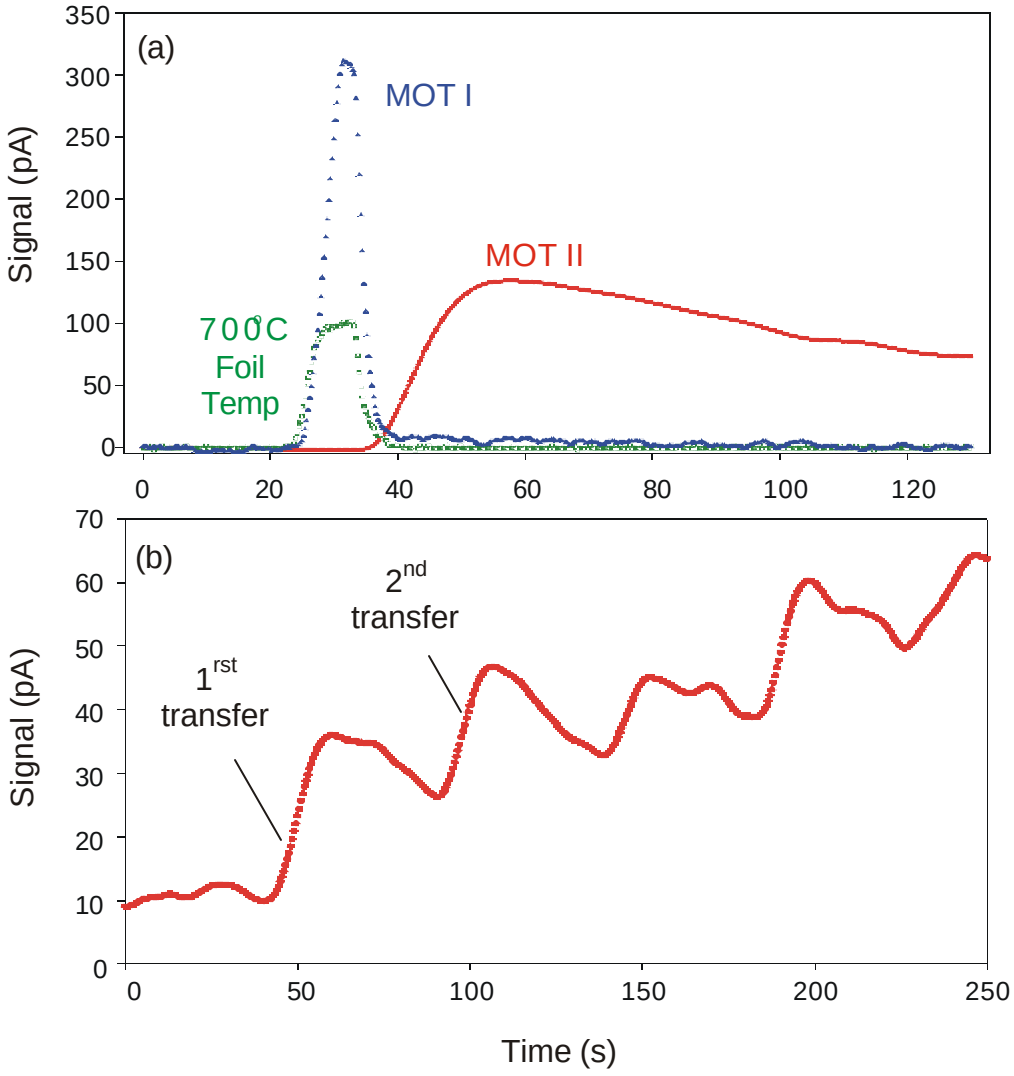

FIG. 29: (a) Demonstration of MOT-to-MOT transfer of ^{82}Rb into the beta-chamber. A laser push pulse accelerates the atoms from the …rst chamber to the second where they are captured by MOT II. This causes the ‡uorescence signal in the …rst MOT I to suddenly drop and the MOT II signal to rise. Lock-in time constants used are 300 ms and 3 s for MOT I and MOT II, respectively. (b) Shows several pulses of ^{82}Rb atoms being accumulated in MOT II. The number of trapped atoms accumulates in steps and eventually reaches equilibrium due to ^{82}Rb loss rate caused by beta-decay and the MOT II lifetime.

MOT and then quickly ramping-up the quadrupole …eld from the MOT II setting of $@B_r=@r$ = 8 G/cm to the 32 G/cm TOP setting, forming a compressed MOT. By tweaking the laser beam alignment and/or the magnetic shim coils surrounding MOT II while monitoring the cloud position using two CCD cameras at di¤erent angles, we are able to …nd a solution such that the high-and low-quadrupole …eld give the same cloud position. This indicates that the MOT II cloud is centered about the zero of the TOP quadrupole …eld gradient.

A sub-Doppler cooling scheme known as ¾ + =¾ ¡ polarization gradient cooling [44, 83], was used to cool the atomic cloud below the MOT II temperature which can be high as few hundred ¹K. The laser cooling setup for this method is particularly simple, requiring two overlapping counter-propagating beams with opposite circular polarization that are detuned by several linewidths from resonance. This is the same con…guration of beams used for each reto-re‡ected pair of the magneto-optical trap. Therefore, molasses cooling can be initiated by simply dropping the quadrupole …eld of MOT II (which falls in < 1 ms) while leaving the laser locked to the trapping transition. A systematic study of the molasses cooling step with a measurement of the …nal temperature has not yet been performed. However, it is evident that molasses cooling is working because the TOP loading e¢ciency has been found to decrease sharply (by an order of magnitude) from the observed maximum of 50% when this step is neglected.

After cooling, we shutter o¤ the laser light with a mechanical shutter on the MOT II beam, removing all the laser light from the beta-chamber before optical pumping begins. We polarize the atoms with a short 10 ¹s pulse of circularly polarized ¾+ laser light having 10 mW/cm^2 intensity. The polarization beam is frequency shifted from the trapping beam, which is still locked to the trapping transition, using the lower sideband of an AOM tuned to 60 MHz. This shifts the

polarization beam frequency to the $5S_{1=2}; F = 3=2 \rightarrow 5P_{3=2}; F = 3=2$ transition in ^{82}Rb (see Fig. 30). Since the $5P_{3=2}; F = 3=2$ state can decay to the lower hyper…ne $5S_{1=2}; F = 1=2$ ground state it is necessary to add a repump component. For this we use an EOM on the polarization beam driven at 1:543 GHz. A small residual magnetic …eld provides the quantization axis for the atoms. In the future, we plan to pulse on a large (» 10 G) laboratory bias …eld along the direction of the polarization beam to more reliably de…ne the quantization axis. Upon each absorption the atoms gain one unit of angular momentum. As a result, the atoms are quickly pumped into the $5S_{1=2}; F = 3=2; m_F = 3=2$ dark state where they can no longer absorb the circularly polarized ¾+ light.

This state is both a weak-…eld seeking state and an electron-nuclear spin stretched state, which allows for magnetic trapping and for alignment of the nuclear spin with the local magnetic …eld of the TOP. By knowing the direction of the TOP bias …eld, the average nuclear-spin direction of the sample can be determined and compared to the positron emission rate. The optical pumping method ensures that the cold atoms will on average absorb only a few photons before they are pumped into the desired dark state. Therefore, they are not signi…cantly accelerated or heated by the polarization pulse. The quadrupole …elds are switched on within 1 ms of the polarization pulse followed by the TOP bias coils » 100 ms later. See Fig. 31 for a schematic of the TOP loading sequence.

To explore the e¤ectiveness of our polarization procedure, we changed the polarization beam to ¾¡ in order to drive the atoms to the $5S_{1=2}; F = 3=2; m_F = -3=2$ state. This state is a strong-…eld seeking state that will not be trapped in the TOP. Under these conditions we found the TOP loading e¢ciency drops to less than 3%, implying that the polarization method e¢ciently manipulates the m_F state population of the atoms. A signi…cant drop in the loading e¢ciency is

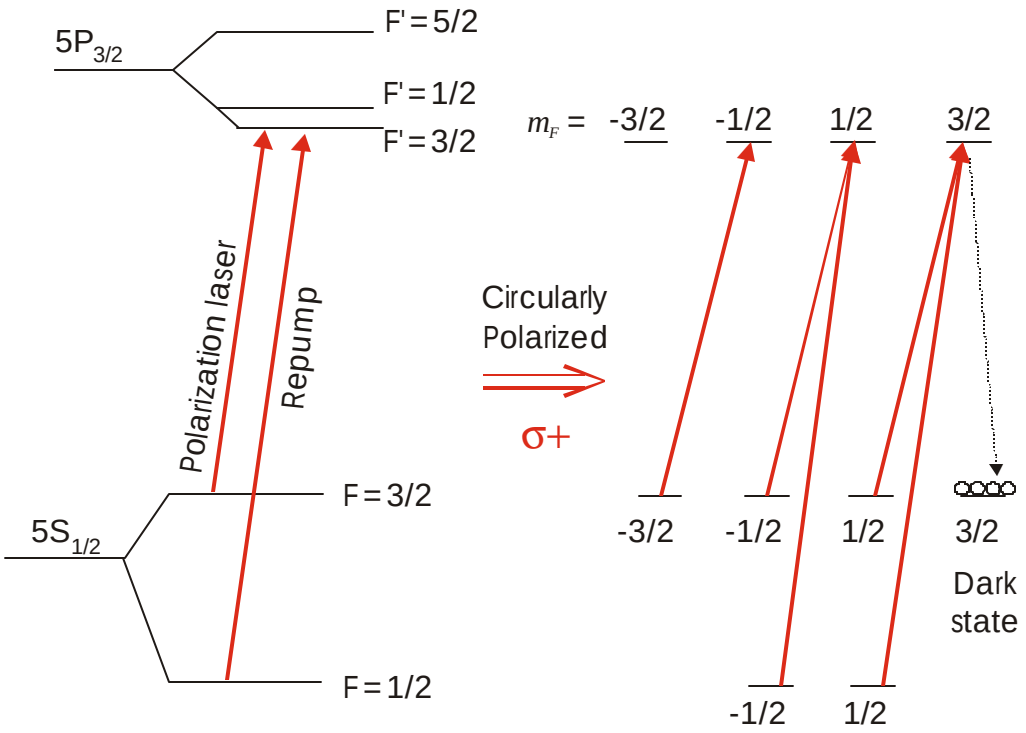

FIG. 30: Optical pumping scheme for preparing ^{82}Rb atoms for TOP loading. A circularly polarized ¾+ laser beam tuned to the $5S_{1=2}; F = 3=2 \; ! \; 5P_{3=2}; F = 3=2$ transition in ^{82}Rb by dipole selection rules can only drive ¢ $m_F = +1$ transitions. After a few absorption cycles the atoms will end up in the $5S_{1=2}; F = 3=2; m_F = 3=2$ state where they can no longer absorb photons from the ¾+ laser. A repump beam is also required to deplete the F = 1=2 hyper…ne ground state.

also observed when the EOM on the polarization beam is shut o¤. This may be explained by the fact that the weak-…eld seeking lower hyper…ne ground state ($5S_{1=2}; F = 1=2; m_F = ¡1=2$) is not bound as tightly in the TOP due to an atomic magnetic moment ($¹ = ¹_B m_F g_F$, where g_F is the Landé g-factor) that is lower than the $F = 3=2; m_F = 3=2$ state by a factor of three. It may be possible to cleanse the m-state population in the atomic sample by setting the quadrupole …eld gradient, or momentarily lowering it after loading the TOP, so that only the stretched state will remain in the trap as the other weak-…eld seeking states drop out due to gravity. Further measurements of this e¤ect are planned.

C TOP, MOT and quad trapping characteristics

Measurements of the MOT I, MOT II, and quadrupole trap lifetimes made with stable ^{85}Rb are shown in Fig. 32(a). The data for MOT I and MOT II was taken by observing the cloud ‡uorescence decay with time using a PMT. Only a small number of atoms were trapped so that light-assisted loss would be suppressed, leaving collision between the background gas and trapped atoms to limit the MOT lifetimes. This is evidenced by the fact that both decays …t well to a single exponential. For the Quad and TOP traps (see Fig. 32 (b), taken with trapped ^{82}Rb) , the lifetime measurements were performed by sequentially loading the trap, waiting for a pre-determined time duration, and then reloading the magnetically trapped atoms into MOT II while noting the change in MOT ‡uorescence. For the trap parameters with conditions described above, the results of exponential …tting give the lifetimes for MOT I (86 § 1 s), MOT II (312 § 10 s), Quad (141 § 8 s) and the TOP (41 § 2 s). Since measurements of the TOP trap were taken with radioactive ^{82}Rb with a known lifetime $¿ = 110(1)$ s, the expected TOP lifetime

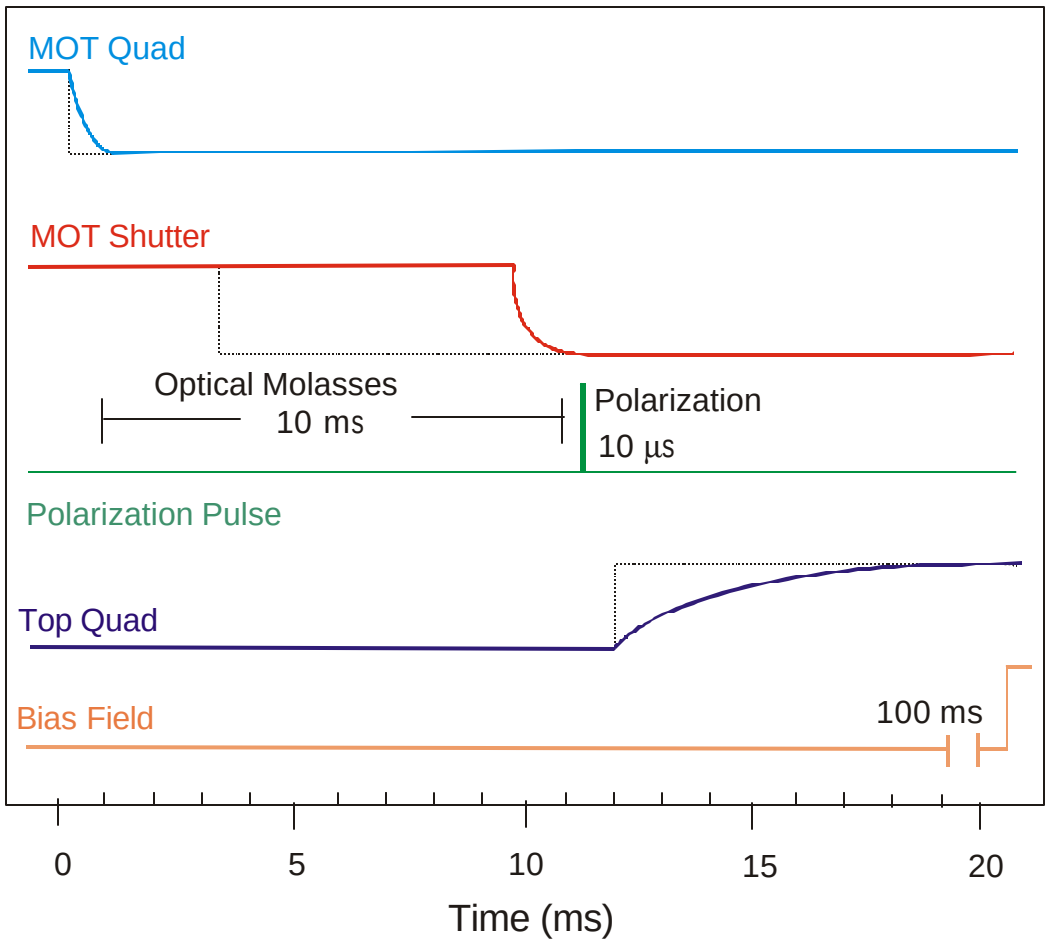

FIG. 31: Typical TOP loading sequence. Dotted lines indicate the control pulse for each component and solid lines shows the instrument response indicating delay and approximate rise and fall times. The optical molasses time starts when the quadrupole …eld of the MOT is turned o¤ and ends when the shutter closes.

with stable atoms can be calculated to be 67(4) s.

One explanation for the factor of two drop in lifetime between the MOT II and the quadrupole magnetic trap is that the larger trap depth of the MOT translates into a lower cross section for losing atoms that collide with the background gas. The MOT can also cool atoms after a glancing collision, whereas there is no cooling mechanism in place for pure magnetic traps. Another possibility is that the magnetic trap can lose atoms via spin-flipping to a strong-field seeking state. This can occur through atom-atom collisions, resonant light absorption, or nonadiabitic transitions near the zero-point of the quad field. Care must be taken to limit the amount of resonant laser light on the optical table while the atoms are confined to the magnetic trap; otherwise, scattered light can enter the beta-chamber and depolarize the atoms. Nearly a factor of two increase in the TOP trap lifetime (see Fig. 32 (b)) was found by blocking the beam near the laser output after loading the magnetic trap.

Nonadiabatic transitions will occur if the rate of change in the magnetic field direction the atoms sees as it moves about the trap is comparable with the Larmor precession frequency $\omega_L = \mu_B B/\hbar$. The most likely place for this to occur is in some small region centered around the $B = 0$ point of the quadrupole trap. As the magnetically trapped sample is cooled, the atoms have a much higher probability of undergoing a spin-flip loss since they spend more time at the bottom of the quadrupole potential. This becomes a detrimental effect for the quadrupole trap as the phase space density is increased.

The TOP trap was invented [68] to circumvent this problem by creating a time-averaged field with no zero point at the center. This is accomplished by adding a rotating bias field that moves the zero of the quadrupole field gradient away from the atoms faster than they will respond to the change in field gradient. Provided

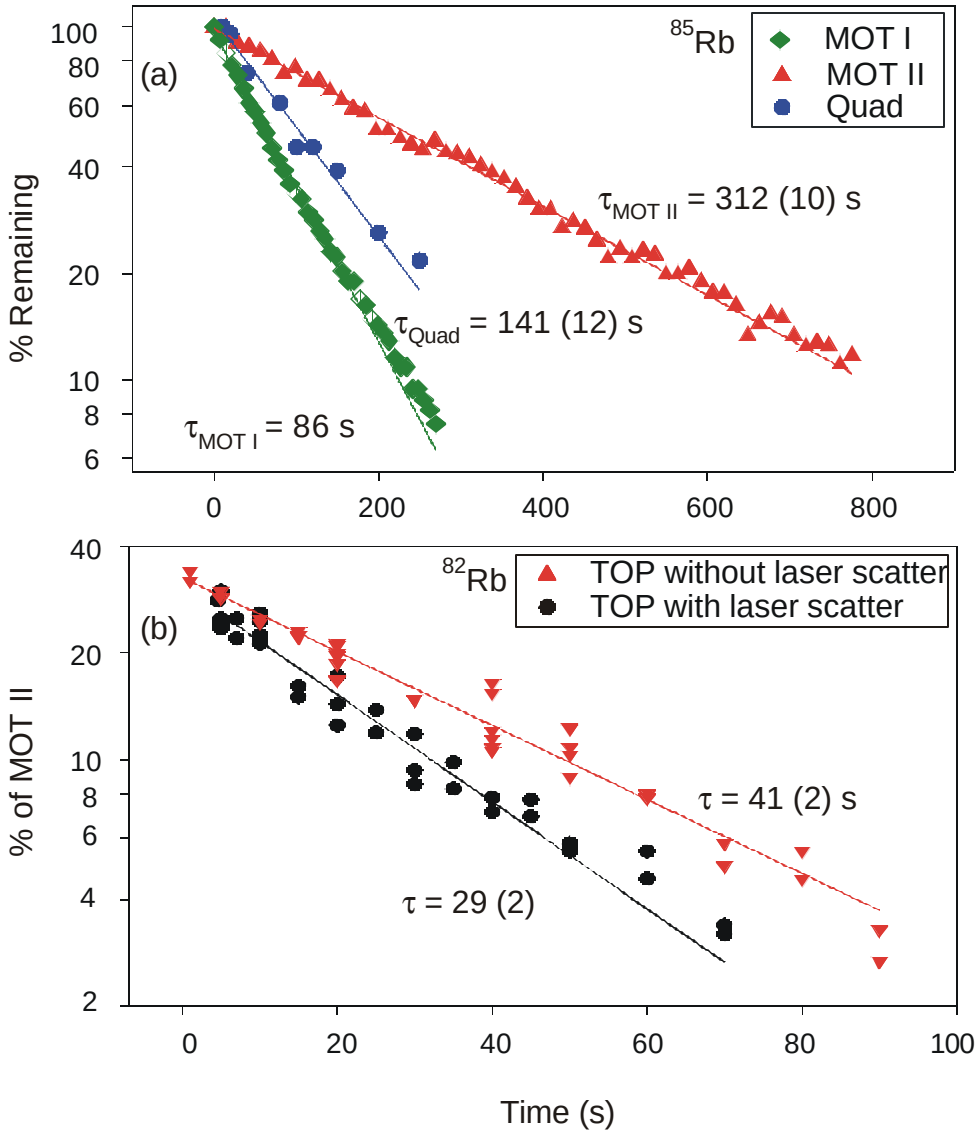

FIG. 32: (a) MOT I, MOT II, and quadrupole magnetic trap lifetime measurements made with trapped ^{85}Rb. The MOT lifetime measurements were taken in the low-density regime, where background gas collisions are the dominant loss mechanism. (b) TOP lifetime measurements showing the e¤ect of scattered laser light on the optical table on the TOP lifetime with ^{82}Rb.

the atomic sample is at a su¢ciently low temperature so that the cloud does not extend into the zero-…eld radius swept out by the rotating bias …eld, nonadiabatic loss will be avoided. The fact that our TOP lifetime is lower than our quad lifetime indicates the temperature of the sample is high and that the zero-…eld radius of the TOP may be moving through some portion of the cloud causing an even larger spin-‡ip loss rate (because there is a larger volume where spin-‡ip can occur) than that of the simple quadrupole trap at the same temperature.

The (relatively) high TOP trap temperature is responsible for the less than optimal 60% average nuclear polarization observed in the beta-asymmetry experiment. By using the TOP trap model for the polarization, the temperature of the cloud can be inferred to be roughly 200 ¹K. The inability to image the trapped cloud prevented the …ne-tuning of the optical molasses cooling and the coupling between MOT II and the TOP. These e¤ects are the most likely candidates for causing a high TOP trap temperature.

In the future, measurement of the TOP cloud temperature will be perfomed using absorption and/or phase-contrast imaging with a Princeton Instruments CCD camera. The spacial extent of the cloud after a certain time delay will give temperature information and time-sequenced images will reveal the presence of oscillatory motion that can result from loading the TOP trap with some initial potential energy. Improvements can be made in the optical molasses step by nulling the ambient magnetic …eld in the beta-chamber using three additional sets of magnetic trim coils, by providing for better molasses beam balance using a six-beam MOT, and by having the ability to quickly increase the trapping transition detuning during the optical molasses. The goal for attaining a TOP trap cloud on the order of 20 ¹K should be realized with these improvements.

IV. ^{82}RB POSITRON-SPIN CORRELATION IN THE STANDARD MODEL

In the positron decay of the ^{82}Rb with half-life $T_{1=2}$ = 75 s (see Fig. 33), the initial state (^{82}Rb) has a nuclear spin $J = 1^+$ and undergoes positron ($\bar{}^+$) decay to ^{82}Kr. The largest branch decays to the $J^0 = 0^+$ ground state (branching ratio b_1 = 86:4%) of ^{82}Kr and a second branch decays to the …rst excited $J^0 = 2^+$ (b_2 = 12:6%), which then promptly decays to the ground state by 776 keV °-emission [74]. All the other branches contribute less than 1% and are neglected given the current accuracy of our measurement.

Multiple transitions can be expressed in terms of the positron kinetic energy (E) and the beta-nuclear spin correlation (characterized by the angle μ between the average nuclear spin and the positron momentum). The probability $P(E;\mu)$ of making a transition between E and E + dE with angle between μ and μ + dμ can be written

$$P(E;\mu) = 1=2 \sum_{i=1}^{X} P_0 b_i f_0(E;Q_i)[1 + A_i P \bar{}(E)\cos(\mu)] \qquad (83)$$

where b_i are the branching ratio for each transition (containing the nuclear matrix elements), P is the average nuclear polarization of the sample, and $\bar{}(E)$ is the electron velocity relative to the speed of light.

The energy dependence for the individual transitions are given by the Fermi theory of beta-decay [4] where

$$f_0(E;Q_i) = kpWF(E;Z)(Q_i \text{ ¡ } E)^2 \qquad (84)$$

is the normalized (via constant k) Fermi shape of the electron distribution with momentum p; total energy W; and kinetic positron endpoint energy Q_i. A Coulomb

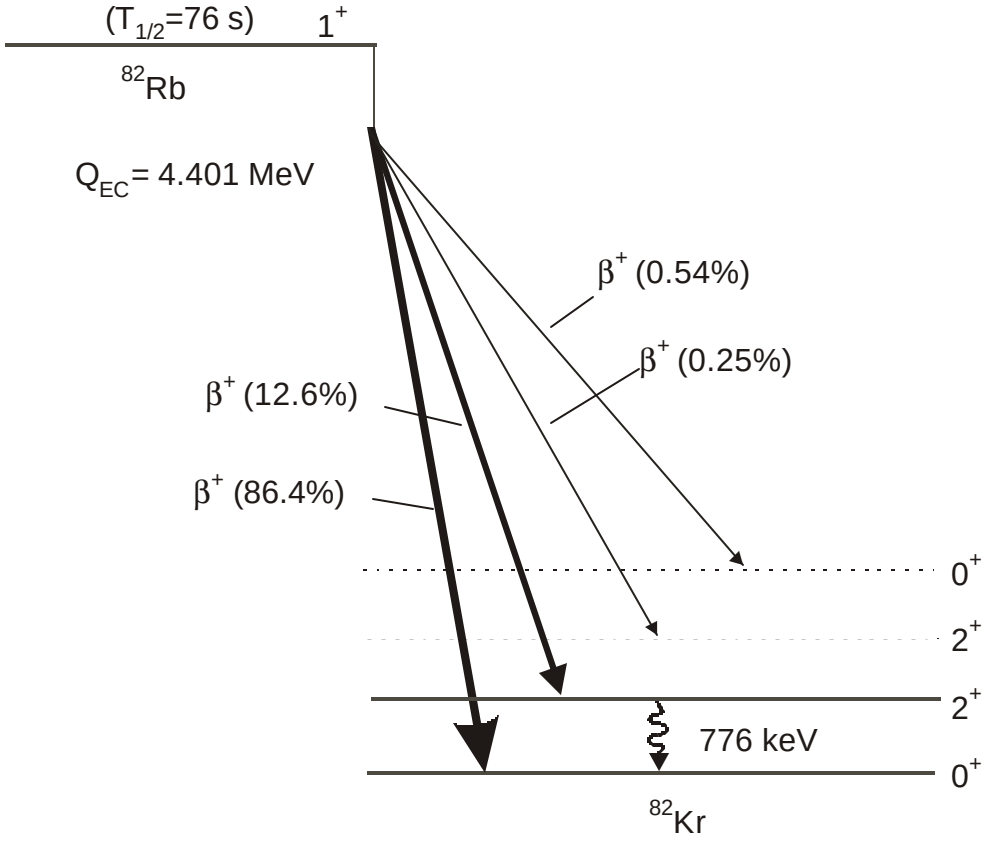

FIG. 33: Beta-decay scheme for ^{82}Rb. The initial state ^{82}Rb ($J^{¼} = 1^+; T_{1=2} = 75$ s) undergoes positron ($^{-+}$) decay to ^{82}Kr. The largest branch decays to the $J^{¼} = 0^+$ ground state (branching ratio $b_1 = 86{:}4\%$) and a second branch decays to the …rst excited $J^{¼} = 2^+$ ($b_2 = 12{:}6\%$) which then promptly decays to the ground state by 776 keV °-emission.

correction factor is included

$$\S F(E;Z) = \acute{}=(1 \text{ ¡ } e^{i\acute{}}) \tag{85}$$

where $\acute{} = 2¼Z®=\bar{}$. Here ® is the …ne structure constant, and Z is the atomic number of the daughter nucleus. The "+" sign in Eq.85 is used for electron decay, and the "¡" for positron decay.

Of particular importance in Eq. 83 is the term A_i known as the beta-nuclear spin (or positron-nuclear spin) correlation coe¢cient. These correlation coe¢cients have a direct relationship to the fundamental couplings for di¤erent types of interactions (i.e., scalar S; vector V; axial-vector A, or tensor T) involved the weak force [3]. With the standard model assumptions of a V ¡ A interaction, the correlations coe¢cients can be written as a function of the fundamental nuclear form factors (g_V and g_A), the Fermi, and the Gamow-Teller nuclear matrix elements (M_i^F and M_i^{GT}) for the i^{th} transition [9]

$$(A_i)^{SM} = \frac{\pm_{J^0J} M_i^F M_i^{GT} \sqrt{\frac{J}{J+1}} g_A g_V \S \, ,_{J^0J} g_A^2 (M_i^{GT})^2}{g_V^2 (M_i^F)^2 + g_A^2 (M_i^{GT})^2}: \tag{86}$$

where

$$,_{J^0;J} = \begin{cases} 1 & J^0 = J \text{ ¡ } 1 \\ 1=(J+1) & J^0 = J \\ J=(J+1) & J^0 = J+1 \end{cases}: \tag{87}$$

The "+" term in Eq. 86 is for electron emission and the "¡" term is for positron emission.

For the transitions in ^{82}Rb, we have a $J^0 \text{ ¡ } J = \text{ ¡ } 1$ for the …rst transition (b_1), and $J^0 \text{ ¡ } J = 1$ for the second (b_2). For both transitions this $j¢Jj = 1$; which violates the selection rules for Fermi transitions (i.e., $¢J = 0$), so that $M_i^F = 0$: This also allows for the cancellation of the Gamow-Teller matrix element M_i^{GT} and

the nuclear form factor g_A in Eq. 86 such that

$$(A_i)^{SM}_{GT} = i\,\delta_{J^0;J}. \tag{88}$$

This accomplishes much more than simplifying the expression for the correlation coefficient because the nuclear matrix elements cannot be calculated except for very simple nuclei. The fact that ^{82}Rb is a pure Gamow-Teller transition allows for a unique prediction for the correlation coefficient in both ^{82}Rb transitions, $A_1 = 1$ and $A_2 = -1/2$. The physical significance of the minus sign for the second transition is that the positron emission is predominantly anti-aligned with the nuclear spin as opposed to aligned for the first transition.

It is convenient to express the transition probability with a single energy dependent amplitude of a cosine function. For ^{82}Rb we can define

$$A(E) \equiv \frac{b_1 f_0(E;Q_1)A_1 + b_2 f_0(E;Q_2)A_2}{b_1 f_0(E;Q_1) + b_2 f_0(E;Q_2)} \tag{89}$$

and

$$F_0(E) \equiv b_1 f_0(E;Q_1) + b_2 f_0(E;Q_2) \tag{90}$$

which allows the transition amplitude to be written

$$P(E;\mu) = \frac{P_0}{2} F_0(E)[1 + A(E)\beta(E)P\cos(\mu)]. \tag{91}$$

By integrating over the angular dependence in Eq. 91, the cosine term vanishes and we see that the significance of $F_0(E)$ is that it represents theoretical positron kinetic energy shape for ^{82}Rb beta-decay (see Fig. 34). This can be compared to the measured ^{82}Rb energy spectrum from the TOP trap. The calculation of $A(E)$; $\beta(E)$; and $\beta(E) \pounds A(E)$ for ^{82}Rb is shown in Fig. 35. The effect of the

second transition in ^{82}Rb with a 12.6 % branching ratio yields an energy-dependent amplitude for the cosine function that departs from the simple $\bar{}(E)$ dependence of a single component transition.

In practice, we observe the angular distribution of the data by integrating over a certain energy interval (E_f ¡ E_i) to gain the statistics needed to study the angular dependence. In this case, we can perform an integration of Eq. 91 over the energy interval and de…ne the result as the angular transition probability amplitude

$$W(\mu) = \int_{E_i}^{E_f} P(E;\mu)dE = W_0(1+ < \bar{}A > P\cos\mu) \tag{92}$$

where

$$W_0 \acute{} \frac{P_0}{2}\int_{E_i}^{E_f} F_0(E)dE \tag{93}$$

and

$$< \bar{}A > \acute{} \frac{\int_{E_i}^{E_f} A(E)\bar{}(E)F_0(E)dE}{\int_{E_i}^{E_f} F_0(E)dE}: \tag{94}$$

A calculation of $< \bar{}A >$ made with $E_f = Q_1$; has been plotted as a function of threshold energy E_i as shown in Fig. 36. Note that in the beta-asymmetry experiment, we will measure $< \bar{}A >$ for a given energy interval and work backwards to …nd what implications this has for the correlation coe¢cients in ^{82}Rb and the standard model.

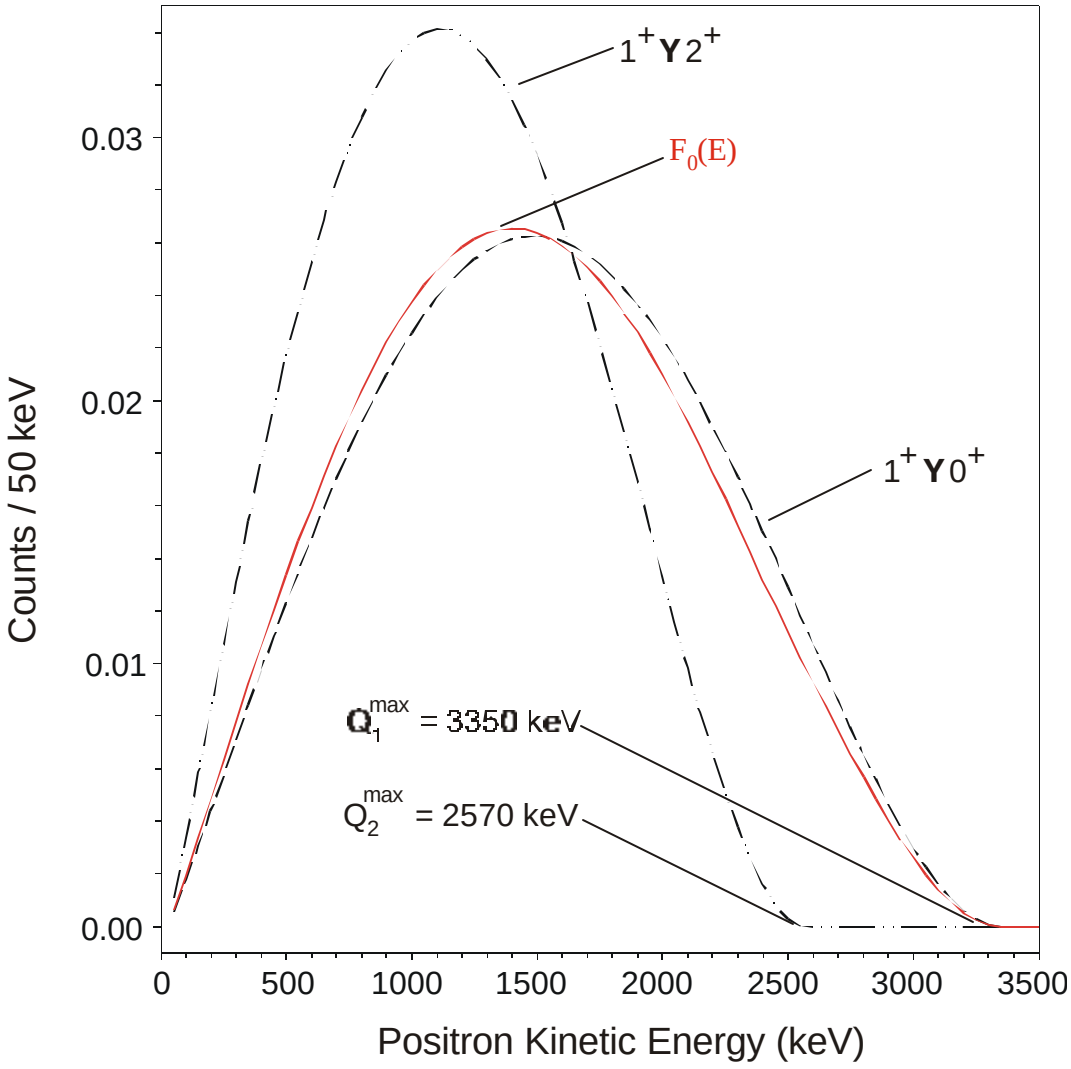

FIG. 34: The theoretical beta-energy shape for the $1^+ \rightarrow 0^+$, the $1^+ \rightarrow 2^+$; and the branching-ratio-scaled shape for the two signi…cant transitions in ^{82}Rb. Note the ^{82}Rb shape is only slightly perturbed from the $1^+ \rightarrow 0^+$ shape because this transition is the dominant branch by a factor of seven.

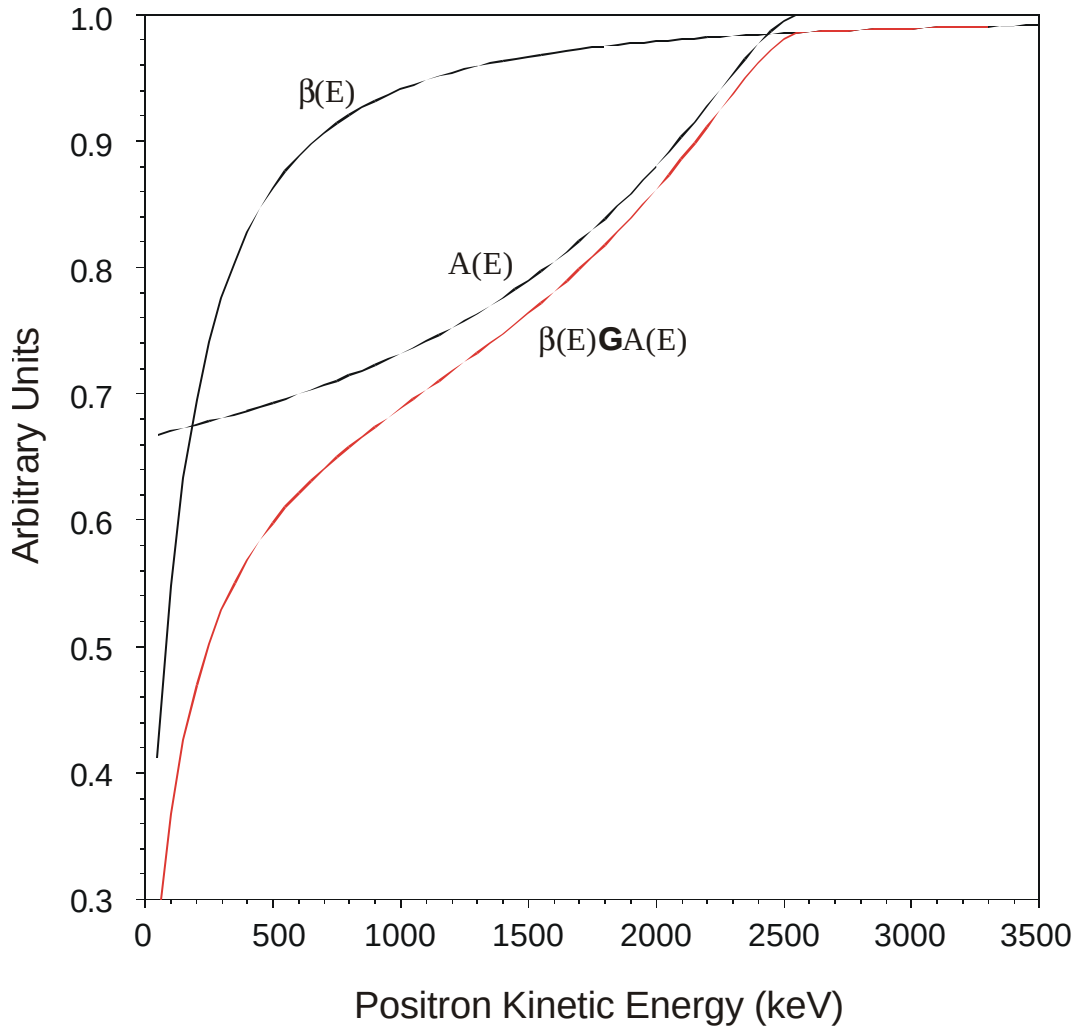

FIG. 35: Plot showing the calculation of the factors ¯(E) and A(E) separately and ¯(E) £ A(E) that contributes to the energy-dependent parity-violating cosine amplitude in ^{82}Rb. These factors are determined from the standard model values for the correlation coe¢cients and the beta energy shape for the two dominant transitions in ^{82}Rb. Note that the positrons that are emitted from the ^{82}Rb nucleus must be treated relativistically.

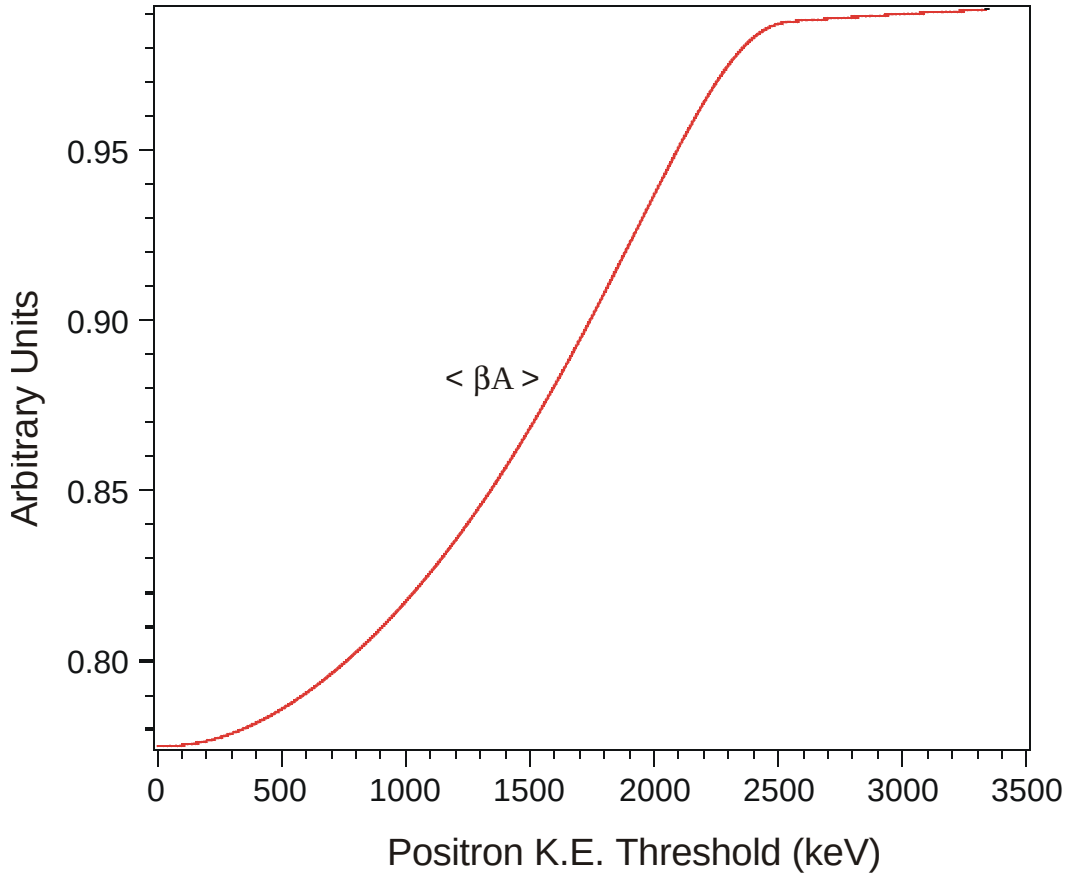

FIG. 36: Plot showing the energy-dependent part of the positron-nuclear spin correlation amplitude $< \bar{A} >$ averaged from the threshold energy (represented by the x-axis) to the endpoint of the ^{82}Rb energy spectrum. This is the term that will be measured experimentally to extract correlation coe¢cients.

V. ANGULAR DISTRIBUTION

A Experimental measurement of the angular distribution

The probability distribution of emitted positrons from an ^{82}Rb sample can be written with a simple cosine dependence of the angle μ between the average nuclear spin $\vec{J}$ and the emitted positron momentum $\vec{p}^-$.

$$W(\mu) = \frac{1}{4\pi} W_0(1 + \langle \bar{A} \rangle P \cos\mu). \tag{95}$$

This angle cannot be measured directly in this experiment. Instead, we measure the currents in the bias coils pairs at the instant of each beta event from which we can reconstruct the average nuclear spin direction of the polarized sample. The collimation hardware limits the detection of positrons to a cone originating at the trap sample and expanding along the detection axis with a full opening angle of 18.2°. This finite detection angle must be accounted for in the experimental data.

Define I_x and I_y as the measured current in the Helmholtz coils pairs that are concentric with the x- and y-axis, respectively (the y-axis is the detection axis). The phase angle ϕ of the sinusoidally driven coils can be determined from the data by scaling the currents so that they have the same amplitude and taking the arctangent

$$\phi = \tan^{-1}\left(\frac{I_x}{I_y}\right). \tag{96}$$

These currents produce a magnetic field that rotates in the xy-plane. The phase of the magnetic field ε is similarly defined as

$$\varepsilon = \tan^{-1}\left(\frac{B_x}{B_y}\right) \tag{97}$$

and related to the current in the bias coils by a phase shift X that is induced by eddy currents in the stainless steel chamber.

$$\© = £ + X \tag{98}$$

For a given spin direction £ there is a range of angles µ in which positrons can be detected that is de…ned by the opening angle of the collimation hardware. In order to parameterize the integration over this range, note that the unit vector p̂– de…ning the direction of the positron momentum can be written in terms of the polar angle ® substended from the y-axis and the angle ' between the projection of p̂– onto the xz-plane and the z-axis (see Fig. 37).

$$\hat{p}_- = \sin(®)\sin('){\hat{}} + \cos(®){\hat{}} + \sin(®)\cos('){\hat{k}}: \tag{99}$$

A unit vector for the average nuclear spin can be written in terms of £

$$\hat{J} = \sin(£){\hat{}} + \cos(£){\hat{}}: \tag{100}$$

We can then write the cosine of the angle µ between the average nuclear spin and the positron momentum in terms of these parameters.

$$\cos(µ) = \hat{p}_- ¢ \hat{J} = \sin(£)\sin(®)\sin(') + \cos(£)\cos(®): \tag{101}$$

To …nd the overall probability for detecting positrons when the average nuclear-spin is at angle £, we must integrate the distribution function for allowed ® and '; which range over the full opening angle of the collimator ±:

$$W(£) = \int_0^{±/2}\int_0^{±/4} W(µ)\sin(®)\,d®\,d'$$

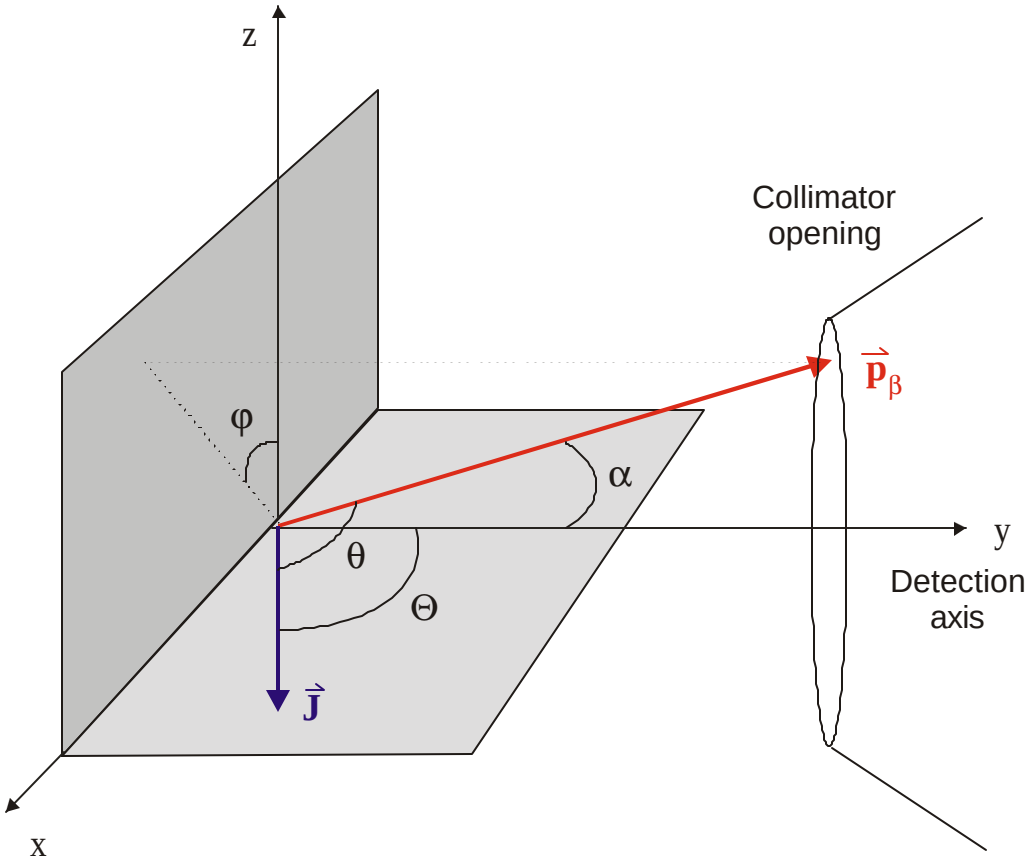

FIG. 37: Schematic showing the relevant angles for detection of a position with momentum vector p– parameterized by angles ® and ': The integration is extended over the opening de…ned by the collimation hardware. Also shown is the angle £ between the detection axis (y-axis) and the nuclear spin J, and the angle μ between the positron momentum p– and the nuclear spin J:

$$= W_0 \int_0^{2\pi}\int_0^{\pi} (1 + \langle \bar{A} \rangle P(\sin(\pounds)\sin(\circledR)\sin('))) + \cos(\pounds)\cos(\circledR)\sin(\circledR))\sin(\circledR)d\circledR d' : \quad (102)$$

Performing the integration yields

$$W(\pounds) = W_0 \acute{} (1 + G \langle \bar{A} \rangle P\cos(\pounds)) \quad (103)$$

where

$$\acute{} = \frac{1}{2}(1 \text{ ¡ } \cos(\pm/2)) \quad (104)$$

$$G = \frac{1}{2}(1 + \cos(\pm/2)) = 1 \text{ ¡ } \acute{} : \quad (105)$$

$G = :994$ for the $\pm = 18:2^{\pm}$ opening angle of the positron collimator. This shows that the experimental e¤ect of the …nite opening angle has a magnitude of less than 1% in the overall amplitude of the asymmetry function and can be understood to good precision.

We now have a fair description of the expected positron decay signal as a function of the experimentally measured phase angle ©. However, there are other contributions to the overall detector signal that must also be accounted for. Two of importance are the presence of an uncorrelated background B that will add a "dc" level to the measured asymmetry function and the detection of Compton electrons in the plastic scintillator that have scattered from 776 keV gamma rays associated with ^{82}Rb. The latter will have some angular dependence (albeit parity conserving) if it arises due to gammas emitted from polarized atoms in the trap region, but we can choose to integrate over an energy scale where the contribution from gammas to the overall signal will be negligible. We can therefore write the expected experimental distribution as

$$N(©_i) = [S(1 + PG \langle \bar{A} \rangle \cos(©_i)) + B]¢=2¼; \quad (106)$$

where $N(\theta_i)$ is the number events about bias current phase angle θ_i with some bin with ϕ. S is the total number of positrons arising from the TOP trap, and B is the total number of background counts which has no angular dependence. It is convenient to rewrite the distribution as

$$N(\theta_i) = N_0(1 + \alpha \cos(\theta_i))\,\phi = 2\pi; \tag{107}$$

where

$$N_0 = S + B; \tag{108}$$

and

$$\alpha = \frac{1}{1 + B/S} \langle \bar{A} \rangle PG: \tag{109}$$

B Wiggle and phase corrections to the angular distribution

The data can be integrated over energy, and binned according to the angle θ that is constructed from the bias coil currents recorded for each event. The result is the raw angular distribution plotted in Fig. 38(a) where we have used a bin width of $5^{\pm}$. A phase-shifted cosine shape is evident with a hint of additional structure at the few percent level. The additional structure was caused by a distortion in the sinusoidal shape fed to the audio amplifiers. This problem was later found to be due to the bias coil attenuators and can easily be fixed for future measurements. It must, however, be accounted for in the measured angular distribution.

The shape can be measured well using a high-statistics ^{22}Na data set (see Fig. 38(b)). The ^{22}Na sample is not polarized, and therefore we expect no angular correlation that is a result of parity violation. This way we can simply make a high-statistics measurement of the angular distortion caused by any instrumental effect. To collect the ^{22}Na data, the experimental apparatus was run exactly as

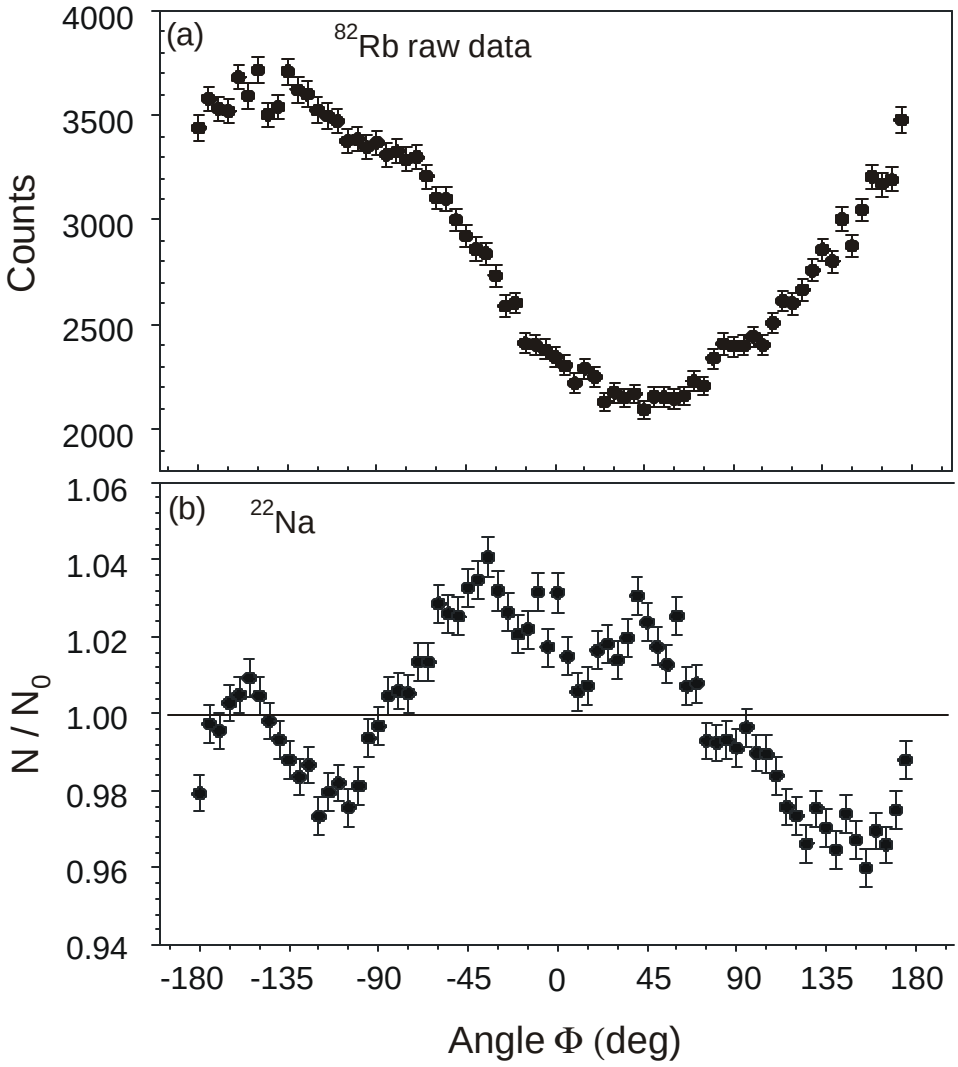

FIG. 38: (a) The ^{82}Rb raw angular data taken with a lower energy threshold of 800 keV and plotted as a function of the measured bias current phase angle © with a ¢ = 5± bin width. There is some structure beyond a simple cosine distribution and a large phase shift is obvious. (b) The angular distribution of the ^{22}Na data which shows the 5% residual wiggle.

before except with no atoms transferred to the beta-chamber. The e¤ects of the instrumental distortion in the angular data can be corrected by dividing out the normalized ^{22}Na shape.

By assuming that the distribution will have a maximum amplitude at £ = 0 as is predicted for a pure Gamow-Teller positron emitter, we can measure the phase shift X using the high-statistics angular distribution. The wiggle-corrected data as a function of © are …t with a cosine function having the phase shift, phase, amplitude and o¤set as variable parameters. This indicates a phase shift of 133:4 § 0:5 degrees that agrees well with an independent determination of the phase shift (131 § 2 degrees) measured with an ac gaussmeter placed at the trapping position inside beta-chamber. The wiggle-corrected and phase-shifted high-statistics data are plotted in Fig. 39 along with the cosine-…t residuals. The …t gives ® = 0:268 § :004 for the cosine amplitude. Given that $< \bar{A} >$ = :80 in the standard model and G = :994, the amplitude indicates we have a signi…cant amount of background present in the high-statistics data set and/or the polarization of the ^{82}Rb sample is less than 100%.

VI. BACKGROUND ANALYSIS AND INFERRED POLARIZATION

A Source of background

A major concern in any beta-decay experiment is the extent to which background is detected and how it a¤ects the desired measurement. Background in our case is any event detected in the plastic scintillator that does not originate from positrons emitted by the TOP-trapped ^{82}Rb sample. These background events can come from a variety of sources such as muons created in the upper atmosphere by cosmic rays, from room or environment background, or from gammas

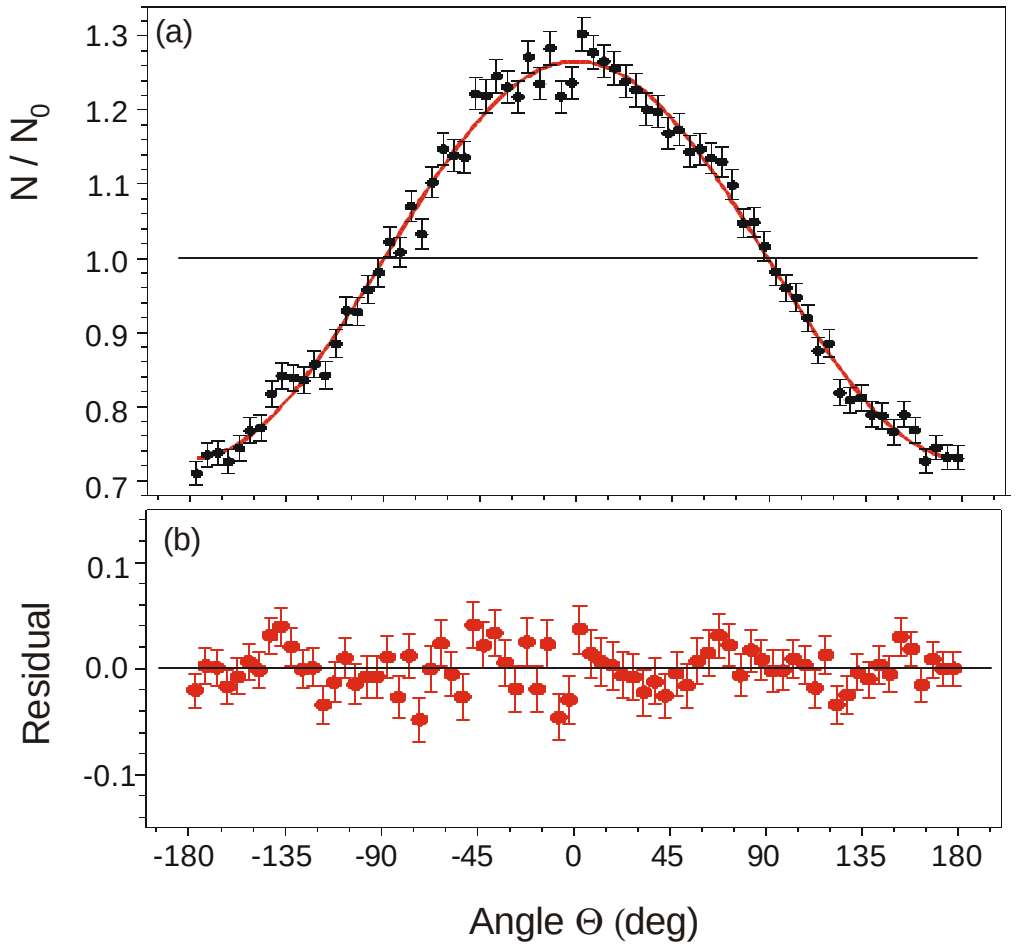

FIG. 39: (a) Angular distribution now plotted with wiggle removed as a function of the angle £ (i.e., phase removed) between the average nuclear spin and the detection axis. The solid line is a cosine …t to the distribution that is in good agreement with the experimental angular distribution. (b) The residual of the cosine …t to the corrected angular distribution.

and positrons emitted from untrapped ^{82}Rb atoms in the beta-chamber among others.

Many of these events can be identified and removed from consideration by choosing an appropriate energy window within the allowed positron energy spectrum of ^{82}Rb, but this is not sufficient to totally eliminate the background. In our experiments, we use a hardware threshold energy of 400 keV and typically consider data up to the 3400 keV endpoint energy of ^{82}Rb positrons. Many events occur in the 400 to 800 keV region that arise from Compton scattering of the 776 keV gamma radiation associated with ^{82}Rb.

The background in the high-statistics data is dominated by atoms that are lost in the trapping process and make their way to the walls of the beta-chamber where they subsequently undergo beta-decay from an unpolarized state. When lost atoms reside on the quadrupole coil wells, their emitted positrons do not have a direct line-of-sight to the detector but can still be detected if they scatter from the inside surface of the collimator as shown in Fig. 40. As a result of this scattering, the energy spectrum for these positrons will be highly distorted toward the low end of the positron energy spectrum. In addition, it is possible for the atoms themselves to pass through the collimator entrance and stick to the thin-foil window, where their decay is detected with high efficiency due to their close proximity to the plastic scintillator.

There are several means by which atoms become lost to the walls of the beta-chamber in this experiment. The first is the MOT I-to-MOT II transfer, which has an efficiency of $\approx$ 20%. Some of the atoms lost in this process can pass into the beta-chamber, interact with the MOT II laser beams and spread to a region where their subsequent beta-decay can be detected. Another 50% loss of atoms occurs during TOP loading. This inefficiency may arise from an atomic cloud

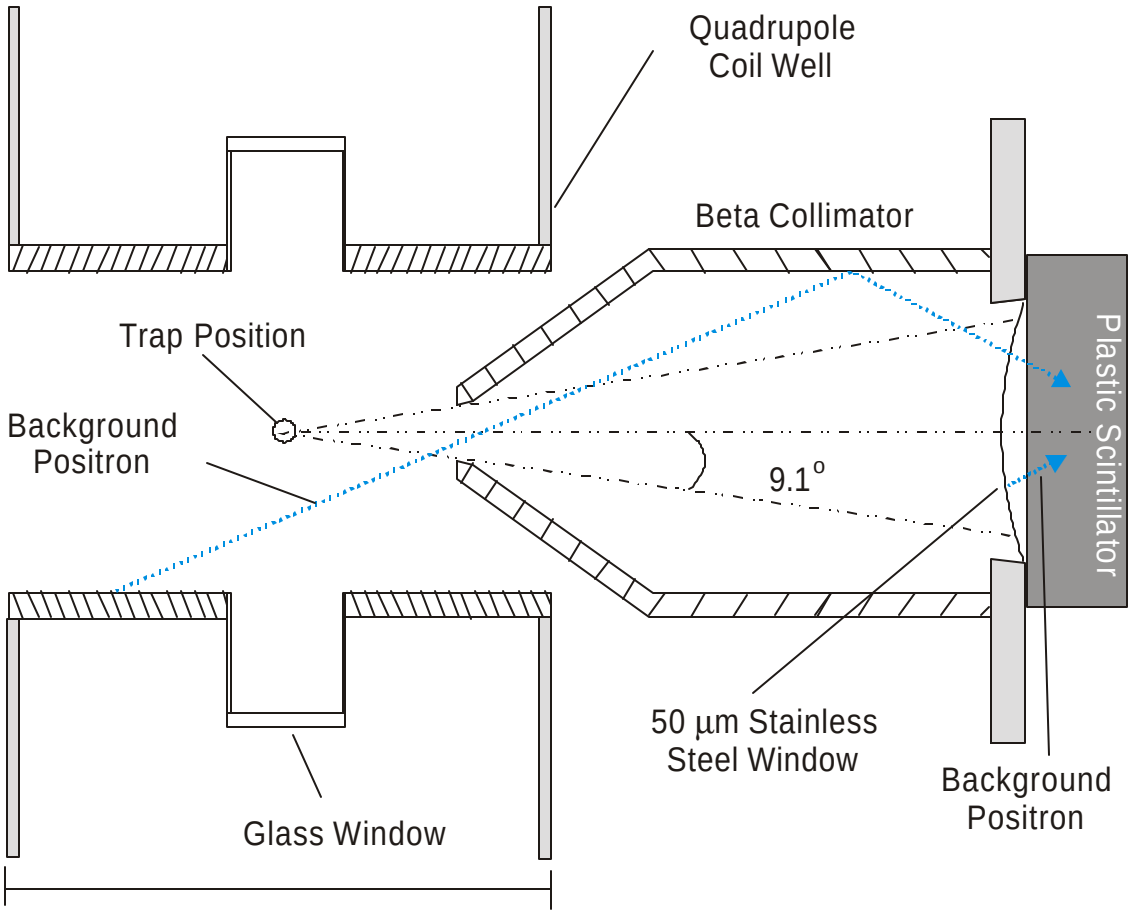

FIG. 40: Diagram showing the detection geometry for the TOP trap. The beta collimator provides an 18:2± full-opening acceptance angle for detection for of positrons from the trap. Positrons emitted from untrapped atoms on the quadrupole wells can only be detected if they scatter from the inside of the collimator. Untrapped atoms that pass through the collimator and end up on the thin-foil window are detected with high probability (» 35%):

that has not been fully polarized to the desired weak-…eld-seeking state or from a cloud temperature that is too high to be con…ned by the TOP trap. Once loaded into the TOP, atoms are still vulnerable to loss because of the …nite TOP trap lifetime that was measured to be $¿_{TOP}$ = 70 s with stable ^{85}Rb atoms. This loss is a result of either background gas collisions with trapped atoms or Majorana transitions to a strong-…eld-seeking state that can occur when an atom nears the zero …eld region of the TOP trap. Consequently, of the remaining ^{82}Rb atoms loaded into the TOP trap, 61% (estimated from the trap lifetime) will be expelled from the trap before they decay radioactively. Atoms lost from the TOP trap due to background gas collisions are likely to have an isotropic distribution. This mechanism is the most likely candidate for placing atoms on the thin-foil window since expelled atoms would have roughly the same solid angle for landing on the foil as emitted positrons from the TOP trap do for being detected.

Background events should have no correlation with the nuclear spin of our TOP trapped sample; therefore, they will diminish the observed parity-violating beta-asymmetry e¤ect by adding an uncorrelated base-level to the real asymmetry data arising from the TOP trap. Precise analysis of the background must be performed, or the background must be shown to contribute below a certain level, to make a measurement of the positron-spin correlation coe¢cient. Because of this, one needs to understand (or reduce the amount of) background with good precision in order to perform a precise beta-asymmetry measurement.

We categorize the background into three di¤erent components that are marked by their temporal character. The …rst component (B_1) accounts for all initial loss while loading the TOP trap. Detected events from these atoms decay with the normal half-life of ^{82}Rb since the alkali atoms are, in essence, permanently stuck to stainless-steel beta-chamber walls. The second component (B_2) is due to

loss of atoms from the TOP trap (after the initial loading) that results from the …nite trap lifetime. This component initially increases with time as atoms leave the trap and then falls due to lifetime of ^{82}Rb. A third component (B_3) is time independent and comes from the ambient background (predominantly from cosmic rays and natural radioactivity).

B Tests performed to determine background

Three background experiments were preformed in situ with the principle asymmetry data collection and used to determine the background in our beta-asymmetry experiment. In the …rst test (called the pulse-&-drop test), we load the TOP trap and then » 100 ms later, shut o¤ the quadrupole …eld allowing the atoms to fall onto the glass window region of quadrupole coil well (see Fig. 40). Positrons emitted from atoms in this region have neither a direct line-of-sight to the detector or an appreciable solid angle for detection after a single scattering. Therefore, the pulse-&-drop data are representative of the B_1 background due to atoms lost during the loading process. We recorded the resultant background with a detection duration of 250 s, allowing for a little more than three half-lives of ^{82}Rb to pass before the next loading cycle began.

In the second background experiment, we simply loaded and monitored the decay from the TOP trap again using the longer 250 s detection interval. The TOP trap lifetime was reduced by neglecting to prevent the scattering of laser light on the optical table. This creates a shorter TOP trap lifetime because the scattered laser light can enter the beta-chamber and depolarize the atoms to an untrapped state. The reduced TOP trap lifetime used for this test (measured to be $¿ = (1=¿_{TOP} + 1=¿_R)^{i\,1} ¼ 20$ s, where $¿_R = \frac{t_{1=2}(^{82}Rb)}{ln2} = 110$ s) accentuates the

B_2 background. Lastly, ambient background from sources other than untrapped ^{82}Rb was measured without transferring ^{82}Rb into the beta-chamber. The other experimental conditions were kept the same for this test, such as implantation and trapping in MOT I and the turning on and o¤ of the TOP's magnetic coils.

C Background analysis in the beta-asymmetry experiment

Assume that N_0 is the number of atoms that gets transferred into the beta-chamber from MOT I in a single push, and that ´ is the fraction of atoms that is loaded into the TOP. There are two channels of loss from the TOP trap. They are 1. through the …nite TOP trap lifetime ($¿_{TOP}$) loss or 2. via ^{82}Rb positron decay to ^{82}Kr (no longer trapped) with a lifetime $¿_R$. Therefore, the rate at which atoms leave the TOP trap is given by

$$\frac{dN_{TOP}}{dt} = ¡ \left(\frac{1}{¿_{TOP}} + \frac{1}{¿_R} \right) N_{TOP}(t) \tag{110}$$

implying

$$N_{TOP} = ´ N_0 e^{¡ \frac{t(¿_R + ¿_{TOP})}{¿_R ¿_{TOP}}} : \tag{111}$$

We also want to know the number of atoms as a function of time that can contribute to the background components B_1 and B_2 which will be represented by N_1 and N_2, respectively. The $(1 ¡ ´)$ atoms that are initially lost in TOP loading will remain on the walls until they decay with the lifetime of ^{82}Rb. Therefore,

$$N_1 = (1 ¡ ´) N_0 e^{¡ \frac{t}{¿_R}} : \tag{112}$$

To calculate the N_2; remember that the total number of atoms in the beta-chamber is

$$N_{\text{beta i chamber}}(t) = N_{TOP}(t) + N_1(t) + N_2(t) = N_0 e^{-\frac{t}{\tau_R}}. \qquad (113)$$

Since we have already found N_1 and $N_1(t)$, we can simply solve for $N_2(t)$ giving

$$N_2(t) = -N_0 \left[e^{-\frac{t}{\tau_R}} - e^{-\frac{t(\tau_R+\tau_{TOP})}{\tau_R\tau_{TOP}}} \right]. \qquad (114)$$

We can now write down the response of the detector by assuming that each component has its own solid angle for detection. Represent this by Ω_0'; Ω_1'; Ω_2' for the TOP, B_1 and B_2 components, respectively. R_3 represents the time independent ambient background rate

$$R_{\text{plastic}}(t) = \Omega_0' \frac{N_{TOP}(t)}{\tau_R} + \Omega_1' \frac{N_1(t)}{\tau_R} + \Omega_2' \frac{N_2(t)}{\tau_R} + R_3. \qquad (115)$$

By making substitution from Eqs (111), (112), (114), and defining $\Omega_0 = -\Omega_0'$; $\Omega_1 = (1 - -)\Omega_1'$, $\Omega_2 = -\Omega_2'$; the detector response rate can be expressed as

$$R_{\text{plastic}}(t) = \frac{N_0}{\tau_R} \left((\Omega_0 - \Omega_2) e^{-\frac{t(\tau_R+\tau_{TOP})}{\tau_R\tau_{TOP}}} + (\Omega_2 + \Omega_1) e^{-\frac{t}{\tau_R}} \right) + R_3. \qquad (116)$$

This shows that the rate we expect to see from the detector will behave as a double exponential function in time.

We want to compare the 250 s lifetime data to the expected rate in Eq. (116). To increase the statistical accuracy, each pulse in the data set is summed with a starting point 3 s after the TOP trap was loaded. The data shown in Fig. 41 were fit both to a three parameter single exponential and a four parameter double

exponential function. In the double exponential …t, one of the lifetime constants (t_2) was held …xed to the known radioactive lifetime of ^{82}Rb ($¿_R$ = 110 s) and the other (t_1) was allowed to vary. The residuals for these …ts show the data does not …t well to the single exponential, but is approximated nicely by the double exponential function as expected. We can relate the constants in front of the exponential functions in Eq. (116) to the constants determined in the …t function $f(t) = Ae^{i\,t=t_1} + Ce^{i\,t=t_2} + Y_o$; such that

$$A = \frac{N_o}{¿_R}(²_0 \text{ i } ²_2); \tag{117}$$

$$C = \frac{N_o}{¿_R}(²_2 + ²_1): \tag{118}$$

We can express the rate expected for the pulse-&-drop background test by letting both $²_0$ and $²_2$ go to zero in Eq. (116). This is the case because only the B_1 background contribution is now present. We sum the pulses in this data set and the accumulated data are …t with a single exponential function (see Fig. 42)

$$g(t) = ae^{i\,t=t_2} + y_o: \tag{119}$$

Since this data has been taken from an entirely di¤erent set of measurements, we must scale it so it can be compared to the 250 s lifetime data. Since the initial number of atoms transferred into the chamber will vary from shot to shot, we can scale the two data sets by looking at the total number of atoms that were transferred into the beta-chamber MOT for each data set. This is done by summing the initial 3 s of the accumulated pulse. We then have

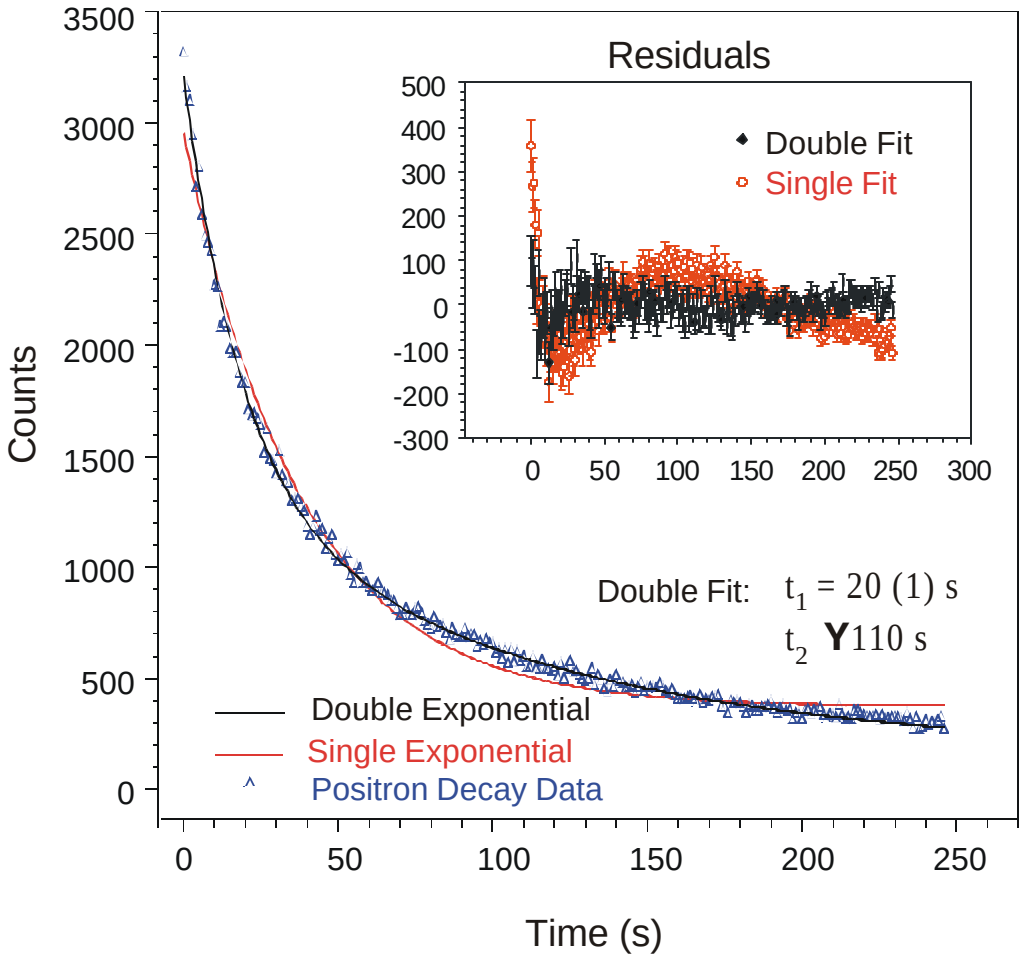

FIG. 41: Accumulated data taken during the 250 s lifetime background test. The data has been …t with both a single- and a double-exponential function. As can be seen from the inset the single exponential does not describe the data nearly as well as the double-exponential function. In the double-exponential …t, one of the lifetime constants (t_2) was held …xed to 110 s, that of ^{82}Rb radioactive decay. The other constant (t_1) was allowed to vary and found to be consistant with the measurement of the TOP trap lifetime (t_1 = 20 (1) s).

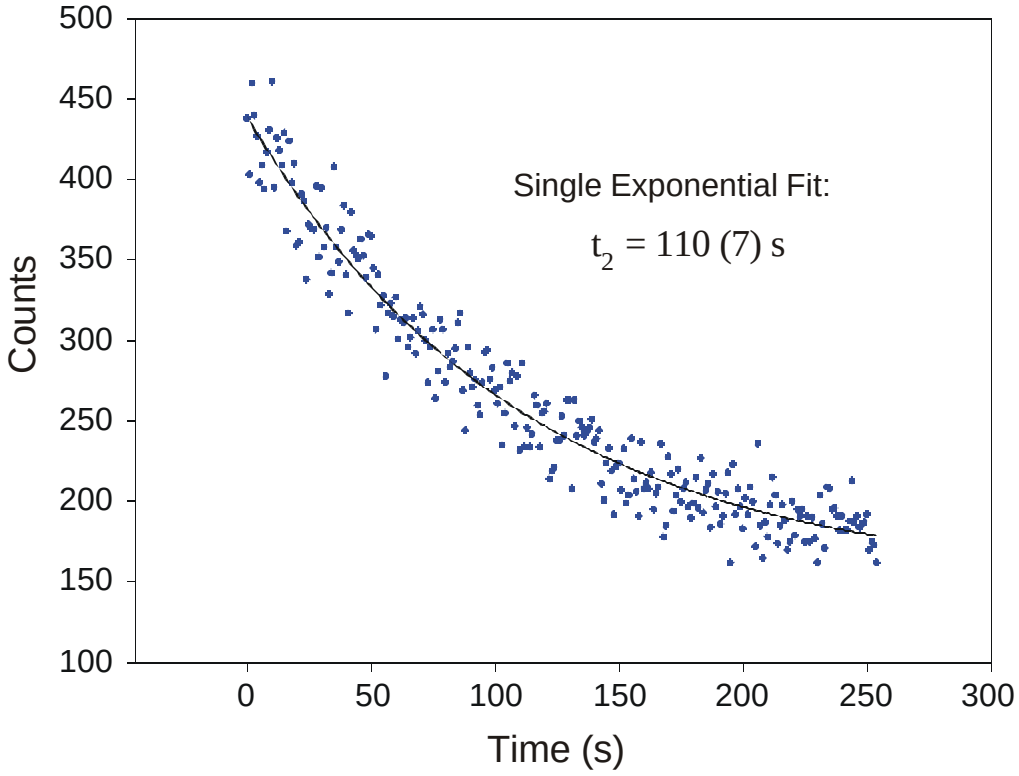

FIG. 42: The accumulation of data taken for the pulse-&-drop background test. This data shows the B_1 background that decays with the radioactive lifetime of ^{82}Rb. The background does not approach zero because ambient background is also present.

$$D = \frac{N_0}{\tau_R}\epsilon_1 = \frac{\sum_{i=1}^{3} R_i \text{ 250 s lifetime}}{\sum_{i=1}^{3} R_i \text{ pulse-\&-drop}}a: \tag{120}$$

We now have enough information to express the ratio for the B_1 and B_2 efficiencies to that of the TOP.

$$\frac{\epsilon_1}{\epsilon_0} = \frac{D}{A + C - D}; \tag{121}$$

$$\frac{\epsilon_2}{\epsilon_0} = \frac{C - D}{A + C - D}: \tag{122}$$

By integrating the rate equation and letting $t >> \tau_R$, we can express the background-to-signal ratio for the ^{82}Rb background components as a function of these efficiency ratios and the TOP and radioactive lifetimes

$$\frac{B_3}{S} = \frac{N_1}{N_{TOP}}(t >> \tau_R) = \frac{\epsilon_1}{\epsilon_0}\frac{\tau_R + \tau_{TOP}}{\tau_{TOP}}; \tag{123}$$

$$\frac{B_2}{S} = \frac{N_2}{N_{TOP}}(t >> \tau_R) = \frac{\epsilon_2}{\epsilon_0}\frac{\tau_R}{\tau_{TOP}}: \tag{124}$$

N_x is the number of events detected for the x-background component.

By integrating over the entire ambient background run and dividing by the total run time, we find the background rate R_3. To get the percentage of this background present during the high-statistics angular correlation data, we use the following relation

$$B_3 = \frac{N_3}{N_{TOP}}(t >> \tau_R) = \frac{R_3\ 4\ t}{N_{total} - N_3}\frac{N_{total} - N_3}{N_{TOP}}: \qquad (125)$$

Here $4t$ is the time elapsed time for the accumulation of the high statistics runs with total number of events N_{total}: The fraction on the right can be expressed in terms of the detection efficiencies, TOP lifetime, and radioactive lifetime

$$\frac{N_{total} - N_3}{N_{TOP}}(t >> \tau_R) = 1 - \frac{\epsilon_2}{\epsilon_0} + \left[\frac{\epsilon_2}{\epsilon_0} + \frac{\epsilon_1}{\epsilon_0}\frac{\tau_R}{\tau_{TOP}} + 1\right]: \qquad (126)$$

The total background-to-signal ratio can then be expressed as the sum of the three components.

$$\frac{B}{S} = \frac{B_1}{S} + \frac{B_2}{S} + \frac{B_3}{S} \qquad (127)$$

The background analysis above was performed using several different positron energy thresholds. The results show that we have a background-to-signal ratio of nearly unity, and are summarized in Fig. 43. Notice that the B_2=S ratio does not change with threshold energy. This indicates that the positron energy spectrum from the B_2 background component and the TOP signal have a similar shape. It is quite plausible the atoms, which are lost after the TOP trap is loaded and contribute to the B_2 background, are emitted from the trap isotropically. In this case the solid angle from atoms being emitted from the trap and landing on the thin-foil window is equal to the solid angle for detecting positrons from the TOP trap. Once these atoms are on the thin-foil window, their decay is detected with »35% probability (estimated from geometry). If detected, the majority of positrons that have arisen from either the TOP trap or the thin-foil window

will directly enter the scintillator without scattering from collimation hardware. Therefore, the positron energy distribution from these sources will look similar. In contrast, if we make the reasonable assumption that most of the B_1 background atoms resides on the quadrupole coil wells, positrons detected from this source must …rst scatter from the collimation hardware before they are detected. The positron energy distribution for the B_1 background will then be shifted toward lower energy. The B_1=S ratio qualitatively re‡ects this behavior.

D Inferred polarization

Eventually, we want to make an independent measurement of the TOP trap average nuclear polarization using atomic physics techniques to enable a true measurement of the positron-spin correlation coe¢cients in ^{82}Rb. Since we did not have the capability to measure the polarization for these experiments, we can use the standard model calculated values for the average ^{82}Rb correlation coe¢cient $< \bar{A} >$ to deduce the polarization of our trapped sample. Having the B=S ratio and the angular correlation amplitude ® (both of which depend on the threshold energy) allows the determination of the polarization as a function of energy threshold

$$P = \frac{(1 + B=S)}{< \bar{A} > G}®: \tag{128}$$

G = :994 is the solid angle factor arising from the collimator.

The results for various threshold values are shown in Fig 44. The polarization does not vary signi…cantly as a function of the threshold energy, which is as expected if the calculation of background as a function of threshold energy is done correctly. There is a small increase in the deduced polarization when increasing the threshold from 400 keV to 800 keV. This comes about because the background

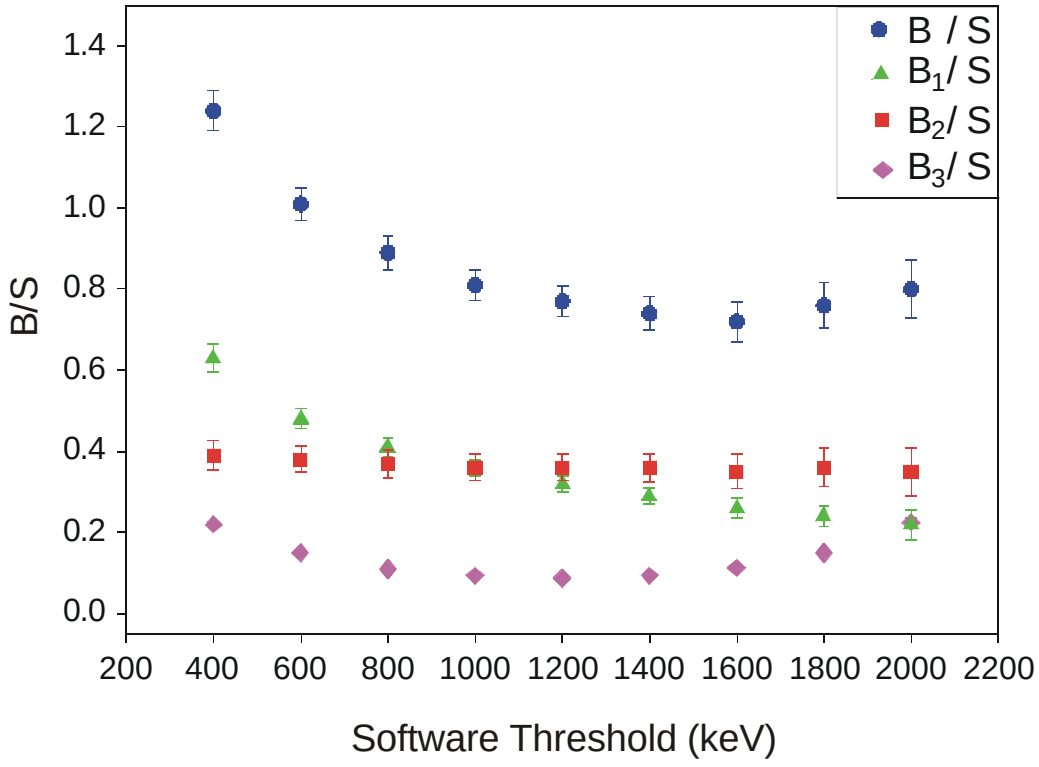

FIG. 43: Determination of the total background-to-signal ratio and also the three background components plotted as a function of threshold energy in the plastic scintillator. A dependence on threshold energy (i.e.,. for B_1 and B_3) suggests that the energy spectrum for these background components is different from that of the true beta signal.

analysis above has not accounted for 776 keV gammas that Compton scatter in the plastic and account for »5% of the trap signal below an 800 keV threshold. The demonstration of » 60% polarization at this stage of the experiment is quite encouraging because it is the …rst time that a weak interaction measurement has been performed using polarized atoms in an atomic trap. This is a signi…cant new development in the production of polarized sample since, up to this point, nuclear polarization has only been demonstrated for cold thin-foil sources and optically pumped vapors and both of these measurement techniques are limited by systematic e¤ects.

The error bars in Fig. 44 are mostly due to the uncertainty associated with the determination of the background-to-signal ratio. It is unlikely that this type of analysis will reach the 1% level of accuracy because of the uncertainties associated with normalization of the di¤erent background tests. This scaling uncertainty was not accounted for in the inferred polarization. The trap lifetime must also be known accurately and this may present a problem because the lifetime is strongly a¤ected by environmental conditions such as the temperature of the chamber and the presence of scattered laser light which can lead to variations of the trap lifetime at the 5-10% level during the course of a run. Given the di¢culties in accurately determining the background, it is best to eliminate it so the e¤ect of background on the signal amplitude is negligibly small.

Further measurements must be done to investigate the discrepancy between the predicted » 96% polarization from the model of the TOP trap. A likely explanation is the molasses cooling step was not su¢cient to bring the cloud to the target temperature of 16 ^{1} K. With a higher temperature, the atoms will spread out more in the nonuniform quadrupole …eld causing lower overall polarization. It is possible that the optical molasses stage has not been fully optimized. The temperature

may be lowered by switching to larger laser detuning during the molasses phase and/or attaining a good balance for the molasses beams.

Another mechanism that would increase the temperature of the TOP sample is a mismatch between the MOT II and TOP cloud positions. This will cause an initial oscillation in the TOP trap that eventually damps out due to collisions between trapped atoms. An initial cloud o¤set of » 1 mm in the vertical direction of the TOP trap has enough potential energy to increase the cloud temperature by »100 ¹K. Another possibility that must be examined is the extent to which the TOP trap contains only the $F = 3=2; m_F = 3=2$ weak-…eld-seeking state. Having a mixture of additional trapped states (i.e., the $F = 1=2; m_F = ¡1=2$ and $F = 3=2; m_F = 1=2$) will reduce the global polarization of the TOP trap cloud since the nuclear spin direction is not necessarily aligned for these states. It is conceivable to produce very high state purity by either adjusting the trap depth so that the unwanted states (which have a 1/3 the magnetic moment of the $m_F = 3=2$ state) will drop out due to gravity or by eliminating the unwanted states using microwave transition.

VII. POSITRON ENERGY DISTRIBUTION

By analyzing the energy of the events detected in the beta-asymmetry measurement, we gather important information about the sources for these events and the processes by which they are detected. Positrons emitted from ^{82}Rb have a characteristic allowed energy distribution. This distribution was masked by background events and e¤ects of the positron detection response function in the beta-asymmetry data. If we can relate the raw energy distribution to the characteristic positron energy shape then we have gained considerable con…dence that we

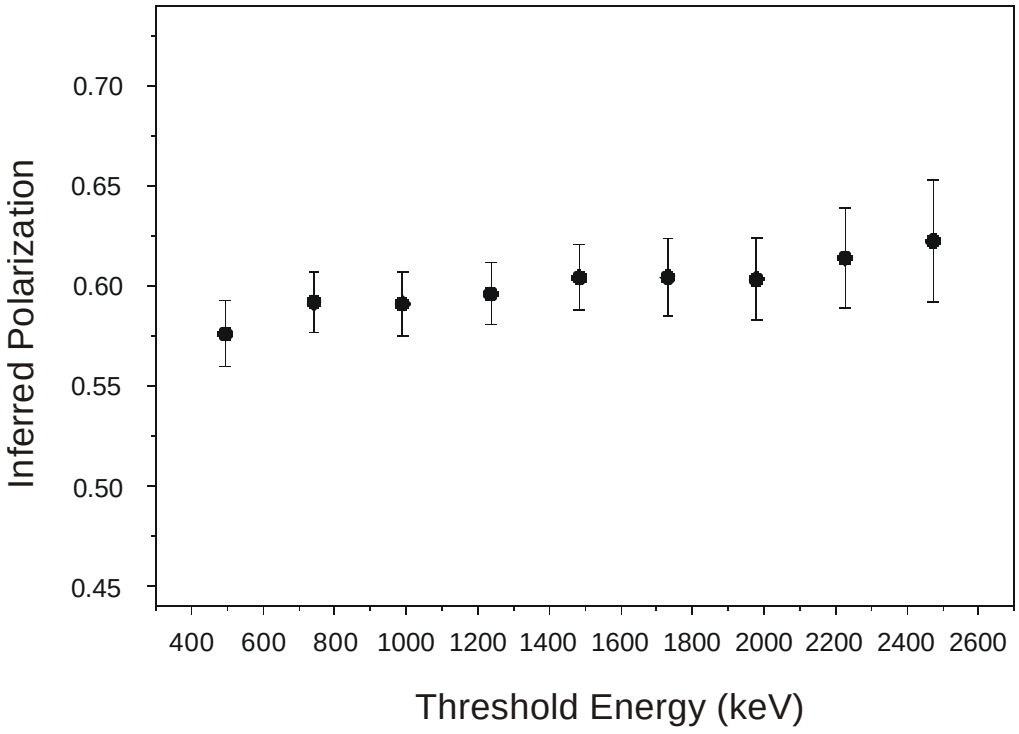

FIG. 44: Polarization inferred from the TOP data using the standard model values for $< \bar{A} >$ and the background analysis. The bulk of the polarization uncertainty shown in the error bars is due to uncertainty in the determination of the background-to-signal ratio.

understand the processes that have caused distortions in the energy distribution. Although this proof-of-principle experiment is not designed to perform a precision measurement of the positron energy distribution, a good measurement of the shape is required to ascertain to what extent instrumental e¤ects will cause a systematic error when extracting the positron-spin correlation from the data.

The …rst order of business is to reduce the raw positron energy shape to one that is representative of events that have been emitted from just the trapped sample (i.e., subtracting the out background events). The high-statistics energy distribution will be the sum of the individual contributions from the trapped signal and from the di¤erent background components. Each component of the total signal will have an energy shape that is characteristic of the particles producing the events and the processes by which they are detected. The total energy spectrum can be written as

$$N(E) = Sf_0(E) + B_1f_1(E) + B_2f_2(E) + B_3f_3(E) \qquad (129)$$

where S is the trap signal B_1, B_2, and B_3 are the background components. Each component is multiplied by an appropriately normalized energy shape factor f_i.

Fig. 45 shows the positron energy distribution for the high-statistics data set, and also the pulse-&-drop and ambient background tests. The high-statistics energy distribution clearly deviates from a theoretically allowed ^{82}Rb shape. Recall from the background analysis that the pulse-&-drop and the ambient background are representative of the B_1 and B_3 contributions to the raw high-statistics spectrum. The shape of the B_1 (trap loading ine¢ciency) background is greatly distorted for an ^{82}Rb positron spectrum and is explained if the positrons …rst scatter from the collimation hardware before being detected. In this case, they lose energy after scattering, which causes a distortion in the shape of the B_1 energy

distribution. Since the pulse-&-drop and the ambient backgrounds were measured independently, we can normalize each distribution to …nd the energy shapes f_1 and f_3. Knowing the background-to-signal ratio B_1=S and B_3=S from the background analysis allows the subtraction of these contributions in the high-statistics spectrum. The results of the subtraction are shown in Fig. 46. Note that the detector energy calibration is only good to »10 % and so the positron kinetic energy in the background subtracted spectrum has been scaled to match the ^{82}Rb endpoint at 3.38 MeV.

This spectrum now contains both the trap signal S as well as the trap loss background B_2. It was not possible to isolate the trap loss background so that a shape for this contribution could be determined. However, we argue that the shapes for the B_2 background and for the trap signal S are nearly the same. If we assume that atoms expelled from the trap are isotropic in distribution, then the lost atoms will have a relatively large solid angle for sticking to the thin window in front of the positron detector, nearly equivalent to the solid angle for positron being detected from the trapped sample. Once on the foil, these atoms have »35% probability of being detected due to their close proximity to the plastic scintillator. Positrons that arise from atoms in the isotropic loss that land in other regions of the chamber can only be detected after scattering from the inside of the collimation hardware and have much less probability of being detected. Therefore, most of the trap loss background will come from atoms that land on the thin window. Furthermore, positrons detected from the beta decay of atoms residing on this window have essentially the same path to enter the detector as those from the trap, which means that B_2 and S should have a very similar energy distribution.

A Monte Carlo calculation has been used to simulate the detector response from positrons originating from the trap region using a realistic geometry for the beta-

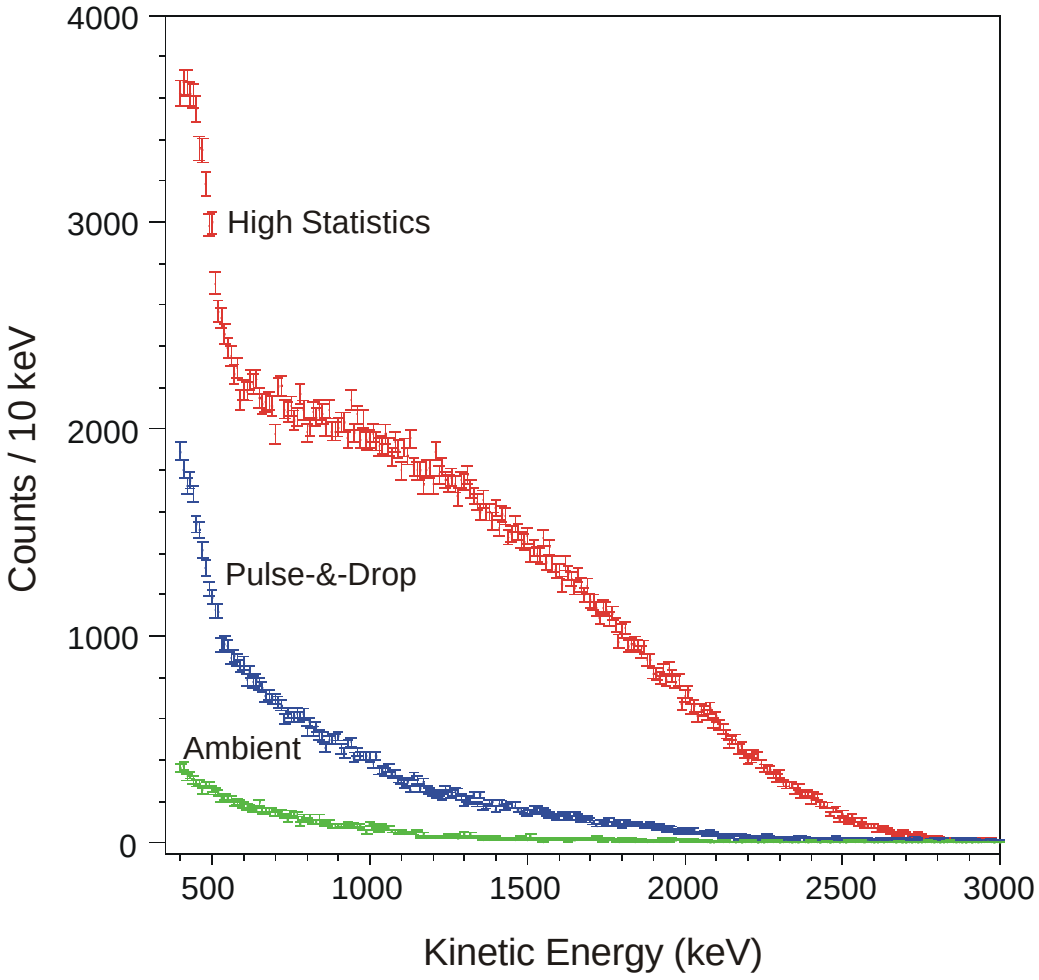

FIG. 45: The positron energy distribution for the high-statistics, pulse-&-drop and ambient background data sets integrated over all polarization directions. The positron energy shape in the high-statistics data is masked by the presence of background and because of Compton scattering of gammas in the plastic scintillator.

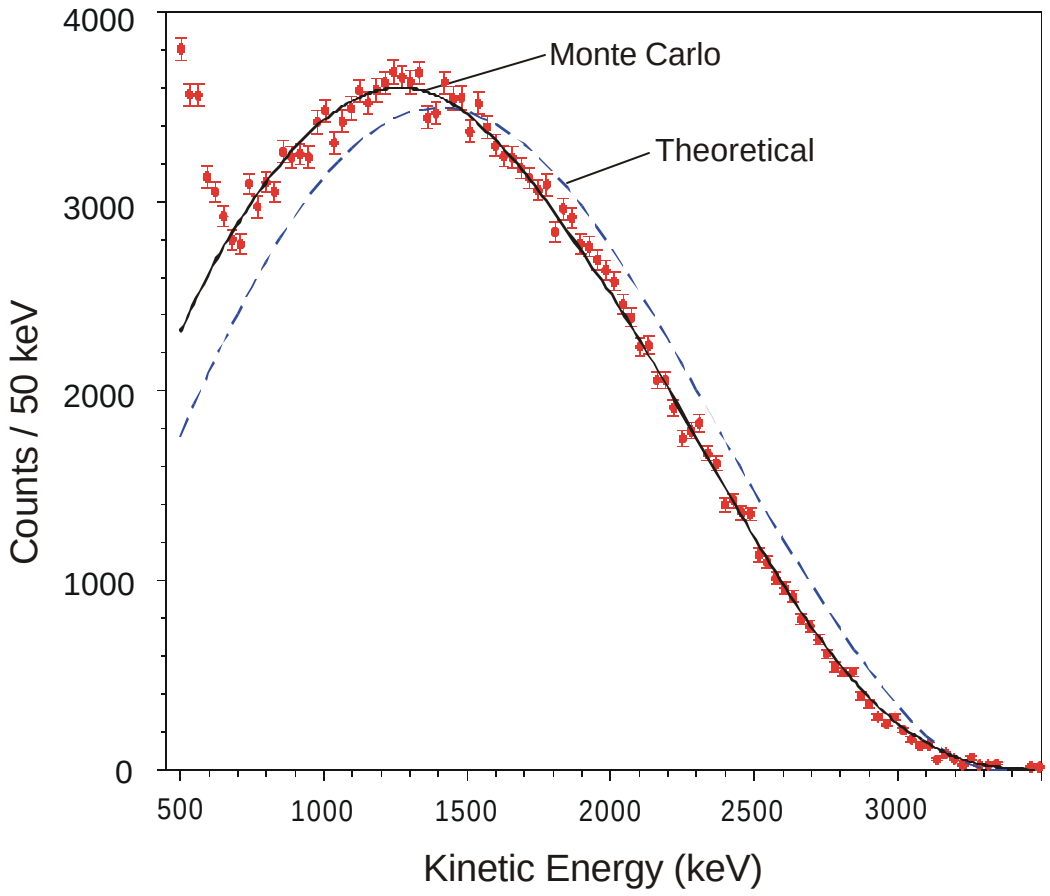

FIG. 46: The positron energy distribution for the high-statistics data set with the normalized pulse-&-drop and ambient background subtracted. The dashed line is the allowed energy shape predicted for ^{82}Rb. The solid line is a Monte Carlo simulation of the experimental positron distribution.

chamber. In addition to positron energy deposition by ionization in the plastic scintillator, there are other physical e¤ects that occur and create problems for measuring the true beta kinetic energy distribution. For example, some portion of positrons can back-scatter and leave the scintillator before depositing their full energy. Another e¤ect is Bremsstrahlung radiation that arises due to the violent deccelerations that occur as the positron scatters through the scintillator. At some point the positron will slow to a stop and annihilate releasing two back-to-back 511 keV gamma rays. It is possible for the positron ionization energy to sum with Compton scattered electrons in the plastic arising from the 511 keV gammas or with the gamma energy deposit in the CsI. Finally, the detector has a …nite energy resolution of » 10 % causing the separate e¤ects to smear in the …nal PMT signal. Fig. 47 shows the Monte Carlo simulation for an 1.5 MeV monoenergetic positron beam impinging upon the plastic scintillator.

To simulate the overall positron energy distribution, the Monte Carlo ^{82}Rb beta shape is constructed from the Monte Carlo-generated monoenergetic distribution. The simulation was tested by using an ^{82}Rb sample prepared on a thin mylar foil and placed in the position where atoms are trapped inside of the beta-chamber. Measurements of the positron decay from this thin foil sample were taken in rough vacuum and in the absence of the TOP magnetic …elds. The observed energy distribution was found to agree well with the Monte Carlo generated shape. This shows that we have a good understanding of the positron optics.

The simulation also generates a good …t to the background subtracted data (see Fig. 46). Since the Monte Carlo only simulates positrons emitted from the trapped sample and the background subtracted data contains both B_2 and S, the …t gives con…dence that B_2 and S have similar energy spectra. It also provides a nice double-check that the background analysis used in the normalization of the

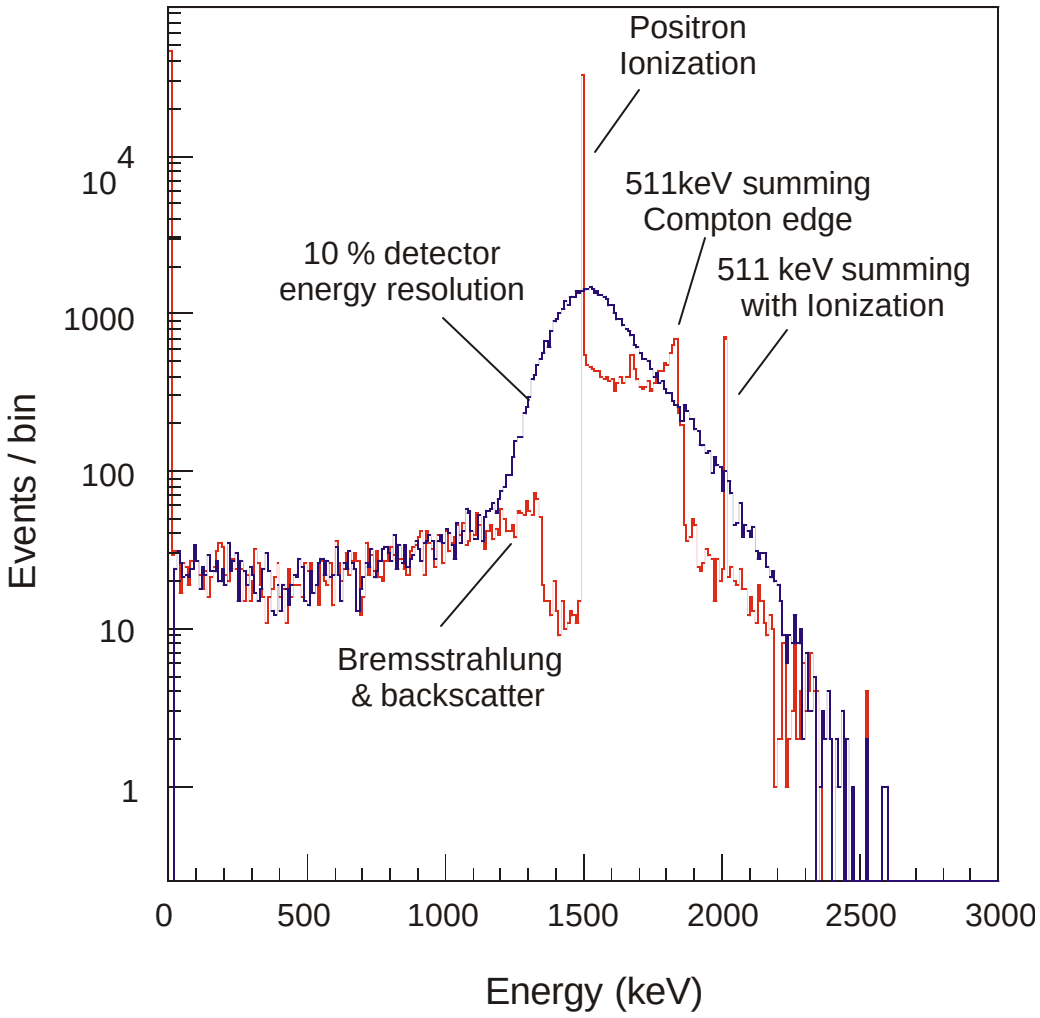

FIG. 47: A Monte Carlo showing the details of the beta detector energy deposition response simulations. The physical processes that arise in the detection of positrons are pointed out in the Monte Carlo generated response to a monoenergetic beam of positrons. The broadening of the features is shown in a simulation using a 10% detector energy resolution.

B_1 and B_3 energy spectra was performed correctly. The sharp deviation of the data from the Monte Carlo at low energies is due to 776 keV gammas emitted from the 2^+ state in the ^{82}Kr daughter that Compton scatter o¤ electrons in the plastic giving rise to a Compton edge at 580 keV. We can exclude the gamma contribution in the angular analysis by setting a low energy threshold above this Compton edge. Such discrimination of gammas is not possible with the lifetime analysis and is one of the bene…ts of understanding the positron energy distribution.

The Monte Carlo shape, to …rst order, is a translation in energy from the theoretically allowed ^{82}Rb shape that has a deviation of nearly 5% at lower energy. Recall that it is the raw data that we have used to study the angular correlation. Supposing that we have an independent measure of the global polarization, we would like to extract the beta asymmetry parameter. To do this we have to measure the energy dependence of the positron distribution which contributes to the asymmetry mostly through the beta velocity term $\bar{}(E) = v=c$ (neglecting one of the ^{82}Rb transitions for now). Positrons that decay from ^{82}Rb are relativistic, and thus $\bar{}(E)$ is a fairly ‡at function of the positron energy. As a result, systematic e¤ects associated with uncertainty in the measured positron kinetic energy contribute in a reduced fashion. Based on the deviation between the background subtracted data and the theoretical energy spectrum, the systematic uncertainty in extracting the positron-spin correlation would be at the 1% level of precision. However, by incorporating the known detector response and instrumental e¤ects modelled with the Monte Carlo simulation when extracting the correlation parameter, we can, in principle, push the related systematic uncertainty below 0:1%.

CHAPTER 4

HYPERFINE STRUCTRURE AND ISOTOPE SHIFT OF ^{82}Rb D_1 AND D_2 TRANSITIONS[3]

ABSTRACT

We report on the hyper…ne structure measurements of the $5P_{1=2}$ and $5P_{3=2}$ states as well as the isotope shift of the D_1 transition of radioactive ^{82}Rb ($t_{1=2}$ = 75 s) atoms trapped in a magneto-optical trap. The systematic e¤ects of light shift (AC Stark shift) and power broadening were explored to verify the accuracy of our trap and probe method against saturation spectroscopy results in ^{85}Rb. The hyper…ne splitting magnetic dipole coe¢cient (A) for the ^{82}Rb $5P_{1=2}$ state and the isotope shift of the D_1 transition ($\pm^{o82\,i\,85}$) were measured for the …rst time to be 122:7 (1:0) MHz and ¡150:8 (2:0) MHz respectively. The hyper…ne splitting for the ^{82}Rb $5P_{3=2}$ state was determined to be 90:3 (1:5) MHz, in agreement with the previous measurement of 89:3 (9:0) MHz [58]. These measurements provide key information that is needed to manipulate and determine the polarization of trapped ^{82}Rb atoms for a parity violating beta-asymmetry measurement.

[3]Coauthored by X. Zhao, S.G. Crane, R. Guckert, D.J. Vieira, Phys. Rev. A. 60, 4730 (1999).

I. INTRODUCTION

Since the demonstration of magneto-optical trapping [46] of neutral atoms, there has been a growing interest in exploiting this technology in atomic and nuclear physics. Trapped $^-$-decaying species will enable a new set of high-precision measurements that will further elucidate the helicity structure of the electroweak interaction and aid in the search of physics beyond the standard model. In many ways, trapped radioactive atoms make an ideal source for $^-$-decay correlation measurements since relatively intense sources can be harnessed that are e¤ectively massless, point-like, and nearly 100% spin-polarized. Consequently, systematic e¤ects associated with electron scattering and polarization uncertainty can be greatly reduced if not eliminated altogether. With the recent success in trapping large numbers (»6 million) of radioactive ^{82}Rb ($t_{1=2}$ = 75 s) atoms [84, 71], a new set of fundamental symmetry $^-$-decay correlation experiments with ^{82}Rb are now possible.

To undertake these precise electroweak-interaction measurements, information on the atomic structure of ^{82}Rb is needed. In particular, we intend to polarize ^{82}Rb atoms by optically pumping them into the $5S_{1=2}; F = 3=2; m_F = 3=2$ weak …eld seeking state and then con…ning them to a time-averaged orbiting potential magnetic trap which will serve as a rotating beacon of spin-polarized nuclei. Since either the D_1 or D_2 transition could be used in the optical pumping or m-state population measurement of polarization, detailed knowledge of these transitions is required. Up to this time, only the D_2 line hyper…ne structure and isotope shift for ^{82}Rb have been reported [58].

In this article we present a …rst-time measurement of the hyper…ne structure in the $5P_{1=2}$ state and the isotope shift of the D_1 transition, as well as an improved measurement of the hyper…ne splitting of the $5P_{3=2}$ state in radioactive ^{82}Rb atoms

con…ned to a magneto-optical trap (MOT). Since atoms in a MOT are intrinsically perturbed by the trapping light and magnetic …eld, systematics, such as the light shift and Zeeman shift, have been minimized and/or corrected to give accurate results.

II. EXPERIMENT

The experiment was performed using ^{82}Rb atoms con…ned in a magneto-optical trap. The system setup and method for trapping ^{82}Rb has been reported earlier [84, 71]. Brie‡y, a chemically concentrated and puri…ed sample is placed in an ion source of a mass separator. Rb is selectively ionized, electrostatically extracted at 20 kV, passed through a mass separator where a single mass line is selected, refocused with an electrostatic quadrapole triplet, and implanted into a small catcher foil located inside a trapping cell. The catcher foil is inductively heated to release the implanted Rb species as neutral atoms into a dry…lm-coated quartz cell where they are trapped by a MOT. The MOT is formed by three retro-re‡ected, circularly polarized laser beams (50 mm $1=e^2$ width) which enter the 75 mm cubic cell through each surface. A set of anti-Helmholtz coils generates the quadrupole …eld gradient of 7 G/cm in the axial direction. A Ti:Sapphire laser tuned to the D_2 line of Rb at 780 nm forms the trapping beams. The relevant ^{82}Rb energy levels and atomic transitions are shown in Fig. 48. The laser frequency is locked 15 MHz below the $5S_{1=2}; F = 3 \; ! \; 5P_{3=2}; F^{0} = 4$ trapping transition in ^{85}Rb using a frequency modulated (FM) sideband technique [60]. A double-pass acoustic optical modulator (AOM) driven at 268 MHz provides the 536 MHz frequency shift needed to excite the $5S_{1=2}; F = 3=2 \; ! \; 5P_{3=2}; F^{0} = 5=2$ trapping transition in ^{82}Rb. In order to repump atoms that fall into the $5S_{1=2}; F = 1=2$ ground state, sidebands are

added to the trapping beam by using an electro-optical modulator (EOM) tuned to 1:470 GHz, which excites the $5S_{1=2}; F = 1=2 \; ! \; 5P_{3=2}; F^{0} = 3=2$ transition. A probe beam is retro-re‡ected and overlapped with the trapped atoms. The ‡uorescence signal from the trapped atoms is modulated by the modulating probe beam and imaged onto a photomultiplier. The trapping signal is then demodulated using a lock-in ampli…er to reject the laser scattered background.

A major change of the experimental setup from Ref. [84, 71] is the addition of a Ti:Sapphire probe laser. This probe laser is locked to the ^{85}Rb saturation lines using the same FM sideband technique mentioned above. The power of the probe beam is kept low ($< 100 \; ^{1}W/cm^2$) to avoid any probe beam light shift as well as probe and trapping light multiphoton e¤ects. In the weak probe light limit, it is well known that a strong pump …eld (trapping light …eld) gives rise to a AC Stark splitting, also known as Autler-Townes splitting, when probing via a third level [85, 86]. For a large detuned …eld, one of the dynamic Stark (single photon) components will only be slightly shifted from the two-level transition frequency, while the other (two photon) resonance will have a negligible intensity. Under this condition, the e¤ect of the pump …eld is to produce a quadratic AC ($/ E^2$) Stark shift and can be understood with second order perturbation theory. We minimized this shift by measuring the light shift at di¤erent laser trapping intensities and then extrapolating the light intensity to zero. The net e¤ect of a small DC magnetic …eld in a MOT is to broaden the D_1 and D_2 lines due to the symmetric splitting of these levels into magnetic substates which could not be resolved in these measurements. To minimize this broadening e¤ect, judicious care was taken to balance the trap so that the center of the trap cloud coincides with the center of the quadrupole …eld where the magnetic …eld is zero. This was essential in obtaining a reproducible light shift.

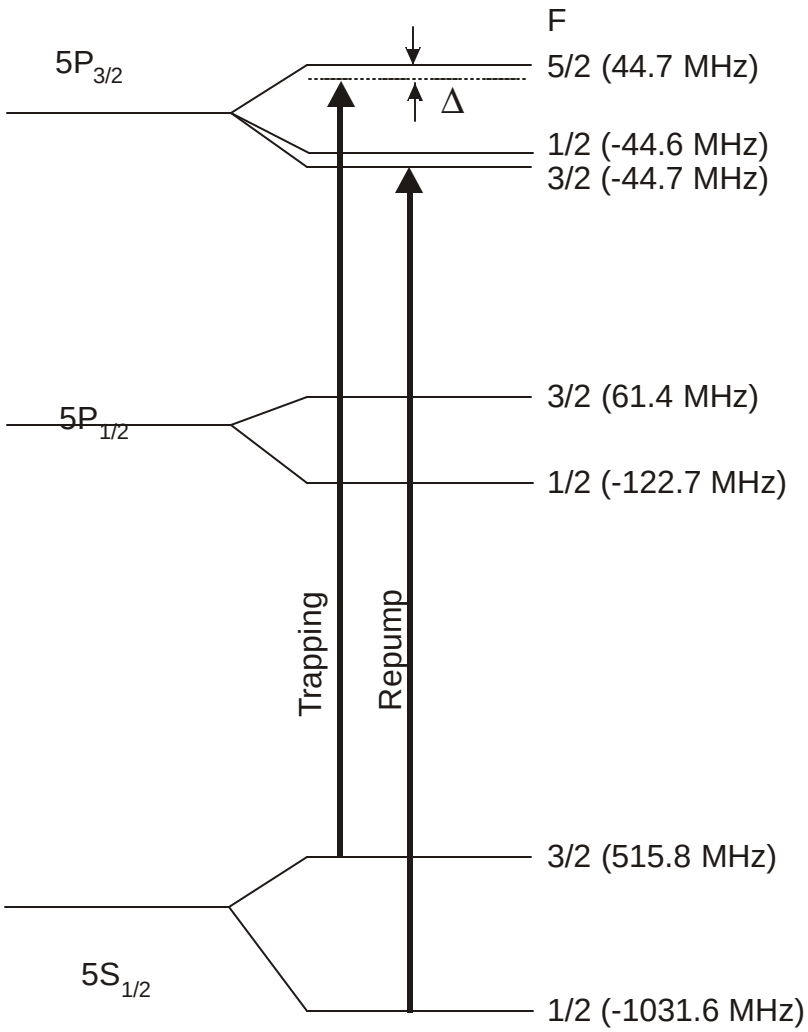

^{82}Rb ($I = 1$, $t_{1/2}$ = 75 s)

FIG. 48: The lowest three energy levels of ^{82}Rb (not to scale). The hyper…ne splittings given in parantheses are results reported herein and those of Ref. [58]. The trapping (detuned by ¢) and repump transitions used to trap atoms in the magneto-optical trap are also shown.

III. RESULTS AND DISCUSSION

A Frequency references

Saturated absorption spectroscopy using Rb vapor cells provides our frequency reference. Here intensities of the probe and pump beams of the saturation absorption are kept low (< 1 mW/cm^2) to avoid any light shift. The accuracy of the frequency locking method was checked (see Fig. 49) with the well-known hyper…ne structure of ^{85}Rb [87] and a repeatable accuracy of 0.5 MHz was achieved when care was taken to adjust the zero o¤set of the di¤erential error signal.

B D_1 transition

For the D_1 line ($5S_{1=2}$! $5P_{1=2}$) measurement, the probe beam is derived from the probe laser and its frequency is shifted with a wide-band EOM. The probe beam frequency is modulated in and out of resonance with the ^{82}Rb D_1 transition to produce a modulation on the ‡uorescence signal of the trapped atoms. Because the probe beam has a de-pumping e¤ect on the trapped atoms, the repump intensity of the trap is kept to a minimum in order to maximize this e¤ect. We …rst tested the accuracy of our method on the ^{85}Rb D_1 line. For this measurement, the probe laser is locked to the cross-over line of $F = 3$! $F^0 = 3;2$ D_1 transitions. An additional AOM is used to shift the probe beam locking point by 31 MHz, so we can distinguish between the upper EOM sideband resonance with the $F = 3$! $F^0 = 3$ transition and the lower EOM sideband resonance with $F = 3$! $F^0 = 2$. These two resonance frequencies were measured at di¤erent trapping laser power and the results are plotted in Fig. 50(a) where the 31 MHz AOM shift has already been taken into account. The slope of the line yields a light shift averaged over all the

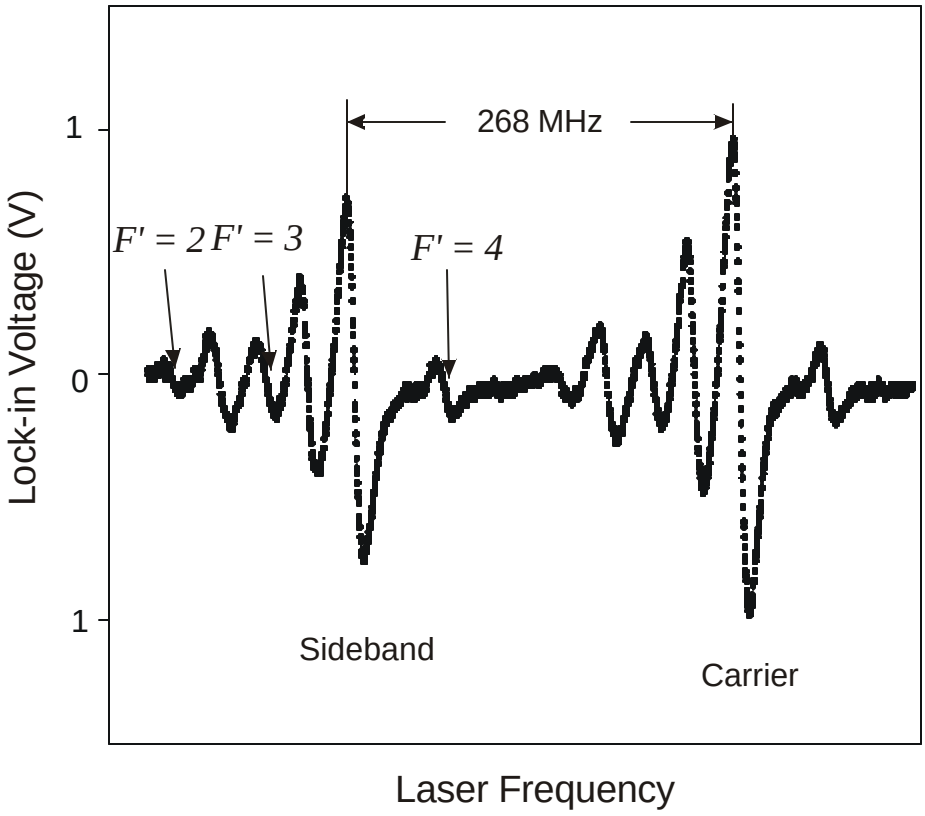

FIG. 49: Laser frequency scan through the FM saturation absorption signal of the ^{85}Rb D_2 line $F = 3 \rightarrow F' = 2; 3; 4$ transitions and their associated cross-over peaks using a rubidium vapor cell. The two sets of identical peaks were generated by the carrier and sideband of an AOM modulator operating at a frequency of 268 MHz.

Zeeman lines of » 0:1 MHz/(mW/cm^2). A linear …t is used to extrapolate the light shift to zero trapping laser power and yields a ^{85}Rb D_1 transition hyper…ne splitting of 362:7 (1:5) MHz. The 1:5 MHz error bar, which is typical for our measurements, results from the quadratic sum of statistical uncertainty associated with the extrapolation error of the …t (1 MHz), systematic errors associated with Zeeman shift (1 MHz), and the relative frequency uncertainty of the probe laser (0:5 MHz). Our measured splitting agrees well with previous saturation spectroscopy measurements of 361:5 (0:5) MHz [87].

For the ^{82}Rb D_1 line measurement, we locked the probe laser to the ^{85}Rb $F = 3 \rightarrow F' = 3$ D_1 transition and the EOM upper sideband was swept through the $F = 3=2 \rightarrow F' = 1=2$ and $F = 3=2 \rightarrow F' = 3=2$ D_1 transitions of the trapped ^{82}Rb atoms. The data taken with approximately 10^5 trapped radioactive atoms are plotted in Fig. 50(b). From the data, we derive a hyper…ne splitting for ^{82}Rb $5P_{1=2}$ state of 184:0 (1:5) MHz. The resulting A coe¢cient is 122:7 (1:0) MHz and the isotope shift for the D_1 transition is determined to be $\pm^{o82\,i\,85} = ¡150{:}8$ (2:0) MHz. To derive the latter, we used the ground state hyper…ne splitting of ^{82}Rb from Ref. [58] and the ^{85}Rb ground state data from Ref. [88]. The D_2 line isotope shift was measured previously to be ¡153:6 (4:4) MHz [58]. These isotope shifts indicate that their J dependence (a relativistic e¤ect) is very small.

C D_2 transition

For the D_2 line ($5S_{1=2} \rightarrow 5P_{3=2}$) measurement, the probe beam is derived directly from the trapping laser and its frequency shifted using two AOMs. This probe beam is chopped on and o¤ to modulate the trap ‡uorescence signal. With the exception of the trapping transition (e.g., $F = 3 \rightarrow F' = 4$), the probe beam has a

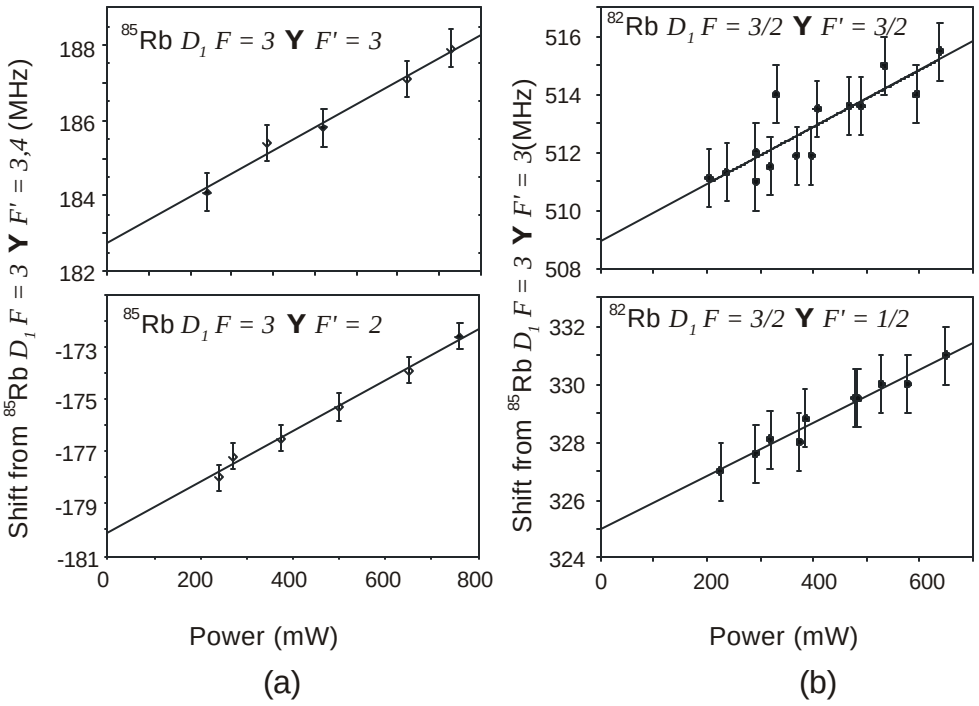

FIG. 50: The D_1 ($5S_{1=2}$! $5P_{1=2}$) transition light shifts for (a) the ^{85}Rb F = 3 ! F^0 = 3 and F = 3 ! F^0 = 2 transitions and (b) the ^{82}Rb F = 3=2 ! F^0 = 3=2 and F = 3=2 ! F^0 = 1=2 transitions as a function of trapping laser power.

depumping e¤ect on the trapped atoms. To maximize this depump modulation, the repump intensity of the trap is kept to a minimum as before. When probing the trapping transition itself, the probe beam is kept particularly weak (» 20 $^{1}W/cm^{2}$) to avoid pushing the atoms out of the zero magnetic …eld region of the trap (the Zeeman shift is » 0:5 MHz/mm in the radial direction). Again, we tested the method on ^{85}Rb $F = 3 \rightarrow F' = 4$ and $F = 3 \rightarrow F' = 3$ D_2 transitions and compared our results with existing saturation spectroscopy results [87]. The data are plotted in Fig. 51(a). From the data, we derive the hyper…ne splitting of the $5P_{3=2}; F' = 4$ and $F' = 3$ transitions to be 121:1 (1:5) MHz, in good agreement with the saturation spectroscopy results of 121:6 (0:5) MHz [87].

The data for the ^{82}Rb D_2 line are plotted in Fig. 51(b). Because, we cannot resolve the $F = 3=2 \rightarrow F' = 3=2$ and $F = 3=2 \rightarrow F' = 1=2$ transitions (the splitting between these two hyper…ne levels was measured previously to be 0.1 MHz [58]), only an average position for these two states could be determined. The $5P_{3=2}; F' = 5=2$ and $F' = 3=2; 1=2$ average hyper…ne splitting was measured to be 90:3 (1:5) MHz, in good agreement with previous measurement of 89:3 (9:0) MHz [58].

D Line broadening

We have also analyzed the line broadening versus trapping laser power used to trap $^{82;85}$Rb atoms. A typical line shape at relatively low trapping laser power is shown in Fig. 5(a) and the linewidth (FWHM) dependence on trapping laser power is shown in Fig. 5(b). There are three e¤ects that contribute to the line broadening in a MOT. One is the radiative broadening of each Zeeman line and the other two e¤ects arise from the fact that each Zeeman line is shifted di¤erently

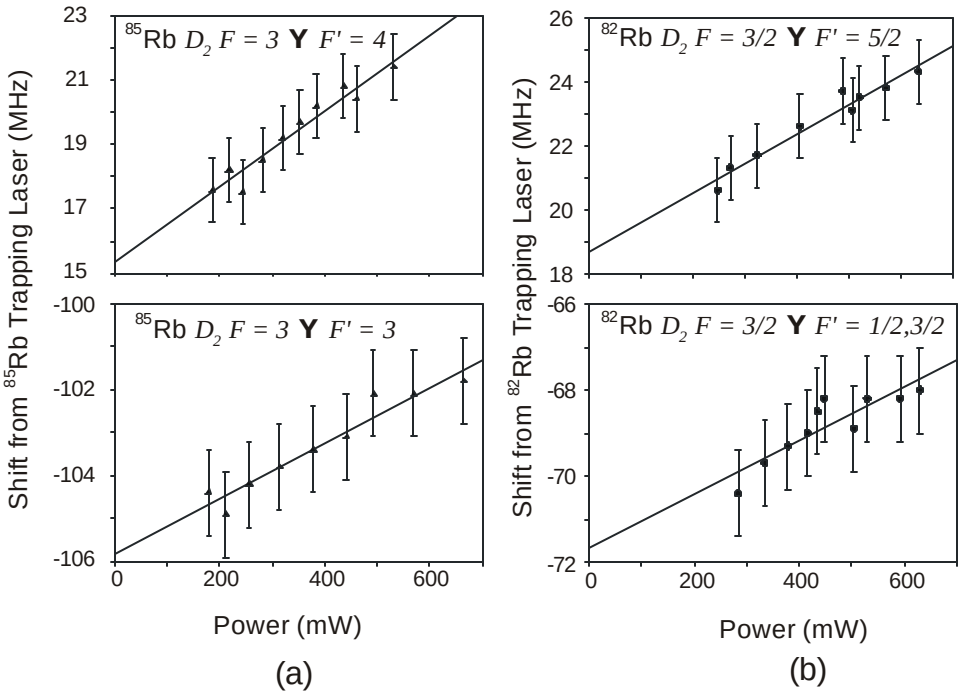

FIG. 51: The $5S_{1=2}$! $5P_{3=2}$ D_2 transition light shifts for (a) the ^{85}Rb F = 3 ! F^0 = 4 and F = 3 ! F^0 = 3 transitions and (b) the ^{82}Rb F = 3=2 ! F^0 = 5=2 and F = 3=2 ! F^0 = 3=2; 1=2 transitions as a function of trapping laser power. The frequency shifts are relative to the …xed frequency of the trapping laser beams used for ^{85}Rb and ^{82}Rb, respectively.

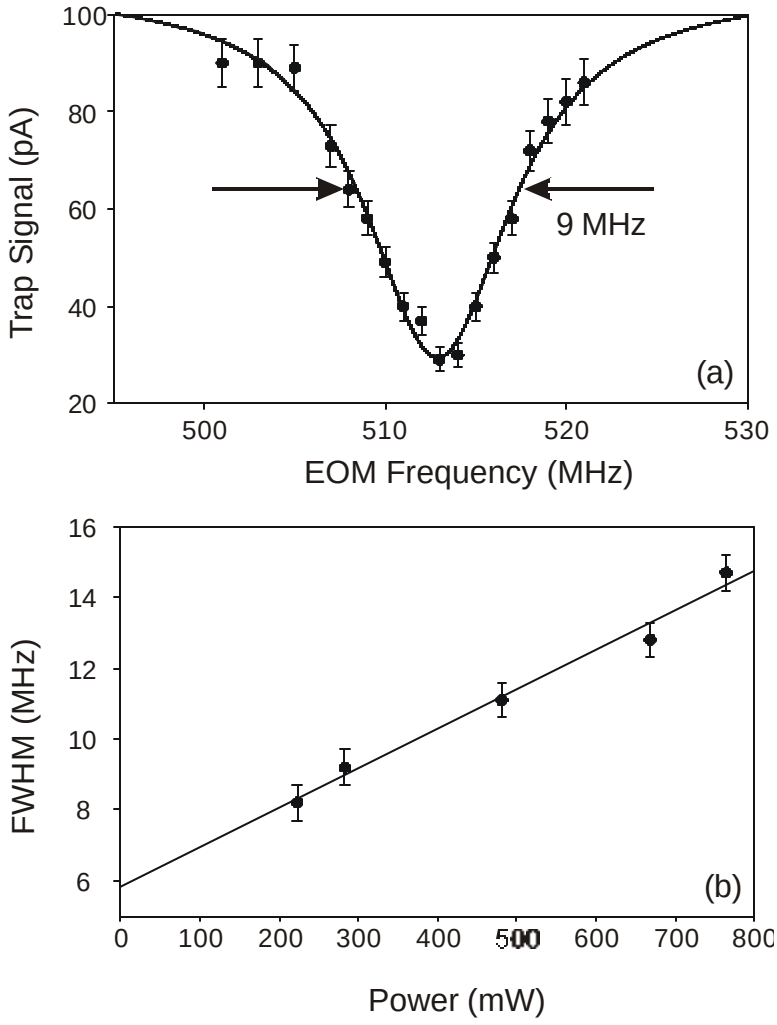

FIG. 52: Line broadening for the D_1 transition. (a) Line shape measurement of the ^{82}Rb D_1 F = 3=2 ! F^0 = 3=2 transition (with 300 mW trapping laser power); the solid line is a Lorentzian …t. (b) ^{85}Rb D_1 F = 3 ! F^0 = 3 transition line width as a function of trapping laser power.

by the light and magnetic …eld [85, 86, 89]. Because atoms in a MOT are cold (» 100 ¹1 K), the Doppler broadened contribution is negligible (» 0:1 MHz). At low trapping light intensity, the radiative broadening is linear with trapping light intensity, while at higher trapping intensity the light splitting of Zeeman lines dominates. The latter splitting is also linear with the trapping light intensity. These e¤ects have been carefully studied [85, 86]. The fact that the extrapolated linewidth at zero trapping laser power yields a D_1 transition linewidth of 5:8 (0:8) MHz, in good agreement with the D_1 natural linewidth of 5:4 (0:1) MHz [90], con…rms that the trapped atoms are situated at the center (within 1 mm) of the quadrupole magnetic …eld where the broadening from Zeeman splitting is small.

IV. SUMMARY

In summary, we have measured the $5P_{1=2}$ hyper…ne structure and isotope shift of ^{82}Rb($t_{1=2}$ = 75 s) in a magneto-optical trap. The magneto-optical trapping and probe beam method can provide useful spectroscopic information for a small number of trapped atoms where conventional saturation spectroscopy would be very di¢cult to carry out. We have determined for the …rst time the $5P_{1=2}$ magnetic dipole coe¢cient to be A = 122:7 (1:0) MHz and D_1 transition isotope shift of $\pm^{o82\,i\,85}$ = ¡ 150:8(2:0) MHz. We also measured more precisely the $5P_{3=2}$ hyper…ne splitting to be 90:3 (1:5) MHz in agreement with the previous measurement of 89:3 (9:0) MHz [58]. These results not only enhance our understanding of ^{82}Rb atomic structure, but also provide useful spectroscopic information that is needed to optically pump and measure the degree of ^{82}Rb polarization in a pure magnetic trap where a high-precision $^{-}$-asymmetry experiment is planned.

CHAPTER 5

TRAPPING AN ISOTOPIC MIXTURE OF FERMIONIC ^{84}Rb AND BOSONIC ^{87}Rb ATOMS[4]

ABSTRACT

We have simultaneously con…ned fermionic ^{84}Rb and bosonic ^{87}Rb atoms in overlapping magneto-optical traps. This is the …rst time that radioactive ^{84}Rb atoms ($t_{1=2}$ = 33 d) have been trapped. We investigated ^{84}Rb trap loss when overlapped with a cloud of ^{87}Rb atoms trapped from a background rubidium vapor. Collision loss measurements were taken with » 5 £ 10^5 and » 4 £ 10^7 atoms of trapped ^{84}Rb and ^{87}Rb, respectively. We have found a trapping solution for which there is negligible additional trap loss for ^{84}Rb due to the presence of ^{87}Rb, showing that the mixture can be readily prepared for a sympathetic cooling experiment.

[4]Coauthored by S.G. Crane, X. Zhao, W. Taylor, D.J. Vieira, Phys. Rev. A. 62, 011402(R) (2000).

The creation of very cold atomic vapor systems is an exciting new arena in which one can study macroscopic e¤ects of quantum mechanics. A great deal of success has been achieved in cooling large numbers of bosonic atoms, which have been shown to collapse into a single motional ground state, known as a Bose-Einstein condensate (BEC)[91]. This work has spawned interest in cooling dilute Fermi systems to a quantum degenerate regime as well. Interesting properties such as linewidth narrowing and the suppression of inelastic collisions [92] have been predicted at phase space densities comparable to those achieved in BEC experiments. A BCS-type phase transition to a super‡uid state may also be observed at still lower temperatures depending on the coupling strength between the cold atoms [93].

For fermionic atoms in identical spin states, s-wave collisions are forbidden and p-wave collisions vanish at low temperatures, which brings evaporative cooling to a halt [94]. One method of avoiding this limitation, sympathetic cooling using two di¤erent spin states, has already shown promising results in ^{40}K [95]. However, there are only two naturally occurring fermionic alkali atoms, ^{6}Li and ^{40}K, which severely limits the number of systems that can be studied. An intriguing alternative is the possibility of trapping radioactive fermionic atoms and cooling them sympathetically with a system of cold, stable bosonic atoms. Recent calculations [96] show that ^{84}Rb ($t_{1=2}$ = 33 d) is a good fermionic candidate because of its large and positive scattering length with ^{87}Rb (a_S = 117 a.u. and a_T = 550 a.u.), which should allow for e¢cient sympathetic cooling [97]. A relatively low-…eld (B ' 100 G) Feshbach resonance is also predicted for the ^{84}Rb ($5S_{1=2}; F = 5=2; m_F = 5=2$) and ($5S_{1=2}; F = 5=2; m_F = 3=2$) states [96]. This may provide a means to control the interaction between cold ^{84}Rb atoms, e¤ectively tuning the BCS phase transition temperature. Thus ^{84}Rb/^{87}Rb o¤ers an interesting system where a mixture of

fermionic/bosonic quantum degeneracy may be realized. In this paper, we report on the …rst loading of a magneto-optical trap (MOT) with radioactive ^{84}Rb atoms and on the simultaneous trapping of ^{84}Rb and ^{87}Rb as an initial step toward a symapathetic cooling experiment. Trap loss of ^{84}Rb is also investigated with and without an overlapped cloud of ^{87}Rb.

The method used to trap radioactive ^{84}Rb atoms is similar to that reported earlier for ^{82}Rb [71]. ^{84}Rb atoms are produced in 750-MeV proton spallation reactions on a molybdenum target at the Los Alamos Neutron Scattering Center. After irradiation, the target is transferred to a hotcell facility where it is dissolved in hydrogen peroxide and the rubidium fraction is chemically extracted and precipitated as Rb_2CO_3. A radioactive sample containing 650 ¹Ci of ^{84}Rb was loaded into a tantalum crucible and installed in the ion source of a mass separator. The radioactive sample also contained 8 mCi of ^{83}Rb ($t_{1=2}$ = 86 d), which was also trapped for the …rst time, but not discussed further here [98]. We monitor the amount of ^{84}Rb activity in the ion source using a collimated NaI counter to detect the number of 886 keV °-rays associated with electron capture of ^{84}Rb. The ion source was run at settings which provided a moderate vaporization rate while maintaining a reasonably high degree of ionization for rubidium by controlling the temperature (typically » 950 ±C) at the tip of the crucible via electron bombardment heating. In this way, an ion beam was obtained with an intensity of » 2£10^8 $^{84}Rb^+$ ions/s that lasted for several weeks. The extracted beam is mass separated, collimated, and focused through a 5 mm Á opening into a dry…lm-coated trapping cell (a 7:6 cm quartz cube), and implanted into an yttrium catcher foil located at the far corner of the cell. After a suitable accumulation period (10-60 min), the catcher foil is inductively heated (» 750 ±C) to release the implanted activity into the quartz cell as an atomic vapor where the ^{84}Rb atoms are trapped. Due to the

slow decay rate of ^{84}Rb, it was not possible to determine a release e¢ciency from the catcher foil by using °-counting; however, based on our earlier measurements with ^{82}Rb [71] we assume that our release e¢ciency is on the order of 20%.

The atomic energy levels relevant to the trapping of ^{84}Rb [58] are shown in Fig. 53(a). The ^{84}Rb magneto-optical trap (MOT) uses large-diameter (50 mm Á, 100 mm $1=e^2$ width), high-intensity (8 mW/cm^2 per beam) laser beams to increase the trapping e¢ciency. Three beams are derived from a Coherent 899-21 ring laser and used in the standard retro-re‡ected con…guration with an axial …eld gradient of 7 G/cm to form the MOT. We use a feature in the ^{85}Rb frequency modulated saturated absorption spectrum (see Fig. 53(b)) which is 89 MHz to the red of the ^{85}Rb $5S_{1=2}; F = 2 \; ! \; 5P_{3=2}; F^{0} = 3$ transition as the locking reference point for the ^{84}Rb trapping beam. We shift the frequency of the trapping beam from this locking point using a combination of acousto-optic modulators (AOMs) on the laser reference arm to give an overall shift of $o^{84}_{trap} ¡ o^{85}_{locking\ point} = ¡557$ MHz. This gives a detuning from the $5S_{1=2}; F = 5=2 \; ! \; 5P_{3=2}; F^{0} = 3=2$ cycling transition of $¢ ' ¡15$ MHz. An electro-optic modulator (EOM) is placed in the main beam and driven at 1:480 GHz so that its second lower sideband will generate the repumping transition in ^{84}Rb ($o^{84}_{repump} ¡ o^{84}_{trap} = ¡2{:}960$ GHz). The system has the bene…cial feature of being able to trap ^{85}Rb (introduced via a getter source) by locking the laser 15 MHz to the red of the ^{85}Rb trapping transition and adjusting the repump EOM drive frequency to 1:464 GHz. This allows optimization of the ^{84}Rb MOT setup (referred to hereafter as MOT I) with ^{85}Rb before we begin experiments with radioactive species.

The trapping light for the ^{87}Rb MOT setup (referred to as MOT II) is generated from a second Coherent 899-21 ring laser locked with a detuning of $¢ ' ¡8$ MHz from the ^{87}Rb $5S_{1=2}; F = 2 \; ! \; 5P_{3=2}; F^{0} = 3$ trapping transition. MOT II has

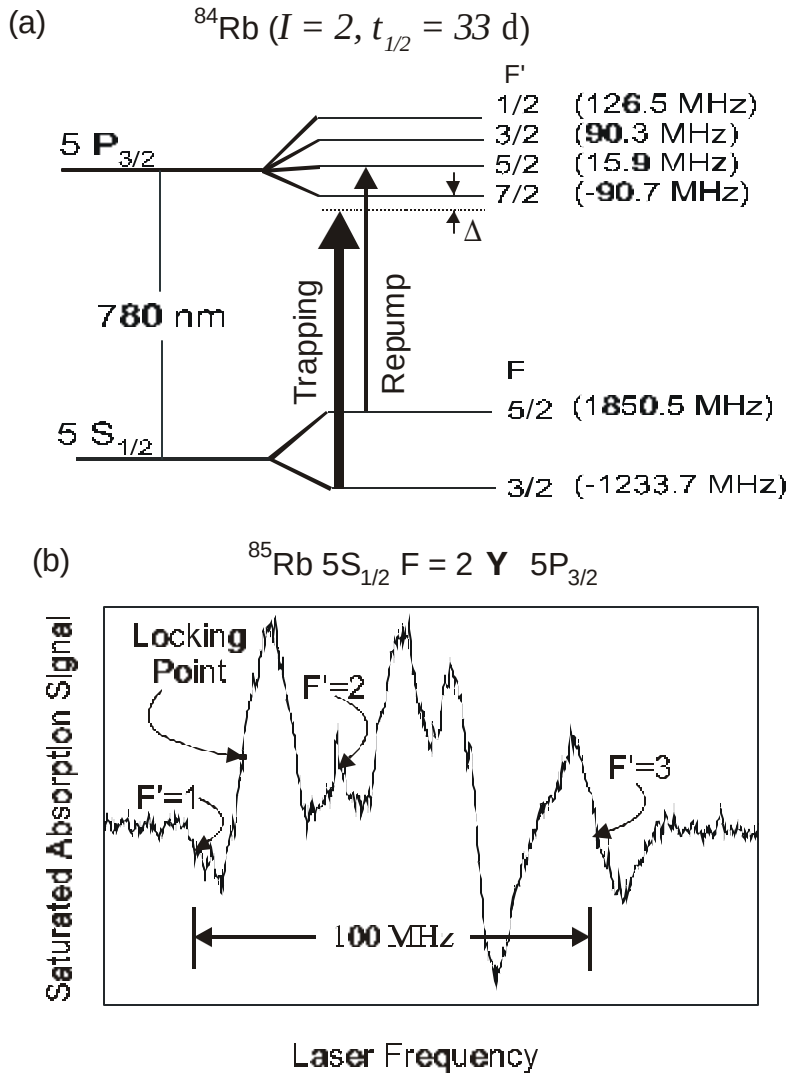

FIG. 53: (a) The ^{84}Rb atomic energy levels (not to scale) relevant for atomic trapping as taken from Ref. [58]. The trapping and repump transitions are shown, where the trapping transition is detuned by the quantity ¢. (b) The Rb reference cell frequency-modulated saturated absorption signal of the ^{85}Rb D_2 line $F = 2 \rightarrow F' = 1;2;3$ transitions. The locking point (shown as a solid circle) is used as a reference for the ^{84}Rb trapping laser. The locking point is measured to be 89 MHz to the red of the ^{85}Rb $F = 2 \rightarrow F' = 3$ transition.

a combined six beam intensity of 12 mW/cm^2: A second EOM driven at 6:834 GHz provides the ^{87}Rb repump. The ^{87}Rb laser beam is brought in collinear with the ^{84}Rb trapping beam just before the expansion and beam splitting optics that lead to the trapping cell. The ‡uorescence from the trapped cloud of ^{84}Rb (^{87}Rb) is modulated at 4:2 (6:0) kHz by switching the repump EOMs on and o¤ at their respective frequencies. The ‡uorescent light is then focused through a 100 ¹m pinhole onto a photomulitiplier tube (PMT) or a calibrated photodiode using a 58 mm f=1:4 lens and demodulated using lock-in ampli…ers in order to reject background due to laser light sattering from the trapping cell surfaces. To ensure good spacial overlap of the ^{84}Rb and ^{87}Rb trapped clouds, we view the trapping region with two charged-coupled device (CCD) cameras positioned at di¤erent angles. Using nearly equivalent sized clouds (» 1 mm Á) of ^{85}Rb in MOT I and ^{87}Rb in MOT II, we adjust the laser alignment until both cameras show minimal spacial deviation when one or the other MOT laser beam is blocked. ^{85}Rb trapped in MOT I was used for this overlapping procedure because the ^{84}Rb clouds were not typically visible on the CCDs. The ^{84}Rb cloud in MOT I and ^{85}Rb in MOT I were shown to occupy the same space in the trapping cell by doing careful position scans using the PMT.

A typical trapping signal for ^{84}Rb is shown in Fig. 54. These data were taken after ^{84}Rb ions had been implanted in the foil for 15 minutes. As the foil temperature rises (trace A) ^{84}Rb is released into the cell and becomes trapped as indicated by the lock-in trapping signal (trace B). We used a calibrated photodiode with a 1 mm Á pinhole to determine the number of trapped atoms. In a calibration run, we implanted ^{84}Rb at a rate of 2 £ 10^8 ions/s for 30 min. Upon releasing, we observed a trapping signal corresponding to » 1:5 £ 10^5 atoms. This gives a trapping e¢ciency of » 2 £ 10$^{i\,6}$, which is » 250 times lower than the e¢ciency we

achieved in trapping ^{82}Rb [71]. We attribute this drop in trapping e¢ciency to the degradation of the dry…lm coating. This is supported by a trapping e¢eciency estimate for single-pass-trapping for hot atoms emitted directly from the foil (i.e., no "bouncing" or temperature re-equilibration with the cell walls occurs). Subsequent cell coatings using SC-77 type dry…lm have yielded trapping e¢ciencies of » 10^{i2} [99].

In order to perform the steps required for loading a fermionic and bosonic mixture into a magnetic trap designed for a sympathetic cooling experiment, it is helpful to obtain long mixed-isotope (^{84}Rb + ^{87}Rb) MOT lifetimes. To this end, we investigated ^{84}Rb lifetimes with and without an overlapped cloud of ^{87}Rb. Since the release of Rb atoms is quickly stopped when the foil heating is turned o¤ (it takes »1 s for the foil to return to room temperature). The decay of ^{84}Rb atoms from a MOT can then be described by

$$\frac{dN_{84}}{dt} = ¡ °N_{84} ¡ ¯_{84;84} \int_{V_{84}} n_{84}^2 dV \qquad (130)$$

where N_{84} is the number of ^{84}Rb in the MOT, V_{84} is the volume of the ^{84}Rb cloud, ° is the loss rate for collisions with hot background gas, $¯_{84;84}$ is the loss rate for light-assisted collisions between trapped ^{84}Rb atoms, and n_{84} is the ^{84}Rb trapped cloud density. We can avoid an analytical solution of Eq. (130) by looking at two trapping regimes. The …rst is the constant density regime which occurs when there is a large number of atoms in the trap, in our case **&** 10^5. In this regime, the density (n_{84}) of the MOT remains constant and the size of the the cloud shrinks as the trap depletes [100]. In this case, the right-hand side (r.h.s.) of Eq. (130) can be simpli…ed to ¡(° + $¯_{84;84}n_{84}$)N_{84}, and we therefore have a pure exponential decay with decay constant $1=¿_1$ = (° + $¯_{84;84}n_{84}$). After the number of atoms

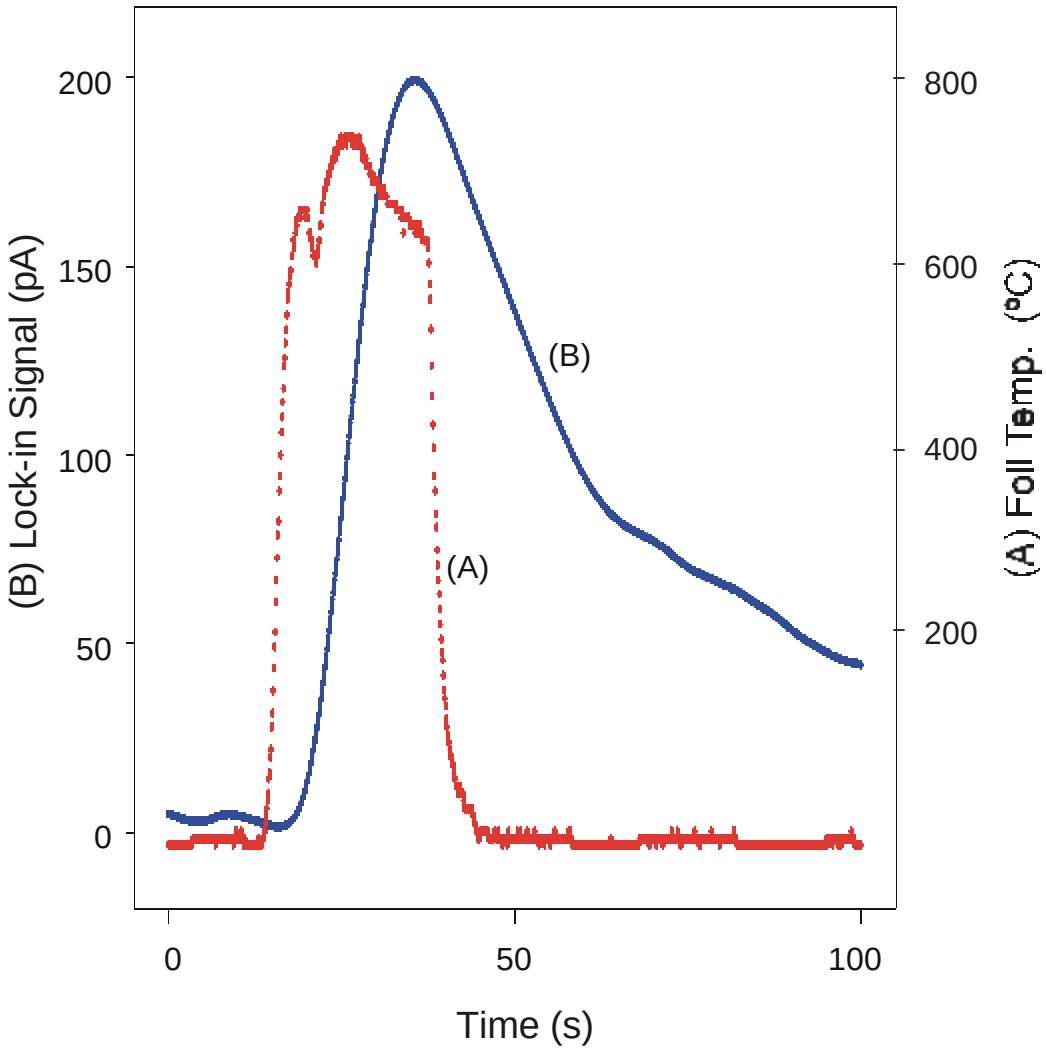

FIG. 54: A typical trapping signal showing the time sequence for the pulsed release and trapping of ^{84}Rb that has accumulated in the yttrium catcher foil for several minutes. Trace (A) is the foil temperature measured with an optical pyrometer. Trace (B) shows the lock-in trapping ‡uorescence signal as the released ^{84}Rb atoms are trapped by the MOT. The lock-in ampli…er has an integration time constant of 3 s.

is reduced to $< 10^4$, the MOT moves into a di¤erent regime where the volume remains approximately constant, but the density diminishes. Since the light-assisted collision term scales as n_{84}^2, the trap loss will eventually be dominated by background gas collisions as the density decreases, leaving $¡ \circ N_{84}$ on the r.h.s. of equation (2) also producing a single exponential ($1=¿_2 = \circ$).

By measuring the ‡uorescence decay from the ^{84}Rb MOT, we …nd that the lifetime …ts very well to a double exponential decay (see Fig. 55) when more than 10^5 atoms are initially loaded into the trap. The di¤erence in lifetime for the short-lived ($¿_1$ = 12:8 (:7) s) as compared to the long-lived component ($¿_2$ = 59 (3) s) of the trap ‡uoresence decay curve indicates that light-assisted collisions are the dominant mechanism for trap loss in the constant density regime (at early times) and this mechanism decreases in signi…cance as the trap depletes. The measurement was taken with a total six beam laser intensity of 48 mW/cm^2, ^{84}Rb trapping transition detuning of $¢ ' ¡15$ MHz and a constant ^{84}Rb density of $3 £ 10^{10}$ cm$^{i 3}$ based on cloud ‡uoresence and size measurements. Using the constant density approximation for equation (2) at early times, we obtain a light-assisted collison trap loss rate of $¯_{84;84} = 3\ (1) £ 10^{i 12}$ cm^{3}s$^{i 1}$, which is in the same range as previous homonuclear light-assisted collision loss rate measured for ^{85}Rb and ^{87}Rb under similar trapping conditions [78]. The uncertainty for $¯_{84;84}$ is mainly due to the absolute uncertainty in measuremed trapped cloud density, which is estimated to be 30%.

We then determined the mixed isotope loss rate for a trapped cloud of ^{84}Rb overlapped with a cloud of ^{87}Rb. To do this, we prepared a stable ^{87}Rb cloud trapped from a vapor as introduced via rubidium getter and then overlapped this with a trapped cloud of ^{84}Rb atoms as released from the catcher foil. The ^{84}Rb

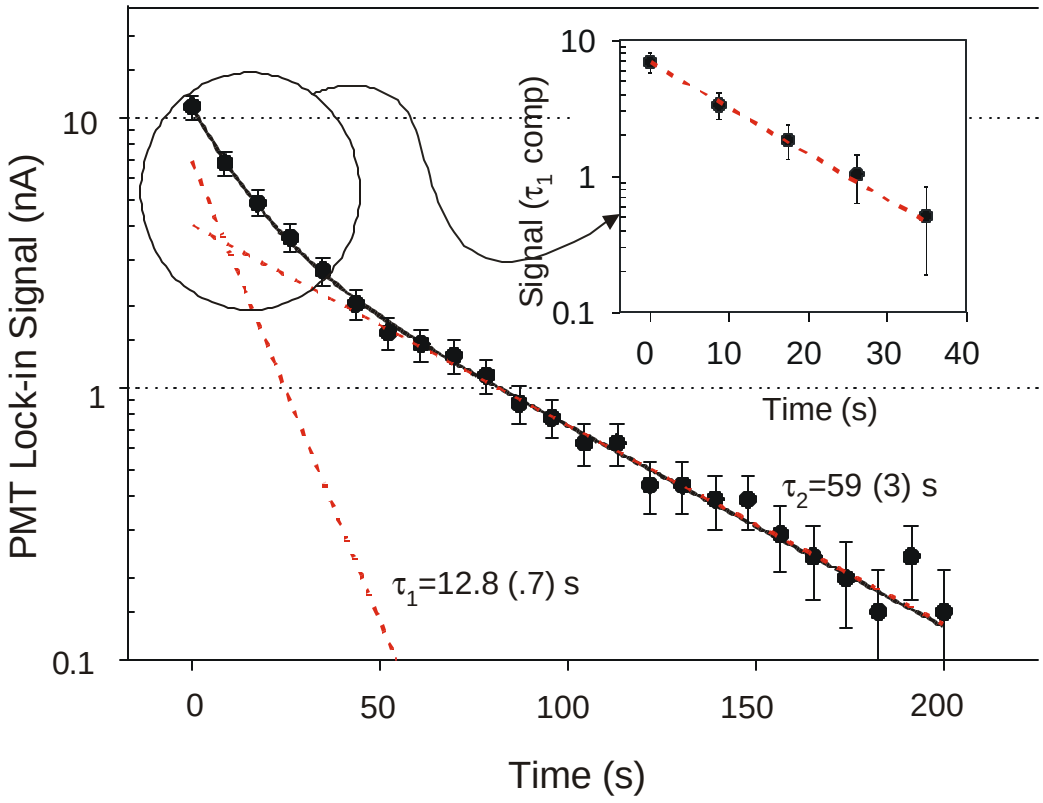

FIG. 55: Plot showing the decay of half a million ^{84}Rb atoms from a MOT. The data …ts well to a double exponential decay (solid line), indicating that there are two loss mechanisms that dominate for di¤erent MOT regimes. At early times, light-assited collisions between trapped ^{84}Rb atoms dominate the trap lifetime giving rise to the fast decay component. As the density of the trap is reduced, light-assisted collisions become less important leaving collisions with the hot background gas as the main loss mechanism, giving rise to the long-lived decay component. The dashed lines are a visual aid showing the long- and short-lived components separately, whereas the solid line is a …t to the experimental data. The inset on the upper right corner is a di¤erence plot for the early part of the decay, which clearly shows a good …t to the fast-lived component.

decay curve is governed by the following

$$\frac{dN_{84}}{dt} = -\frac{N_{84}}{\tau} - \beta_{84;84}\int_{V_{84}} n_{84}^2 dV - \beta_{87;84}\int_{V_{84}} n_{87} n_{84} dV \qquad (131)$$

where the additional term arises from the mixed isotope light-assisted collision loss rate $\beta_{84;87}$. By measuring the short-lived component (τ_1) of the ^{84}Rb signal with and without the ^{87}Rb cloud present, we could determine if any additional loss was introduced due to mixed isotope collisions. Measurements were taken when both species were in the constant density regime with $\approx 5 \times 10^5$ trapped ^{84}Rb atoms in MOT I and $\approx 4 \times 10^7$ ^{87}Rb atoms in MOT II (see Fig.56). Fitting the ^{84}Rb lifetime in this regime gives $\tau_1 = 13.4\,(.7)$ s without the ^{87}Rb cloud, and $\tau_1 = 11.1\,(.5)$ s with the ^{87}Rb cloud overlapped. The ^{87}Rb and ^{84}Rb MOT densities were both measured to be 3×10^{10} cm^{-3}; which gives $\beta_{87;84} = 5\,(3) \times 10^{-13}$ cm^{3}s^{-1}. This measurement of the mixed isotope light-assisted collision loss rate was taken with a six beam laser intensity for ^{87}Rb (^{84}Rb) in MOT II (I) of 12 mW/cm^2 (48 mW/cm^2) and trapping transition detuning of $\delta_{87} = -8$ MHz ($\delta_{84} = -15$ MHz). $\beta_{87;84}$ is small because the low trapping light intensity for ^{87}Rb in MOT II reduces the likelyhood for light-assisted collisions that will expel atoms from the trap. This is further substantiated by the fact the …lltime for ^{87}Rb in MOT II was measured to be 60 s, suggesting a lifetime that is dominated only by hot background gas collision. This shows that under these trapping conditions a ^{84}Rb/^{87}Rb mixture can be simutaneously trapped in overlapping MOTs without signi…cant additional loss of ^{84}Rb. Moreover, without a signi…cant change in MOT lifetime the loading of the magnetic trap for the sympathetic cooling experiment is not very time critical.

Our future plans for the sympathetic cooling experiment are to complete construction of the magnetic trap and to couple it to the …rst trapping cell. A

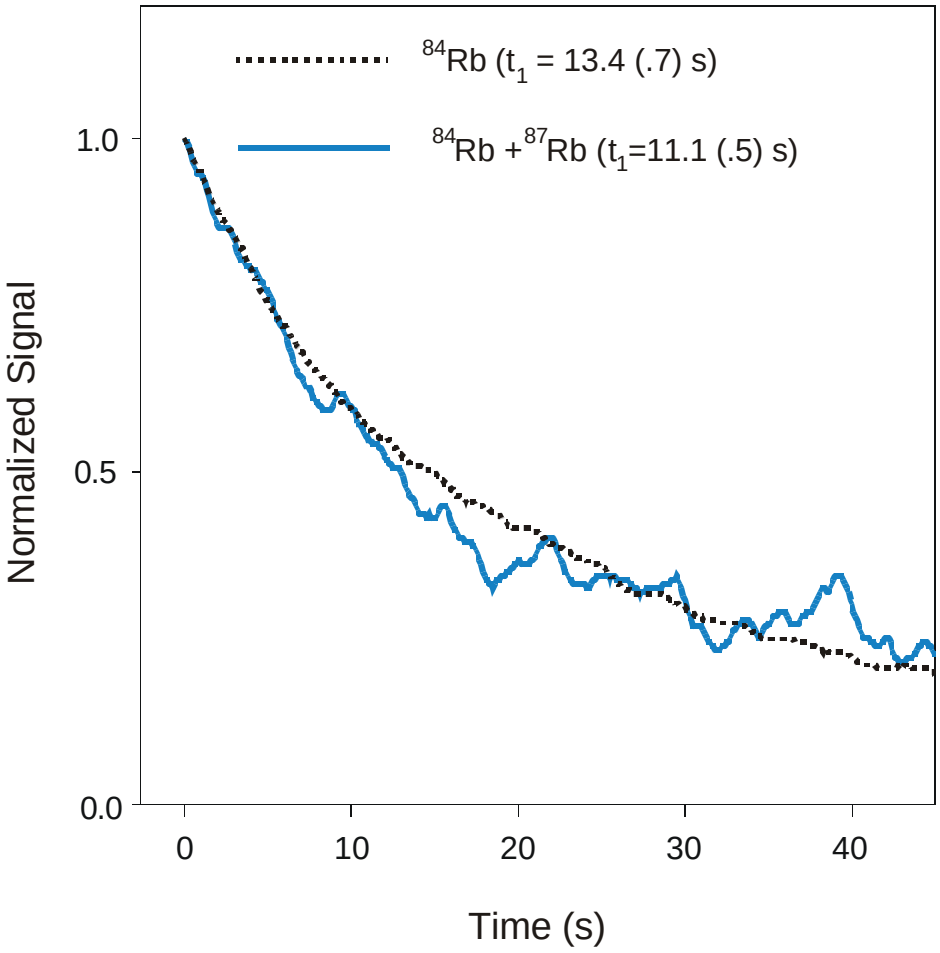

FIG. 56: A normalized lifetime plot for ^{84}Rb without (dotted line) and with (solid gray line) an overlapped cloud of ^{87}Rb. These data were taken with both ^{84}Rb in MOT I and ^{87}Rb in MOT II under the constant-density regime. Numerical …ts of the data yield the lifetime (¿) for each case.

trapped mixture of ^{84}Rb/^{87}Rb will then be transferred to the second cell using a push/magnetic guidance technique [72] that we already have working in our laboratory. We will then explore the sympathetic cooling of ^{84}Rb with a Bose-Einstein condensate of ^{87}Rb in order produce and study Fermi degeneracy in ^{84}Rb.

In summary, we have trapped radioactive ^{84}Rb atoms for the first time and demonstrated the simultaneous trapping of a ^{84}Rb/^{87}Rb mixture in overlapping magneto-optical traps. We have also found trapping parameters for which the addition of a stable ^{87}Rb cloud does not significantly affect the trap lifetime of the ^{84}Rb MOT. With an improved coating [99], it now appears promising to trap a sufficient number of ^{84}Rb atoms to proceed with the sympathetic cooling of ^{84}Rb with a Bose-Einstein condensate of ^{87}Rb in order to explore Fermi degeneracy in ^{84}Rb and investigate ultra-cold mixtures of Fermionic and Bosonic matter.

CHAPTER 6

SUMMARY AND DISCUSSION

This dissertation demonstrates the feasibility of a new method to study parity violation in nuclear beta decay using recently developed atomic physics tools to load a polarized sample into a pure magnetic TOP trap. The signature of a polarized source was demonstrated through the measurement of the positron-spin correlation in the beta decay of ^{82}Rb. This is the …rst time that this parity-violating correlation has been measured as a continuous function of both the positron energy and the emission angle. The distributions were shown to be consistent with expectations for the allowed ^{82}Rb decay given our knowledge of the experimental apparatus.

Major challenges concerning the e¢cient collection and manipulation of radioactive atoms were overcome and su¢cient data were collected to perform a 1% statistical measurement of the correlation in approximately six hours of data collection. The design uses a high-e¢ciency magneto-optical trap (MOT) coupled to an o¤-line mass separator to introduce the short-lived ^{82}Rb ($t_{1=2}$ = 75 s) into the trapping cell after decay of the long-lived ^{82}Sr ($t_{1=2}$ = 26 d) parent source. The trapping e¢ciency is enhanced through the use of a special dry…lm coating and also due to the improved capture velocity of the intense, large-diameter MOT trapping beams.

Measurements of the ^{82}Rb hyper…ne structure for the D_1 and D_2 lines were performed on a sample of trapped atoms held in a MOT. The spectroscopy was complicated by the ac light-shift caused by the MOT laser beams and required a method to account for this e¤ect. The hyper…ne measurements are important for

understanding the optical polarization used in preparation for the beta-asymmetry measurements. Collision properties of a two-component MOT containing both ^{87}Rb and ^{84}Rb were also investigated. These investigations were important in understanding the processes by which atoms are lost in a MOT due to collisions and were a …rst step toward performing sympathetic cooling in a magnetic trap. Sympathetic cooling could be used in the beta-asymmetry measurement to further reduce the temperature ^{82}Rb atoms by evaporatively cooling a co-trapped cloud of stable ^{87}Rb.

The extraction of the ^{82}Rb position-spin correlation coe¢cient awaits an independent determination of the trapped sample polarization. The TOP trap model indicates that the pointing-type polarization can be pushed arbitrarily close to its maximum value, determined from the cloud's droop under gravity, by reducing the temperature of the TOP trapped cloud. The initial goal is to perform a 1% measurement of the correlation-coe¢cient, which requires either a 1% measurement of the cloud distribution or the reduction of the temperature to below 5 ^{1}K. The m-state population must also be investigated and should be an easier problem to solve. In addition, techniques were developed to measure the uncorrelated background and this information will be invaluable in reducing background in future experiments.

A measurement of the positron-spin correlation at the 1% level would be the most precise for a pure Gamow-Teller transition and comparable to measurements made in free neutrons (mixed transition) and pure Fermi-transitions. Any discovery in contradiction to the standard model dictated (V-A) form will require elucidation from the various transitions since a general weak interaction Hamiltonian contains couplings of vector, axial-vector, tensor, and scalar interactions that arise from eight di¤erent coupling coe¢cients (the standard model prescription

reduces the number to two). These couplings cannot be isolated with a single measurement from one type of transition. The trapped atom method has the promise to improve the search for physics beyond the standard model and, in principle, it may be possible to push even beyond the 1% level of accuracy using this technique.

REFERENCES

[1] T.D. Lee and C.N. Yang, Phys. Rev. 104, 254 (1956).

[2] C.S. Wu et al., Phys. Rev. 105, 1413 (1957).

[3] J.D. Jackson, S.B. Treiman and H.W. Wyld, Phys. Rev. 111, 354 (1958).

[4] E. Segre', Nuclei and Particles, 2nd Ed. W.A. Benjamin Inc., Reading, MA (1977), Chap. 9.

[5] E.G. Adelberger et al., Phys. Rev. Lett. 89, 1299 (1999).

[6] C.H. Johnson et al., Phys. Rev. 132, 1149 (1963).

[7] J.D. Ullman et al., Phys. Rev. 122, 536 (1961).

[8] M. Goldhaber, L. Grodzins, A.W. Sunyar, Phys. Rev. 109, 1015 (1958).

[9] J. Deutsch and P. Quin, Symmetry-Tests in Semileptonic Weak Interactions: a Search for New Physics, in Precision Tests of the Standard Electroweak Model, Advanced Series on Directions in High Energy Physics, Vol. 14, P. Langacker, Ed. (World Scientific, NJ, 1995).

[10] P. Bopp et al., Phys. Rev. Lett. 56, 919 (1986).

[11] B.G. Erozolimskii et al., Phys. Lett. B 263, 33 (1991).

[12] M.T. Burgy et al., Phys. Rev. 120, 1829 (1960).

[13] S. Weinberg, Phys. Rev. Lett. 19, 1264 (1967).

[14] A. Salam, in Elementary Particle Theory: Relativistic Groups and Analyticity , edited by N. Svartholm, Nobel Symposium No. 8, (Almqvist and Wiksell, Stockholm, 1969) p. 367.

[15] S.L. Glashow, J. Iliopoilos, and L. Maiani, Phys. Rev. D 2, 1285 (1970).

[16] J.J. Sakurai, Nuovo. Cim 7, 649 (1958).

[17] R.P. Feynman and M. Gell-Mann, Phys. Rev. 109, 193 (1958).

[18] P. Langacker and S.U. Sankar, Phys. Rev. D 40, 1569 (1989).

[19] L.M. Chirovsky et al., Phys. Lett. 94B, 127 (1980).

[20] W.D. Phillips and H. Metcalf, Phys. Rev. Lett. 48, 596 (1982).

[21] E.L. Raab et al., Phys. Rev. Lett. 59, 2631 (1987).

[22] Z.-T. Lu et al., Phys. Rev. Lett. 72, 3791 (1994).

[23] G. Gwinner et al., Phys. Rev. Lett. 72, 3795 (1994).

[24] J.E. Simsarian et al., Phys. Rev. Lett. 76, 3522 (1996).

[25] J.A. Behr et al., Phys. Rev. Lett. 79, 375 (1997).

[26] Z.-T. Lu et al., Phys. Rev. Lett. 79, 994 (1997).

[27] M. Rowe et al., Bull. Am. Phys. Soc. 42, 1627 (1997).

[28] G.J. Beyer et al., Nucl. Instrum. Meth. 96, 437 (1971).

[29] R. Guckert et al. (unpublished).

[30] M. Stephens and C. Wieman, Phys. Rev. Lett. 72, 24 (1994); M. Stephens, R. Rhodes, and C. Wieman, J. Appl. Phys. 76, 3479 (1994).

[31] J.L. Hall et al., Appl. Phys. Lett. 39, 680 (1981).

[32] C. Thibault et al., Phys. Rev. C 23, 2720, (1981).

[33] J. Doyle et al., Phys. Rev. Lett. 67, 603 (1991).

[34] R. Guckert et al., Nucl. Instrum. Meth. Phys. Res. B 126, 383 (1997).

[35] C.J. Myatt et al., Opt. Lett. 21, 290, (1996).

[36] W. Petrich et al., Phys. Rev. Lett. 74, 3352 (1995).

[37] D. Wineland et al., Bull. Am. Phys. Soc. 20, 637 (1975).

[38] T. Hänsch and A. Schawlow, Opt. Commun. 13, 68 (1975).

[39] D. Wineland and W. Itano, Phys. Rev. A 20, 1521 (1979).

[40] S. Stenholm, Rev. Mod. Phys. 58, 699 (1986).

[41] S. Chu et al., Phys. Rev. Lett. 55, 48 (1985).

[42] P.D. Lett et al., Phys. Rev. Lett. 61, 169 (1988).

[43] Jean Dalibard and C. Cohen Tannoudji, J. Op. Soc. Am. B6, 2023 (1989).

[44] C.S. Adams and E. Riis, Prog. Quant. Electr. 21, 1 (1997).

[45] H. Metcalf and P. van der Straten, Physics Reports 244, 203 (1994).

[46] E.L. Raab et al., Phys. Rev. Lett. 59, 2631 (1987).

[47] M. Drewsen, et al., Appl. Phys. B59, 283 (1984).

[48] Z.T. Lu et al., Phys. Rev. Lett. 72, 3791 (1994).

[49] W.D. Phillips and H. Metcalf, Phys. Rev. Lett. 48, 596 (1982).

[50] Z.T. Lu et al., Phys. Rev. Lett. 79, 994 (1997).

[51] A. Gorelov et al., Hyper. Inter. 127, 373 (2000) .

[52] J.E. Simsarian et al., Phys. Rev. A 57, 244 (1998).

[53] J. M. Grossman et al., Phys. Rev. A. 6206,. 2502 (2000).

[54] C.S. Wood et. al., Science 275, 1759 (1997).

[55] M.A. Rowe et al., Phys Rev. A 59, 1869 (1998).

[56] R. Guckert, Ph.D. Dissertation, University of Giessen, Hessen, Germany (1998).

[57] Choice of Zr foil was suggested by John Behr of TRIUMF (1999).

[58] C. Thibault, et al., Phys. Rev. C 23, 2720 (1981).

[59] C. Thibault, et al., Nucl. Phys A367, 1 (1981).

[60] J.L. Hall et. al., Appl. Phys. Lett. 39, 680 (1981).

[61] W.L. Wiese, M.W. Smith, and B.M. Miles, Atomic Transition Probabilities (Na through Ca–A Critical Data Compilation), National Standard Reference Data Series, National Bureau of Standards 22, Vol II, U.S. Government Printing O¢ce, Washington, D.C. (1969).

[62] M. Pearson, L. Orozco, G. Sprouse, private communication (1999).

[63] R.E. Marshak, Riazuddin, and C.P. Ryan, Theory of Weak Interactions in Particle Physics, Monagraphs and Texts in Physics and Astronomy, Vol. 24, R.E. Marshak Ed. (Wiley, NY, 1969).

[64] P. Herczeg, Beta Decay and Muon Decay Beyond the Standard Model; a Search for New Physics, in Precision Tests of the Standard Electroweak Model, Advanced Series on Directions in High Energy Physics, Vol. 14, P. Langacker, Ed. (World Scienti...c, NJ, 1995).

[65] A.L. Migdall et al., Phys. Rev. Lett. 54, 2596 (1985).

[66] G. Gwinner et al., Phys. Rev. Lett. 72, 3795 (1994).

[67] J.A. Behr et al., Phys. Rev. Lett. 79, 375 (1997).

[68] W. Petrich et al., Phys. Rev. Lett. 74, 3352 (1995).

[69] A. Hime et al., "Fundamental Symmetries with Trapped Atoms", Los Alamos Directed Research and Development Proposal, 1999.

[70] H. Behrens et al., Annals of Physics 115, 276 (1978).

[71] R. Guckert et al., Phys. Rev. A 58, R1367 (1998).

[72] C.J. Myatt et al., Opt. Lett. 21, 290 (1996).

[73] P.D. Lett et al., J. Opt. Soc. Am. B 6, 2084 (1989).

[74] R.B. Firestone et al., Table of Isotopes, edited by V.S. Shirley (Wiley, New York, 1996).8th ed.

[75] S.J. Brice, "Some Useful Physics and Equations for the TOP Trap", Los Alamos National Laboratory unpublished report, 1997.

[76] T.B. Swanson, D. Asgeirsson, J.A. Behr, and D. Melconian, J. Opt. Soc. Am. B 15, 2641 (1998).

[77] R.S. Williamson III, P.A. Voytas, R.T. Newell, and T. Walker, Optics Express 3, 111 (1998).

[78] S.D. Gensemer, et al., Phys Rev A 56, 4055 (1997).

[79] M. Kasevich, et al., PRL 66, 2297.

[80] A. Clarion et al., Europhys. Lett. 16, 165 (1991).

[81] Z.T. Lu et al., PRL 77, 3331 (1996).

[82] E. Riis, D.S. Weiss, K.A. Moler, and S. Chu, PRL 64, 1658 (1990).

[83] J. Dalibard and C. Cohen-Tannoudji, J. Opt. Soc. Am. B6, 2023 (1989).

[84] X. Zhao, R. Guckert, S. G. Crane, and D. J. Vieira, Proc. SPIE 3270, 70 (1998).

[85] F. S. Cataliotti, C. Fort, M. Prevedelli, and M. Inguscio, Can. J. Phy. 75, 767 (1997).

[86] S. A. Hopkins, E. Usadi, H. X. Chen, and A. V. Durrant, Optics Comm. 138, 185 (1997).

[87] G. P. Barwood, P. Gill, and W. R. C. Rowley, Appl. Phys. B 53, 142 (1991).

[88] G. H. Fuller, J. Phys. Chem. Ref. Data 5, 835 (1976).

[89] N. Yu, et al., Phys. Rev. A 50, 2738 (1994).

[90] A. Gallagher and E. L. Lewis, Phys. Rev. A 10, 231 (1974).

[91] M.H. Anderson et al., Science 269, 198 (1995); K.B. Davis et al., Phys. Rev. Lett. 75, 3969 (1995); C.C Bradley et al., ibid. 75, 1687 (1995); C.C Bradley et al., ibid.79, 1170 (1997).

[92] J.M.K.V.A. Koelman et al., Phys. Rev. Lett. 59, 676 (1987); A. Imamoglu and L. You, Phys. Rev. A 50, 2642 (1994); J. Javanainen and J. Ruostekoski, Phys. Rev. A 52, 3033 (1995); T. Bush et al., Europhys. Lett. 44, 1 (1998).

[93] M. Houbier et al., Phys. Rev. A 56, 4864 (1997).

[94] H.F. Hess, Phys. Rev. B 34, 3476 (1986); H.F. Hess et al.,Phys. Rev. Lett. 59, 672 (1987).

[95] B. DeMarco and D.S. Jin, Science 285, 1703 (1999).

[96] J.P. Burke, Jr. and J.L. Bohn, Phys. Rev. A 59, 1303 (1999).

[97] C.J. Myatt et al., Phys. Rev. Lett. 78, 586 (1997).

[98] The relevant ^{83}Rb trapping transitions were measured to be very close to those reported by Thibault [58]. The $5S_{1=2}; F = 3 \; ! \; 5P_{3=2}; F^{0} = 4$ trapping

transistion was referenced directly to the $5S_{1=2}; F = 3 \; ! \; 5P_{3=2}; F^{0} = 2$ saturated absorption line in ^{85}Rb and the $5S_{1=2}; F = 2 \; ! \; 5P_{3=2}; F^{0} = 3$ repump transition was generated from the second lower sideband produced by an electro-optic modulator driven at 1:592 GHz.

[99] The authors have recently produced cell coatings using SC-77 type dry…lm, which has enhanced our trapping e¢ency to » $10^{i 2}$: Manuscript in preparation.

[100] T. Walker et al., Phys. Rev. Lett. 64, 408 (1990).